UNIVERSITY
OF OSLO

Harish Pruthviraj Jain

Collective Emergent Behaviour of Active Cellular Systems

Thesis submitted for the degree of Philosophiae Doctor

Department of Physics
Faculty of Mathematics and Natural Sciences

Njord Centre for Studies of the Physics of the Earth



2025

© Harish Pruthviraj Jain, 2025

Series of dissertations submitted to the
Faculty of Mathematics and Natural Sciences, University of Oslo
No. 2673

ISSN 1501-7710

All rights reserved. No part of this publication may be
reproduced or transmitted, in any form or by any means, without permission.

Cover: UiO.
Print production: Graphic center, University of Oslo.

Dedicated to my sister, Komal

Abstract

Using multi-phase field models, we study the collective emergent behavior of a monolayer of active, deformable interacting cells, with an emphasis on neighbour exchange process involving four cells called T1 transition, also known as cell intercalation. The cells undergo drastic shape deformations during T1 transitions, leading to a buildup of energy prior to the T1 transitions and a subsequent release of energy post T1 transitions near the sites where junctions remodel. These deformations have a dual impact: cells losing neighbours relax their shapes, while cells gaining neighbours elongate. T1 transitions contribute to a transient quadrupolar flow field where the cells undergoing these transitions acquire high speeds. The relative dispersion of cells within a monolayer is solely determined by the cumulative number of T1 transitions, highlighting the importance of T1 transitions in mixing of cells. By analyzing the spatial relationships between successive T1 transitions undergone by a cell, we observe an emergent directional migration of cells that depends on the underlying topological changes in the neighborhood. Lastly, we utilize Minkowski Tensor-based p-atic order parameters as robust shape descriptors to describe cell shape rotational symmetries in both experimental and simulated monolayers.

Sammendrag

Vi benytter multifasefeltmodeller til å studere emergente fenomener i et aktivt monolag bestående av deformerbare celler som interagerer med hverandre. Her har vi særlig fokus på en prosess kjent som T1-transisjon hvor to cellepar utveksler naboer. I løpet av disse transisjonene blir celleformene kraftig deformert. Dette fører til en opphopning av energi i områdene hvor cellekontakten deformeres før et nabobytte, og deretter en energifrigjøring. Disse celledeformasjonene har to konsekvenser: i) celler som mister en nabo relakserer formen sin, ii) mens celler som får en ekstra nabo forlenges. T1-transisjonene bidrar til et bevegelsesmønster med fire virvler, hvor cellene som utveksler naboer oppnår høyere hastigheter. Den relative spredningen av cellene i monolaget avhenger kun av antall T1-transisjoner. Dette viser at T1-transisjoner er nøkkelen til celleblanding og relative cellebevegelser i vevet. Vi observerer at cellene begynner å bevege seg på en målrettet måte, avhengig av på hvordan påfølgende T1-transisjoner er plassert i forhold til hverandre. Til slutt bruker vi p-atiske ordensparametere basert på Minkowski-tensorer som en robust beskrivelse av celleformsymmetrier i eksperimentelle og simulerte monolag.

Preface

This thesis is submitted in partial fulfillment of the requirements for the degree *Philosophiae Doctor* at the University of Oslo, Norway. The research presented here was conducted at Njord Centre for Studies of the Physics of the Earth, University of Oslo. The research has been undertaken under the supervison of Professor Luiza Angheluta. The thesis is a collection of four papers discussing collective emergent behavior of a monolayer of active, deformable interacting cells. Large language models available at *https://gpt.uio.no* were used to correct some grammatical errors. This thesis is my original work and I take full responsibility for its content.

Acknowledgements

First and foremost, I would like to express my profound gratitude to Professor Luiza Angheluta for her exceptional guidance, enthusiastic scientific discussions, and for fostering a friendly atmosphere for research. Her continuous support and encouragement throughout this journey have been invaluable.

I would also like to extend my heartfelt thanks to Axel Voigt, Richard D. Jun-Geet Ho, Lea Happel, Amin Doostmohammadi, Griseldis Oberschelp, Rastko Sknepnek, and Valeriia Grudstyana for their brilliant collaboration and engaging discussions. Their insights and expertise significantly contributed to the progress of my research.

I am deeply appreciative of Jonas, Vidar, Dag, Franzi, Silja, Ali, Emily, Nigar, Thomas, and Marie for the engaging scientific discussions on physics of life and beyond, and for making the research journey enjoyable through their camaraderie.

A special thanks to the extraordinarily supportive atmosphere at Njord Centre and Porelab, sustained by an amazing set of people, which made it a delight to come to work every day.

I am grateful to all my friends who have been my companions through various phases of my life.

Finally, I wish to express my deepest gratitude to my family - my mom, Alka, my dad, Pruthviraj, my sister, Komal, and my brother, Gourav, for their unwavering support.

Thank you all for being an indispensable part of this journey.

Harish Pruthviraj Jain
Oslo, December 2024

List of publications

The following four papers form the foundation of my PhD:

Paper I: *Robust statistical properties of T1 transitions in a multi-phase field model of cell monolayers*, Harish P. Jain, Axel Voigt, Luiza Angheluta, Scientific Reports 13.1 (2023): 10096 [1].

Paper II: *From cell intercalation to flow, the importance of T1 transitions*, Harish P. Jain, Axel Voigt, Luiza Angheluta, Physical Review Research, 2024, 6.3: 033176 [2].

Paper III: *Emergent cell migration from cell shape deformations and T1 transitions*, Harish P. Jain, Axel Voigt, Luiza Angheluta, arXiv preprint, 2024, arXiv:2412.19686 [3]. *Submitted to Physical Review Research*

Paper IV: *Quantifying the shape of cells - from Minkowski tensors to p-atic order*, Lea Happel, Griseldis Oberschelp, Valeriia Grudtsyna, Harish P. Jain, Rastko Sknepnek, Amin Doostmohammadi, Axel Voigt, bioRxiv preprint, 2025, pp.2025-01 [4]). *Submitted to ELife*

In addition to the above listed publications, I have co-authored two articles that were published during my PhD. However, the research was done prior to my PhD, and are thus not included within the thesis. The articles are :

1: *Impact of contact inhibition on collective cell migration and proliferation*, Harish P. Jain, Dennis Wenzel, Axel Voigt, Physical Review E, 2022, 105.3: 034402 [5].

2: *Evolution of phenotypic plasticity leads to tumor heterogeneity with implications for therapy*, Simon Syga, Harish P. Jain, Marcus Krellner, Haralampos Hatzikirou, Andreas Deutsch, PLOS Computational Biology, 2024, 20.8: e1012003 [6].

Contents

1 Introduction 1
1.1 Cell-based life 1
1.2 Epithelial monolayers 3
1.3 Models 7
1.3.1 Vertex model 7
1.3.2 Cellular Potts model 9
1.3.3 Multi-Phase field model 10
1.4 Thesis structure 11
1.5 Notation 12
2 Multi-phase field model 13
2.1 Cell as a phase field 13
2.2 Cahn Hilliard energy 16
2.3 Interaction energy 20
2.4 Activity 24
2.5 Multicellularity 28
2.6 Boundary conditions 30
2.7 Initial conditions 30
3 Numerical Methods 33
3.1 Introduction 33
3.2 The notion of weak derivatives 34
3.3 Weak formulation of a partial differential equation 35
3.4 Spatial discretisation of the weak form 36
3.5 Discretisation of the weak form of the multi-phase field model . 38
3.6 Time discretisation 41
3.7 Software and hardware 43
3.8 Mesh refinement 43
3.9 Parallel computation 44
4 Supplementary results 45
4.1 Morphological influence of activity and deformability 45
4.2 Shape index 45
4.3 Center of mass 48
4.4 T1 transitions 49
4.5 P-atic shape descriptors 51

5 Summary of papers and outlook 53
5.1 Introduction 53
5.2 Paper I: Robust statistical properties of T1 transitions in a multi-phase field model of cell monolayers. 53
5.3 Paper II: From cell intercalation to flow, the importance of T1 transitions. 55
5.4 Paper III: Emergent cell migration from cell shape deformations and T1 transitions 56
5.5 Paper IV: Quantifying the shape of cells - from Minkowski tensors to p-atic order 58
5.6 Outlook. 59
Bibliography 61

Paper I Robust statistical properties of T1 transitions in a multi-phase field model of cell monolayers 73

Paper II From cell intercalation to flow, the importance of T1 transitions 89

Paper III Emergent cell migration from cell shape deformations and T1 transitions 101

Paper IV Quantifying the shape of cells - from Minkowski tensors to p-atic order 117

List of Figures

1 Embryonic development 2
2 Migration of Epithelial cells 3
3 Cellular structures 5
4 Variants of vertex models 8
5 Cellular Potts model 9

6 Phase field of a cell 14
7 Double well potential 16
8 Cahn Hilliard energy 16
9 Circular cell 19
10 Interaction energy as function of phasefield 21
11 Interaction energy as function of spatial coordinates 22
12 Advection field 24
13 Shape deformation tensor 25
14 Cells and their polarity 27
15 Wall collision 28
16 Periodic boundary conditions 30
17 Initial condition 31

18 Triangulated grid 36
19 Mesh of interacting cells 40

20 Effect of activity and deformability 46
21 Shape index and shape deformation tensor 46
22 Distribution of shape index and speed 47
23 Global fields 48
24 Distribution of number of neighbours 49
25 T1 transition statistics 50
26 Cell and its shape descriptors 52

Chapter 1

Introduction

> The key to every biological problem must finally be sought in the cell; for every living organism is, or at some time has been, a cell
>
> *E. B. Wilson*

> How can things so small be so important?
>
> *Isaac Asimov*

1.1 Cell-based life

Cells are the simplest entities that can be considered alive. Life as we know it cannot be described without cells. The word cell is derived from the latin word for a small room, *cellula*. Just like a room consists of myriads of objects, a cell is filled with numerous subcellular components that are specialised in their function. The hallmark behavior of cells is their ability to self-replicate, which results in the prolonged survival of the genes inside the cells. Once in a while, the genes undergo mutation which may or may not affect the observed characteristics (phenotype) of the cells. Evolution by natural selection results in prolonged survival of genes with better survival and reproductive potential. The rich biodiversity of our planet has developed due to the emergence of a vast variety of cells that interact with each other and their environment, modifying and reacting to their surroundings, and adapting to all sorts of ecological niches thanks to evolution by natural selection.

Marvelously, two living organisms, however different—such as an elephant and a tomato plant—are made up of cells whose functionality is encoded in a chemical structure known as DNA [8]. The information encoded within the DNA, along with the conditions of the external environment, together define the development and function of all living creatures. Cells can function as "alive" organisms by

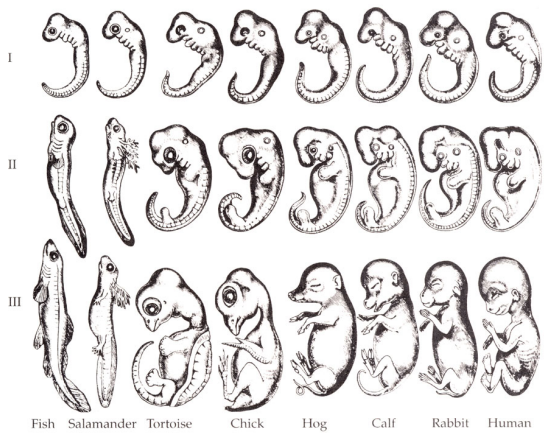


Figure 1: *Inaccurate* drawings of embryonic development of several organisms by George Romanes, 1892 Adapted from Ref [7], Public Domain

themselves, like most single cellular organisms including bacteria and archaea. Additionally, cells can form collections of similar or dissimilar cell types to create more complex multicellular organisms, such as animals, plants, and fungi, which are considered "alive" only as a collective. As the opening quote suggests, all multicellular organisms were once just a single cell. This single cell undergoes division and specialization in subsequent generations to form complex multicellular organisms. In its DNA, this single cell contains all the information necessary to form a complex, functional organism such as a human, which comprises over 10^{13} cells of over 200 types [8]. In fact, this thesis is written by a collection of cells that possesses the mysterious emergent property of consciousness that thinks about itself and the universe in which it resides.

Every multicellular living creature is a pattern, and not a random collection of cells lumped together. In fact, they are multi-scale spatiotemporal patterns. A DNA molecule is not a random structure made up of nucleotides; rather, its specific pattern encodes all the information necessary for the functioning of an organism. Cells are fluid and organelle-filled bodies that perform a specific set of roles thanks to their distinct structural and biochemical patterns. A large collection of cells of different types coordinate in a specific pattern to make the heart beat the way it does. Human beings are patterned structures who can be individually identified based on their visual appearance. Living organisms also form temporal patterns; The proper functioning of the heart relies on the timing of opening of the valves of the heart.

The marvelous robustness in the formation of these patterns has enabled complex life to flourish on this planet. Collective behaviour renders formation of complex migration patterns at scales larger than those of individual cells. Every multi-cellular organism is a pattern formed from the collective emergent behavior of cells in a process called morphogenesis. The most drastic form of collective cellular behavior is encountered in the early development of a multi-cellular organism. Most multi-cellular organisms develop from a sexually fertilized single-cell zygote and undergo significant changes to become full-fledged organisms.

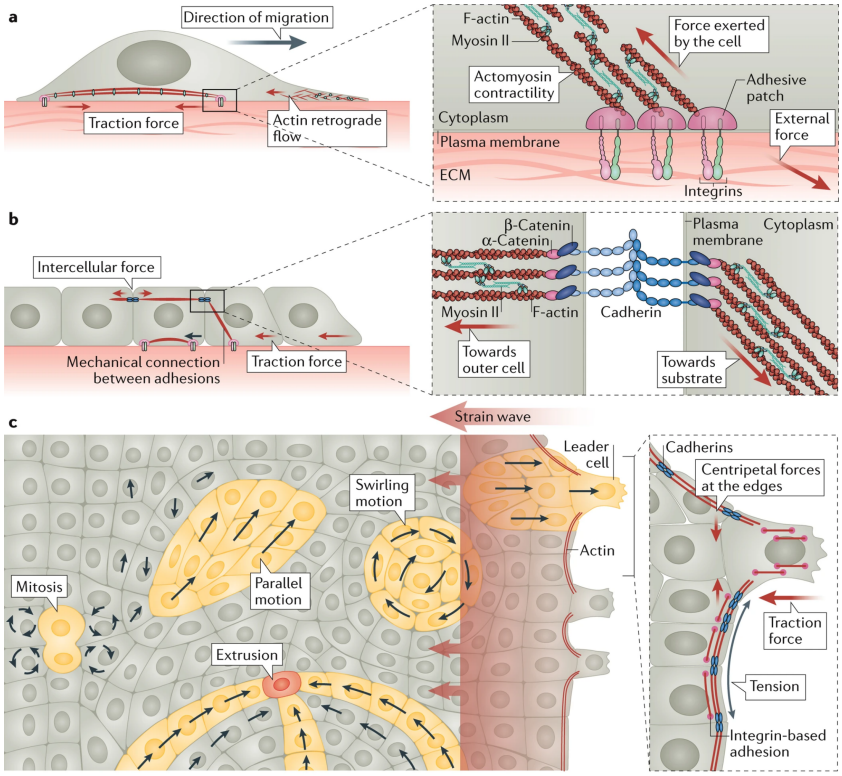


Figure 2: (a) Single epithelial cell migrates by crawling on a substrate. (b) Collection of cells linked together by Cadherin bonds exert traction force on a substrate. (c) Modes of migration within a monolayer, and at the invading front. Adapted from Ref [11] with permissions from Springer Nature.

As illustrated in Figure 1, drawings of embryonic development of various organisms were made by George Romanes but were incorrectly attributed to Ernst Haeckel, who presented them as his own creations. Although these drawings were found to be fraudulent [9], they depict the idea that different organisms start very similarly in their early stages of development. Over time, these organisms accumulate several small changes leading to various distinct morphologies. While the drawings are inaccurate, the underlying concept of small differences accumulating to create rich variations has been observed at several stages of developmental biology [10].

1.2 Epithelial monolayers

Tackling the formation of patterns at different length and time scales across various cell types and organisms is far beyond the scope of this thesis. Instead, we will restrict our focus to the emergent patterns that result from the collective active behavior of cells that form a confluent monolayer. A confluent monolayer consists of a single layer of tightly packed cells, with dynamics mostly restricted to a two-dimensional (2D) layer, which can either be flat or curved. Specifically, we will consider confluent monolayers of epithelial cells. Epithelial tissues are one of the four most simple types of animal tissues along with connective tissue,

nervous tissue and muscle tissue. They form the outer surface of the skin and line the surface of several organs. They play a crucial role in protection, secretion, absorption and transport, and usually form different types of structures such as flat or curved sheets, and tubes [8].

Epithelial cells migrate during several key processes pertaining to morphogenesis, wound healing and cancer metastasis [12, 13]. The migration of single epithelial cells, shown in Figure 2a, relies on elaborate cellular machinery involving the cytoskeleton, adhesive molecular complexes, and substrate characteristics. Actin filaments, one of the primary structures that make up the cytoskeleton, are polymerized at the leading edge of the cell, creating a protrusion at the front called the lamellipodia [8, 11]. The actin filaments are disassembled at the rear of the cell, giving the appearance that the cytoskeleton is moving from the rear to the front. This process is known as actin treadmilling. At the same time, cells form attachments called focal adhesions with the underlying substrate through integrin-based complexes. Myosin II, a molecular motor, binds to the actin filaments mostly in the middle and rear of the cell, creating structures known as actomyosin networks. The Myosin II motors generate contractile forces through ATP (Adenosine Triphosphate) hydrolysis, which are transmitted to the substrate through focal adhesions. This process coordinates with actin treadmilling to generate traction forces that move the cell, making it appear as if the cell is crawling.

Epithelial cells are not only mechanically coupled to the substrate; they are also mechanically coupled to other epithelial cells. The intercellular coupling between epithelial cells is primarily mediated through E-Cadherin-based adherens junctions, as shown in Figure 2b. Forces are transmitted across cells through cytoskeletal filaments like actin, linking cell-cell adhesion junctions and cell-substrate adhesion junctions with one another [14]. These junctions dynamically remodel themselves to change the topology of the epithelial cell cluster, which allows for emergent flow behavior in the cell layer. This remodeling of cell junctions enables epithelial monolayers to adapt their shape and function in response to biochemical, mechanical and environmental cues.

A remarkable feature of epithelial cells is their ability to form sheets of tightly packed cells. These sheets are ubiquitous in many animals, such as in the lining of our guts or the epidermis layer of our skin [8]. When epithelial sheets form a single layer of tightly packed cells, it is termed a confluent epithelial monolayer.

Confluent epithelial monolayers bear a striking resemblance to other cellular structures. Cellular structures are primarily defined by two phases: one phase forms a thin boundary enclosing the other bulk phase, which constitutes the cells. These cells, which are primarily polygonal in 2D or polyhedral in 3D, form a tessellation known as cellular structures. [15]. There are several examples of cellular structures in nature at various length scales, see Figure 3. For instance, soap bubbles confined between two plates self-organize into structures called foams [16]. Similarly, columnar basalts comprise rocks separated by fractures that are organized as polygonal prisms [17]. Cellular patterns also arise after the dewetting of polymer films when annealed above glass transition temperatures [18].

Epithelial cells form *active cellular structures* in which individual cells are active. These cells are self-propelled particles that convert energy from ATP



Figure 3: (left) Confocal section of embryonic tissue within zebrafish embryo. Adapted from Reference [20] with permissions from Springer Nature. (middle) Basalt columns at Giant's Causeway, Northern Ireland. Adapted from Wikipedia, Public domain. (right) Soap bubbles. CC0 License.

hydrolysis to reorganize their cytoskeleton and adhesive junctions, enabling them to migrate and change shape [19]. In contrast to passive systems, energy transition happens locally within a cell. Due to their resemblance to foams, they are also referred to as active foams [20].

As epithelial cells are active, they undergo complex emergent collective motion, which is essential for the early development of an organism, wound healing, and cancer metastasis [12, 21]. In epithelial sheets exposed to a free surface, the cells at the leading edge are polarized, meaning they have a directional orientation, and exhibit stronger traction forces than the cells in the bulk, as shown in Figure 2c. The cells at the leading edge are linked together through a thick actin belt that spans across multiple cells, connecting the leader cells to their followers [11]. In the context of wound healing, the leader cells are polarized and migrate to close the wound, effectively pulling the trailing cells along with them. [13, 21, 22].

However, away from the free edge, within the bulk, cells exhibit coordinated migration in the apparent absence of any free space. Figure 2c shows different forms of collective migrations within the bulk of a confluent epithelial monolayer. Cells can form small clusters that polarize and move collectively in the same direction. Alternatively, cells can exhibit migration patterns that change the neighbourhood topology of the monolayer. The neighbourhood topology changes when the neighbours of the cells change, and this is mediated through three elementary types of topological transitions called T1 (junction remodelling without change in cell number), T2 (cell death), and T3 transitions (cell division) [11, 15].

T1 transitions, also called cell intercalations, are neighbour exchange events that involve two neighbouring cells breaking contact and two of their neighbours making contact. T1 transitions alter the neighbourhood topology of the monolayer without changing the total number of cells. In passive systems such as foams, T1 transitions occur either due to external forces or when the system relaxes to an equilibrium [15]. In a system of active self propelled deformable particles, T1 transitions could arise as a result of shape deformations arising due to the interplay between activity and interactions with neighbours [1]. Also, in biological systems, apart from activity due to self propulsion, additional activity that changes the structural properties of cells could also give rise to T1 transitions. In some situations, the molecular motor Myosin II is enriched between two cell

junctions [23, 24]. Localization of Myosin II, along with its activity, causes remodeling of adherens junctions, leading to junction shrinkage. The exact biochemical mechanisms of this process is still unknown [25]. In such situations, T1 transitions can also be polarised, i.e., the cell junction that shrinks/expands has a fixed orientation, as observed during the convergence-extension of the Drosophila germband during gastrulation [23, 26]. T1 transitions also induce morphological changes of flat sheets in three dimensions through folding such as archenetron elongation in sea urchin embryos and tube formations in Drosophila embryos [27, 28]. Several examples of T1 transitions among biological cells are discussed in the Review [29]. In some tissues, higher order junctions known as rosettes(where 4 or more cells meet) can be stable, as cells can regulate their rigidity by controlling their cytoskeletal structures and adhesive complexes [29].

T2 transitions, also known as apoptosis or cell death, occur when a cell is either extruded out of the monolayer by its neighbours or when the cell shrinks and vanishes [30]. Epithelial monolayers often function as tight barriers to protect other tissues, and cell apoptosis could potentially cause a rupture in this barrier. However, cells undergoing apoptosis coordinate their death with the help of their neighbours. As the apoptotic cell shrinks or is extruded, the neighbouring cells flow into the vacated space, ensuring that the barrier remains intact and functional [31]. T2 transitions are also observed within passive systems such as foams [15]. Furthermore, T2 transitions are linked to nematic defects within the epithelial monolayer. Due to their shape anisotropy, epithelial cells align to collectively exhibit nematic order. At sites of ($+1/2$) topological defects, stresses generated result in the extrusion of cells [30].

T3 transitions involve the division of cellular units and are observed only within active systems. The most important characteristic of life is the ability of cells to self-replicate, making T3 transitions fundamental to all forms of life, whether single-celled or multicellular. In epithelial monolayers, T3 transitions contribute to dipolar flow [32]. T3 transitions also play significant role in tissue development [33] and cancer formation [34].

T2 and T3 transitions in tissues are interrelated as their balance is essential for maintaining cell number dependent tissue homeostasis. Excessive T3 transitions can lead to the crowding of cells, necessitating T2 transitions (apoptosis) to extrude cells and maintain homeostasis [35]. Disruptions in this balance between T2 and T3 transition rates occur during cancer, where mutant cells either fail to undergo apoptosis at the appropriate time, undergo uncontrolled cell division, or induce apoptosis in healthy cells [36].

Collective migration in epithelial cells is also affected by the geometry of their confinements. Collective directed migration is induced in neural crest cells through geometrical constraints [37]. In vitro, cells that were restricted to a circular geometry exhibited persistent rotational movement that was dependant on cell density and confinement sizes [38]. Cells that were confined to rectangular shaped confinements exhibited different modes of migration depending on the width of the confinement [39].

A key phenomenon essential to functioning of epithelial monolayers is the jamming transition. Cell motion is arrested in some epithelial monolayers when

cell density increases due to crowding [40]. The appearance of a wound results in reduction of density, and cells unjam to fill in the wound [21]. Epithelial cells can also unjam at high densities. For instance, in asthmatic airway epithelium, cells fluidise by modifying their shape [41].

The rich variety of collective behaviour due to self-organisation of cells in epithelial monolayers, and their important role in morphogenesis, cancer migration and wound healing, merits studying them through multi-disciplinary approaches involving biology, physics, mathematics, chemistry, and computation. An important approach to study these tissues is by using mathematical and computational models as elucidated in the next section.

1.3 Models

To begin understanding cells and their collective behaviour, we have to first make a representation of the cells. This is achieved through models. The first model of a cell emerged in the mind of Robert Hooke when he first saw cells through a microscope. Over the years with advances in microscopy techniques, several aspects of cells were highlighted. Illustrators would also combine the knowledge to create visual cellular models to represent cells, such as one in Figure 2. Such visual models allows us to develop an intuitive feel of the cellular behaviour.

We would like the models to help us predict cellular behaviour and understand the fundamentals of biological pattern formation. To aid with this, mathematical models, some of which deeply rooted in physics have proved to be tremendously beneficial [42]. As mathematical models of biological systems are approximate representations of much more complex reality, extreme care must be taken while choosing the underlying assumptions and in generalising the observed behaviour. If the theory proposed in the form of the model is based on experimental evidence, then it is likely to predict experimental observations with a higher accuracy. Additionally, use of models allow for studying some aspects about animals without explicit animal testing making them ethically relevant.

We will outline three classes of models used extensively to study epithelial monolayers namely the Vertex model, Cellular Potts model and Multi-phase field model. For comprehensive reviews on different classes of models including the 3 models discussed here, see References [43–46]

1.3.1 Vertex model

Vertex models are among the most popular models for representing epithelial tissue. The earliest of these models were not only used to describe epithelial monolayers [48], but also other cellular structures such as soap bubbles [49], foams [50], and grain growth [51]. In vertex models, cells are represented as polygons or polyhedrons that share junctions and vertices. The Figure 4 shows some variants of vertex models for epithelial monolayers.

The dynamics of these models are defined in terms of the equations of motion of the vertices [47]. Vertices are points that are common to three or more cells. The shape of each cell is described by the set of vertices that form its boundaries.

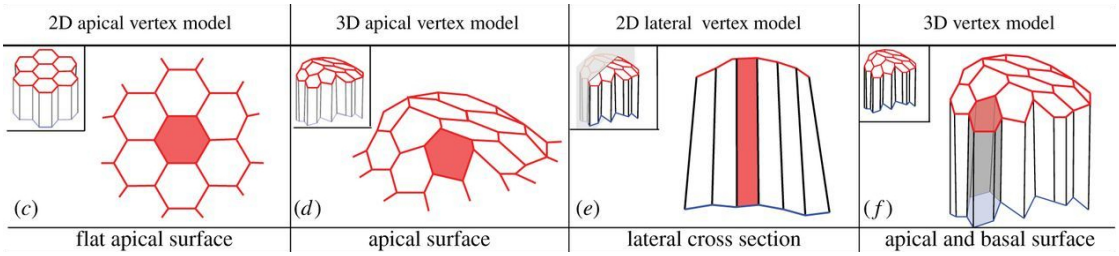


Figure 4: Variants of vertex models differentiated based on the dimension of space or the portion of epithelial monolayer. Reproduced from the Ref [47], Creative Common Attribution License

Typically, first-order dynamics are assumed by ignoring inertia. The external and internal forces that develop are balanced by the drag force. If the viscous drag coefficient is η and F_i is the total force on vertex i, the vertex dynamics can be described as follows

$$\eta \frac{d\mathbf{x}_i}{dt} = \mathbf{F}_i \tag{1.1}$$

Forces can be directly defined or arise as a result of energy minimization, such that given an energy E, the forces can be determined as $\mathbf{F} = -\nabla E$. Typically, this energy consists of terms related to surface and line tension. The surface tension term is minimized at a given target cell area, while the line tension is minimized at a given target cell perimeter.

Vertex models have successfully reproduced several experimentally observed behaviors, such as tissue elongation during amphibian gastrulation and Drosophila germ-band extension [52], solid-fluid transitions in tissues [53], and three-dimensional morphological changes such as invagination and evagination [54], among others. T1 transitions involve the annihilation and creation of vertices and are usually introduced through ad-hoc methods [55, 56]. When a cell-cell junction falls below a certain threshold length, the junction is removed between the two cells, and a new junction is created between two of their neighbours. T1 transitions with biochemical couplings to simulate planar polarized T1 transitions have also been explored and modeled [57–59]. Additionally, T1 transitions of finite duration with intermediate extracellular gap have been modeled using vertex models [20].

Vertex models are computationally efficient compared to other models, such as multi-phase field models, and allow for the easy incorporation of a large number of cells [44]. However, the restriction to polygonal shapes is a notable disadvantage. This geometric limitation can impact the accuracy of simulations when cells undergo significant shape changes during developmental processes. Despite this, vertex models remain a powerful tool due to their balance of computational efficiency and the ability to capture essential cell-cell interactions in both 2D and 3D contexts. For reviews on vertex models applied to biological systems, see References [47, 60, 61]

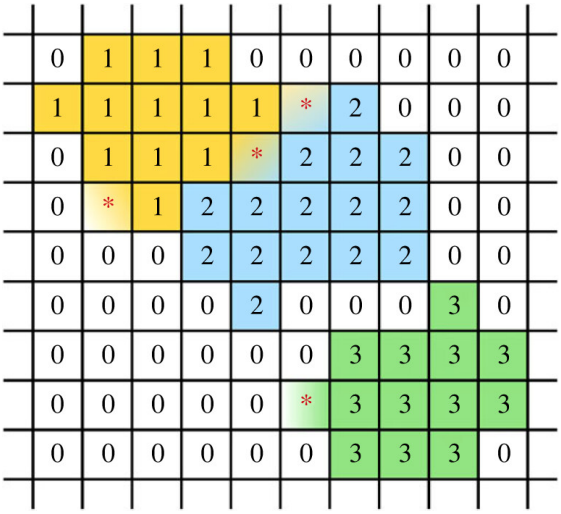


Figure 5: Cellular Potts Model. A cell is a collection of pixels with the same value. The value 0 denotes the extracellular matrix. Pixels marked with asterisk are selected for state update. Adapted from Ref. [62], Creative Commons Attribution License

1.3.2 Cellular Potts model

Cellular Potts Model (CPM) was first used to model cell sorting emerging due to mismatched interactions between cells [63, 64]. In CPM, cells are represented as a collection of pixels with a particular index value on a discrete lattice (See References [65, 66] for reviews). Figure 5 shows a lattice state for a cellular Potts model. Three cells are marked with the indices 1, 2, and 3, while the extracellular matrix is marked with 0. This description allows for non-polygonal cell shapes. In CPM models, a Hamiltonian (H) is defined to model cellular phenomena including cell-cell interactions, cell-extracellular matrix interactions, cell activity, growth, division, and apoptosis. An example of an Hamiltonian in CPM is given as

$$H = \sum_{i \neq j} J(\sigma_i, \sigma_j) + \sum_i \lambda (A_i - A^0)^2 + \sum_i \gamma (P_i - P^0)^2 \tag{1.2}$$

where σ_i and σ_j are the states of neighbouring lattice sites i and j, $J(\sigma_i, \sigma_j)$ is the interaction energy between these sites. A_i and P_i is the area and perimeter of cell i, respectively. A^0 and P^0 are the target area and perimeter, respectively.

In each time step, a random collection of lattice sites is chosen, marked by an asterisk in Figure 5. The change in the Hamiltonian when the lattice site swap its state with one of its randomly chosen neighbour is calculated. The lattice sites are updated according to the Metropolis algorithm [67]. If the Hamiltonian reduces then the change is accepted. If the Hamiltonian increases then the change is accepted with a probability that is inversely proportional to the magnitude of the change in Hamiltonian, according to

$$P(\Delta H) = \exp\left(-\frac{\Delta H}{T}\right) \tag{1.3}$$

where ΔH is the change in Hamiltonian, and T is an effective temperature that tendency to accept positive changes in Hamiltonian. This probabilistic acceptance

of state change which increase the Hamiltonian can aid is escaping local minima of the Hamiltonian.

In the context of collective cell behaviours, CPM have been used to model cancer migration and growth [62, 65], convergent-extension of the frog Xenopus laevis' embryo [68], morphogenetic development such as tube formations [66] glassy dynamics of biological tissues [69], epithelial-mesenchymal transitions [70], and wound closure in epithelia [71].

One key disadvantage of the CPM is that the states of cells are updated through Monte Carlo steps, making physical time ill-defined [44]. This limitation prevents interpreting the results in terms of physical laws that depend on continuous time representation. However, CPMs are easy to implement and computationally inexpensive, allowing for the modeling of a large number of cells. One advantage of CPMs is their high accuracy in resolving cell shapes compared to vertex models

1.3.3 Multi-Phase field model

Several systems involve an inhomogeneity of phases separated by an interface. Examples include oil droplets immersed in water, subcellular vesicles within the cytoplasm of cells, and cells amidst their extracellular environments. Gibbs introduced the concept of a diffuse interface separating two phases such that the concentration of each phase varies continuously across the interface between where it is abundant and where it is scarce [72].

In phase field methods, an order parameter field called the phase field ϕ is used to differentiate the different phases in space and time [73]. The phase field has a specific value in each of the two bulk phases and varies continuously across the thin diffuse interface between the two phases. The values of either $\phi = 0$ and $\phi = 1$, or $\phi = -1$ and $\phi = 1$ are used to represent the two bulk phases. The dynamical equations, based on a free energy approach, govern the evolution of the interface between the two phases. The continuous field description allows for the flexible representation of arbitrary shapes. The shape is inferred indirectly from the shape of the diffuse interface that separates the two phases.

Phase field methods have been used to model microstructure evolution in contexts such as solidification, grain growth, dislocation microstructures, and dendritic growth [73, 74]. Fluid flow can be incorporated with additional fields to model flowing multi-phase systems [75]. Recently, several advances have been made to model biological soft matter systems, detailed in the reviews [44, 73, 76, 77]. In a biological context, phase field models have been used to model vesicles [78], amoeboid migration [79], collisions of deformable cells [80], and active deforming organisms such as Hydra [81].

In order to model a confluent epithelial monolayer, multiple phase fields need to be defined, and interactions between them are introduced through an appropriate free energy description [82]. Using the multi-phase field approach, several collective phenomena of confluent cells have been studied. It has been found that differences in the elasticity of cells can enhance the motility of cancer cells [83]. Phase field models have reproduced several topological features of active epithelial monolayers [84], including Lewis' law [85] and the Aboav-Weaire Law [86]. Unlike

in vertex models, T1 transitions occur spontaneously within these models [1, 2, 84]. Colonies of epithelial cells that grow and divide have been modeled in agreement with several experimentally observed behaviors [5, 82]. In the context of considering epithelial tissues as active p-atic systems, phase field models have been used to study the emergence of nematic order [87, 88] and hexatic order [89]. Cell extrusion events have been known to occur at the location of $(+1/2)$ nematic defects, and these results have been reproduced by phase field models [90, 91]. There are also several realizations of phase field models with 3D cells, which is an essential step towards more realistic simulations of morphogenesis [82, 91, 92].

It is also possible to introduce other auxiliary fields that can be coupled to the phase field, such as flow fields to study immersion of cells in fluid [93, 94], nematic fields, polarization fields to include subcellular details [84, 88, 93], and tensor fields such as nematic order fields to include nematodynamics [95–97].

Multi-phase field models are our choice of modeling approach to study the collective behavior of deformable cells with high shape resolution. The high shape resolution allows to capture intricate details of cell morphology, providing deeper insights into how cell shape and deformability influence collective dynamics and cell-cell interactions. The spontaneous generation of T1 transitions simplifies the modeling of dynamic tissue rearrangements, capturing essential processes of morphogenesis and tissue remodeling without the need for ad-hoc methods.

However, due to the high shape resolution, these models are computationally expensive, and large datasets arising from simulations need to be post-processed. The models are defined in terms of coupled, nonlinear systems of partial differential equations, posing significant challenges for analysis. Advanced numerical methods and substantial computational resources are required to solve these equations effectively.

1.4 Thesis structure

This thesis is composed of two parts. In the first part, background information related to the methods used in the articles is provided along with the summaries of the articles. The background information contains relevant information about the methods used by the author of this thesis, and excludes methods used by the co-authors where the author of the thesis did not contribute primarily.

In the Chapter 2, we describe the multi-phase field models used in the articles. This includes definition of the system of partial differential equation in terms of phase fields used to model the confluent monolayer along with the boundary and initial conditions. The Chapter 3 includes the description of the finite element method applied to our model along with computational details. The Chapter 4 provides some additional results that supplements the results from our papers. Finally, in Chapter 5, we summarise the papers and provide an outlook. The Papers I, II, III, and IV are appended after the Chapter 5.

The recommended reading order is to read the Chapters 2 and 3, followed by the Papers I, II, III and IV, and then the Chapters 4 and 5.

1.5 Notation

The notation is different across the papers as they were prepared at different times with a different set of collaborators. However, the notation from Chapter 2-4 is as described here.

The subscript i is always used to indicate a cell with index i. Vectors are written in boldface such as $\mathbf{u}$. Matrices or second order tensors are either written in capital boldface such as $\mathbf{A}$ or in blackboard bold such as $\mathbb{a}$. The vector components are indexed with characters other than i such as u_j represents the j-th component of the vector $\mathbf{u}$.

The component j of a vector $\mathbf{u}_i$ associated with cell i is indexed as

$$(u_i)_j$$

Einstein summation convention is used for every index other than the cell index i. The dot product $\mathbf{a} \cdot \mathbf{b}$ or $\mathbf{Au}$ is a contraction over the last two indices using Einstein summation convention such that $\mathbf{a} \cdot \mathbf{b} = a_j b_j$ and $\mathbf{Au} = A_{jk} u_k$.

Derivative of a function f with respect to x are either written as $\frac{df}{dx}$ or in shorthand as f'. Likewise, higher order derivatives in shorthand are written as $f'', f''', \ldots$

The spatial coordinate vector $\mathbf{x}$ consists of the horizontal component x_1 and vertical component x_2. The gradient operator denoted by ∇ is defined as

$$\nabla = \frac{\partial}{\partial x_1}\hat{x}_1 + \frac{\partial}{\partial x_2}\hat{x}_2,$$

where $\hat{x}_1$ and $\hat{x}_2$ are unit vectors in the horizontal and vertical direction.

The divergence operator, denoted by $\nabla\cdot$ applied to a vector field $\mathbf{a}$ is defined as:

$$\nabla \cdot \mathbf{a} = \frac{\partial a_1}{\partial x_1} + \frac{\partial a_2}{\partial x_2},$$

where a_1 and a_2 are the components of $\mathbf{a}$ in the x_1 and x_2 directions, respectively.

The Laplacian operator, denoted by Δ, is the divergence of the gradient and is defined as:

$$\Delta = \nabla \cdot \nabla = \frac{\partial^2}{\partial x_1^2} + \frac{\partial^2}{\partial x_2^2}$$

δ_{jk} is the kronecker delta function such that $\delta_{jk} = 1$ if $j = k$ and $\delta_{jk} = 0$ otherwise.

Chapter 2

Multi-phase field model

Only when you can be extremely pliable and soft, can you be extremely hard and strong.

Zen Proverb

If you do not change direction, you may end up where you are heading.

Siddhartha Gautama, The Buddha

2.1 Cell as a phase field

We consider the analogy of a binary mixture to represent a cell and its surroundings, ignoring its intercellular and extracellular machinery. Consider a binary mixture of two types of particles: interior and exterior particles of a cell, whose local concentrations are given by $c_{int}(\mathbf{x}, t)$ and $c_{ext}(\mathbf{x}, t)$, respectively. The cell interior and exterior are homogenous such that

$$\begin{array}{rcl} c_{ext} \approx 0 & : & \text{inside the cell} \\ c_{int} \approx 0 & : & \text{outside the cell} \end{array} \tag{2.1}$$

The binary mixture resides in a square two dimensional domain $\Omega \subset \mathbb{R}^2$ of side length L, and is modeled for the time duration $t = [0, T]$. We introduce an order parameter field called the phase field $\phi(\mathbf{x}, t) : \Omega \times [0, T] \to [-1, 1]$ such that

$$\phi = \frac{c_{int} - c_{ext}}{c_{int} + c_{ext}}. \tag{2.2}$$

The cell is implicitly represented by ϕ such that the interior of the cell is represented by the region of Ω where $\phi \approx 1$, see Figure 6. The phase field value

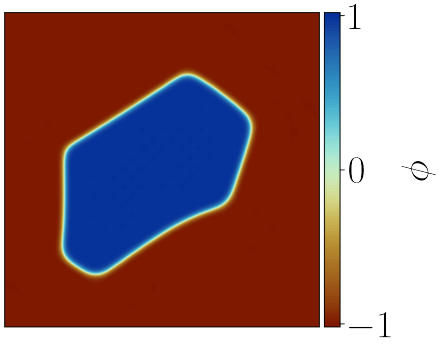


Figure 6: Phase field description of an arbitrary cell. $\phi \approx 1$ (blue) and $\phi \approx -1$ (red) represents the interior and exterior of the cell, respectively. The cell membrane is represented by the thin transition region between the two phases, also known as the diffuse interface.

$\phi \approx -1$ represents the exterior of the cell. The cell boundary is demarcated by the transition region $[-1+\nu, 1-\nu]$, where ν is a small number (empirically, we use $\nu = 0.05$). The width of this transition region is about $\mathcal{O}(\epsilon)$, where $\epsilon \in \mathbb{R}$ is a parameter that will be described in Section 2.2. As the cell is represented by a continuous field variable, cell shape is resolved at a very high resolution, allowing the modeling of curved cells.

Let, $\hat{\phi} = 0.5\phi + 0.5$ be the rescaled phase field which is analogous to an indicator function, then the cell volume(or area) V is defined as

$$V = \int_{\Omega} \hat{\phi} dx. \tag{2.3}$$

Alternatively, the volume can be described by replacing $\hat{\phi}$ by $\hat{\phi}^2$. To model the cell's evolution in time, along with various cellular properties, we utilize a partial differential equation (PDE) description. Throughout this text, we consider that cell growth is arrested and cell volume is conserved.

To evolve the phase field in time while conserving its volume, we use the continuity equation

$$\frac{\partial \phi}{\partial t} + \nabla \cdot \mathbf{J}_m = 0, \tag{2.4}$$

where $\mathbf{J}_m$ is the mass flux. Cell growth (or shrinking) can be included through an additional reactive term to the above equation [5, 82].

The mass flux $\mathbf{J}_m$ is governed by a free energy, $\mathcal{F}[\phi]$. The chemical potential μ is given by the variational derivative of the free energy with respect to ϕ as

$$\mu = \frac{\delta \mathcal{F}}{\delta \phi}. \tag{2.5}$$

Essentially, the chemical potential at a given location is the change in free energy resulting from a local change in the relative concentration of the particles that constitute the interior and exterior of the cell. Suppose, the free energy F is a function of both ϕ and its gradient $\nabla\phi$, and can be written in the form

$$F[\phi, \nabla\phi] = \int_{\Omega} f(\phi, \nabla\phi) dx, \tag{2.6}$$

where f is the free energy density. Following variational calculus, the variational derivative of F with respect to ϕ is given as

$$\frac{\delta \mathcal{F}}{\delta \phi} = \frac{\partial f}{\partial \phi} - \nabla \cdot \frac{\partial f}{\partial (\nabla \phi)}. \tag{2.7}$$

Assuming that the mass flux is driven by local differences in the chemical potential,

$$\mathbf{J}_m = -M_b \nabla \mu = -M_b \nabla \frac{\delta \mathcal{F}}{\delta \phi}, \tag{2.8}$$

where M_b is the mobility that controls the timescale of energy relaxation. Essentially, $\mathbf{J}_m$ is a vector field that locally points in the direction of greatest decrease in the chemical potential. For simplicity, we will consider $M_b = 1$ from hereon. For more complicated representations that involve additional intercellular machinery, M_b could vary both spatially and temporally.

Introducing Equation 2.8 into Equation 2.4 with $M_b = 1$, we arrive at

$$\frac{\partial \phi}{\partial t} = \Delta \mu. \tag{2.9}$$

Equation 2.9 is commonly referred to as Model B of the Hohenberg-Halperin classification [98]. Model B evolution equation is a PDE that models the evolution of a conserved order parameter such as ϕ. Evolving the phase field ϕ as per Equation 2.9 ensures that the cell area (2D volume) V remains constant.

The time rate of change of the free energy is given as

$$\frac{d\mathcal{F}}{dt} = \int_\Omega \frac{\delta \mathcal{F}}{\delta \phi} \frac{d\phi}{dt} dx. \tag{2.10}$$

Using the definition of μ from Equation 2.5 and Equation 2.9, we get

$$\frac{d\mathcal{F}}{dt} = \int_\Omega \mu \Delta \mu dx. \tag{2.11}$$

Integrating by parts (there are no boundary terms as periodic boundary conditions are considered, see Section 2.6),

$$\frac{d\mathcal{F}}{dt} = -\int_\Omega (\nabla \mu)^2 dx. \tag{2.12}$$

As the term inside the integral is always positive, the free energy has a tendency to reduce over time.

Self propulsion(activity) of cells is introduced through an advective flux $\mathbf{J}_a$ within Equation 2.4 as

$$\frac{\partial \phi}{\partial t} + \nabla \cdot \mathbf{J}_a + \nabla \cdot \mathbf{J}_m = 0. \tag{2.13}$$

Let, $\mathbf{J}_a = \mathbf{v}\phi$, where $\mathbf{v} = \mathbf{v}(\mathbf{x}, t)$ is the advection velocity field. Assuming incompressibility $\nabla \cdot \mathbf{v} = 0$, we have

$$\frac{\partial \phi}{\partial t} + \mathbf{v} \cdot \nabla \phi = \Delta \mu. \tag{2.14}$$

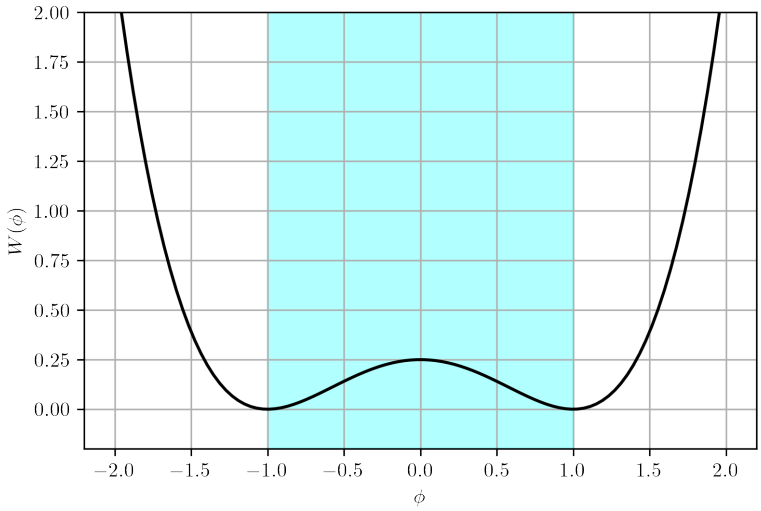


Figure 7: Double well potential, $W(\phi) = \frac{(\phi^2-1)^2}{4}$ with minima at $\phi = -1$ and $\phi = 1$.

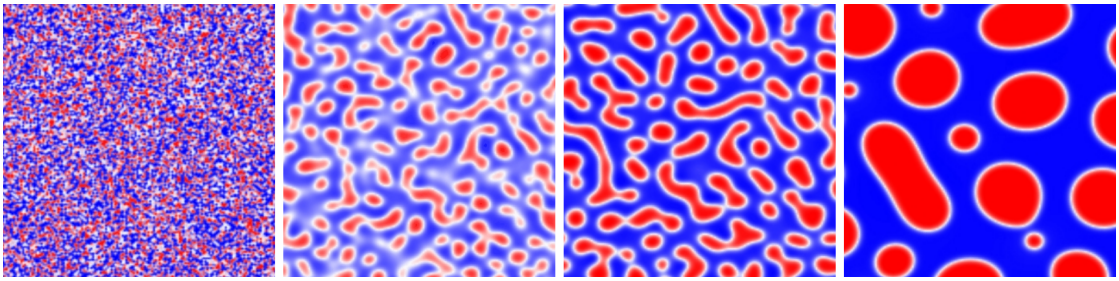


Figure 8: Cross section of frames of a two-phase system evolving from random initial conditions. First, the system phase separates into tiny droplets of dispersed phase within the other phase. Eventually, the droplets coalesce in a process known as Ostwald Ripening. Adapted from Wikipedia article titled *Cahn–Hilliard equation*, Creative Commons Attribution License

The phase field model is constructed by appropriately defining the free energy $\mathcal{F}[\phi]$ and an advection field $\mathbf{v}$ in the above equation, followed by boundary and initial conditions. The free energy $\mathcal{F}$ includes two terms: An energy of surface called Cahn Hilliard Energy, and an energy of interaction between cells. These two energies are defined in the Section 2.2 and Section 2.3

2.2 Cahn Hilliard energy

We introduce a surface energy in the form of the Cahn Hilliard energy [99] given as

$$\mathcal{F}_{CH}[\phi] = \frac{1}{Ca}\int_{\Omega} \frac{W(\phi)}{\epsilon} + \frac{\epsilon|\nabla\phi|^2}{2} dx, \tag{2.15}$$

where $W(\phi) = 0.25(\phi^2 - 1)^2$ is the double well potential as shown in the Figure 7, and ϵ is a parameter that controls the interfacial width. Ca is the capillarity number, which is used to tune the relative contribution of the Cahn Hilliard

energy. The term with the double well potential is the energy of demixing. The homogenous well mixed state is unstable due to the concativity of $W(\phi)$ between $\phi = -1$ and $\phi = 1$. Maxwell tangent construction can be used to show that the heterogenous phase separated state has a lower energy than the homogenous mixed state [100]. The second term penalises gradients in the phase field. Cahn Hilliard energy can be derived by considering a system of binary particles on a lattice such that the interactions between particles of the same kind are energetically favourable over interactions between particles of different kinds [101].

The chemical potential associated with the Cahn Hilliard energy is computed using the Equation 2.7, and is given as

$$\mu_{CH} = \frac{\delta \mathcal{F}_{CH}}{\delta \phi} = \frac{1}{Ca}\left(\frac{W'(\phi)}{\epsilon} - \epsilon \Delta \phi\right), \tag{2.16}$$

where $W'(\phi) = \phi^3 - \phi$. Inserting Equation 2.16 in the Model B order parameter evolution equation (Equation 2.9), we get

$$\frac{\partial \phi}{\partial t} = -\frac{1}{Ca}\Delta\left(\frac{W'(\phi)}{\epsilon} - \epsilon \Delta \phi\right). \tag{2.17}$$

Figure 8 shows snapshots from the evolution of a randomly initialized phase field governed by the Cahn Hilliard energy. Immediately, due to the demixing energy, the system phase separates into two bulk phases to minimize the demixing free energy [101]. Over longer time scales, due to the penalization of the gradients, the small droplets of the dispersed phase coalesce together in a process called Ostwald ripening. Eventually, only a single connected subregion of circular shape of one phase within the other will remain. Throughout this process, the total concentration of each of the bulk phases remains constant. This equilibrium configuration has the lowest Cahn Hilliard energy. The width of the interface that separates the two phases is of the length scale $\mathcal{O}(\epsilon)$.

In our simulations, we always start with an initial condition where each cell is represented by a phase field, which comprises a connected region of $\phi \approx 1$ enclosed in a single closed curve. In absence of other effects such as cell-cell interactions or activity, a cell of arbitrary shape would become circular to minimise the Cahn Hilliard energy.

In arbitrary dimensions, the zero-level set of a phase field ϕ is given as $Z_\phi = \{\mathbf{x} \in \Omega \mid \phi(\mathbf{x}) = 0\}$. For a phase field ϕ of an arbitrary cell as shown in Figure 6, where the cell interior is completely enclosed by exterior with a diffuse interface separating the two phases, we can define the signed distance function $d(\mathbf{x})$ as

$$d(\mathbf{x}) = -\frac{\phi(\mathbf{x})}{|\phi(\mathbf{x})|} \min\left\{|\mathbf{x} - \mathbf{x}_{Z\phi}|| \; \mathbf{x}_{Z\phi} \in Z_\phi\right\}, \tag{2.18}$$

such that $d(\mathbf{x})$ is negative inside the cell and positive outside, with its absolute value being the minimum distance to a point on the zero level set.

For a one dimensional domain of infinite length, at equilibrium, the closed form solution to the Equation 2.17 with boundary conditions $\phi(-\infty) = -1$ and $\phi(\infty) = 1$ is known [99]. The phase field at equilibrium can be written in terms

of the signed distance function $d(x) = x - x_0$ from the zero-level i.e. $\phi(x_0) = 0$ as a tanh profile given as

$$\phi(x) = \tanh\left(\frac{d(x)}{\sqrt{2}\epsilon}\right). \tag{2.19}$$

For a circle with radius r and center $\mathbf{c}$, the signed distance function is given by

$$d_{circle}(\mathbf{x}) = |\mathbf{x} - \mathbf{c}| - r.$$

Assuming a tanh profile for a circular cell, we can define a phase field ϕ_{circle} of a circular cell with diffuse interface of thickness ϵ as

$$\phi_{circle} = -\tanh\frac{d_{circle}(\mathbf{x})}{\sqrt{2}\epsilon}. \tag{2.20}$$

An example of a phase field of a circular cell, ϕ_{circle} is plotted in the Figure 9a along with the corresponding signed distance function $d_{circle}(\mathbf{x})$ in the Figure 9b. The Figures 9c and 9d show the free energy density of the demixing and gradient penalisation component of the Cahn Hilliard energy for the circular cell. The energy is nonzero only at the interface, whose cross section has a tanh profile.

The polynomial demixing term in the Cahn Hilliard energy that comprises of the double well potential given in Equation 2.15 is an approximation of a more general form of surface energy that can be phenomelogically derived by a lattice based model of phase separation of a binary mixture due to thermal quenching [100]. The demixing part of the Cahn Hilliard energy comprising the double well potential is an approximation of a form that is proportional to

$$\xi\left((1+\phi)\ln(1+\phi) + (1-\phi)\ln(1-\phi)\right) + \frac{(1-\phi^2)}{2},$$

where, ξ is the Flory-Huggins parameter related to the temperature of the mixture and interaction energies between the particles of the binary mixture. The inaccuracies due to this approximation, and inherent numerical inaccuracies involved in solving the discretised form of Equation 2.17, lead to additional diffusion contributions in the bulk along with the diffusion in the interface [102]. To counteract this, a diffusion restriction function $g(\phi)$ given as

$$g(\phi) = \frac{2}{3(1+\phi_i)(1-\phi_i)}, \tag{2.21}$$

is introduced in the Cahn Hilliard energy. $g(\phi)$ is singular in the bulk phases i.e. the interior and the exterior of the cell. The modified Cahn Hilliard energy is defined as

$$\mathcal{F}_{CHmod}[\phi] = \frac{1}{Ca}\int_\Omega g(\phi)\left(\frac{W(\phi)}{\epsilon} + \frac{\epsilon|\nabla\phi|^2}{2}\right)dx. \tag{2.22}$$

Evolving Equation 2.17 with this modified energy does not alter the asymptotic limit and allows for more accurate solutions [102]. Within the bulk, a small value $\zeta\epsilon$, where $\zeta \ll 1$, is added to the numerator to prevent numerical blowup.

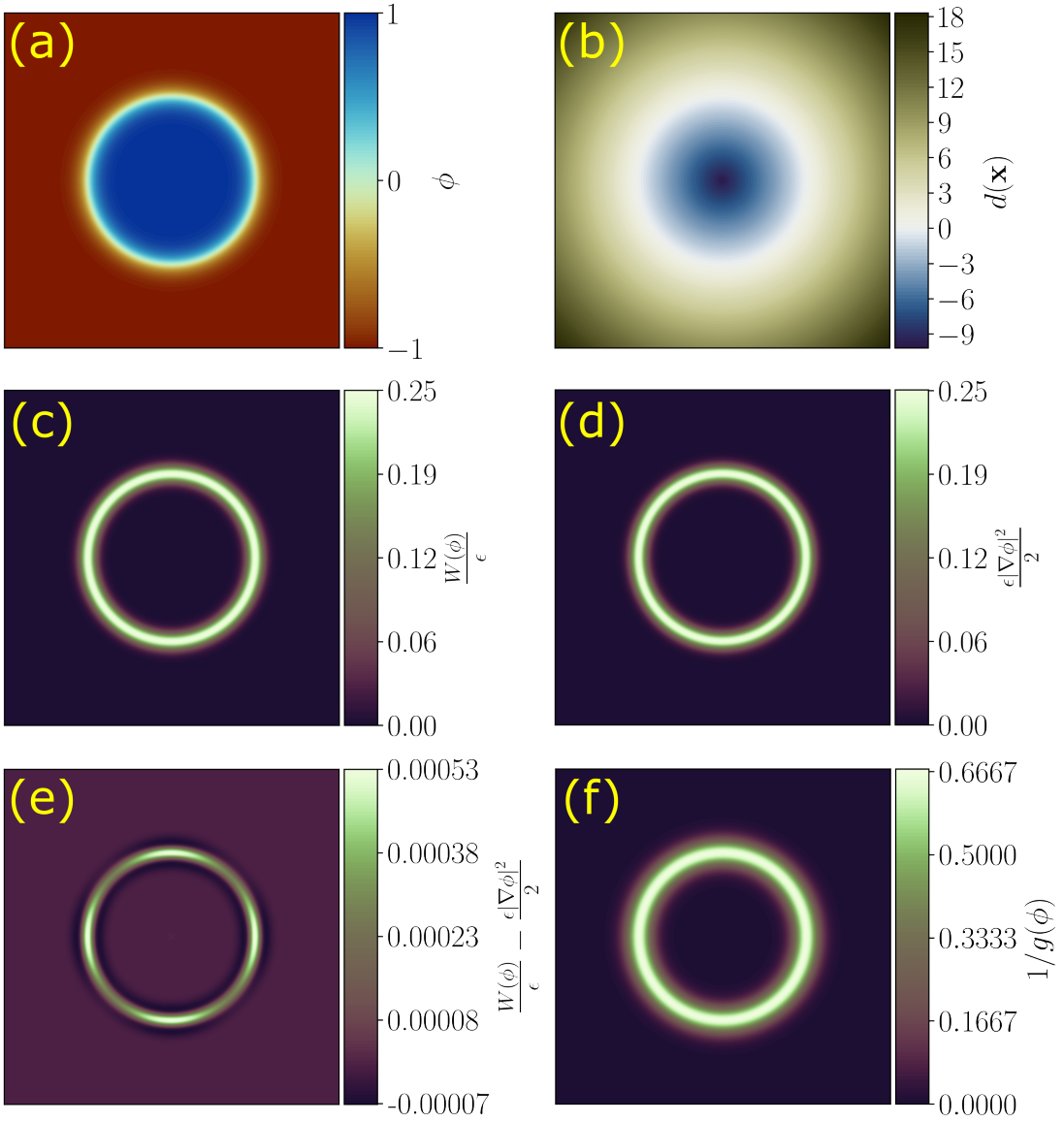


Figure 9: *A circular cell*: (a) Phase field $\phi = \phi_{circle}$, (b) the signed distance function $d_{circle}(\mathbf{x})$, (c) the demixing free energy density $\frac{W(\phi)}{\epsilon}$, (d) the gradient free energy density $\frac{\epsilon|\nabla\phi|^2}{2}$, (e) the difference of demixing and gradient free energy, and (f) the reciprocal of diffusion restriction function $g(\phi)$) are plotted.

Given the free energy density, $f_{CHmod} = \frac{1}{Ca}\left(g(\phi)\left(\frac{W(\phi)}{\epsilon} + \frac{\epsilon|\nabla\phi|^2}{2}\right)\right)$,

$$\frac{\partial f_{CHmod}}{\partial \phi} = \frac{1}{Ca}\left(\frac{g(\phi)W'(\phi)}{\epsilon} + g'(\phi)\left(\frac{W(\phi)}{\epsilon} + \frac{\epsilon|\nabla\phi|^2}{2}\right)\right) \tag{2.23}$$

and

$$\frac{\partial f_{CHmod}}{\partial(\nabla\phi)} = \frac{\epsilon}{Ca}g(\phi)\nabla\phi, \tag{2.24}$$

the chemical potential corresponding to the modified Cahn Hilliard energy is

$$\mu_{CHmod} = \frac{1}{Ca}\left(\frac{g(\phi)W'(\phi)}{\epsilon} + g'(\phi)\left(\frac{W(\phi)}{\epsilon} + \frac{\epsilon|\nabla\phi|^2}{2}\right) - \nabla\cdot(\epsilon g(\phi)\nabla\phi)\right). \tag{2.25}$$

As $\nabla\cdot(\epsilon g(\phi)\nabla\phi) = \epsilon g(\phi)\Delta\phi + \epsilon g'(\phi)|\nabla\phi|^2$, we arrive at

$$\mu_{CHmod} = \frac{1}{Ca}\left(g(\phi)\left(\frac{W'(\phi)}{\epsilon} - \epsilon\Delta\phi\right) + g'(\phi)\left(\frac{W(\phi)}{\epsilon} - \frac{\epsilon|\nabla\phi|^2}{2}\right)\right). \tag{2.26}$$

At equilibrium, $\frac{W(\phi)}{\epsilon} \approx \frac{\epsilon|\nabla\phi|^2}{2}$ (see Figures 9c-9e)[102], we can write

$$\mu_{CHmod} = \frac{1}{Ca}\left(g(\phi)\left(\frac{W'(\phi)}{\epsilon} - \epsilon\Delta\phi\right)\right). \tag{2.27}$$

We will drop the *mod* suffix and refer to the above chemical potential as μ_{CH}. Figure 9f shows the term $\frac{1}{g(\phi)}$. $g(\phi)$ is essentially a mobility restriction function as it prevents diffusion into the bulk.

2.3 Interaction energy

In epithelial tissues, cells form strong connections with each other through Cadherin-based adherens junctions [11]. These interactions between cells play a critical role in the transmission of stresses and in collective behaviour [103, 104]. These junctions continuously remodel themselves based on different mechanical and biochemical cues through topological transitions [11].

We introduce cellular interactions through a contribution to the free energy such that cell-cell adhesion occurs by allowing overlap of cell interfaces to be energetically favourable. Also, cells do not overlap their interiors due to steric repulsion, and this has to be appropriately included in our model as cell-cell repulsion. This would also allow us to simulate situations where cell-cell adhesion is restricted by knocking out E-Cadherin.

There are two general methods which we use to model cell interactions. The first one, used in Paper 1, is inspired by distance-based potential methods used in [84, 93, 105] and first introduced in [5]. Consider two cells represented by the phase fields ϕ_1 and ϕ_2, and let d_1 and d_2 be their signed distance functions, respectively. The distance based approaches are typically of the form where energy of interaction of cell ϕ_1 in presence of cell ϕ_2 is proportional to

$$\int_\Omega B(\phi_1)w(d_2(\mathbf{x})).$$

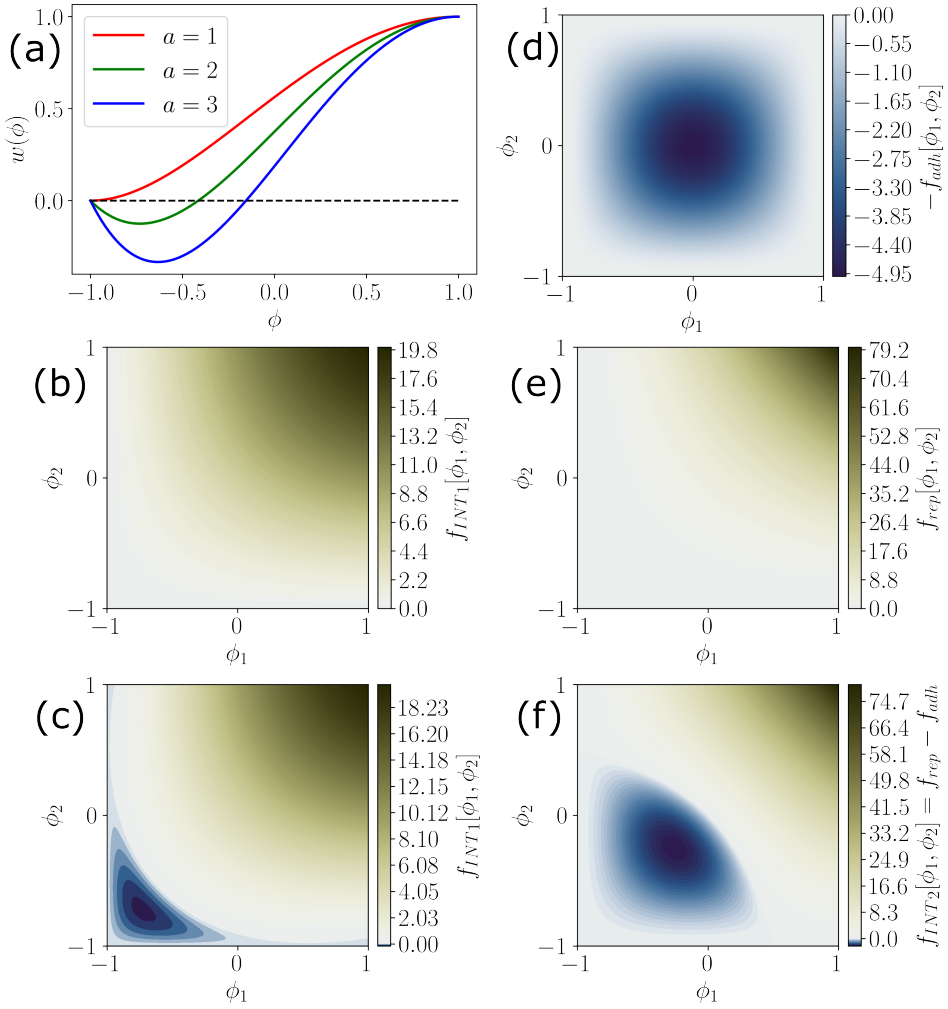


Figure 10: (a) Interaction potential $w(\phi)$ plotted as function of ϕ for different values of a. The interaction free energy densities: (b) f_{INT_1} for $a = 1$, (c) f_{INT_1} for $a = 2$, (d) $-f_{ADH}$ for $a_a = 1$, (e) f_{REP} for $a_r = 1$ and (f) $f_{REP} - f_{ADH}$ for $a_a = 1$ and $a_r = 1$ are plotted as function of values of the phase fields ϕ_1 and ϕ_2. The symbol f corresponds to free energy density of the free energy given by $\mathcal{F}$.

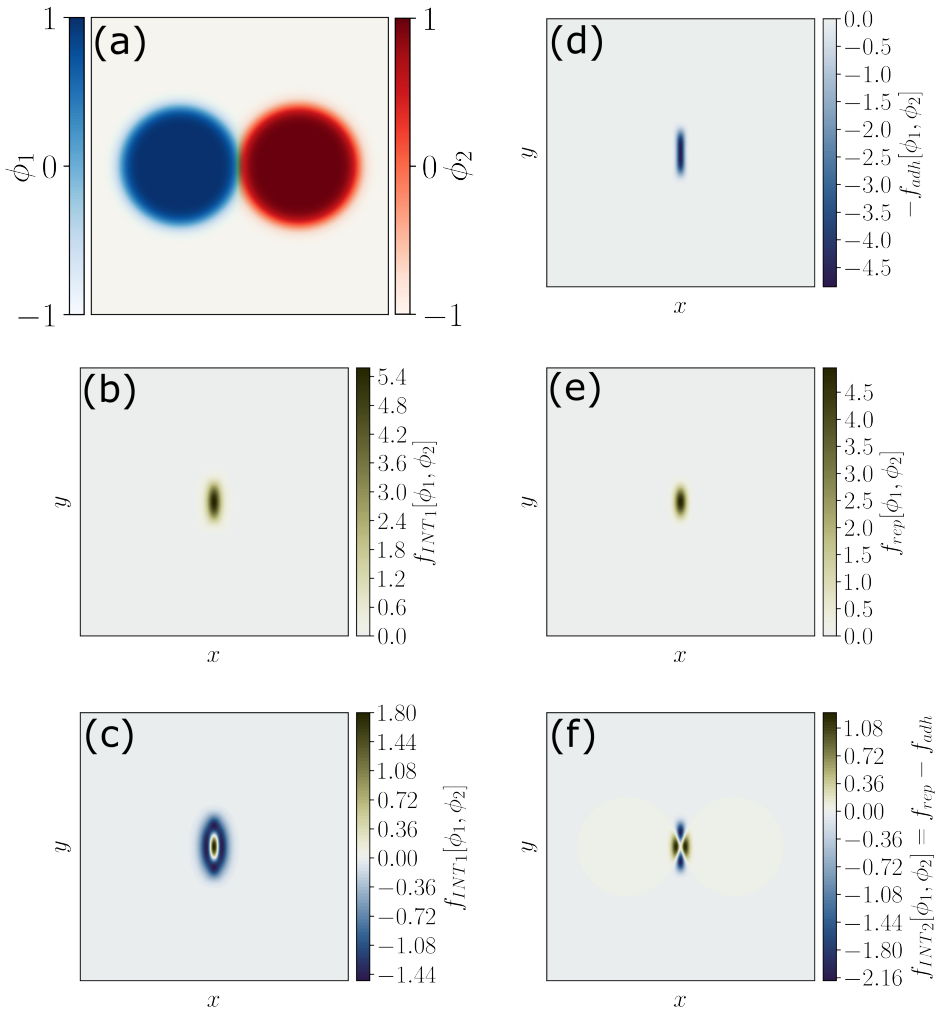


Figure 11: (a) Phase field of two cells in blue (ϕ_1) and red (ϕ_2). The interaction free energy densities: (b) f_{INT_1} for $a = 1$, (c) f_{INT_1} for $a = 2$, (d) $-f_{ADH}$ for $a_a = 1$, (e) f_{REP} for $a_r = 1$, and (f) $f_{REP} - f_{ADH}$ for $a_a = 1$ and $a_r = 1$ are plotted as function of spatial coordinates. The symbol f corresponds to free energy density of the free energy given by $\mathcal{F}$.

Here, $B(\phi_1)$ could be thought of as a field equipped with cell ϕ_1 that senses a potential $w(d_2)$ of cell ϕ_2. The potential here is described in terms of the signed distance from the cell interface. In [5], instead of representing w in terms of signed distance d_2, it is formulated in terms of a polynomial of ϕ_2. Let, $B(\phi) = \hat{\phi}$ and

$$w(\phi) = 1 - (a+1)\left(\frac{\phi-1}{2}\right)^2 + a\left(\frac{\phi-1}{2}\right)^4. \tag{2.28}$$

The interaction energy between two cells ϕ_1 and ϕ_2 is then defined as

$$\mathcal{F}_{INT1}[\phi_1, \phi_2] = \frac{1}{In}\int_\Omega \left(\hat{\phi_1} w(\phi_2) + \hat{\phi_2} w(\phi_1)\right) dx. \tag{2.29}$$

The parameter In is used to scale the interaction energy. As epithelial cell-cell adhesion bonds are symmetrical [8], Equation 2.29 includes the appropriate two terms. Figure 10a shows the plot of $w(\phi)$ for different values of a. The parameter a is used to tune between two different modes of cell interactions. Cells repel each other if $a = 1$ since $w(\phi) > 0$ and the interaction energy is always positive, being zero only if either ϕ_1 or ϕ_2 are 0, so any overlap between the two cells is energetically unfavourable. To include both repulsion and adhesion, we use $a > 1$, as $w(\phi)$ is negative for some values of ϕ corresponding to cell interface. Increasing a increases the range of ϕ for which $w(\phi)$ is negative.

The Figures 10b and 10c show the free energy density corresponding to $\mathcal{F}_{INT1}$ as a function of ϕ_1 and ϕ_2 for $a = 1$ and $a = 2$, respectively. The free energy density is always positive for $a = 1$ and is minimum when either ϕ_1 or ϕ_2 are equal to -1. This situation models cell-cell repulsion as both overlap of interface and interior is penalised. For $a = 2$, the free energy density is negative when the interfaces of the two cells overlap and positive when the interiors overlap. This situation models cell-cell adhesion by promoting overlap of the interface while still allowing repulsion between cell interiors.

An alternative method to allow for cell adhesion by promoting overlap of cell interfaces relies on the fact that the interface is characterised by the region where the gradients $\nabla\phi_i$ and $\nabla\phi_j$ are nonzero. Naturally, this allows us to define an energy which is proportional to

$$-\int_\Omega |\nabla\phi_i||\nabla\phi_j| dx,$$

which promotes overlap of cell interfaces [82, 106]. We can use the approximation $\frac{\epsilon}{2}|\nabla\phi|^2 \approx \frac{W(\phi)}{\epsilon}$ to define the an adhesion energy as

$$\mathcal{F}_{ADH}[\phi_1, \phi_2] = \frac{a_a}{In}\int_\Omega 2(\phi_1^2 - 1)^2(\phi_2^2 - 1)^2 dx. \tag{2.30}$$

The parameter a_a is used to scale the contribution of the adhesion energy. $\mathcal{F}_{ADH}[\phi_1, \phi_2]$ is zero if either of the two phase fields is 1 or -1 and thus nonzero if the cell interfaces overlap. Likewise, the repulsion energy is given as

$$\mathcal{F}_{REP}[\phi_1, \phi_2] = \frac{a_r}{In}\int_\Omega 2((\phi_1 + 1)^2(\phi_2 + 1)^2) dx, \tag{2.31}$$

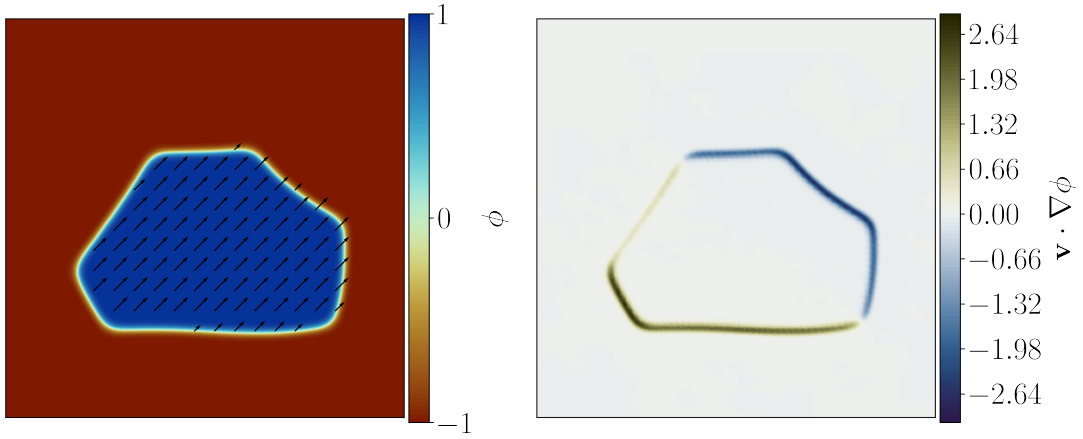


Figure 12: (left) A phase field of a cell with the advection velocity field marked with arrows. (right) The corresponding advective term of phase field evolution equation.

which prevents overlap of cell interiors. The parameter a_r is used to scale the contribution of the repulsion energy. $\mathcal{F}_{REP}[\phi_1, \phi_2]$ is nonzero if both ϕ_1 and ϕ_2 are greater than -1. Combining these to define an alternative interaction energy as

$$\mathcal{F}_{INT2}[\phi_1, \phi_2] = \mathcal{F}_{REP}[\phi_1, \phi_2] - \mathcal{F}_{ADH}[\phi_1, \phi_2]. \tag{2.32}$$

This form was first introduced in [94] and has been explored further in [2, 107]. Figure 10d shows the free energy density corresponding to the negative of $\mathcal{F}_{ADH}$ as a function of ϕ_1 and ϕ_2 . The energy density is minimum at the overlap of zero level sets of ϕ_1 and ϕ_2. Figure 10e shows the free energy density corresponding to $\mathcal{F}_{REP}$ which has a peak when the interior of the cells overlap. Figure 10f shows the free energy density corresponding to $\mathcal{F}_{REP} - \mathcal{F}_{ADH}$. The figure is qualitatively similar to Figure 10c such that in both situations the minima lies at phase values where the cell boundaries overlap. Albeit, the phase values corresponding to the minima are different.

To further illustrate the effect of both these interaction energies, we consider two circular cells as shown in Figure 11a. The free energy densities for this state corresponding to energies $\mathcal{F}_{INT1}$ for $a = 1$, $\mathcal{F}_{INT1}$ for $a = 1.5$, $\mathcal{F}_{ADH}$, $\mathcal{F}_{REP}$, and $\mathcal{F}_{INT2} = \mathcal{F}_{REP} - \mathcal{F}_{ADH}$ are plotted in the Figures 11b-1f. The repulsion free energy density in both the interaction energies are similar, however, when adhesion is included, the free energy densities exbibit different patterns.

2.4 Activity

Epithelial cells are deformable active matter that converts stored chemical energy through ATP hydrolysis to migrate alone or in collectives [8, 108]. The direction of their self propulsion (activity) is defined through various cell polarities [109–111] mechanical stresses from neighbouring cells [11], geometry and topology [39, 112]. We introduce cell activity through an advection term $\mathbf{v} \cdot \nabla\phi$, where $\mathbf{v}$ is the advection field defined as

$$\mathbf{v}(\mathbf{x}, t) = v_0 \mathbf{e}(t) \hat{\phi}(\mathbf{x}, t). \tag{2.33}$$

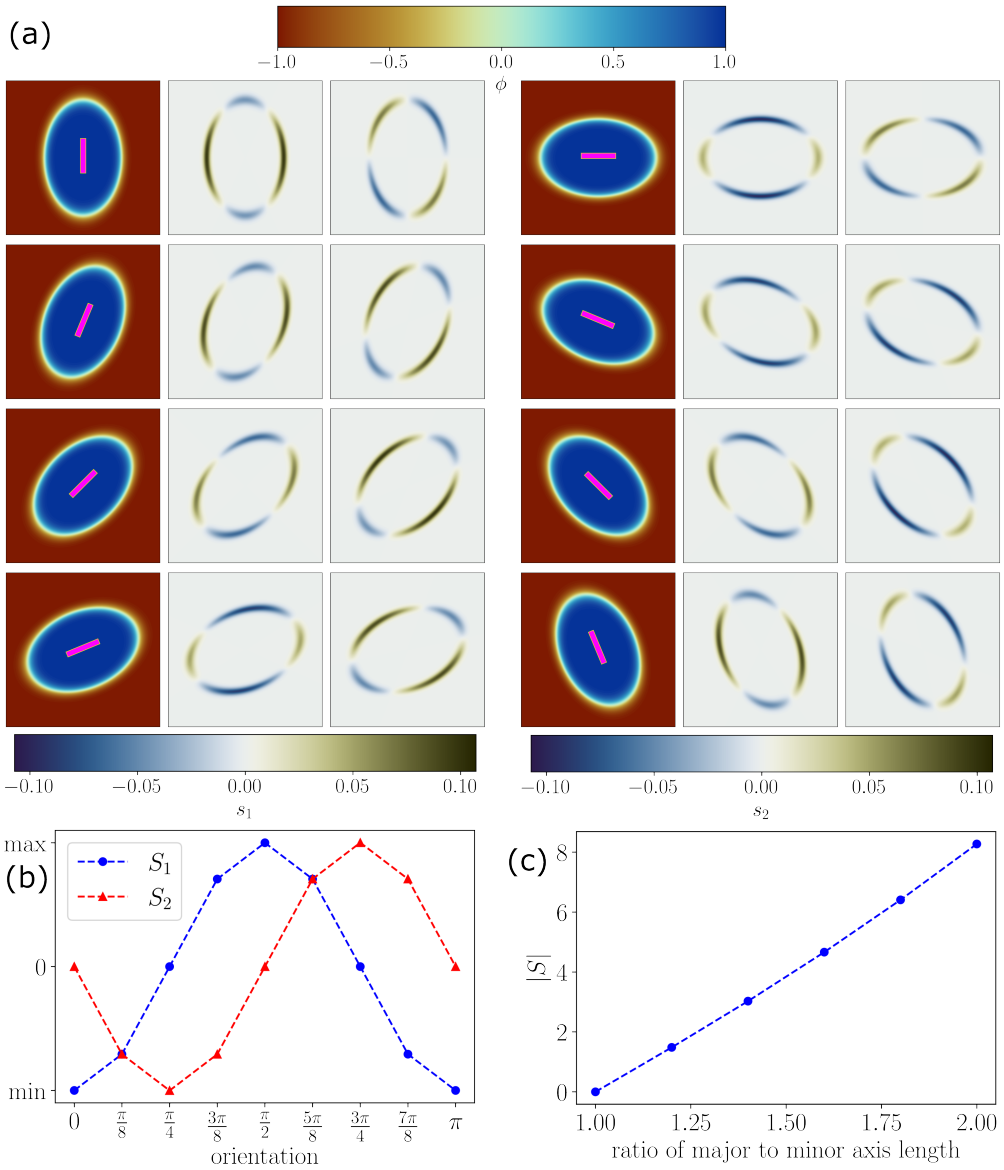


Figure 13: (a) For different orientations, the phase fields of an elliptical cell are plotted in the leftmost columns. The pink bar is parallel to the elongation axis of the cell. In the middle and right column, the corresponding fields s_1 and s_2 are plotted, respectively. (b) For cells in (a), the two independent values of the $\mathbf{S}$ are plotted as function of ellipse orientation. (c) For an elliptical cell of varying ratio of major axis to minor axis length, the largest eigenvalue of the shape deformation tensor $\mathbf{S}$ is plotted. The minor axis length is equal to 10 and $\epsilon = 1$ for (a-c). The major axis length in (a) is 15.

The advection field points in the direction $\boldsymbol{e}(t) = [\cos(\theta(t)), \sin(\theta(t))]$, where $\theta(t)$ is self propulsion orientation. v_0 is the parameter used to tune the magnitude of activity. A higher value of v_0 leads to faster cells. The only spatially dependent term in the advection field is $\hat{\phi}$. This means that the advection field is 0 outside of a cell, and has a magnitude equal to v_0 inside the cell. The magnitude of the advection field at the zero level set is $v_0/2$. The left panel of Figure 12 shows the advection field with an arbitrary orientation is plotted for a arbitrary cell, whose phase field is also shown. The corresponding advection component $\mathbf{v} \cdot \nabla\phi$ is shown in the right panel.

The orientation of activity evolves as per the stochastic differential equation

$$d\theta = \sqrt{2D_r}dW(t) + \alpha(\beta(t) - \theta(t))dt. \tag{2.34}$$

The first term is a rotational diffusivity component with diffusion coefficient D_r, and the second term aligns the orientation of activity with the orientation of the polarity of the cell defined by β. α controls the timescale of this alignment. Cells exhibit vastly different migration behaviours depending upon the timescale of observation [113, 114]. For instance, if a tissue is imaged with very short intervals between images, then the cell would appear to undergo ballistic motion, whereas for larger intervals the cell might be diffusive. The values of D_r, α and dt indirectly control the relative timescale of such behaviour in our model.

There are myriads of polarities that are associated with epithelial cells. In an epithelial monolayer, the apical-basal polarity characterises the top and bottom of the monolayer. The apical layer is the 'top' layer where most of the cell-cell adherens junctions are located [11], while the basal layer is attached to a substrate through integrin, and provides friction to cell movement [8]. Here, the polarity vector can be defined to be pointing from the basal to the apical layer. Epithelial cells also possess planar cell polarity, wherein a set of proteins called PCP proteins localise in the cell such as to define a front and a back [110]. These proteins help define the direction of surface features such as scales, hairs, and bristles, and also help in morphological alignments [111]. Here, the polarity vector can be defined based on the chemical concentration of PCP proteins. The cells also possess polarity described by their shape as a result of structural features such as orientations of actin filaments and lamellopodia [8]. The polarity vector here is parallel to the principal axis of cell elongation. Often a migrating epithelial cluster consists of leader cells whose migration direction defines the polarity orientation for the whole monolayer such that it appears as if the whole monolayer acts as a single large cell. These leader cells guide the flow of the rest of the tissue (See Figure 2). The polarity vector points from the bulk of the monolayer to the leader cells.

We assume that the cell in our model has the tendency to align with its shape polarity, i.e. principal axis of elongation of a cell. To quantify the elongation of the cell, we consider the shape deformation tensor of the phase field [87, 115], which is a 2×2 symmetric traceless tensor given as

$$\boldsymbol{S}(\phi) = \mathbf{S} = \begin{bmatrix} S_1 & S_2 \\ S_2 & -S_1 \end{bmatrix} \tag{2.35}$$

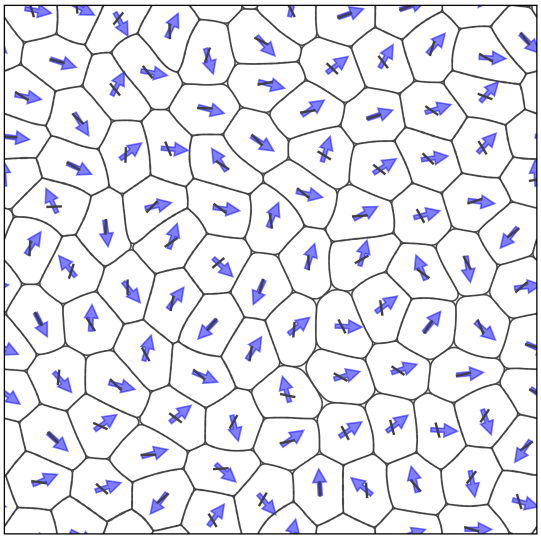


Figure 14: A tissue snapshot with the axis of elongation marked with a black bar positioned at cell center. The orientation of activity is marked with blue arrows.

where,

$$S_1 = \int_\Omega s_1 = \frac{1}{8}\int_\Omega \left[\left(\frac{\partial\phi}{\partial x_2}\right)^2 - \left(\frac{\partial\phi}{\partial x_1}\right)^2\right] \tag{2.36}$$

and

$$S_2 = \int_\Omega s_1 = -\frac{1}{4}\int_\Omega \left(\frac{\partial\phi}{\partial x_1}\frac{\partial\phi}{\partial x_2}\right) \tag{2.37}$$

The eigenvalues of the $\mathbf{S}$ are real, equal and opposite in sign and are given as $\lambda^{\pm} = \pm\sqrt{S_1^2 + S_2^2}$. The corresponding eigen vectors of $\mathbf{S}$ are given as

$$\boldsymbol{\eta}^{\pm} = \left(\frac{S_1 + \lambda^{\pm}}{S_2}, 1\right). \tag{2.38}$$

Figure 13a shows elliptical cells which are oriented at different angles. The pink bar represents the primary axis of elongation of the cell and is parallel (or antiparallel) to $\boldsymbol{\eta}^+$. For each case, the corresponding integrand fields s_1 and s_2 are also plotted. The values of S_1 and S_2 are plotted in Figure 13b. S_1 and S_2 are dependent on the orientation of the ellipse, however the largest eigenvalue which we will denote by $|S| = \sqrt{S_1^2 + S_2^2}$ is rotationally invariant. $|S|$ increases with increase in the shape anisotropy, i.e., ratio of major axis to minor axis length of the ellipse, see Figure 13c. $|S|$ can thus also be used as a measure for cell elongation. The elongation axis of the cell is oriented along the direction $\boldsymbol{\eta}^+$, or $-\boldsymbol{\eta}^+$. The polarity orientation β is chosen as the orientation of either $\boldsymbol{\eta}^+$ or $-\boldsymbol{\eta}^+$ depending upon which of the two is the closest to θ as

$$\beta(t) = \begin{cases} \arg(\boldsymbol{\eta}^+(t)) & : \quad \mathbf{e}(t)\cdot\boldsymbol{\eta}^+(t) > 0 \\ \arg(-\boldsymbol{\eta}^+(t)) & : \quad \mathbf{e}(t)\cdot\boldsymbol{\eta}^+(t) < 0 \end{cases} \tag{2.39}$$

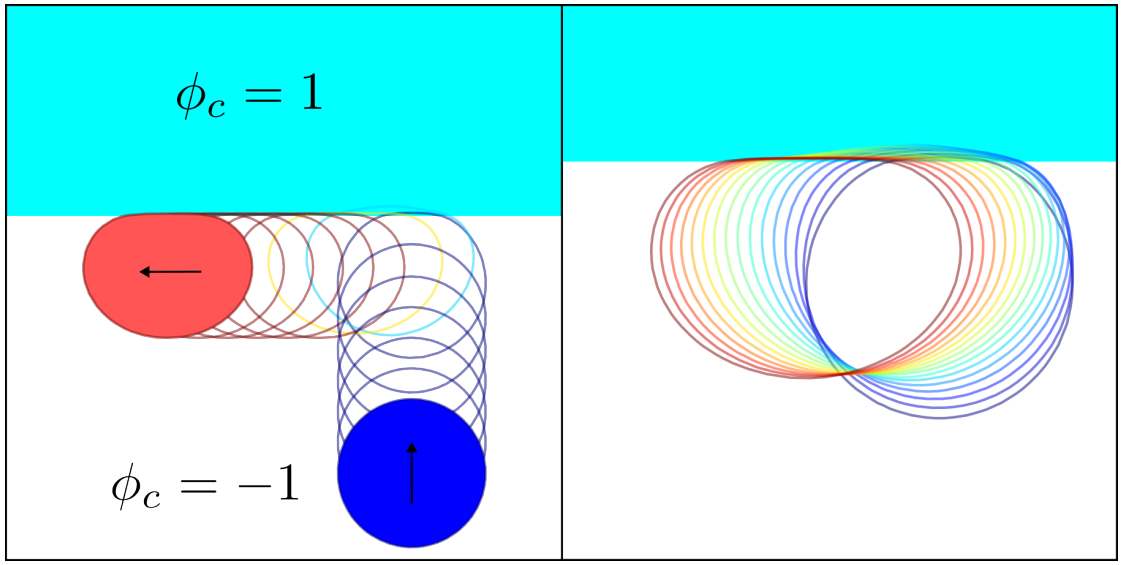


Figure 15: (left) A cell initialised with a velocity in the vertical direction collides with a wall $\phi_c = 1$ with which it has repulsive interactions. The cell undergoes deformation such that it elongates along the wall and its direction of self propulsion realigns to the direction of its elongation. (right) More frames corresponding to the time of impact of the cell phase field shown in the left panel.

Figure 14 shows a tissue snapshot from one of our simulations with black lines at the center of mass of the cells indicating the elongation axis of the cell, which is parallel to $\boldsymbol{\eta}_i^+$. The orientation of the advection field is indicated with blue arrows.

The form of activity chosen bears some similarity to that of the Vicsek model [116]. Rather than the orientation of activity being dependent on that of their neighbours as in the Vicsek model, the orientation of activity depends on the cell's shape which is influenced by the interaction with their neighbours.

To illustrate the polarity alignment, we consider a circular cell as shown in Figure 15, initialised with a velocity pointing vertically upwards and $D_r = 0$ colliding with a static phase field ϕ_c, i.e., $\frac{\partial \phi_c}{\partial t} = 0$, representing a wall. We consider repulsive interactions between the cell and the wall. Upon collision with the wall, the cell deforms and elongates along the edge of the wall. This results in the change in orientation of its activity such that the continues to glide along the wall.

Some models also include a passive thermodynamical stress [117] that affects the advection fields such as in the References [83, 87]. Passive stresses have been shown to increase the range of parameters for which a tissue is jammed [118]

2.5 Multicellularity

To represent a confluent monolayer, we first consider a set of N cells each represented by a phase field ϕ_i, where $i = 1, 2, 3, \ldots N$. The total Cahn-Hilliard energy of the system is the sum of the Cahn Hilliard energy of each cell such that

$$\mathcal{F}_{CH}[\{\phi_i\}] = \frac{1}{Ca} \sum_{i=1}^{N} \int_\Omega g(\phi_i) \left(\frac{W(\phi_i)}{\epsilon} + \frac{\epsilon |\nabla \phi_i|^2}{2} \right) dx. \tag{2.40}$$

The chemical potential corresponding to the Cahn-Hilliard energy of the system with respect to cell ϕ_i is given as

$$\mu_{CH_i} = \frac{g(\phi_i)}{Ca}\left(\frac{W'(\phi_i)}{\epsilon} - \epsilon\Delta\phi_i\right). \tag{2.41}$$

The total interaction energy for the monolayer consists of the sum of interaction energies between every pair of cells. One form of total interaction energy used in Paper I is given as

$$\mathcal{F}_{INT_1}[\{\phi_i\}] = \frac{1}{In}\sum_{i=1}^{N}\int_\Omega \hat{\phi}_i \sum_{j\neq i} w(\phi_j)dx. \tag{2.42}$$

and the interaction chemical potential corresponding to cell i is given as

$$\mu_{INT_{1,i}} = \frac{1}{In}\sum_{j\neq i}\left(\frac{w(\phi_j)}{2} + \hat{\phi}_j w'(\phi_i)\right). \tag{2.43}$$

The other form of total interaction energy used in Paper II, III and IV is given as $\mathcal{F}_{INT_2}[\{\phi_i\}] = \mathcal{F}_{REP}[\{\phi_i\}] - \mathcal{F}_{ADH}[\{\phi_i\}]$

$$\mathcal{F}_{REP}[\{\phi_i\}] = \frac{a_r}{2In}\sum_{i=1}^{N}\int_\Omega \sum_{j\neq i}(\phi_i+1)^2(\phi_j+1)^2 dx \tag{2.44}$$

$$\mathcal{F}_{ADH}[\{\phi_i\}] = \frac{a_a}{2In}\sum_{i=1}^{N}\int_\Omega \sum_{j\neq i}(\phi_i^2-1)^2(\phi_j^2-1)^2 dx \tag{2.45}$$

The repulsion chemical potential corresponding to cell i is given as

$$\mu_{REP_i} = \frac{a_r}{In}(\phi_i+1)\sum_{j\neq i}(\phi_j+1)^2, \tag{2.46}$$

and the adhesion chemical potential corresponding to cell i is given as

$$\mu_{ADH_i} = \frac{2a_a}{In}(\phi_i^3-\phi_i)\sum_{j\neq i}(\phi_j^2-1)^2, \tag{2.47}$$

and therefore $\mu_{INT_{i,2}} = \mu_{REP_i} - \mu_{ADH_i}$. The total interaction potential, μ_{INT_i} is either $\mu_{INT_{i,1}}$ or $\mu_{INT_{i,2}}$ depending on the interaction energy used.

The evolution of the confluent monolayer is then described by the system of N equations given as

$$\frac{\partial\phi_i}{\partial t} + \boldsymbol{v_{0_i}}\cdot\nabla(\phi_i) = \Delta\frac{\delta\mathcal{F}[\{\phi_i\}]}{\delta\phi_i}. \tag{2.48}$$

Equation 2.48 is a set of N-coupled, non-linear fourth order partial differential equations. The system can be decomposed further into a set of 2N-coupled non-linear second order PDEs such that

$$\begin{aligned}\frac{\partial\phi_i}{\partial t} + \boldsymbol{v}\cdot\nabla\phi_i &= \Delta\mu_i \\ \mu_i &= \mu_{CH_i} + \mu_{INT_i}\end{aligned} \tag{2.49}$$

Equations 2.49 along with boundary conditions (see Section 2.6) and initial conditions (see Section 2.7) complete our multi-phase field model description for an active confluent layer of interacting, deformable cells.

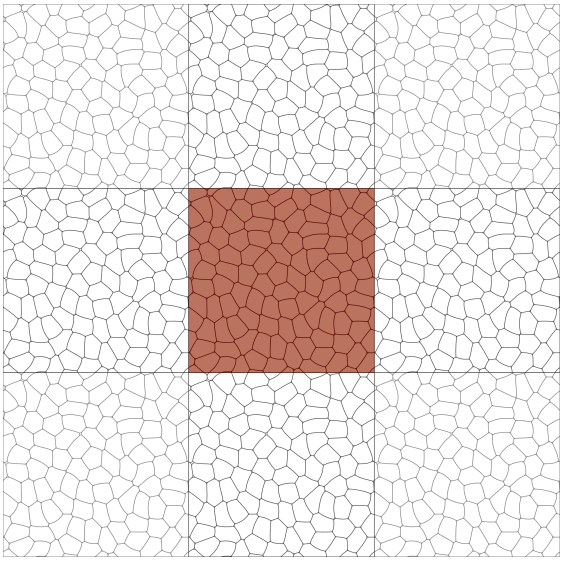


Figure 16: *Periodic boundary conditions.* The computational domain is represented in brown. The domain is repeated and stacked to highlight the periodicity along both axes.

2.6 Boundary conditions

In vivo, epithelial tissues are either surrounded by other tissues, folded into tubes, or are exposed to a free surface as in wounds [8]. In vitro, epithelial monolayers are either exposed to a free surface, or confined to a specific geometry [38, 39, 119]. Multi-phase field models incorporating confined geometry are explored in [5] and cells on a sphere and torus are explored in [107, 120]. In our study, we wish to probe the behaviour far from the boundary. This step is a simplification as boundaries have significant impact on cellular behaviour. To achieve this, we consider periodic boundary conditions along both axes, as shown in Figure 16. This representation of the domain is topologically equivalent to a donut. If the domain is sufficiently large, periodic boundary conditions allows to represent a psuedoinfinite domain. As the dynamical behaviour of the model at every point in the domain Ω is same, numerically, having periodic boundary conditions has no spatial influence.

2.7 Initial conditions

As our model is volume preserving, we need to initialise the cells with the appropriate volume. Generating a confluent tissue with a randomised distribution of cell shapes is tricky as closed form equations for such a collection of phase fields do not exist. We can however generate a regular phase field as shown in the left panel of Figure 17 comprising of a grid of square cells. The signed distance function for a square phase field is given as

$$d_{square}(\mathbf{x}) = |\mathbf{x} - \mathbf{c}|_\infty - 0.5l \tag{2.50}$$

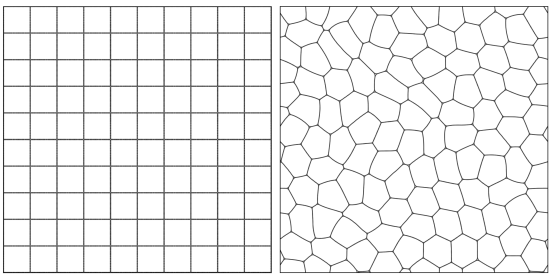


Figure 17: *Initial Conditions*: (left) a grid of 100 square phase fields are initialised in a simulation for a short time period until cells appear sufficiently random. The end state of the simulation (right) is then used as an initial condition.

where, $\mathbf{c}$ is the center of the square, l is its side length and $||_\infty$ denotes the infinite norm i.e. the maximum value of the enclosed vector. A square phase field is then generated as

$$\phi_{square} = -\tanh\left(\frac{d_{square}}{\sqrt{2}\epsilon}\right). \tag{2.51}$$

An initial condition prepared as shown in the left panel of Fig 17 is then evolved with our model to generate a state of cells of arbitrary shape as shown in the right panel of Figure 17. This well mixed state serves as an initial condition for our experiments.

Chapter 3

Numerical Methods

The question is not what you look at, but what you see.

Henry David Thoreau

Truth is stranger than fiction, but it is because fiction is obliged to stick to possibilities; Truth isn't.

Mark Twain

3.1 Introduction

The closed-form analytical solution of System of Equations 2.49, i.e., $\{\phi_i(t)\}$ is unknown. However, we can instead find a numerical approximation to the solution, denoted by $\{\tilde{\phi}_i(t)\}$, to the system. Our chosen method to find the numerical solution is the Finite Element Method (FEM). In FEM, the set of partial differential equations is written in an integral form, the notion of its derivatives is *weakened*, a set of basis functions in a finite dimensional vector space, is used to construct an approximation to the solution. This approach eventually leads to a matrix-vector product form $A_{kj}(\tilde{\phi}_i)_j = b_k$. The numerical solution $\tilde{\phi}_i$ is then obtained at discrete locations indexed by j. We will briefly detail the journey from the set of partial differential equations to obtaining the form $A_{kj}(\tilde{\phi}_i)_j = b_k$. The method we will describe is specific to our model and boundary conditions. For mathematical details and the theory about FEM, textbooks such as References [121, 122] can be consulted. Once we arrive at the description of the numerical solution, we will discuss its implementation.

3.2 The notion of weak derivatives

First, we introduce some function spaces defined over our domain Ω. These functions spaces help us narrow down the choice of functions with which we will approximate our solution and to aid with other steps in defining our FEM procedure.

$\mathcal{C}^p(\Omega)$ are functions that are differential p times.

The *Lebesque space*, $L_p(\Omega)$, is the set of all functions that are integrable upto p-th power. Essentially,

$$L_p(\Omega) = \{f(x) : \Omega \to \mathbb{R} \mid \int_\Omega |f(x)|^p dx < \infty\}.$$

The *Hilbert space*, $H^1(\Omega)$ is the set of all functions defined over Ω such that the functions and their first derivatives are square integrable. Essentially,

$$H^1(\Omega) = \{f(x) : \Omega \to \mathbb{R} \mid f(x) \in L_2(\Omega), f'(x) \in L_2(\Omega)\}.$$

The Hilbert space, $H^1(\Omega)$ is also equipped with a scalar product such that for $f, g \in H^1(\Omega)$, the scalar product is defined as

$$< f, g >:= \int_\Omega fg dx + \int_\Omega \nabla f \nabla g dx$$

We will now introduce the concept of a weak derivative of a function which will prove to be tremendously useful in redefining our model into a form suitable for FEM.

Consider a function $f(x) : \Omega \to \mathbb{R}$ such that $f(x) \in L_1(\Omega)$, and a test function $\vartheta \in \mathcal{C}^1(\Omega)$, then if there exists a function $g(x)$ such that

$$\int_\Omega g\vartheta dx = -\int_\Omega f\vartheta' dx \tag{3.1}$$

is true $\forall \vartheta \in \mathcal{C}^1(\Omega)$, then $g(x)$ is the weak derivative of f.

The above definition of a derivative doesn't rely on the classical differentiability of $f(x)$. Even if the classical derivative of f, i.e., f' doesn't exist, in some situations, we can find its weak derivative.

To illustrate with an example, let us briefly assume a one-dimensional domain and the function $f(x) = |x|$. $f(x)$ is not differentiable at $x = 0$. However, the piecewise function

$$g(x) = \begin{cases} -1 & : \quad x < 0 \\ C_g & : \quad x = 0 \\ 1 & : \quad x > 0 \end{cases}$$

is the weak derivative of $f(x)$ as it satisfies Equation 3.1. $C_g \in \mathbb{R}$ is a constant, and hence there are infinitely many weak derivatives for $f(x) = |x|$. The classical derivative is also a weak derivative, but the opposite is not true. In two dimensions, we will use the so called "hat" functions as a basis with which we construct our approximate solution $\tilde{\phi}_i$. The hat functions are not classically differentiable but are rather piecewise differentiable and their weak derivatives exist. The notion

of weak derivatives help us describe the differential operators like the gradient or laplacian of hat functions.

To further generalise the concept of weak derivatives to higher dimensions, consider $\Omega \in \mathbb{R}^n$ and $L_1(\Omega) = \{f : \Omega \to \mathbb{R} \mid |f| < \infty\}$. Let $\vartheta(x)$ be test functions that are infinitely differentiable and let $f \in L_1(\Omega)$. If

$$\int_\Omega \mathbf{g}(x)\vartheta(x)dx = -\int_\Omega f(x)\nabla\vartheta(x)dx \tag{3.2}$$

then $\mathbf{g}(x)$ is the weak derivative of f.

In this chapter, from here on we will drop the term "dx" within the integrals for the sake of conciseness.

3.3 Weak formulation of a partial differential equation

Consider, a scalar field $u(\mathbf{x})$ over periodic domain Ω. The general form of reaction-diffusion-convection equation with respect to $u(\mathbf{x})$ is given as

$$-a(\mathbf{x})\Delta u + (\mathbf{b}(\mathbf{x}) \cdot \nabla u) + c(\mathbf{x})u = f(\mathbf{x}), \tag{3.3}$$

where a, b, c, f are the diffusion coefficient field, advection coefficient field, reaction coefficient field and force field, respectively. This form of reaction-diffusion-convection equation is termed as a *strong* form. Multiplying the above equation with test function $\vartheta(\mathbf{x}) \in H^1(\Omega)$ and integrating over the domain, we get

$$-\int_\Omega a\Delta u\vartheta + \int_\Omega (\mathbf{b} \cdot \nabla u)\vartheta + \int_\Omega cu\vartheta = \int_\Omega f\vartheta. \tag{3.4}$$

As we are restricting ourselved to domains with periodic boundary conditions, which essentially means having no boundary at all, the first term above can be integrated by parts and the boundary terms are 0, such as

$$-\int_\Omega a\Delta u\vartheta = \underbrace{-\int_{\partial\Omega} a(\nabla\phi \cdot \mathbf{n})\vartheta}_{=0} + \int_\Omega a\nabla\phi \cdot \nabla\vartheta.$$

With this, we get the so called weak formulation of the general reaction diffusion equation given as

$$\int_\Omega a\nabla u\nabla\vartheta + \int_\Omega (\mathbf{b} \cdot \nabla u)\vartheta + \int_\Omega cu\vartheta = \int_\Omega f\vartheta. \tag{3.5}$$

The solution of the weak form does not have to solve the strong form. In contrast to the strong form, the requirements of differentiability on u are *weaker*. u only needs to be differentiable once, i.e., $u \in H^1(\Omega)$. As both u and ϑ are in $H^1(\Omega)$, all integrals in Equation 3.5 are bounded.

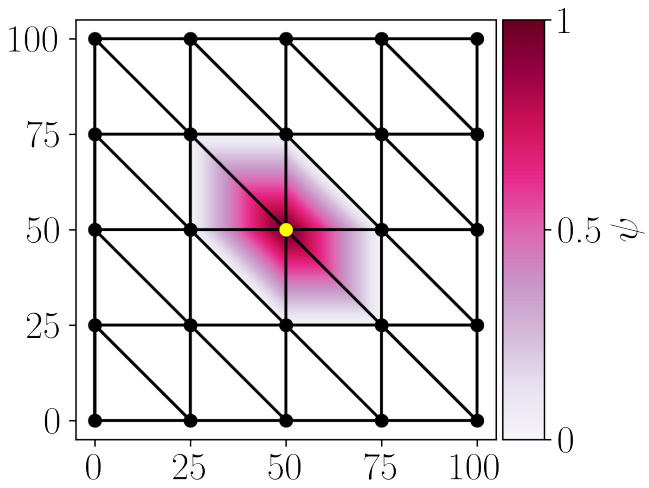


Figure 18: A triangulated grid for a square domain. The hat function corresponding to the yellow point is plotted.

3.4 Spatial discretisation of the weak form

Despite the possibility that Equation 3.5 has many more solutions than the strong form of the reaction diffusion convection system, arriving at a closed-form solution given a test function, ϑ, can remain extremely complicated. In many problems, numerical methods have proven very successful in determining the solution at a finite number of points in Ω, with some error depending on the numerical method used and its hyperparameters.

We wish to compute the numerical solution $\tilde{u}$ that satisfies the weak form at a finite set of N_p points called as *nodes*, in the domain Ω, denoted by the set $\{\tilde{\mathbf{x}}_j\}$, where $j = 1, 2, \ldots, N_p$. We tile our two dimensional domain Ω with N_e triangular *elements* given by the set $\{T_k\}$, where $k = 1, 2, \ldots, N_e$, whose vertices are chosen from node set $\{\tilde{\mathbf{x}}_j\}$. Since Ω is a square domain, we can tile it with triangles that fill the whole domain. If Ω were non polygonal, it could not be tiled with a finite set of triangles, and we would rather have to approximate the domain. The members of the set $\{T_k\}$ are all disjoint in Ω, i.e., they do not overlap. There are numerous ways to create a triangulation for a given set of points. Figure 18 shows an example of a square grid discretised using triangles.

The choice of N_p, N_e, and vertices of the triangles have significant impact on the numerical solution $\tilde{u}$. A larger number of N_p and N_e generally increases numerical accuracy, provided the triangulation is appropriate for a given problem, but also increases computational overhead. The relative sizes of the sides of the triangle could also affect the solution depending on the problem being solved.

Before we proceed to represent the numerical solution on the grid, we introduce the function space of all piecewise polynomials defined over the set $\{T_k\}$ as

$$\tilde{V} = \{ \underbrace{v : \Omega \to \mathbb{R}}_{\text{globally defined}} \mid \underbrace{v|_T \in \mathbb{P}_1(T) \; \forall \; T \in \{T_k\}}_{\text{locally a polynomial on each element}} \}.$$

Note that, $\tilde{V} \subset H^1(\Omega)$.

Similar to how every vector $\mathbf{r} \in \mathbb{R}^n$ can be described as linear products of n coefficients $\{r_j\}$ and a set of n basis vectors $\{\mathbf{e}_j\}$ in $\mathbb{R}^n$, each function in $\tilde{V}$ can be described as a linear product of set of N_p coefficients and a set of N_p basis functions $\{\psi_j\}$, i.e. for every $v \in \tilde{V}$, if $v_j = v(\mathbf{x}_j)$ we can write $v = \sum_{N_p} \tilde{v}_j \psi_j$. There are infinitely many set of basis to choose from $\tilde{V}$. We consider the set of basis $\{\psi_j\}$ as per the lagrange basis condition given by

$$\psi_j(\mathbf{x}_k) = \delta_{jk},$$

and $\psi_j \in \tilde{V}$ to obtain a unique set of basis. We can link each point in the domain to a basis function such that the basis function is 1 at that point and 0 at every other point. These basis functions are sometimes also called hat functions. See Figure 18, which shows the hat (basis) function corresponding to the point marked in yellow. The hat function is a piecewise linear polynomial in each of the elements and is non-zero only within the elements adjacent to the node to which it belongs. The hat function is 1 at the corresponding node and zero at every other node.

As previously mentioned, we require the approximate solution to satisfy the weak form such that

$$\int_\Omega a \nabla \tilde{u} \nabla \vartheta + \int_\Omega (\mathbf{b} \cdot \nabla \tilde{u}) \vartheta + \int_\Omega c \tilde{u} \vartheta = \int_\Omega f \vartheta. \tag{3.6}$$

Now, we are ready to represent our approximate solution such that

$$\tilde{u} = \sum_{N_p} u_j \psi_j, \tag{3.7}$$

where $u_j = \tilde{u}(\mathbf{x}_j) \in \mathbb{R}$ are the values of the approximate solution at nodes, and are referred to as degrees of freedom. We now define the degree of freedom vector as $\mathfrak{u} = [\tilde{u}_1, \tilde{u}_2, \ldots, \tilde{u}_{Np}]$. Now we insert the approximate solution, which is obtained through our linear polynomial constraints into the weak form in a so called Ritz-Galerkin approximation to obtain

$$\int_\Omega a \sum_{N_p} u_j \nabla \psi_j \nabla \vartheta + \int_\Omega (\mathbf{b} \cdot \sum_{N_p} u_j \nabla \psi_j) \vartheta + \int_\Omega c \sum_{N_p} u_j \psi_j \vartheta = \int_\Omega f \vartheta. \tag{3.8}$$

The above equation has N_p unknowns: u_j. To be able to solve for N_p unknowns, we need N_p equations. We can arrive at N_p equations, by substituting the test function ϑ for each of the basis functions $\{\psi_k\}$. This results in system of N_p equation given by

$$\int_\Omega a \sum_{N_p} u_j \nabla \psi_j \nabla \psi_k + \int_\Omega (\mathbf{b} \cdot \sum_{N_p} u_j \nabla \psi_j) \psi_k + \int_\Omega c \sum_{N_p} u_j \psi_j \psi_k = \int_\Omega f \psi_k, \tag{3.9}$$

where $k = 1, 2, \ldots, N_p$. The above equation can be represented in matrix-vector product form as

$$\mathfrak{s}\mathfrak{u} = \mathbb{l}, \tag{3.10}$$

where $\mathbb{s}$ is $N_p \times N_p$ matrix called the stiffness matrix, and is given as

$$\mathbb{s}_{kj} = \int_\Omega a\nabla\psi_j\nabla\psi_k + \int_\Omega (\mathbf{b}\cdot\nabla\psi_j)\psi_k + \int_\Omega c\psi_j\psi_k, \tag{3.11}$$

and $\mathbb{l}$ is a vector of length N_p called the load vector, and is given as

$$\mathbb{l} = \int_\Omega f\psi_k. \tag{3.12}$$

The use of the words *stiffness* and *load* has its origin in continuum mechanics where FEM is widely used. The degrees of freedom of the solution can then be obtained as $\mathbb{u} = \mathbb{s}^{-1}\mathbb{l}$.

Next, to study non-stationary problems, we consider a time-varying reaction diffusion and advection equation given by

$$m\frac{\partial u}{\partial t} - a(\mathbf{x})\Delta u + (\mathbf{b}(\mathbf{x})\cdot\nabla u) + c(\mathbf{x})u = f(\mathbf{x}). \tag{3.13}$$

The weak form of above equation is written as

$$\int_\Omega m\frac{\partial u}{\partial t}\vartheta + \int_\Omega a\nabla u\nabla\vartheta + \int_\Omega (\mathbf{b}\cdot\nabla u)\vartheta + \int_\Omega cu\vartheta = \int_\Omega f\vartheta. \tag{3.14}$$

Inserting the approximate form of u and using the hat functions as test functions, and expressing it in the matrix-vector form, we get

$$\mathbb{m}\frac{\partial \mathbb{u}}{\partial t} + \mathbb{s}\mathbb{u} = \mathbb{l}. \tag{3.15}$$

M is conventionally called the mass matrix and is given as

$$\mathbb{m}_{kj} = \int_\Omega m\psi_j\psi_k. \tag{3.16}$$

The solution u can then be obtained by choosing appropriate methods to discretise in time, and iterating over finite time steps. See Section 3.6 for details on time discretisation.

3.5 Discretisation of the weak form of the multi-phase field model

We now derive the weak form and apply the Ritz-Galerkin approximation to our model. Consider again the system of equations

$$\frac{\partial\phi_i}{\partial t} + \boldsymbol{v}\cdot\nabla\phi_i = \Delta\mu_i \tag{3.17}$$

and

$$\mu_i = -\frac{\epsilon}{Ca}\Delta\phi_i + \frac{W'(\phi_i)}{\epsilon Ca} + \mu_{INT_i}[\{\phi_i\}]. \tag{3.18}$$

The above system can be written as

$$\begin{bmatrix} 1 & 0 \\ 0 & 0 \end{bmatrix} \begin{bmatrix} \frac{\partial \phi_i}{\partial t} \\ \frac{\partial \mu_i}{\partial t} \end{bmatrix} + \begin{bmatrix} \mathbf{v} \cdot \nabla & -\Delta \\ \frac{\epsilon}{Ca}\Delta & 1 \end{bmatrix} \begin{bmatrix} \phi_i \\ \mu_i \end{bmatrix} = \begin{bmatrix} 0 \\ \frac{W'(\phi_i)}{\epsilon Ca} + \mu_{INT_i}[\{\phi_i\}] \end{bmatrix}. \tag{3.19}$$

Considering $\mathbf{u}_i = [\phi_i, \mu_i]^T$ which we will call the solution vector. This allows us to write our system in the form

$$\mathbf{M}_i \frac{\partial \mathbf{u}_i}{\partial t} - \mathbf{A}_i \Delta \mathbf{u}_i + \mathbf{B}_i \cdot \nabla \mathbf{u}_i + \mathbf{C}\mathbf{u}_i = \mathbf{f}_i, \tag{3.20}$$

where

$$\mathbf{M}_i = \begin{bmatrix} 1 & 0 \\ 0 & 0 \end{bmatrix}, \mathbf{A}_i = \begin{bmatrix} 0 & 1 \\ -\frac{\epsilon}{Ca} & 0 \end{bmatrix}, \mathbf{B}_i = \begin{bmatrix} \mathbf{v}_i \\ 0 \end{bmatrix}, \mathbf{C}_i = \begin{bmatrix} 0 & 0 \\ 0 & 1 \end{bmatrix}, \mathbf{f}_i = \begin{bmatrix} 0 \\ \frac{W'(\phi_i)}{\epsilon Ca} + \mu_{INT_i}[\{\phi_i\}] \end{bmatrix} \tag{3.21}$$

As previously mentioned in Section 1.5, Einstein summation convention is not applicable for the index i. We multiply the system by the test function ϑ and integrate to get

$$\int_\Omega \mathbf{M}_i \frac{\partial \mathbf{u}_i}{\partial t} \vartheta + \int_\Omega \mathbf{A}_i \nabla \mathbf{u}_i \cdot \nabla \vartheta + \int_\Omega (\mathbf{B}_i \cdot \nabla \mathbf{u}_i)\vartheta + \int_\Omega \mathbf{C}\mathbf{u}_i \vartheta = \int_\Omega \mathbf{f}_i \vartheta, \tag{3.22}$$

which is the weak form of our multi-phase field model. As each cell has a distinct shape and location, it is appropriate to define a unique triangular grid for each cell. For each cell i, let $\{(\mathbf{x}_i)_j\}$ be the set of N_{p_i} nodes and $\{(T_i)_k\}$ be the set of N_{ei} elements that together define the grid for cell i. Figure 19 shows two nearby cells with their unique grid.

For the cell i, the function space of all piecewise polynomials over the set $\{(T_i)_k\}$ is given as

$$\tilde{V}_i = \{ \underbrace{v : \Omega \to \mathbb{R}}_{\text{globally defined}} \mid \underbrace{v|_T \in \mathbb{P}_1(T)\ \forall T \in \{(T_i)_k\}}_{\text{locally a polynomial on each element}} \}.$$

Restricting ourselves to a unique basis based on the lagrange basis conditions, we arrive at the set of basis $\{(\psi_i)_j\}$ such that $(\psi_i)_j((\mathbf{x}_i)_k) = \delta_{jk}$. Let, $(\tilde{\phi}_i)_j = \tilde{\phi}_i((\mathbf{x}_i)_j)$ and $(\tilde{\mu}_i)_j = \tilde{\mu}_i((\mathbf{x}_i)_j)$ be the values of the approximate solution at the nodes of the grid $(\mathbf{x}_i)_j$ of cell i, then the approximate solution can be described in terms of the basis as

$$\tilde{\phi}_i = \sum_{N_{p_i}} (\tilde{\phi}_i)_j (\psi_i)_j,$$

and

$$\tilde{\mu}_i = \sum_{N_{p_i}} (\tilde{\mu}_i)_j (\psi_i)_j.$$

Let $\mathbb{u}_i = [(\tilde{\phi}_i)_1, (\tilde{\mu}_i)_1, (\tilde{\phi}_i)_2, (\tilde{\mu}_i)_2, \ldots, (\tilde{\phi}_i)_{N_{p_i}}, (\tilde{\mu}_i)_{N_{p_i}}]$ be defined as the degree of freedom vector of cell i, we can write

$$\mathbb{m}_i \frac{\partial \mathbb{u}_i}{\partial t} + \mathbb{s}_i \mathbb{u}_i = \mathbb{l}_i, \tag{3.23}$$

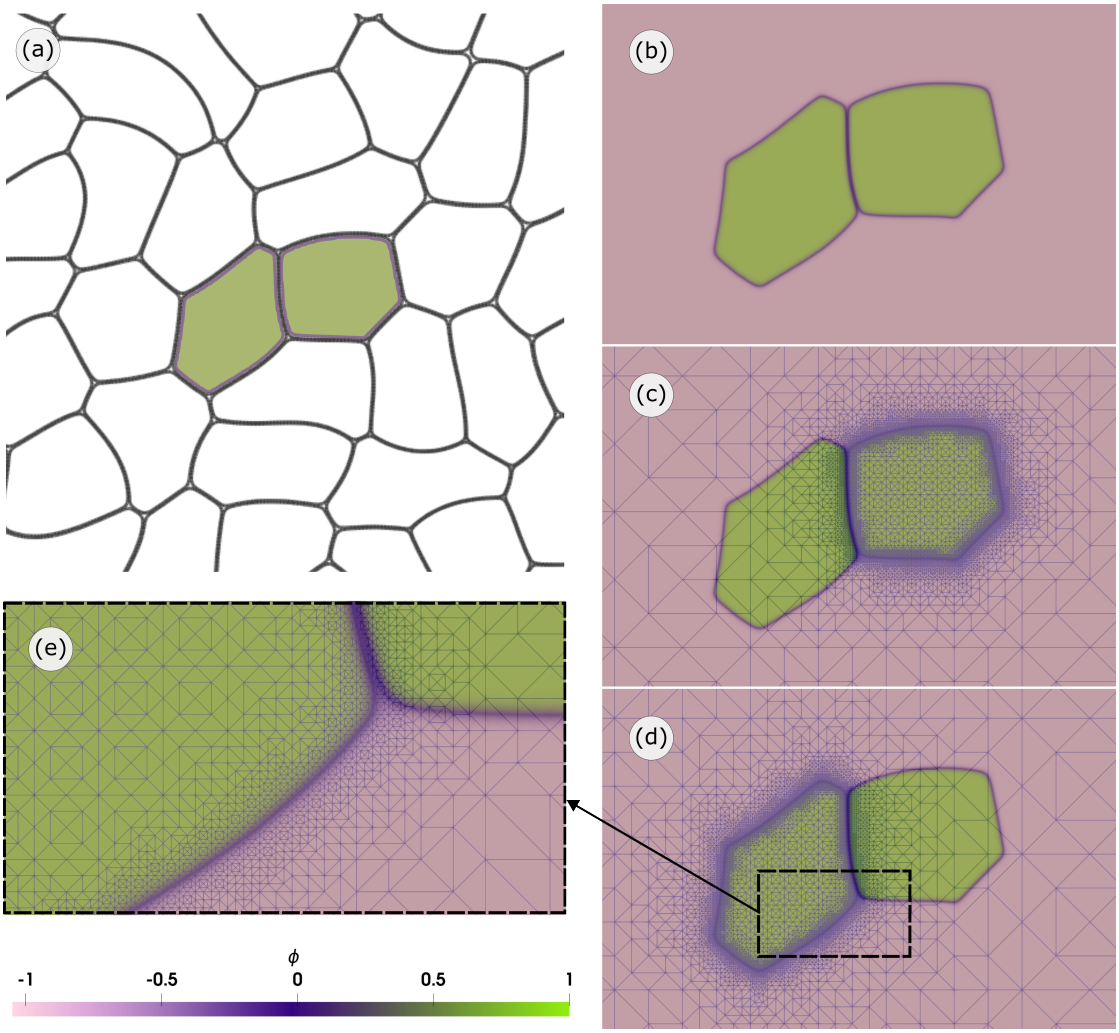


Figure 19: (a) Two highlighted neighbouring cells within a confluent monolayer are shown in (b-e) without visualising other cells. (c) and (d) shows the triangulated mesh of each cell, with (e) showing the zoomed mesh in (d)

where $\mathbb{m}_i$ is a $2N_{p_i} \times 2N_{p_i}$ matrix such that

$$\mathbb{m}_i = \begin{bmatrix} (\mathbb{m}_i)_{11} & (\mathbb{m}_i)_{12} & \cdots & (\mathbb{m}_i)_{1N_{p_i}} \\ (\mathbb{m}_i)_{21} & \ddots & & \vdots \\ \vdots & & & \\ (\mathbb{m}_i)_{N_{p_i}1} & \cdots & & (\mathbb{m}_i)_{N_{p_i}N_{p_i}} \end{bmatrix}, \tag{3.24}$$

where

$$(\mathbb{m}_i)_{kj} = \int_\Omega \mathbf{M}_i(\psi_i)_j(\psi_i)_k. \tag{3.25}$$

$\mathbb{s}_i$ is a $2N_{p_i} \times 2N_{p_i}$ matrix such that

$$\mathbb{s}_i = \begin{bmatrix} (\mathbb{s}_i)_{11} & (\mathbb{s}_i)_{12} & \cdots & (\mathbb{s}_i)_{1N_{p_i}} \\ (\mathbb{s}_i)_{21} & \ddots & & \vdots \\ \vdots & & & \\ (\mathbb{s}_i)_{N_{p_i}1} & \cdots & & (\mathbb{s}_i)_{N_{p_i}N_{p_i}} \end{bmatrix}, \tag{3.26}$$

where

$$(\mathbb{s}_i)_{kj} = \int_\Omega \mathbf{A_i}\nabla(\psi_i)_j \cdot \nabla(\psi_i)_k + \int_\Omega (\mathbf{B}_i \cdot \nabla(\psi_i)_j)(\psi_i)_k + \int_\Omega \mathbf{C}_i(\psi_i)_j(\psi_i)_k \tag{3.27}$$

$\mathbb{l}_i$ is vector of length N_p given as

$$\mathbb{l}_i = [(\mathbb{l}_i)_1, (\mathbb{l}_i)_2, \ldots, (\mathbb{l}_i)_{Np}]^T, \tag{3.28}$$

where

$$(\mathbb{l}_i)_k = \int_\Omega \mathbf{f}_i((\mathbf{x}_i)_k)(\psi_i)_k \tag{3.29}$$

All the integrals are calculated using exact Gaussian quadrature rules.

Equation 3.23 can be solved by first discretising in time, and then iterating over finite time steps.

3.6 Time discretisation

Consider a function of form

$$\frac{du}{dt} = f(t). \tag{3.30}$$

Suppose, the evolution of u is tracked from time $t = 0$ to $t = T$ at discrete time intervals given by the set $\{0, \tau, 2\tau, \ldots, T - \tau, T\}$. Suppose, the values of u, f and $\frac{du}{dt}$ at the n^{th} timestep is given as u^n, f^n and $\frac{du}{dt}^n$. If the initial value of u i.e. u^n for $n = 1$ is known, then subsequent values can be numerically approximated based on the choice of time discretisation. We will consider first order time-stepping schemes to discretise in time. There are two main forms of first order time-stepping: explicit and implicit time-stepping schemes. Using the taylor series approximation

$$\frac{du}{dt}^n \approx \frac{u^{n+1} - u^n}{\tau}, \tag{3.31}$$

we can define the first order time stepping scheme as

$$\frac{u^{n+1}-u^n}{\tau} = \kappa f^{n+1} + (1-\kappa) f^n \tag{3.32}$$

If $\kappa = 0$, the time-stepping is said to be explicit. Here, the value of τ plays a crucial role in the stability of the numerical solution. If $\kappa = 1$, the time-stepping is said to be implicit. Implicit schemes are unconditionally stable and large values of τ can be used. However, they involve inversion of matrices.

Given our system in Equation 3.20, we will discretise it using a semi-implicit method such that

$$\mathbf{M}_i^n \frac{\mathbf{u}_i^{n+1}-\mathbf{u}_i^n}{\tau} - \mathbf{A}_i^n \Delta \mathbf{u}_i^n + \mathbf{B}_i^n \cdot \nabla \mathbf{u}_i^n + \mathbf{C}^n \mathbf{u}_i^n = \mathbf{f}_i^{n+1} \tag{3.33}$$

As

$$\mathbf{f}_i^{n+1} = \begin{bmatrix} 0 \\ \frac{W'(\phi_i)^{n+1}}{\epsilon Ca} + {\mu_{INT}}_i^{n+1}[\{\phi_i\}] \end{bmatrix}, \tag{3.34}$$

we decompose $\mathbf{f}_i^{n+1}$ as

$$\mathbf{f}_i^{n+1} = {\mathbf{F}_1}_i^n \mathbf{u}_i^{n+1} + {\mathbf{f}_2}_i^n, \tag{3.35}$$

where ${\mathbf{F}_1}_i^n$ and ${\mathbf{f}_2}_i^n$ are some functions of $\{\phi_i^n\}$ and $\{\mu_i^n\}$. This allows us to rewrite Equation 3.33 as

$$\mathbf{M}_i^n \frac{\mathbf{u}_i^{n+1}-\mathbf{u}_i^n}{\tau} - \mathbf{A}_i^n \Delta \mathbf{u}_i^n + \mathbf{B}_i^n \cdot \nabla \mathbf{u}_i^n + \mathbf{C}^n \mathbf{u}_i^n = {\mathbf{F}_1}_i^n \mathbf{u}_i^{n+1} + {\mathbf{f}_2}_i^n, \tag{3.36}$$

and then by rearranging we get

$$\mathbf{M}_i^n \mathbf{u}_i^{n+1} - \tau {\mathbf{F}_1}_i^n \mathbf{u}_i^{n+1} = \mathbf{M}_i^n \mathbf{u}_i^n + \tau \left(\mathbf{A}_i^n \Delta \mathbf{u}_i^n - \mathbf{B}_i^n \cdot \nabla \mathbf{u}_i^n - \mathbf{C}^n \mathbf{u}_i^n + {\mathbf{f}_2}_i^n \right) \tag{3.37}$$

This allows us to write the solution at $n+1$-th timestep as

$$\mathbf{u}_i^{n+1} = \left(\mathbf{M}_i^n - \tau {\mathbf{F}_1}_i^n \right)^{-1} \left(\mathbf{M}_i^n \mathbf{u}_i^n + \tau \left(\mathbf{A}_i^n \Delta \mathbf{u}_i^n - \mathbf{B}_i^n \cdot \nabla \mathbf{u}_i^n - \mathbf{C}^n \mathbf{u}_i^n + {\mathbf{f}_2}_i^n \right) \right) \tag{3.38}$$

We now describe the decomposition of $\mathbf{f}_i^{n+1}$ by describing the decomposition of the individual terms. The decomposition of the derivative of the double well potential is performed as follows: Using Taylor series approximation, we get

$$\begin{aligned} W'(\phi_i^{n+1}) &\approx W'(\phi_i^n) + W''(\phi_i^n)(\phi_i^{n+1} - \phi_i^n) \\ &\approx (W'(\phi_i^n) - \phi_i^n W''(\phi_i^n)) + W''(\phi_i^n)(\phi_i^{n+1}) \end{aligned}.$$

Similarly, the interaction chemical potential can be represented as

$$\begin{aligned} {\mu_{INT}}_i^{n+1}[\{\phi_i\}] &\approx {\mu_{INT}}_i^n[\{\phi_i\}] + {\mu'_{INT}}_i^{n+1}[\{\phi_i\}](\phi_i^{n+1} - \phi_i^n) \\ &\approx ({\mu_{INT}}_i^{n+1}[\{\phi_i\}] - {\mu'_{INT}}_i^{n+1}[\{\phi_i\}]\phi_i^n) + {\mu'_{INT}}_i^{n+1}[\{\phi_i\}](\phi_i^{n+1}) \end{aligned}.$$

Therefore,

$${\mathbf{F}_1}_i^n = \begin{bmatrix} 0 & 0 \\ \frac{W''(\phi_i^n)}{\epsilon Ca} + {\mu'_{INT}}_i^{n+1}[\{\phi_i\}] & 0 \end{bmatrix}, \tag{3.39}$$

and

$$\mathbf{f}_{2_i}^{\,n} = \begin{bmatrix} 0 \\ \frac{(W'(\phi_i^n) - W''(\phi_i^n)\phi_i^n)}{\epsilon Ca} + ({\mu_{INT}}_i^{n+1}[\{\phi_i\}] - {\mu'_{INT}}_i^{n+1}[\{\phi_i\}]\phi_i^n) \end{bmatrix}. \tag{3.40}$$

Equation 3.38 can then be spatially discretised using finite elements as described in Section 3.5. For simplicity, we did not include $g(\phi)$ in deriving the numerical scheme. $g(\phi)$ is always considered explicitly.

3.7 Software and hardware

Now that we have discussed the spatial and temporal discretisation of our model, we now describe some computational details regarding the implementation. The iterative solution in Equation 3.38 is implemented using the open source C++ FEM framework called *AMDiS (Adaptive Multi-Dimensional Solutions) v1.2*. The framework has been developed by the Institute of Scientific Computing, Technische Universität Dresden, Germany, and the software repository can be found at [123]. For more details and examples refer to [124–126]. The implementation of the model in this thesis closely follows the implementations of [5, 84].

AMDiS allows for defining multiple meshes and efficient parellisation. The iteration in Equation 3.38 for each cell is computed on a different CPU core. The communications between the cores is handled through MPI. The post processing of data is performed using *Python* and its libraries. *Paraview* is used to visualise and interpret the solution over the unstructured grid. The simulations were performed on resources provided by Sigma2 - the National Infrastructure for High-Performance Computing and Data Storage in Norway.

3.8 Mesh refinement

Each cell possesses its own unique triangulated grid, also referred to as a mesh. A naive implementation that considers elements of the same size distributed uniformly across the domain results in the wastage of computational resources, because our model defines the bulk phases, i.e., $\phi \approx 1$ and $\phi \approx -1$ as exhibiting minimal dynamical change. Most changes are concentrated at the interface, and this fact is used to create a non-uniform distribution of element sizes and locations such that the interface comprises very small elements, as shown in Figure 19.

If h is the length of the longest edge of an element, then the interface is composed of elements such that h is of length $\mathcal{O}(0.5\epsilon)$. The interior and exterior of a cell is composed of elements such that h is of length $\mathcal{O}(5\epsilon)$ and $\mathcal{O}(10\epsilon)$, respectively. At every time step, based on how the interface moves, the mesh needs to be either refined or coarsened. To maintain regularity, the mesh is defined in a hierarchical manner such that an initial coarse macro mesh exists, which is iteratively refined or coarsened based on the value of ϕ.

3.9 Parallel computation

The iteration in Equation 3.38 for each cell is calculated on a separate CPU core. Each cell possesses its own triangulated mesh. The only term in our model that depends on multiple phase fields is the interaction energy. However, the interaction energy between two cells is nonzero only if their interfaces overlap. The contribution to interaction energy for two faraway cells is zero. This allows us to define a criterion for transferring phase information between cells that lie within a certain threshold distance from each other. This drastically reduces the computational load of transferring phase information from one mesh to another. For each cell, the phase fields of nearby cells are linearly interpolated on the cell's mesh and used for calculating the appropriate terms related to interaction energy.

Chapter 4

Supplementary results

In this chapter, we describe results that supplement the papers. Some results outlined in this chapter are better understood in the context of the results in the papers.

4.1 Morphological influence of activity and deformability

Cell activity (v_0) and cell deformability (Ca) are the primary control parameters in our studies. Figure 20 shows tissue snapshots from simulations for different values of v_0 and Ca, with parameters according to Paper II. Cells with low deformability have a higher energetic cost for deformations and are typically less elongated than cells with high deformability. The extracellular gaps between three cells, which form concave triangles, are larger in the low deformability scenario. Since the cell area (2D volume) is the same for all situations shown in the figure, the larger extracellular gap suggests a higher degree of cell overlap.

Cells with low deformability tend to be polygonal-shaped, while cells with high deformability also possess curved cell-cell junctions. Additionally, the cells are more elongated at higher activity levels because higher activity contributes to shape fluctuations. The changes in cell morphologies due to variations in the parameters v_0 and Ca highlight the important role these two parameters play in the emergent behavior of cells in our model.

4.2 Shape index

The shape anisotropy of cells can be characterised by a non-dimensional number called the shape index. Shape index is defined as

$$p_{si} = \frac{\text{Perimeter of cell } i}{\sqrt{\text{Area of cell } i}}. \tag{4.1}$$

The area (2d volume) of the cell was previously defined by using the rescaled phase field as an indicator function as $V_i = \int_\Omega \hat{\phi}_i$. The perimeter is obtained by

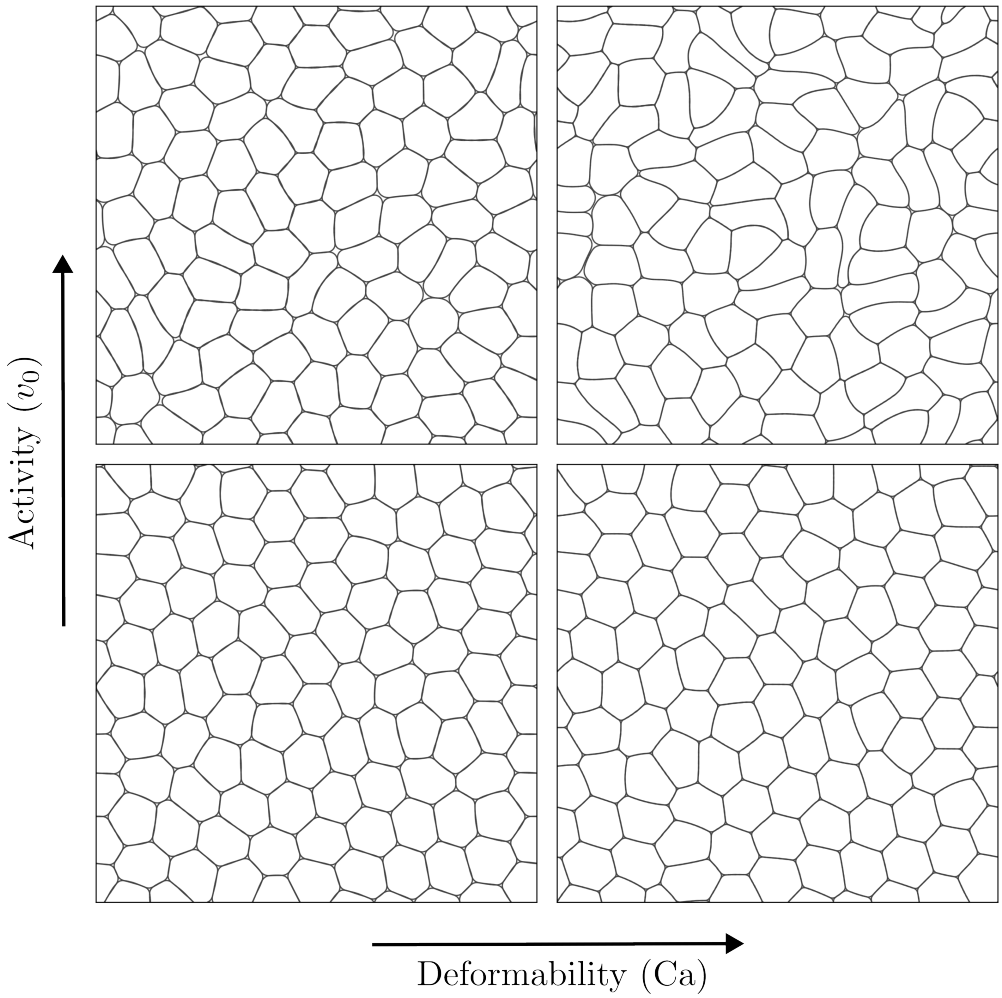


Figure 20: Tissue snapshots for different values of v_0 and Ca. v_0 varies from 0.1 to 1.0, while Ca varies from 0.05 to 0.02. Other model parameters are according to Paper II.

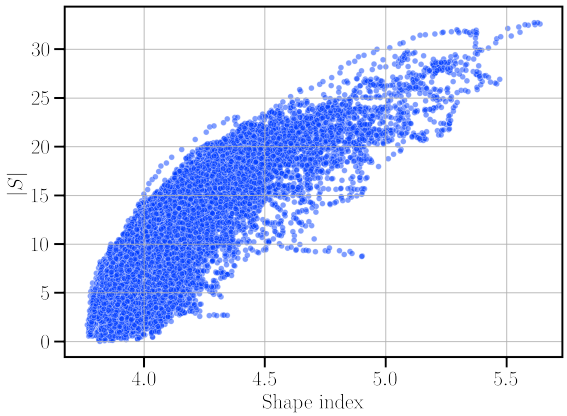


Figure 21: Largest eigenvalue of shape deformation tensor $|\mathbf{S}|$ plotted against shape index p_s. The parameters are the same as those in Paper II.

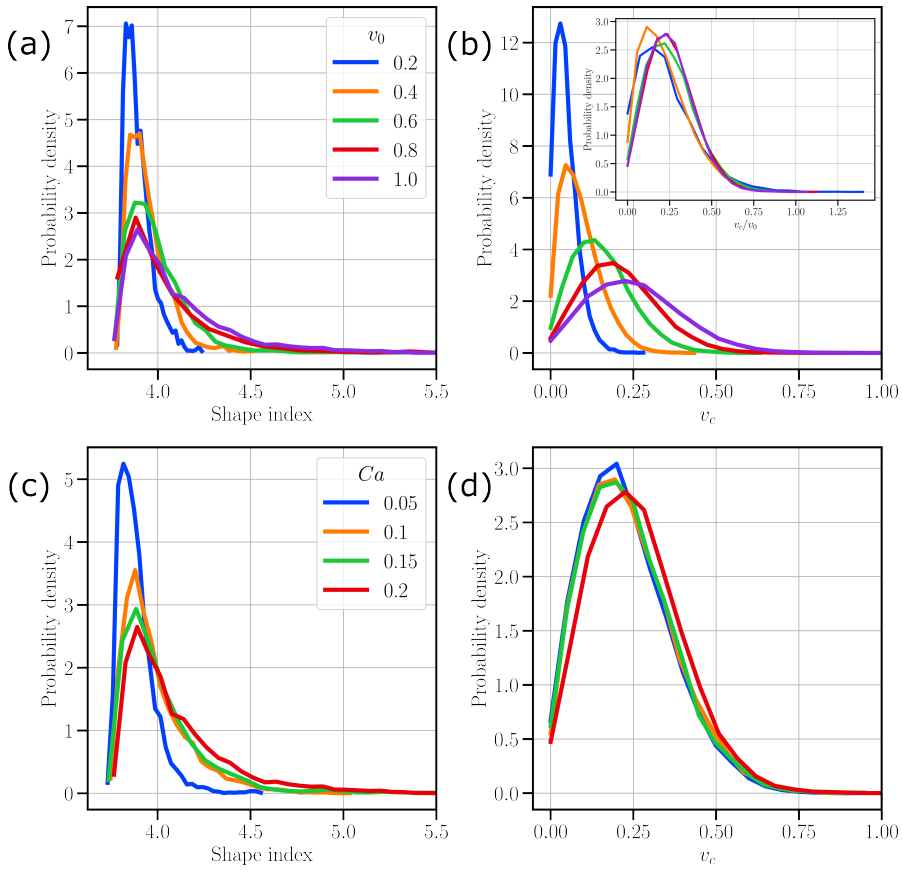


Figure 22: Probability density of shape index for varying (a) v_0 and (c) Ca, and of cell speed for varying (b) v_0 and (d) Ca. The distribution is calculated for all cells and for all times after a transient initial time. The inset in (b) shows the probability of cell speed normalised by activity v_0. Other parameters are the same as those in Paper II.

numerically integrating over the length of the zero-level contour using the *VTK* library in *Python*. Since the area of our cells remains constant due to conservative dynamics, the shape index depends only on the perimeter. Thus, cells with a larger shape index have a longer interface and, consequently, a higher interface energy. The shape index has been shown to be an important structural order parameter in the context of jamming transitions [41, 53], where $p \approx 3.81$ was found to be the critical shape index below which cells are jammed. This critical shape index is approximately equal to the shape index of a regular pentagon. Within the multi-phase field model, we do observe some T1 transitions below this critical shape index; however, this might also be influenced by the presence of extracellular gaps [1]. Figure 21 shows the comparison of shape index of cells and the largest eigenvalue of the shape deformation tensor, $|\mathbf{S}|$. Both of these shape descriptors are typically correlated with each other for shape morphologies obtained within the multi-phase field simulations. The Figure 22a and 22c shows the distribution of shape index of cells as the activity v_0 and deformability Ca are varied. The mean and the variance of the shape index of cells increases with both activity and deformability.

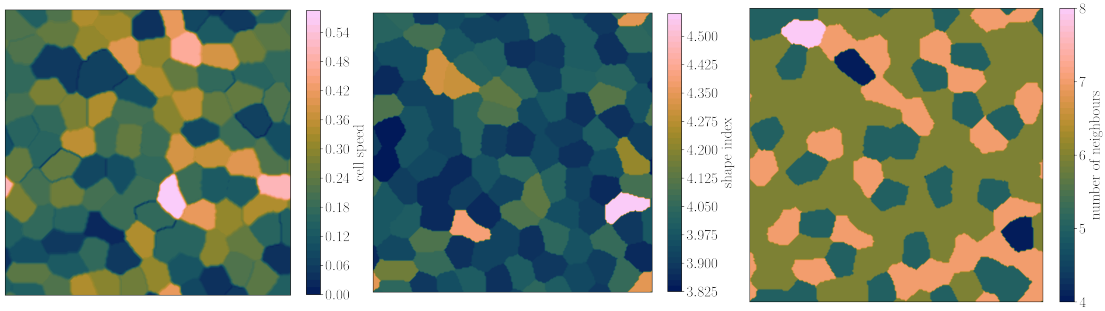


Figure 23: A tissue snapshot with cells coloured as per the values of their (left) cell speed v_c, (middle) shape index, p_s and (right) number of neighbours. The parameters are the same as those in Paper II.

4.3 Center of mass

The location of the center of mass of the cell i is found as

$$\mathbf{r}_i(t) = \frac{\int_\Omega \mathbf{x}\hat{\phi}_i(\mathbf{x},t)dx}{\int_\Omega \hat{\phi}_i(\mathbf{x},t)dx}. \tag{4.2}$$

The instantaneous velocity of center of mass at a given time step is then calculated as

$$\mathbf{v}_{ci}(t) = \frac{\mathbf{r}_i(t) - \mathbf{r}_i(t-\tau)}{\tau}. \tag{4.3}$$

This velocity is dependent upon the time-step size τ considered. For different values of τ, the velocity could have different magnitudes and orientations. The velocity either stays constant or reduces with increasing values of τ. Cells exhibit different anomalous diffusive behaviours depending on the time step size considered [113]. Thus, the simulation time step size impacts the observed behaviour.

The cell speed is given by $v_{ci}(t) = |\mathbf{v}_{ci}(t)|$. Figure 22b and 22d shows the distribution of cell speeds as function of v_0 and Ca. The cell speeds are higher for higher v_0, but if the distribution are normalised by v_0, as shown in the inset in Figure 22b, the normalised distributions appear similar. On the other hand, the distribution of cell speed does not vary significantly with Ca. Cells with higher Ca undergo more T1 transitions, whereas cells with lower Ca move together in smaller clusters [2].

One of the key disadvantages of multi-phase field models is the inability to resolve the instantaneous velocity field across the cell. In other words, given two points inside a cell, it is not possible to keep track of their relative velocities. The center of mass itself is a property of cell shape rather than a property inherent to a particular "particle" inside of the cell. Whereas in experiments, cells could be injected with fluorescent tracking particles and a instantaneous velocity field of different parts of the cells can be obtained by tracking the individual particles. Cells are also heterogenous in appearance and specific features within cells could be tracked by tracking inhomogeneities such as organelles. In multi-phase field models, the cell interior is a homogenous (textureless) phase. However, in practice,

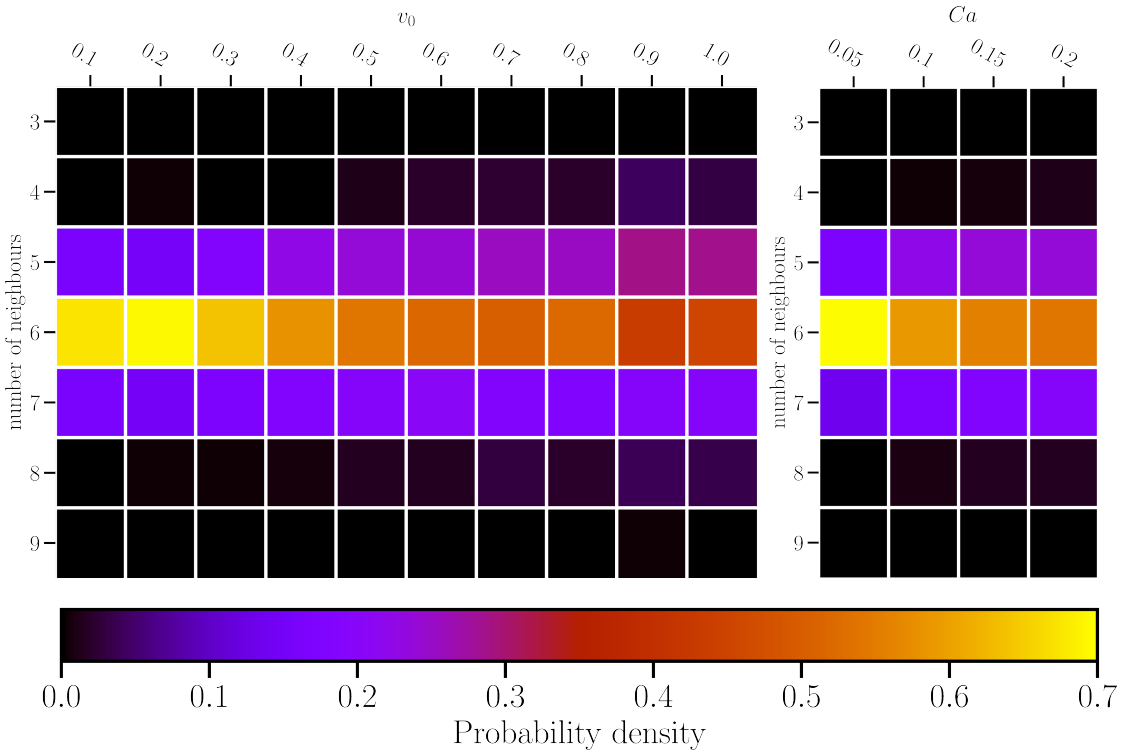


Figure 24: Distribution of number of neighbours for varying v_0 and Ca. Other parameters are the same as those in Paper II.

the velocity field is obtained by different coarse graining procedures of the center of mass velocities. One method utilises the phase field as an indicator function to define the instantaneous velocity field as

$$\hat{\phi}_i(\mathbf{x}, t)\mathbf{v}_{ci}(t). \tag{4.4}$$

Using this approach, the global velocity field of a monolayer can be described in an ad-hoc manner as

$$\mathbf{v}_g(\mathbf{x}, t) = \sum_i \hat{\phi}_i(\mathbf{x}, t)\mathbf{v}_{ci}(t). \tag{4.5}$$

Figure 23 shows the global velocity field along with the shape index field (cells are marked with their shape index) and the number of neighbours field (cells are marked with their number of neighbours). The figure displays heterogeneous distributions of cell speeds across the tissue. In Paper I and Paper II, we show that T1 transitions cause changes in cell speed, contributing to the heterogeneous distributions of cell speed [1, 2].

4.4 T1 transitions

Let, N be the total number of cells in the monolayer. We can represent the monolayer with the set

$$\mathcal{M} = \{1, 2, \ldots, N\} \tag{4.6}$$

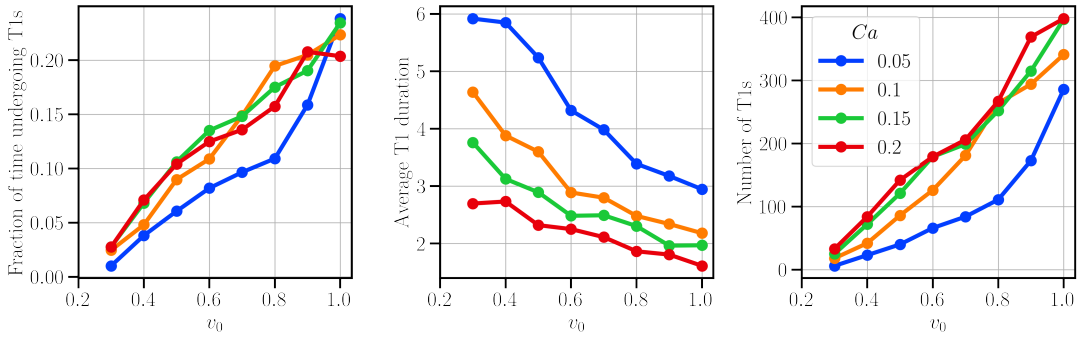


Figure 25: (left) Fraction of time a cell is undergoing a T1 transition, (middle) average duration of a T1 transtition, and (right) number of T1 transitions as function of v_0 and coloured as per Ca. Legend in last panel applies to all panels. The parameters are the same as those in Paper II.

We can define a neighbour adjacency matrix $\mathcal{N}_{N\times N}$ at a particular time t such that

$$\mathcal{N}_{ij}(t) = \begin{cases} 1 & : \quad i,j \in \mathcal{M} \text{ are neighbours at t and } i \neq j \\ 0 & : \quad \text{otherwise} \end{cases}$$

Essentially, two cells i and j are neighbours if they touch other. Empirically, we compute $\int_\Omega \hat{\phi}_i \hat{\phi}_j dx$. If this crosses a certain threshold value, then the cells are considered to be neighbours.

Figure 24 shows the distribution of number of neighbours of cells for varying v_0 and Ca. The mean number of neighbours is approximately 6 for all situations; however, the standard deviation increases with increasing v_0 and Ca.

In multi-phase field models, T1 transitions are finite time events which initiates when two neighbouring cells A and B lose contact, and concludes when two of their neighbours C and D make contact [1, 2]. Such a T1 transition can be represented by a set $\mathcal{T} = \{A, B, C, D\}$ and its start time and end time are denoted as $t = t_{\mathcal{T}}^-$ and $t = t_{\mathcal{T}}^+$, respectively.

The changes in the neighbourhood topology during a T1 are

$$\mathcal{N}_{CD}(t_{\mathcal{T}}^-) = 1 \Rightarrow \mathcal{N}_{CD}(t_{\mathcal{T}}^+) = 0$$
$$\mathcal{N}_{AB}(t_{\mathcal{T}}^-) = 0 \Rightarrow \mathcal{N}_{AB}(t_{\mathcal{T}}^+) = 1,$$

Other connections involving the four cells remain same during $\Delta t_{\mathcal{T}} = t_{\mathcal{T}}^+ - t_{\mathcal{T}}^-$, which is the duration of the T1. The left panel of Figure 25 shows the fraction of time that a cell is undergoing T1 transitions during the simulation as a function of v_0 and Ca. Cells spend significantly more time undergoing T1 transitions at higher activities, but there is no strong dependence on cell deformability. The middle panel of Figure 25 shows the average duration of a T1 transition as a function of v_0 and Ca. Slower and less deformable cells take longer to undergo a T1 transition. Even though deformability does not affect the fraction of time a cell undergoes T1 transitions, less deformable cells undergo fewer T1 transitions because they take longer to conclude a T1 transition, as shown in the right panel of Figure 25. Unsurprisingly, cells with higher activities undergo more T1 transitions.

4.5 P-atic shape descriptors

We have discussed two cell shape descriptors; the shape index p_s and the largest eigenvalue of the shape deformation tensor $|S|$. However, to study emergence of nematic and hexatic order, we need shape descriptors that can quantitatively describe p-atic symmetry. A shape is said to possess p-atic symmetry if it remain invariant under rotation by $\frac{2\pi}{p}$, with p being an integer. In essence, we need descriptors to compare a cell shape to a regular p-sided polygon. For an arbitrary integer $p \in \mathbb{Z}$ such that for $p > 2$, we require an order parameter that is equal to 1 for a p-sided regular polygon and has a lower value for other shapes depending on how similar the shape is to the regular polygon. Previously, in the study of epithelial monolayers, two methods were used to generate such an order parameter. One method relies on the location of the vertices of the cells to generate a shape function γ_p [89], while the other relies on the location of the center of mass of the neighbours of the cells to define a bond order parameter Ψ_p^{bond} [127, 128]. In the first method, $\gamma_p = 1$ if vertices of the shape constitute vertices of a p-sided regular polygon. While in the second method, $\Psi_p^{bond} = 1$ if the center of mass of the neighbours together form a p-sided regular polygon. Paper IV and Reference [129] show that both these methods are not robust, respectively. Paper IV instead proposes the use of Minkowski Tensors which allows for defining p-atic shape order parameters $q_p \in [0, 1]$, that are robust because small changes in the shape results in small changes in the q_p. The robustness of the p-atic order parameters is essential to capture irregular and continuous shape changes within the monolayer. For more details on Minkowski Tensors, see Paper IV. Note, the notation in this section deviates from the notation of the rest of the thesis, and is based on the notation of the Paper IV for easy comparison with the paper.

Provided a contour $\partial\mathcal{C}$ of a cell, the Minkowski tensors are used to define a complex number

$$\psi_p = \int_{\partial\mathcal{C}} e^{ip\theta_{\boldsymbol{n}}}\, d\partial\mathcal{C}, \tag{4.7}$$

where $p \in \mathbb{Z}$, $i = \sqrt{-1}$ and θ_n is the orientation of the normal vector of the contour. The p-atic shape order parameter is then defined as

$$q_p = \frac{|\psi_p|}{\psi_0}, \tag{4.8}$$

where $\psi_0 = \frac{1}{2}\int_{\partial\mathcal{C}} d\partial\mathcal{C}$. $q_p \in [0, 1]$ defines the strength of the p-atic order. $q_p = 1$ if the cell is a p-sided regular polygon. For $p = 2$, $q_2 = 1$ if a cell shape corresponds to a line. The Figure 26 shows the contours of an arbitrarily selected cell from a multi-phase field simulation along with several shape descriptors. The cell undergoes continuous shape deformations and several discrete changes in its neighbourhood topology. The quantity, d_z, is the mean distance of the points in the zero level set Z_ϕ of the cell from its center of mass and is generally correlated with the shape index. As the cell undergoes continuous changes in its shape, so does q_p, p_s and d_z, whereas the number of neighbours change discretely.

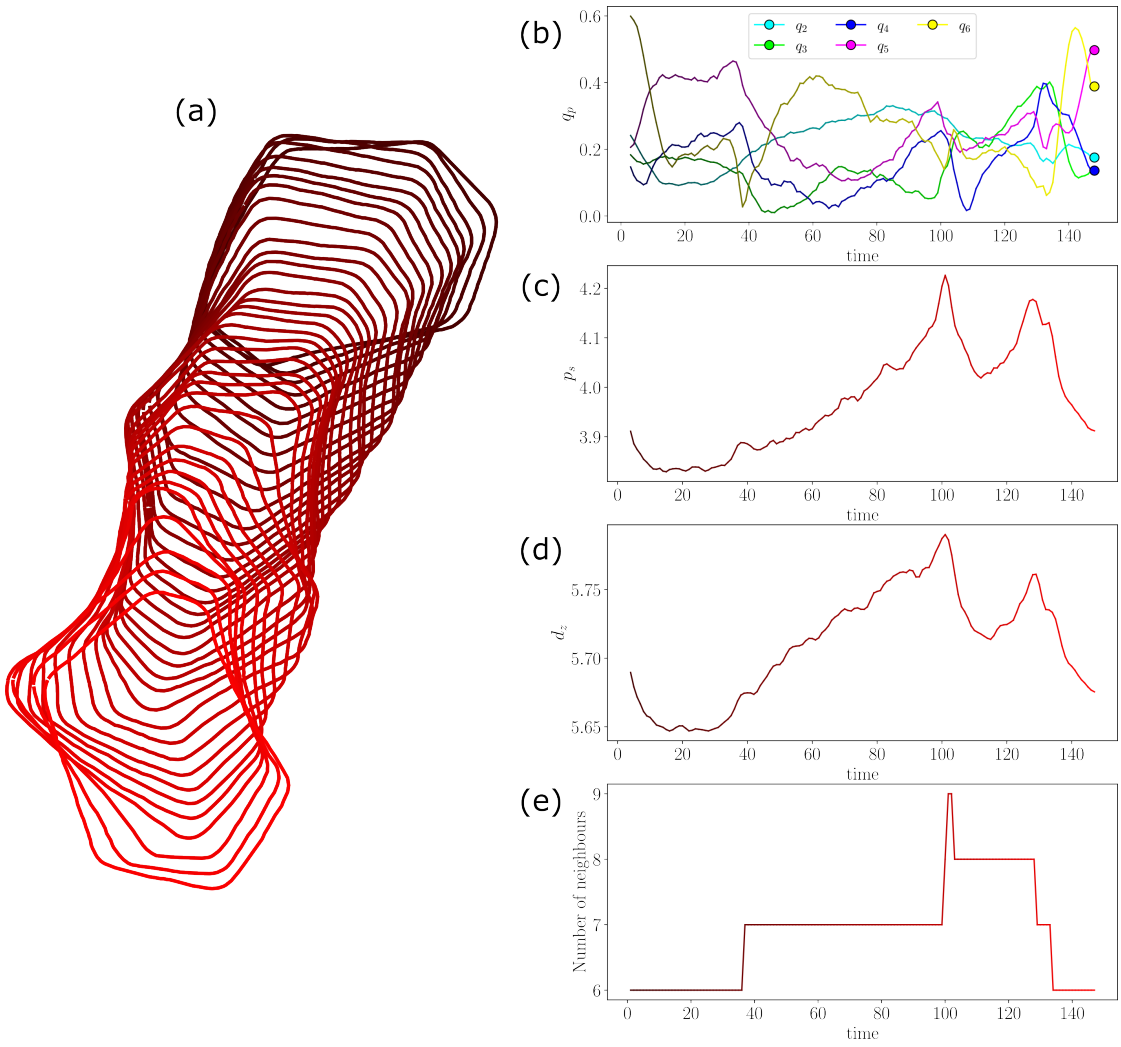


Figure 26: (a) Plots of the boundaries of a cell as it evolves through time with the evolution of some of its properties in (b-e). The colours increase in lightness with time. Note that the cell is within a confluent monolayer interacting with other cells which are not visualised. Evolution of (b)$|q_p|$ for $p = 2, 3, 4, 5, 6$, (c) shape index, (d) mean distance from cell center and (e) number of neighbours. The parameters are the same as those in Paper II.

Chapter 5

Summary of papers and outlook

Every number other than 0 and ∞ is strange

Me

For a moment, nothing happened. Then, after a second or so, nothing continued to happen.

Douglas Adams, The Hitchhiker's Guide to the Galaxy

5.1 Introduction

In this chapter, we summarise and connect the main results from Papers I, II, III and IV. Wherever necessary, we will cross reference the four papers in their respective summaries depending on the relationships between them.

In terms of the differences in model parameters, Paper I uses F_{INT1} as the interaction energy, while Papers II, III and IV uses F_{INT2} as the interaction energy. Empirically, the use of F_{INT2} allows for simulation with much higher activities.

Paper IV is a collaboration across simulations, experiments, and data analysis. My contribution to this paper is related to the simulations of the multi-phase field model and the corresponding data analysis.

5.2 Paper I: Robust statistical properties of T1 transitions in a multi-phase field model of cell monolayers

Paper I recognizes T1 transitions as finite-time neighbour exchange events involving four cells within the multi-phase field model. T1 transitions begin when

two cells lose contact and conclude when two of their neighbours make contact. Paper I introduces the concept of an *epicenter* of a T1 transition, which is defined as the location of a point whose sum of distances to the boundaries of all cells involved in the T1 transition is minimal. The location of the *epicenter* is fixed for a given T1 transition and is found midway during the T1 transition. The *epicenter* lies inside the extracellular gap created during the T1 transition. The duration of the T1 transition corresponds to the lifetime of this extracellular gap. The concept of an *epicenter* proves extremely useful in measuring several key properties of T1 transitions in Papers I, II, and III.

In our model, the phase fields of the cells evolve to minimize a free energy $\mathcal{F}$ while preserving cell area. This free energy is minimized when cells relax to an equilibrium where the interface length is at a minimum. For a confluent tissue, this state is characterized by a tiling of hexagonal cells. However, the presence of activity in our model injects energy at the individual cell level, causing cells to move, deform their neighbours, and undergo deformations themselves. These deformations increase with activity v_0 and if cell deformability Ca is high. A larger value of Ca reduces the energetic cost associated with the deformations.

In Paper I, we coarse-grain the free energy density to reveal that the energy is concentrated near the vertices shared by three cells. To present an alternative explanation to the ones presented in Paper I, consider a circular ring with a radius about 20% of the size of the cell. This ring can be moved across the domain, and one can compute the total length of the cell-cell junction within that ring. Essentially, the coarse-grained energy density defined in the Paper I at a location is approximately proportional to the cell-cell junction length (and is equal to the average free energy density) within a ring corresponding to the coarse-graining radius placed at that location.

Next, we observe how this coarse-grained energy evolves at the *epicenter* of a T1 transition. The mean evolution of this coarse-grained energy at the *epicenter* for relative time before and after a T1 transition is plotted in Paper I. It is immediately recognizable that the evolution of energy is asymmetric about the T1 transition. Since energy is shape-dependent, the shape deformations before and after a T1 transition are asymmetric. The energy rises slowly before the start of a T1, reaches a peak during the T1, experiences a sharp fall immediately after the T1, and then follows with a slower relaxation towards the mean. Since energy is related to the length of the cell-cell junctions, this means that the shrinkage of a cell-cell junction before a T1 is slower than the expansion of the junction after a T1. We also show that the evolution of this energy is dependent on activity v_0 and deformability Ca, while other parameters do not have a significant impact.

The peak value of energy attained during the T1 is independent of v_0. However, cells spend a longer time reaching the peak energy if v_0 is low and take longer to relax back to the average energy. This also means that the two vertices that coalesce during a T1 do so faster if activity is high, and the two vertices that are generated during a T1 transition move away faster after the T1 transition. The duration of T1 transitions decreases with increasing v_0.

The deformability Ca is a parameter that affects the relative contribution of the Cahn-Hilliard energy, which is why for varying deformability, the energy profile

is normalized with the maximum energy, after which the curves appear similar for different values of Ca, indicating the rate at which the junctions shrink before T1 transition or the rate at which the junctions expand after T1 transition are independent of cell deformability within the explored parameter regime. However, deformability influences the duration of T1 transition, which reduce with increasing deformability.

Through montages of cells undergoing T1 transitions, Paper I shows that most deformations due to T1 transitions occur near the epicenter, with some minor deformations at cell edges away from the epicenter. The loser cells appear to be pinched by the gainer cells near the *epicenter* until they lose contact. All four cells involved in the T1 transition experience significant shape deformations, and the differences between the shape deformations of loser and gainer cells will be further explored in Paper III. The four cells undergoing T1 transition generate a quadrupolar flow field, as shown in Paper II.

The shape index of a cell is linked to the energy associated with the cell because a larger shape index indicates a longer interface (while the cell area remains fixed), resulting in a higher energy. Paper I shows that the shape index of cells increases before the T1 transition, reaches a peak value during the T1 transition, and decreases afterward. This behavior indirectly reflects the mean energy evolution of the four cells involved in the T1 transition in terms of shape index. Whereas, the energy evolution shown in Figure 4 of Paper I provides information about the spatial concentration of energy near the epicenter. The shape index also increases with an increase in Ca and an increase in v_0. So do the number of T1 transitions. Paper III will further explore the connection between cell shape and T1 transitions, providing insights into the asymmetry of the energy and shape index profiles before and after the T1 transition, with a focus on the deformations of the cells that gain and lose neighbours during the T1 transition.

5.3 Paper II: From cell intercalation to flow, the importance of T1 transitions

In Paper II, we illustrate the flow field generated by T1 transitions and show that pair separation distance between cells is dependent linearly on the number of T1 transitions.

Paper II considers the orientation of a T1 transition as the orientation of the cell-cell junction created after the T1 transition and shows that this new junction is approximately perpendicular to the cell-cell junction that vanishes due to the T1 transition.

With the help of this orientation and the notion of *epicenter* defined in Paper I, Paper II illustrates a series of steps to transform the global velocity field $\mathbf{v}_g(\mathbf{x}, t)$ to calculate the ensemble-averaged flow field associated with T1 transitions. The ensemble-averaged flow field due to T1 transitions comprises quadrupolar vortices with alternating circulation centered at the *epicenter* of T1 transitions. The direction of flow field near the *epicenter* is governed by the direction of motion of cells losing and gaining neighbours.

The evolution of the magnitude of the velocity field near the *epicenter* follows a profile similar to the one obtained for the average speed of cells undergoing a T1 transition in Paper I. The cell speed near the *epicenter* remains constant before the T1 transition, rises during the T1 transition, reaches its peak at the end of the T1 transition, and then falls.

The paper also defines a velocity polarization field, which is a scalar field varying between 0 and 1 that informs the likelihood of the observed flow field. The high values of the velocity polarization field near the *epicenter* reveal the *average shape* of cells undergoing the T1 transition. The *average shape* at the end of the T1 transition shows that the cell interface away from the *epicenter* is rounded, while the cell shape near the interface experiences a sharp change. At the end of the T1 transition, the velocity polarization near the *epicenter* is higher than at any other time, suggesting that the flow field observed near the *epicenter* at the end of the T1 transition is very likely to occur in all T1 transitions.

To study how cells mix within the tissue due to T1 transitions, we introduce the notions of a cell pair and a cell triplet. A cell pair is a set of two cells that were neighbours at some initial time. The distance between these two cells is called the pair separation distance. A cell triplet is a triangle formed by a collection of cells that at some initial time shared a vertex. The area spanned by this triangle is called the triplet area. If cell activity is not sufficient, cells are caged among their neighbours and may undergo minor fluctuations in shape, pair separation distance, or triplet area. The pair separation distance and triplet area remain almost constant even if the cells move as a flock without undergoing any T1 transitions. However, if cells undergo T1 transitions, then the pair separation distance and the triplet area start to diverge. Thus, the pair separation distance and the triplet area capture the relative dispersion of cells.

The mean pair separation distance $\Pi(t)$, the mean triplet area $\Lambda(t)$, and the mean squared displacement $\sigma^2(t)$ increase with both time and activity v_0. The increase of $\Pi(t)$ and $\Lambda(t)$ suggests that cell move away from each other over time.

To understand how T1 transitions influence σ^2, Π and Λ, we plot these quantities against the cumulative number of T1 transitions. This reveals that Π increases linearly with the number of T1 transitions at the same rate, irrespective of the model parameters, whereas Λ is proportional to $\sqrt{\Pi}$. In other words, the mixing rate of cells encoded by Π increases linearly with the number of topological changes. Such a dependence on the number of T1 transitions was not observed for σ^2. This behaviour can be easily tested in other models and experiments. If found to be valid across many systems, then mixing rates of particles in dense systems can be related to the number of changes in the neighbourhood topology.

5.4 Paper III: Emergent cell migration from cell shape deformations and T1 transitions

Paper III explores the spatial and temporal properties of how T1 transitions influence each other using a multi-phase field (MPF) model and an active elastic solid (AES) model. The MPF model allows for the resolution of arbitrary cell

shapes resulting from deformations due to interactions. In contrast, in the AES model, cells are active point-like particles that interact with their neighbours through spring-like forces. We compare the spatiotemporal properties of neighbour exchanges within both models and reveal that shape plays an important role in the spatial correlations of T1 transitions.

In both the MPF and AES models, T1 transitions are neighbour-exchange events involving four cells and have a finite duration. In the MPF model, these events are detected by tracking cell-cell junction remodeling between four cells, while in the AES model, they are identified through geometric relations between cell positions. The geometric relations used in the AES model do not differentiate between T1 transitions and neighbour-exchange events involving more than four cells at a given time. Thus, when discussing T1 transitions in the AES model, the statistics also include these higher-order neighbour-exchange events, which are less numerous than T1 transitions. In the MPF model, neighbour-exchange events involving more than four cells at a given time are extremely rare.

The waiting time between successive T1 transitions involving a common cell is exponentially distributed in both the MPF and AES models. On average, the waiting time decreases with increasing activity in both models. The exponential distribution suggests that successive T1 transitions involving a common cell might not be temporally related.

Next, we plot the radial distribution functions $g_\omega(r)$ for pairs of T1 transitions that take place within a fixed time window of size ω. In both models, we observe that T1 transitions are non-homogeneously distributed in space. In the AES model, the peaks of $g_\omega(r)$ occur at distances characteristic of cell width. By contrast, in the MPF model, there is an additional peak at very low values of r, the location of which requires further exploration of cell shape for clarification. In the MPF model, the epicenters of T1 transitions lie in the vicinity of cell-cell junctions, and thus the profile of $g_\omega(r)$ should be related to the locations of cell-cell junctions. Increasing the time window ω results in a flattening of $g_\omega(r)$, suggesting that spatial correlations between T1 transitions diminish over time. This occurs because, over time, T1 transitions remodel the junctions within the monolayer, destroying the spatial correlations. The spatial correlations captured by $g_\omega(r)$ decrease with increasing activity due to a higher number of junction remodelings from T1 transitions.

We show that T1 transitions play a dual role in both cell shape relaxation and cell shape tension, depending on how the neighbourhood topology of the cell changes. The shape index of cells, on average, increases with an increase in the number of neighbours. Thus, cells that lose neighbours experience a reduction in shape index, while cells that gain neighbours experience a rise in shape index. Since cell areas are fixed, the shape index of the cells is linearly proportional to the length of the interface and, thus, to the energy associated with a cell. Therefore, by losing neighbours, the energy associated with a cell reduces as it relaxes its shape, and vice versa for the cells that gain neighbours.

Additionally, cells that gain or lose neighbours undergo distinct shape deformations before and after T1 transitions. Both types of cells elongate transiently due to T1 transitions, despite the overall effect of T1 transitions being

elongation for gaining cells and contraction for losing cells. During this transient elongation, the cells that lose neighbours attain their peak shape index before the start of the T1 transition, while the cells that gain neighbours attain it after the end of the T1 transition. The transient shape deformations are more pronounced in cells that lose neighbours, which attain a higher peak shape index even though the net effect of a T1 transition is to reduce the shape index of these cells. The shape index of loser and gainer cells are similar at the end of a T1 transition, which can be compared with the velocity polarization field in Paper II where the *average shape* of all four cells involved in the T1 transition appear to be similar at the end of the T1 transition.

Lastly, we explore how successive T1 transitions involving a common cell are spatially distributed with respect to the cell's center of mass. We identify four different scenarios of successive T1 transitions, namely *loser-loser*, *loser-gainer*, *gainer-loser*, and *gainer-gainer*, depending on whether the cell is losing or gaining neighbours in both T1 transitions. We then find the relative orientation of the vertex that participated in the first T1 transition with respect to the vertex that participated in the second T1 transition, measured relative to the center of mass of the cell at time corresponding to the start of the second T1. This relative orientation varies from 0 to π. The lower the value of the relative orientation, the closer the vertices are to each other.

The distribution of relative orientations is different for all four scenarios of successive T1 transitions, suggesting that changes in neighbourhood topology during two successive T1 transitions affect the relative spatial distributions of these transitions. In most situations, the relative orientation is either low (near 0) or high (near π). This non-uniform distribution gives rise to directed migration depending on the four scenarios. Such directed migration could give rise to coherent, non-random flow patterns at a larger scale than that typical of a T1 transition.

5.5 Paper IV: Quantifying the shape of cells - from Minkowski tensors to p-atic order

As cell shape is critical to the collective behavior of cells, it is important to have cell shape descriptors that quantitatively capture various aspects of cell shape. In Papers I and III, the shape index serves as a shape descriptor that reveals several details about T1 transitions, shape deformations, and their interdependence. There are several other ways to characterize cell shape, and one such method involves finding an order parameter $q_p \in [0, 1]$, which helps to identify if a given shape has p-atic symmetry. Paper IV introduces such p-atic order parameters based on Minkowski Tensors, applying them for the first time to shapes of cells in a monolayer obtained from experiments and simulations. Paper IV considers two different computational models: our multi-phase field model used in Papers II and III, as well as an active vertex model. In both models, two primary control parameters are used to tune cell activity and cell deformability. The use of Minkowski Tensors also allows us to define θ_p, which, for a regular p-sided polygon, determines the orientation of the polygon with respect to the horizontal axis.

Paper IV shows that p-atic order parameters based on Minkowski tensors are robust, meaning small changes in cell shape lead to small changes in the order parameters. This is because of the continuity property of the Minkowski tensors as they are defined as integrals of smooth contours. In contrast, Paper IV also shows that a method relying solely on the location of vertices, such as the ones used in Reference [89], is not robust.

Paper IV shows that for both the multi-phase field and active vertex models, the hexatic order parameter q_6 is high for low activity and deformability. This behavior is expected as further reducing activity and deformability would lead to a jammed state characterized by mostly hexagonal cells. As activity and deformability are increased, the variability in q_2 and q_6 also increases, while the mean values of q_2 increase, and the mean value of q_6 decreases. q_2 tends to 1 as cell shape approaches a straight line through elongation, while $q_6 = 1$ for a regular hexagon.

It is possible for cells to approach the shape of a regular hexagon, but it is unlikely for the cell shape to collapse to a line, which explains why the range of values spanned by q_2 is smaller than that spanned by q_6. We observed in Paper III that cells elongate transiently due to T1 transitions. The increase in the mean and variance of q_2 with increased activity and deformability is likely due to a higher number of T1 transitions. The increase in the variability of both q_2 and q_6 is also due to the higher number of T1 transitions, as they introduce shape fluctuations. The results also suggest that q_2 and q_6 are largely independent of each other.

The cell shape quantification was also performed on cell shapes obtained from monolayers of MDCK cells of two varieties: wild type and with E-cadherin knocked out. We do not observe a significant difference in q_2 and q_6 for both varieties. The ranges and distribution of q_2 and q_6 appear to be similar to those of cells in the multi-phase field model with high activity and high deformability.

It has been suggested that in epithelial cells, hexatic order dominates at short length scales, and nematic order dominates at larger length scales [89, 130]. These results were obtained with non-robust p-atic shape descriptors. Using a Minkowski Tensor-based approach, we do not observe the transition from hexatic to nematic behavior with increasing length scales. Instead, at larger length scales, both hexatic and nematic order reduce.

5.6 Outlook

The ability to model arbitrarily deformable cell shapes and undergo spontaneous T1 transitions within the multi-phase model has allowed us to study the interplay between cell shape and emergent flow structures, particularly with respect to variations in cell activity and deformability. The multi-phase field model includes several parameters that can be adjusted. The role of cell-cell interaction, which is extremely essential, remains largely unexplored within these models. In practice, we found that cell-cell interaction is influenced by cell size and packing. However, due to the limitations of available computational resources, a comprehensive study involving cell-cell interaction along with cell size and packing has yet to be conducted. Improving the computational performance of the model is also

critical. This requires collaboration among several research groups to develop and maintain open-source code.

The linear relationship between mean pair-separation distance and the number of T1 transitions can be easily verified in several other models and experiments involving dense particles. The results from other models would help us understand if this behaviour holds fundamental importance in mixing.

The distinct shape deformations of gainer and loser cells, as well as the order of topological changes, rendered effective directional migration for cells within the model. Here, the interdependence of two T1 transitions was explored. However, to study flow patterns that emerge at larger scales, longer chains of T1 transitions need to be examined. This would also require studying a monolayer with a larger number of cells. A larger monolayer would also allow us to explore coarse-grained studies of multi-phase models at the hydrodynamic limit.

T2 transitions [5, 82] and T3 transitions [91] have been incorporated into multi-phase field models. The flow within the bulk of the monolayer is affected by T1, T2, and T3 transitions. The combined effect and interdependence of these three topological changes could further our understanding of emergent flows in confluent monolayers especially in the context of morphogenesis and homeostasis.

Geometry [38, 39] and topology [107], as well as the mechanical properties of the underlying substrate [119], impact the observed collective behavior of epithelial cells. It remains to be seen if the spatiotemporal interdependence of T1 transitions affects the observed collective behavior in these systems.

A natural extension of our study would be to examine three-dimensional cells [82]. When epithelial cells are destined for apoptosis by extrusion, they are pushed out of the monolayer by surrounding cells, and modeling this requires capturing three-dimensional shape deformations [91]. However, the flow associated with these extrusion events is still largely unexplored. The study of formation of tubes and folded structures also requires modeling of three dimensional cells, or two-dimensional cells on a surfaces in three dimension [107, 120].

The evolution of p-atic shape descriptors q_p and θ_p due to T1 transitions can be studied similarly to shape index, cell speed, and coarse-grained energy discussed in Papers I and III. This would allow us to determine how T1 transitions affects shape symmetries. T1 transitions break down existing p-atic order due to the quadrupolar flow pattern and large deformations accompanied by them.

In conclusion, several extensions of our study are possible due to the phenomenological richness of epithelial monolayers. The complex interplay between cell shape and emergent collective behavior, which is essential to morphogenesis, cancer metastasis, and wound healing, merits approaching this problem through various classes of mathematical models. Future advancements in experimental studies both in vivo and in vitro will likely necessitate reevaluating several of our conclusions.

Bibliography

[1] Harish P. Jain, Axel Voigt and Luiza Angheluta. 'Robust Statistical Properties of T1 Transitions in a Multi-Phase Field Model of Cell Monolayers'. In: *Scientific Reports* 13.1 (June 2023), p. 10096.

[2] Harish P. Jain, Axel Voigt and Luiza Angheluta. 'From Cell Intercalation to Flow, the Importance of T1 Transitions'. In: *Physical Review Research* 6.3 (Aug. 2024), p. 033176.

[3] Harish P Jain, Richard DJG Ho and Luiza Angheluta. 'Emergent cell migration from cell shape deformations and T1 transitions'. In: *arXiv preprint arXiv:2412.19686* (2024).

[4] Lea Happel, Oberschelp Griseldis, Valeriia Grudtsyna, Harish P Jain, Rastko Sknepnek, Amin Doostmohammadi and Axel Voigt. 'Quantifying the shape of cells-from Minkowski tensors to p-atic order'. In: *bioRxiv* (2025), pp. 2025–01.

[5] Harish P. Jain, Dennis Wenzel and Axel Voigt. 'Impact of Contact Inhibition on Collective Cell Migration and Proliferation'. In: *Physical Review E* 105.3 (Mar. 2022), p. 034402.

[6] Simon Syga, P. Jain, Marcus Krellner, Haralampos Hatzikirou and Andreas Deutsch. 'Evolution of Phenotypic Plasticity Leads to Tumor Heterogeneity with Implications for Therapy'. In: *PLOS Computational Biology* 20.8 (Aug. 2024), e1012003.

[7] George John Romanes and Conwy Lloyd Morgan. *Darwin and after Darwin: An exposition of the Darwinian theory and a discussion of post-Darwinian questions*. Open Court, 1896.

[8] Bruce Alberts, Alexander Johnson, Julian Lewis, Martin Raff, Keith Roberts and Peter Walter. *Molecular Biology of the Cell*. 5th ed. New York: W.W. Norton & Company, Dec. 2007.

[9] Elizabeth Pennisi. 'Haeckel's Embryos: Fraud Rediscovered'. In: *Science* 277.5331 (Sept. 1997), pp. 1435–1435.

[10] Brian K Hall. *Evolutionary developmental biology*. Springer Science & Business Media, 2012.

[11] Benoit Ladoux and René Marc Mège. 'Mechanobiology of Collective Cell Behaviours'. In: *Nature Reviews Molecular Cell Biology* 18.12 (2017), pp. 743–757.

[12] Peter Friedl and Darren Gilmour. 'Collective Cell Migration in Morphogenesis, Regeneration and Cancer'. In: *Nature Reviews Molecular Cell Biology* 10.7 (2009), pp. 445–457.

[13] Agustí Brugués, Ester Anon, Vito Conte, Jim H. Veldhuis, Mukund Gupta, Julien Colombelli, José J. Muñoz, G. Wayne Brodland, Benoit Ladoux and Xavier Trepat. 'Forces Driving Epithelial Wound Healing'. In: *Nature Physics* 10.9 (Sept. 2014), pp. 683–690.

[14] Elsa Bazellières, Vito Conte, Alberto Elosegui-Artola, Xavier Serra-Picamal, María Bintanel-Morcillo, Pere Roca-Cusachs, José J. Muñoz, Marta Sales-Pardo, Roger Guimerà and Xavier Trepat. 'Control of Cell–Cell Forces and Collective Cell Dynamics by the Intercellular Adhesome'. In: *Nature Cell Biology* 17.4 (Apr. 2015), pp. 409–420.

[15] J Stavans. 'The Evolution of Cellular Structures'. In: *Reports on Progress in Physics* 56.6 (June 1993), pp. 733–789.

[16] Denis Weaire, Stefan Hutzler, Denis Weaire and Stefan Hutzler. *The Physics of Foams*. Oxford, New York: Oxford University Press, Aug. 2001.

[17] William B. Krantz, Kevin J. Gleason and Nelson Caine. 'Patterned Ground'. In: *Scientific American* 259.6 (1988), pp. 68–77.

[18] Günter Reiter. 'Dewetting of Thin Polymer Films'. In: *Physical Review Letters* 68.1 (Jan. 1992), pp. 75–78.

[19] M. C. Marchetti, J. F. Joanny, S. Ramaswamy, T. B. Liverpool, J. Prost, Madan Rao and R. Aditi Simha. 'Hydrodynamics of Soft Active Matter'. In: *Reviews of Modern Physics* 85.3 (2013), pp. 1143–1189.

[20] Sangwoo Kim, Marie Pochitaloff, Georgina A. Stooke-Vaughan and Otger Campàs. 'Embryonic Tissues as Active Foams'. In: *Nature Physics* 17.7 (July 2021), pp. 859–866.

[21] M. Poujade, E. Grasland-Mongrain, A. Hertzog, J. Jouanneau, P. Chavrier, B. Ladoux, A. Buguin and P. Silberzan. 'Collective Migration of an Epithelial Monolayer in Response to a Model Wound'. In: *Proceedings of the National Academy of Sciences of the United States of America* 104.41 (Oct. 2007), pp. 15988–15993.

[22] William Wood, Antonio Jacinto, Richard Grose, Sarah Woolner, Jonathan Gale, Clive Wilson and Paul Martin. 'Wound Healing Recapitulates Morphogenesis in Drosophila Embryos'. In: *Nature Cell Biology* 4.11 (Nov. 2002), pp. 907–912.

[23] Claire Bertet, Lawrence Sulak and Thomas Lecuit. 'Myosin-Dependent Junction Remodelling Controls Planar Cell Intercalation and Axis Elongation'. In: *Nature* 429.6992 (June 2004), pp. 667–671.

[24] Matteo Rauzi, Pascale Verant, Thomas Lecuit and Pierre-François Lenne. 'Nature and Anisotropy of Cortical Forces Orienting Drosophila Tissue Morphogenesis'. In: *Nature Cell Biology* 10.12 (Dec. 2008), pp. 1401–1410.

[25] Matteo Rauzi. 'Cell Intercalation in a Simple Epithelium'. In: *Philosophical Transactions of the Royal Society B: Biological Sciences* 375.1809 (Oct. 2020), p. 20190552.

[26] Kenneth D. Irvine and Eric Wieschaus. 'Cell Intercalation during Drosophila Germband Extension and Its Regulation by Pair-Rule Segmentation Genes'. In: *Development* 120.4 (Apr. 1994), pp. 827–841.

[27] Jeffrey D. Hardin and Louis Y. Cheng. 'The Mechanisms and Mechanics of Archenteron Elongation during Sea Urchin Gastrulation'. In: *Developmental Biology* 115.2 (June 1986), pp. 490–501.

[28] Yara E Sanchez-Corrales, Guy B Blanchard and Katja Röper. 'Radially Patterned Cell Behaviours during Tube Budding from an Epithelium'. In: *eLife* 7 (July 2018). Ed. by Didier YR Stainier and Stefan Luschnig, e35717.

[29] Elise Walck-Shannon and Jeff Hardin. 'Cell Intercalation from Top to Bottom'. In: *Nature Reviews Molecular Cell Biology* 15.1 (Jan. 2014), pp. 34–48.

[30] Thuan Beng Saw, Amin Doostmohammadi, Vincent Nier, Leyla Kocgozlu, Sumesh Thampi, Yusuke Toyama, Philippe Marcq, Chwee Teck Lim, Julia M. Yeomans and Benoit Ladoux. 'Topological Defects in Epithelia Govern Cell Death and Extrusion'. In: *Nature* 544.7649 (2017), pp. 212–216.

[31] Jody Rosenblatt, Martin C. Raff and Louise P. Cramer. 'An Epithelial Cell Destined for Apoptosis Signals Its Neighbors to Extrude It by an Actin- and Myosin-Dependent Mechanism'. In: *Current Biology* 11.23 (Nov. 2001), pp. 1847–1857.

[32] Ninna S. Rossen, Jens M. Tarp, Joachim Mathiesen, Mogens H. Jensen and Lene B. Oddershede. 'Long-Range Ordered Vorticity Patterns in Living Tissue Induced by Cell Division'. In: *Nature Communications* 5 (Dec. 2014), p. 5720.

[33] Yusuke Toyama, Xomalin G. Peralta, Adrienne R. Wells, Daniel P. Kiehart and Glenn S. Edwards. 'Apoptotic Force and Tissue Dynamics During Drosophila Embryogenesis'. In: *Science* 321.5896 (Sept. 2008), pp. 1683–1686.

[34] Gloria M. Slattum and Jody Rosenblatt. 'Tumour Cell Invasion: An Emerging Role for Basal Epithelial Cell Extrusion'. In: *Nature Reviews Cancer* 14.7 (July 2014), pp. 495–501.

[35] George T. Eisenhoffer, Patrick D. Loftus, Masaaki Yoshigi, Hideo Otsuna, Chi-Bin Chien, Paul A. Morcos and Jody Rosenblatt. 'Crowding Induces Live Cell Extrusion to Maintain Homeostatic Cell Numbers in Epithelia'. In: *Nature* 484.7395 (Apr. 2012), pp. 546–549.

[36] Douglas Hanahan and Robert A. Weinberg. 'Hallmarks of Cancer: The next Generation'. In: *Cell* 144.5 (Mar. 2011), pp. 646–674.

[37] András Szabó, Manuela Melchionda, Giancarlo Nastasi, Mae L. Woods, Salvatore Campo, Roberto Perris and Roberto Mayor. 'In Vivo Confinement Promotes Collective Migration of Neural Crest Cells'. In: *Journal of Cell Biology* 213.5 (May 2016), pp. 543–555.

[38] Kevin Doxzen, Sri Ram Krishna Vedula, Man Chun Leong, Hiroaki Hirata, Nir S. Gov, Alexandre J. Kabla, Benoit Ladoux and Chwee Teck Lim. 'Guidance of Collective Cell Migration by Substrate Geometry'. In: *Integrative Biology (United Kingdom)* 5.8 (2013), pp. 1026–1035.

[39] Sri Ram Krishna Vedula, Man Chun Leong, Tan Lei Lai, Pascal Hersen, Alexandre J. Kabla, Chwee Teck Lim and Benoît Ladoux. 'Emerging Modes of Collective Cell Migration Induced by Geometrical Constraints'. In: *Proceedings of the National Academy of Sciences* 109.32 (Aug. 2012), pp. 12974–12979.

[40] Thomas E. Angelini, Edouard Hannezo, Xavier Trepat, Manuel Marquez, Jeffrey J. Fredberg and David A. Weitz. 'Glass-like Dynamics of Collective Cell Migration'. In: *Proceedings of the National Academy of Sciences* 108.12 (Mar. 2011), pp. 4714–4719.

[41] Jin Ah Park, Jae Hun Kim, Dapeng Bi, Jennifer A. Mitchel, Nader Taheri Qazvini, Kelan Tantisira, Chan Young Park, Maureen McGill, Sae Hoon Kim, Bomi Gweon, Jacob Notbohm, Robert Steward, Stephanie Burger, Scott H. Randell, Alvin T. Kho, Dhananjay T. Tambe, Corey Hardin, Stephanie A. Shore, Elliot Israel, David A. Weitz, Daniel J. Tschumperlin, Elizabeth P. Henske, Scott T. Weiss, M. Lisa Manning, James P. Butler, Jeffrey M. Drazen and Jeffrey J. Fredberg. 'Unjamming and Cell Shape in the Asthmatic Airway Epithelium'. In: *Nature Materials 2014 14:10* 14.10 (Aug. 2015), pp. 1040–1048.

[42] James D Murray. *Mathematical biology: I. An introduction*. Vol. 17. Springer Science & Business Media, 2007.

[43] Előd Méhes and Tamás Vicsek. 'Collective Motion of Cells: From Experiments to Models'. In: *Integrative Biology* 6.9 (Sept. 2014), pp. 831–854.

[44] B. A. Camley and W.-J. Rappel. 'Physical Models of Collective Cell Motility: From Cell to Tissue'. In: *Journal of Physics D: Applied Physics* 50.11 (Feb. 2017), p. 113002.

[45] Ricard Alert and Xavier Trepat. 'Physical Models of Collective Cell Migration'. In: *Annual Review of Condensed Matter Physics* 11.1 (2020), pp. 77–101.

[46] Andreas Buttenschön and Leah Edelstein-Keshet. 'Bridging from Single to Collective Cell Migration: A Review of Models and Links to Experiments'. In: *PLOS Computational Biology* 16.12 (Dec. 2020), e1008411.

[47] Silvanus Alt, Poulami Ganguly and Guillaume Salbreux. 'Vertex Models: From Cell Mechanics to Tissue Morphogenesis'. In: *Philosophical Transactions of the Royal Society B: Biological Sciences* 372.1720 (May 2017).

[48] Hisao Honda and Goro Eguchi. 'How Much Does the Cell Boundary Contract in a Monolayered Cell Sheet?' In: *Journal of Theoretical Biology* 84.3 (June 1980), pp. 575–588.

[49] M. Marder. 'Soap-Bubble Growth'. In: *Physical Review A* 36.1 (July 1987), pp. 438–440.

[50] Tohru Okuzono and Kyozi Kawasaki. 'Intermittent Flow Behavior of Random Foams: A Computer Experiment on Foam Rheology'. In: *Physical Review E* 51.2 (Feb. 1995), pp. 1246–1253.

[51] Kyozi Kawasaki, Tatsuzo Nagai and Katsuya Nakashima. 'Vertex Models for Two-Dimensional Grain Growth'. In: *Philosophical Magazine B* 60.3 (Sept. 1989), pp. 399–421.

[52] Hisao Honda, Tatsuzo Nagai and Masaharu Tanemura. 'Two Different Mechanisms of Planar Cell Intercalation Leading to Tissue Elongation'. In: *Developmental Dynamics: An Official Publication of the American Association of Anatomists* 237.7 (July 2008), pp. 1826–1836.

[53] Dapeng Bi, J. H. Lopez, J. M. Schwarz and M. Lisa Manning. 'A Density-Independent Rigidity Transition in Biological Tissues'. In: *Nature Physics* 11.12 (Dec. 2015), pp. 1074–1079.

[54] Satoru Okuda, Yasuhiro Inoue, Tadashi Watanabe and Taiji Adachi. 'Coupling Intercellular Molecular Signalling with Multicellular Deformation for Simulating Three-Dimensional Tissue Morphogenesis'. In: *Interface Focus* 5.2 (Apr. 2015), p. 20140095.

[55] Michael Weliky and George Oster. 'The Mechanical Basis of Cell Rearrangement I. Epithelial Morphogenesis during Fundulus Epiboly'. In: *Development* 109.2 (June 1990), pp. 373–386.

[56] Matthew C. Gibson, Ankit B. Patel, Radhika Nagpal and Norbert Perrimon. 'The Emergence of Geometric Order in Proliferating Metazoan Epithelia'. In: *Nature* 442.7106 (Aug. 2006), pp. 1038–1041.

[57] Daniel L. Barton, Silke Henkes, Cornelis J. Weijer and Rastko Sknepnek. 'Active Vertex Model for Cell-Resolution Description of Epithelial Tissue Mechanics'. In: *PLOS Computational Biology* 13.6 (June 2017), e1005569.

[58] Charlie Duclut, Joris Paijmans, Mandar M. Inamdar, Carl D. Modes and Frank Jülicher. *Active T1 Transitions in Cellular Networks*. Mar. 2022.

[59] Rastko Sknepnek, Ilyas Djafer-Cherif, Manli Chuai, Cornelis Weijer and Silke Henkes. 'Generating Active T1 Transitions through Mechanochemical Feedback'. In: *eLife* 12 (Apr. 2023). Ed. by Karsten Kruse and Aleksandra M Walczak, e79862.

[60] Alexander G. Fletcher, Miriam Osterfield, Ruth E. Baker and Stanislav Y. Shvartsman. 'Vertex Models of Epithelial Morphogenesis'. In: *Biophysical Journal* 106.11 (2014), pp. 2291–2304.

[61] Satoru Okuda, Yasuhiro Inoue and Taiji Adachi. 'Three-Dimensional Vertex Model for Simulating Multicellular Morphogenesis'. In: *Biophysics and Physicobiology* 12 (2015), pp. 13–20.

[62] Andreas Christ Sølvsten Jørgensen, Ciaran Scott Hill, Marc Sturrock, Wenhao Tang, Saketh R. Karamched, Dunja Gorup, Mark F. Lythgoe, Simona Parrinello, Samuel Marguerat and Vahid Shahrezaei. 'Data-Driven Spatio-Temporal Modelling of Glioblastoma'. In: *Royal Society Open Science* 10.3 (Mar. 2023), p. 221444.

[63] François Graner and James A. Glazier. 'Simulation of Biological Cell Sorting Using a Two-Dimensional Extended Potts Model'. In: *Physical Review Letters* 69.13 (Sept. 1992), pp. 2013–2016.

[64] James A. Glazier and François Graner. 'Simulation of the Differential Adhesion Driven Rearrangement of Biological Cells'. In: *Physical Review E* 47.3 (Mar. 1993), pp. 2128–2154.

[65] András Szabó and Roeland M. H. Merks. 'Cellular Potts Modeling of Tumor Growth, Tumor Invasion, and Tumor Evolution'. In: *Frontiers in Oncology* 3 (Apr. 2013).

[66] Tsuyoshi Hirashima, Elisabeth G. Rens and Roeland M. H. Merks. 'Cellular Potts Modeling of Complex Multicellular Behaviors in Tissue Morphogenesis'. In: *DGD* 59.5 (2017), pp. 329–339.

[67] Nicholas Metropolis, Arianna W. Rosenbluth, Marshall N. Rosenbluth, Augusta H. Teller and Edward Teller. 'Equation of State Calculations by Fast Computing Machines'. In: *The Journal of Chemical Physics* 21.6 (June 1953), pp. 1087–1092.

[68] Mark Zajac, Gerald L Jones and James A Glazier. 'Simulating convergent extension by way of anisotropic differential adhesion'. In: *Journal of Theoretical Biology* 222.2 (2003), pp. 247–259.

[69] M. Chiang and D. Marenduzzo. 'Glass Transitions in the Cellular Potts Model'. In: *Europhysics Letters* 116.2 (Dec. 2016), p. 28009.

[70] Shreyas U. Hirway, Christopher A. Lemmon and Seth H. Weinberg. 'Multicellular Mechanochemical Hybrid Cellular Potts Model of Tissue Formation during Epithelial-Mesenchymal Transition'. In: *Computational and Systems Oncology* 1.4 (2021), e1031.

[71] Adrian R. Noppe, Anthony P. Roberts, Alpha S. Yap, Guillermo A. Gomez and Zoltan Neufeld. 'Modelling Wound Closure in an Epithelial Cell Sheet Using the Cellular Potts Model'. In: *Integrative Biology* 7.10 (Oct. 2015), pp. 1253–1264.

[72] Josiah Willard Gibbs. 'A method of geometrical representation of the thermodynamic properties by means of surfaces'. In: *Transactions of Connecticut Academy of Arts and Sciences* (1873), pp. 382–404.

[73] Heike Emmerich. 'Advances of and by Phase-Field Modelling in Condensed-Matter Physics'. In: *Advances in Physics* 57.1 (Jan. 2008), pp. 1–87.

[74] Long-Qing Chen. 'Phase-Field Models for Microstructure Evolution'. In: *Annual Review of Materials Research* 32.Volume 32, 2002 (Aug. 2002), pp. 113–140.

[75] D. M. Anderson, G. B. McFadden and A. A. Wheeler. 'Diffuse-interface Methods in Fluid Mechanics'. In: *Annual Review of Fluid Mechanics* 30.Volume 30, 1998 (Jan. 1998), pp. 139–165.

[76] Adrian Moure and Hector Gomez. *Phase-Field Modeling of Individual and Collective Cell Migration*. Vol. 28. Springer Netherlands, 2019.

[77] Romain Mueller and Amin Doostmohammadi. 'Phase Field Models of Active Matter'. In: *arXiv:2102.05557 [cond-mat, physics:physics]* (Feb. 2021).

[78] Thierry Biben, Klaus Kassner and Chaouqi Misbah. 'Phase-Field Approach to Three-Dimensional Vesicle Dynamics'. In: *Physical Review E* 72.4 (Oct. 2005), p. 041921.

[79] Adrian Moure and Hector Gomez. 'Computational Model for Amoeboid Motion: Coupling Membrane and Cytosol Dynamics'. In: *Physical Review E* 94.4 (Oct. 2016), p. 042423.

[80] Jakob Löber, Falko Ziebert and Igor S. Aranson. 'Collisions of Deformable Cells Lead to Collective Migration'. In: *Scientific Reports* 5.1 (Mar. 2015), p. 9172.

[81] Luuk Metselaar, Julia M. Yeomans and Amin Doostmohammadi. 'Topology and Morphology of Self-Deforming Active Shells'. In: *Physical Review Letters* 123.20 (Nov. 2019), p. 208001.

[82] Makiko Nonomura. 'Study on Multicellular Systems Using a Phase Field Model'. In: *PLOS ONE* 7.4 (Apr. 2012), e33501.

[83] Benoit Palmieri, Yony Bresler, Denis Wirtz and Martin Grant. 'Multiple Scale Model for Cell Migration in Monolayers: Elastic Mismatch between Cells Enhances Motility'. In: *Scientific Reports* 5.November 2014 (2015), pp. 1–13.

[84] Dennis Wenzel, Simon Praetorius and Axel Voigt. 'Topological and Geometrical Quantities in Active Cellular Structures'. In: *Journal of Chemical Physics* 150.16 (2019).

[85] Frederic T Lewis. 'The correlation between cell division and the shapes and sizes of prismatic cells in the epidermis of cucumis'. In: *The anatomical record* 38.3 (1928), pp. 341–376.

[86] DA Aboav. 'The arrangement of grains in a polycrystal'. In: *Metallography* 3.4 (1970), pp. 383–390.

[87] Romain Mueller, Julia M. Yeomans and Amin Doostmohammadi. 'Emergence of Active Nematic Behavior in Monolayers of Isotropic Cells'. In: *Physical Review Letters* 122.4 (Feb. 2019), p. 048004.

[88] Dennis Wenzel, Michael Nestler, Sebastian Reuther, Maximilian Simon and Axel Voigt. 'Defects in Active Nematics – Algorithms for Identification and Tracking'. In: *Computational Methods in Applied Mathematics* 21.3 (July 2021), pp. 683–692.

[89] Josep-Maria Armengol-Collado, Livio Nicola Carenza, Julia Eckert, Dimitrios Krommydas and Luca Giomi. 'Epithelia Are Multiscale Active Liquid Crystals'. In: *Nature Physics* 19.12 (Dec. 2023), pp. 1773–1779.

[90] Lakshmi Balasubramaniam, Amin Doostmohammadi, Thuan Beng Saw, Gautham Hari Narayana Sankara Narayana, Romain Mueller, Tien Dang, Minnah Thomas, Shafali Gupta, Surabhi Sonam, Alpha S. Yap, Yusuke Toyama, René-Marc Mège, Julia M. Yeomans and Benoît Ladoux. 'Investigating the Nature of Active Forces in Tissues Reveals How Contractile Cells Can Form Extensile Monolayers'. In: *Nature Materials* 20.8 (Aug. 2021), pp. 1156–1166.

[91] Siavash Monfared, Guruswami Ravichandran, José Andrade and Amin Doostmohammadi. 'Mechanical Basis and Topological Routes to Cell Elimination'. In: *eLife* 12 (Apr. 2023). Ed. by Pierre Sens and Jonathan A Cooper, e82435.

[92] Xiangyu Kuang, Guoye Guan, Chao Tang and Lei Zhang. 'MorphoSim: An Efficient and Scalable Phase-Field Framework for Accurately Simulating Multicellular Morphologies'. In: *npj Systems Biology and Applications* 9.1 (Feb. 2023), pp. 1–11.

[93] Wieland Marth and Axel Voigt. 'Collective Migration under Hydrodynamic Interactions: A Computational Approach'. In: *Interface Focus* 6.5 (Oct. 2016), p. 20160037.

[94] Lingyue Shen, Ping Lin, Zhiliang Xu and Shixin Xu. 'Diffuse Interface Model for Cell Interaction and Aggregation with Lennard-Jones Type Potential'. In: *Computer Methods in Applied Mechanics and Engineering* 415 (Oct. 2023), p. 116257.

[95] Luca Giomi and Antonio DeSimone. 'Spontaneous Division and Motility in Active Nematic Droplets'. In: *Physical Review Letters* 112.14 (Apr. 2014), p. 147802.

[96] Tong Gao and Zhaorui Li. 'Self-Driven Droplet Powered By Active Nematics'. In: *Physical Review Letters* 119.10 (Sept. 2017), p. 108002.

[97] Dennis Wenzel and Axel Voigt. 'Multiphase Field Models for Collective Cell Migration'. In: *Physical Review E* 104.5 (Nov. 2021), p. 054410.

[98] Pierre C Hohenberg and Bertrand I Halperin. 'Theory of Dynamic Critical Phenomena'. In: *Reviews of Modern Physics* 49.3 (1977), pp. 435–479.

[99] John W. Cahn and John E. Hilliard. 'Free Energy of a Nonuniform System. I. Interfacial Free Energy'. In: *The Journal of Chemical Physics* 28.2 (1958), pp. 258–267.

[100] Christoph A Weber, David Zwicker, Frank Jülicher and Chiu Fan Lee. 'Physics of Active Emulsions'. In: *Reports on Progress in Physics* 82.6 (June 2019), p. 064601.

[101] Nikolas Provatas and Ken Elder. 'Phase-Field Methods in Materials Science and Engineering'. In: *Phase-Field Methods in Materials Science and Engineering* (2010).

[102] Marco Salvalaglio, Maximilian Selch, Axel Voigt and Steven M. Wise. 'Doubly Degenerate Diffuse Interface Models of Anisotropic Surface Diffusion'. In: *Mathematical Methods in the Applied Sciences* June (2020), pp. 1–21.

[103] Thomas Lecuit, Pierre-François Lenne and Edwin Munro. 'Force Generation, Transmission, and Integration during Cell and Tissue Morphogenesis'. In: *Annu. Rev. Cell Dev. Biol* 27 (2011), pp. 157–184.

[104] Thomas Lecuit and Alpha S. Yap. 'E-Cadherin Junctions as Active Mechanical Integrators in Tissue Dynamics'. In: *Nature Cell Biology* 17.5 (2015), pp. 533–539.

[105] Siqi Ling, Wieland Marth, Simon Praetorius and Axel Voigt. 'An Adaptive Finite Element Multi-Mesh Approach for Interacting Deformable Objects in Flow'. In: *Computational Methods in Applied Mathematics* 16.3 (2016), pp. 475–484.

[106] Brian A. Camley, Yunsong Zhang, Yanxiang Zhao, Bo Li, Eshel Ben-Jacob, Herbert Levine and Wouter Jan Rappel. 'Polarity Mechanisms Such as Contact Inhibition of Locomotion Regulate Persistent Rotational Motion of Mammalian Cells on Micropatterns'. In: *Proceedings of the National Academy of Sciences of the United States of America* 111.41 (2014), pp. 14770–14775.

[107] Lea Happel and Axel Voigt. 'Coordinated Motion of Epithelial Layers on Curved Surfaces'. In: *Physical Review Letters* 132.7 (Feb. 2024), p. 078401.

[108] Frank Schweitzer and J Doyne Farmer. *Brownian agents and active particles: collective dynamics in the natural and social sciences*. Vol. 1. Springer, 2003.

[109] David G. Drubin and W. James Nelson. 'Origins of Cell Polarity'. In: *Cell* 84.3 (Feb. 1996), pp. 335–344.

[110] Jennifer A. Zallen. 'Planar Polarity and Tissue Morphogenesis'. In: *Cell* 129.6 (June 2007), pp. 1051–1063.

[111] Paul N. Adler. 'Planar Signaling and Morphogenesis in Drosophila'. In: *Developmental Cell* 2.5 (May 2002), pp. 525–535.

[112] Grégoire Peyret, Romain Mueller, Joseph d'Alessandro, Simon Begnaud, Philippe Marcq, René-Marc Mège, Julia M. Yeomans, Amin Doostmohammadi and Benoît Ladoux. 'Sustained Oscillations of Epithelial Cell Sheets'. In: *Biophysical Journal* 117.3 (Aug. 2019), pp. 464–478.

[113] Gilberto L. Thomas, Ismael Fortuna, Gabriel C. Perrone, James A. Glazier, Julio M. Belmonte and Rita M. C. de Almeida. 'Parameterizing Cell Movement When the Instantaneous Cell Migration Velocity Is Ill-Defined'. In: *Physica A: Statistical Mechanics and its Applications* 550 (July 2020), p. 124493.

[114] Peter Dieterich, Rainer Klages, Roland Preuss and Albrecht Schwab. 'Anomalous Dynamics of Cell Migration'. In: *Proceedings of the National Academy of Sciences of the United States of America* 105.2 (Jan. 2008), pp. 459–463.

[115] Marius Asipauskas, Miguel Aubouy, James A. Glazier, François Graner and Yi Jiang. 'A Texture Tensor to Quantify Deformations: The Example of Two-Dimensional Flowing Foams'. In: *Granular Matter* 5.2 (July 2003), pp. 71–74.

[116] Tamás Vicsek, András Czirók, Eshel Ben-Jacob, Inon Cohen and Ofer Shochet. 'Novel Type of Phase Transition in a System of Self-Driven Particles'. In: *Physical Review Letters* 75.6 (Aug. 1995), p. 1226.

[117] Michael E. Cates and Elsen Tjhung. 'Theories of Binary Fluid Mixtures: From Phase-Separation Kinetics to Active Emulsions'. In: *Journal of Fluid Mechanics* 836 (Feb. 2018), P1.

[118] Michael Chiang. 'Multiphase Field Model of Cells on a Substrate: From Three Dimensional to Two Dimensional'. In: *Physical Review E* 110.4 (2024).

[119] Raimon Sunyer, Vito Conte, Jorge Escribano, Alberto Elosegui-Artola, Anna Labernadie, Léo Valon, Daniel Navajas, José Manuel García-Aznar, José J. Muñoz, Pere Roca-Cusachs and Xavier Trepat. 'Collective Cell Durotaxis Emerges from Long-Range Intercellular Force Transmission'. In: *Science* 353.6304 (Sept. 2016), pp. 1157–1161.

[120] Lea Happel, Dennis Wenzel and Axel Voigt. 'Effects of Curvature on Epithelial Tissue —Coordinated Rotational Movement and Other Spatiotemporal Arrangements'. In: *Europhysics Letters* 138.6 (July 2022), p. 67002.

[121] Philippe G Ciarlet. *The finite element method for elliptic problems*. SIAM, 2002.

[122] Susanne C Brenner. *The mathematical theory of finite element methods*. Springer, 2008.

[123] Simon Praetorius, Thomas Witkowski, Simon Vey, Peter Gottschling, Rainer Backofen, Andreas Naumann, Siqi Ling and Sebastian Reuther. *Adaptive Multi-Dimensional Simulations Repository*. https://gitlab.math.tu-dresden.de/iwr/amdis. v1.2. (Visited on 16/11/2024).

[124] Simon Vey and Axel Voigt. 'AMDiS: Adaptive MultiDimensional Simulations'. In: *Computing and Visualization in Science* 10 (2007), pp. 57–67.

[125] Thomas Witkowski, Siqi Ling, Simon Praetorius and Axel Voigt. 'Software concepts and numerical algorithms for a scalable adaptive parallel finite element method'. In: *Advances in Computational Mathematics* 41.6 (2015), pp. 1145–1177.

[126] S Praetorius and A Voigt. 'Collective cell behavior-a cell-based parallelization approach for a phase field active polar gel model'. In: *Proceedings of the 9th NIC Symposium* 49 (2018), pp. 369–376.

[127] David R. Nelson and B. I. Halperin. 'Dislocation-Mediated Melting in Two Dimensions'. In: *Physical Review B* 19.5 (Mar. 1979), pp. 2457–2484.

[128] Yan-Wei Li and Massimo Pica Ciamarra. 'Role of Cell Deformability in the Two-Dimensional Melting of Biological Tissues'. In: *Physical Review Materials* 2.4 (Apr. 2018), p. 045602.

[129] Walter Mickel, Sebastian C. Kapfer, Gerd E. Schröder-Turk and Klaus Mecke. 'Shortcomings of the Bond Orientational Order Parameters for the Analysis of Disordered Particulate Matter'. In: *The Journal of Chemical Physics* 138.4 (Jan. 2013), p. 044501.

[130] Julia Eckert, Benoît Ladoux, René-Marc Mège, Luca Giomi and Thomas Schmidt. 'Hexanematic Crossover in Epithelial Monolayers Depends on Cell Adhesion and Cell Density'. In: *Nature Communications* 14.1 (Sept. 2023), p. 5762.

Paper I

Robust statistical properties of T1 transitions in a multi-phase field model of cell monolayers

scientific reports

Check for updates

OPEN

Robust statistical properties of T1 transitions in a multi-phase field model of cell monolayers

Harish P Jain[1]✉, Axel Voigt[2,3,4] & Luiza Angheluta[1]

Large-scale tissue deformation which is fundamental to tissue development hinges on local cellular rearrangements, such as T1 transitions. In the realm of the multi-phase field model, we analyse the statistical and dynamical properties of T1 transitions in a confluent monolayer. We identify an energy profile that is robust to changes in several model parameters. It is characterized by an asymmetric profile with a fast increase in energy before the T1 transition and a sudden drop after the T1 transition, followed by a slow relaxation. The latter being a signature of the fluidity of the cell monolayer. We show that T1 transitions are sources of localised large deformation of the cells undergoing the neighbour exchange, and they induce other T1 transitions in the nearby cells leading to a chaining of events that propagate local cell deformation to large scale tissue flows.

Collective motion of cells is essential to several processes including development of an embryo, tissue morphogenesis, wound healing, homeostasis and cancer metastasis[1–3]. These biological processes are highly complex and orchestrate mechanical, chemical and biochemical interactions across multiple scales[4–7]. Through the interplay between directed motion, neighbour alignment and mechanical interactions, cell monolayers exhibit emergent structures and dynamics that are crucial for their biological function. A fundamental underlying process for emergent large-scale behavior is the topological rearrangement of neighbouring cells known as T1 transition (also known as cell intercalation). It is a local, dissipative event that leads to remodelling of the tissue architecture and influences the large-scale flow properties of cell monolayers that affects tissue homeostasis and epithelial morphogenesis[8–10].

In confluent monolayers, the tissue architecture can change in several ways. To isolate the tissue dynamics driven by spontaneous T1 transitions, we consider an idealised situation where apoptosis and cell division are neglected, cells have a constant volume, identical mechanical properties, and their total number is fixed. During a T1 transition, typically two neighbouring cells move apart, while two of their neighbours come towards each other and make contact as illustrated in Fig. 1. The average number of neighbours before and after the T1 transition is invariant. Through T1 transitions, cells undergo large deformations and shape changes, and encounter an energy barrier that they have to overcome through their activity[11,12]. Albeit, there are several competing scenarios of the mechanical-chemical-biological feedback involved in a T1 transition, our understanding of these coupled processes is still elusive[13].

T1 transitions are common features also in granular matter and foams under external forcing[14–16]. The energy relaxation after a T1 transition has been studied in foams by measuring the length of T1 junctions[17]. This concept was adapted for active tissues[18], where the length of the T1 junction before and after a T1 transition has been measured. During a T1 transition in dry foams[15], the cells form a rosette where either four or more edges meet. It has been shown that a junction is energetically stable for three edges incident at 120 degrees. So, while undergoing a T1 transition, the cells pass from one metastable state to another via an unstable state comprising of a rosette. In confluent monolayers, extracellular spaces (gaps) change this process[19]. Rosettes and tri-junctions can no longer be defined by the number of edges meeting but are placed where gaps are formed.

Also, various mathematical models have been used to study different facets of T1 transitions in foams and tissues[11,19–23]. They are mainly based on vertex models, which approximate cells by polygonal shapes. However, cell shape plays a crucial role in T1 transitions and the ability to accurately describe complex cell shapes, beyond polygons, might be advantageous[19,24,25]. We consider a multi-phase field model that allows for spontaneous T1 transitions while capturing the cell shape at a high resolution, and allowing for large shape deformations.

[1]Njord Centre, Department of Physics, University of Oslo, 0371 Oslo, Norway. [2]Institute of Scientific Computing, Technische Universität Dresden, 01062 Dresden, Germany. [3]Center of Systems Biology Dresden, Pfotenhauerstr. 108, 01307 Dresden, Germany. [4]Cluster of Excellence - Physics of Life, TU Dresden, 01062 Dresden, Germany. ✉email: harishpj@fys.uio.no

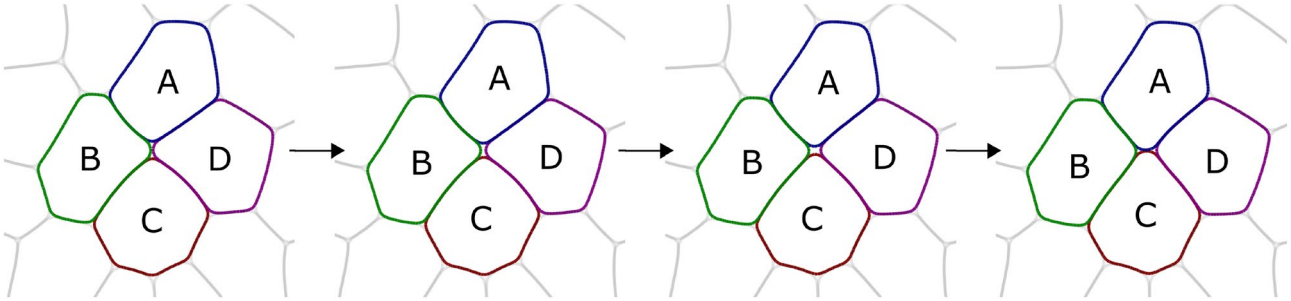


Figure 1. Successive time snapshots of tissue section undergoing a T1 transition, a finite-time neighbour exchange process between cells A, B, C and D. The transition starts when cells B and D lose contact and is completed when cells A and C make contact. During the T1 transition an extracellular space (gap) is formed between cells A, B, C and D. Also see Supplementary Movie 1.

Multi-phase field models have been used to probe several questions pertaining collective motion of cells[26–34]. These models consider cells as active incompressible droplets and unlike vertex models, T1 transitions emerge spontaneously as a result of shape deformations. In vertex models, extracellular spaces (gaps) need explicit modelling with ad-hoc assumptions[19], whereas in multi-phase field models they are emergent.

In this paper, we focus on characterising the energy profile preceding and succeeding T1 transitions. We show that this energy profile is statistically robust to changes in several model parameters. It is characterized by an asymmetric profile with a fast increase in energy before the T1 transition, a sudden drop after the T1 transition, followed by a slow relaxation. The relaxation profile provides insights into the flow properties of the monolayer. Previously, the relaxation has been indirectly studied in tissues by examining the relaxation of an ellipsoid droplet immersed in a tissue[17,19,35]. The relaxation profile was attributed to yield stress due to limitations in the measurement timescales[35], and also associated with the fluidization of the tissue[19,36]. We further consider the duration of T1 transitions and find that the average duration scales inversely to the maximum average energy attained during the T1 transition. Also, we show that T1 transitions may trigger the creation of other T1 transitions nearby and the chaining of T1 transitions leads to large-scale deformation and fluid-like behaviour.

We introduce the multi-phase field model in "Multi-phase field model" section and discuss results on local statistical properties of T1 transitions in "Results" section. We further analyse the dependency of these statistical properties on various model parameters. The effect of cell deformability and activity is considered in detail. We study the impact of chaining of T1 transitions on flow at larger scales. In "Discussion" section, we relate these finding to mechanical and rheological properties of the tissue and postulate that they can be used to characterize fluidization. Details on the numerical methods, the initialization and characterization of T1 transitions are provided in "Numerical methods" section.

Multi-phase field model

We represent a two-dimensional confluent cell monolayer within a multi-phase field model following formulations[28,32–34]. We consider a system of N cells of equal area occupying a square domain of size $[0, L] \times [0, L]$. Each cell is represented by a scalar phase field $\phi_i(\mathbf{x}, t)$ as an indicator function of the domain occupied by each cell labeled by $i = 1, 2, \cdots, N$. Namely, the bulk phase values $\phi_i \approx 1$ and $\phi_i \approx -1$ indicate the interior and exterior of the cell, respectively. The cell boundary is defined by the localised transition region between the two bulk values. We use periodic boundary conditions, i.e. the fields are periodic in space over the system size L such that $\phi_i(x_1, x_2, t) = \phi_i(x_1 + L, x_2 + L, t)$. The time evolution of the i-th phase field follows conservative dynamics which preserves the cell areas and is given by

$$\partial_t \phi_i + \mathbf{v}_i \cdot \nabla \phi_i = \Delta \frac{\delta \mathscr{F}}{\delta \phi_i}, \tag{1}$$

where Δ is the two-dimensional Laplacian applied to the variational derivative of a free energy functional $\mathscr{F}$ with respect to the phase field ϕ_i. Due to this term, the phase field evolves to minimise the free energy locally while the total cell volume is kept fixed. The free energy $\mathscr{F} = \mathscr{F}_{CH} + \mathscr{F}_{INT}$ contains the Cahn-Hilliard energy

$$\mathscr{F}_{CH} = \frac{1}{Ca} \sum_{i=1}^{N} \int_{\Omega} \left(\frac{\epsilon}{2} ||\nabla \phi_i||^2 + \frac{1}{4\epsilon} (\phi_i^2 - 1)^2 \right) d\mathbf{x}, \tag{2}$$

and the interaction energy[28,34]

$$\mathscr{F}_{INT} = \frac{1}{In} \sum_{i=1}^{N} \int_{\Omega} B(\phi_i) \sum_{j \neq i} w(\phi_j) d\mathbf{x}. \tag{3}$$

The capillary number Ca and interaction number In are tuning parameters for the cell deformability and the strength of mutual repulsion/attraction interactions, respectively. In Eq. 2, the Cahn-Hilliard energy has a local free energy density given by the double-well potential with the minima corresponding to the two bulk values, and a gradient term corresponding to the interfacial energy. The Cahn-Hilliard energy ensures phase separation

into two bulk regions which are separated by a thin, diffuse interface. The parameter ϵ controls the width of this diffuse interface. This energy alone is minimised by cells with circular shapes. In Eq. 3, each cell's interior and interface ($B(\phi_i) = (\phi_i + 1)/2$) is coupled with every other cell through a local interaction potential,

$$w(\phi_j) = 1 - (a+1)\left(\frac{\phi_j - 1}{2}\right)^2 + a\left(\frac{\phi_j - 1}{2}\right)^4,$$

where the parameter $a = 1$ models repulsion, while $a > 1$ models attraction and repulsion (see[34] for a detailed analysis of role of a).

Cell activity is introduced through the advection velocity field $\mathbf{v}_i(\mathbf{x}, t)$ in Eq. 1 and is given by

$$\mathbf{v}_i(\mathbf{x}, t) = v_0 B(\phi_i)\mathbf{e}_i(t), \tag{4}$$

where v_0 is a constant parameter that controls the magnitude of the activity, $\mathbf{e}_i = [\cos\theta_i(t), \sin\theta_i(t)]$ where θ_i is the orientation of the self-propulsion which evolves as

$$d\theta_i = \sqrt{2D_r}dW_i(t) + \alpha(\beta_i(t) - \theta_i(t))dt. \tag{5}$$

The first term on the right side of Eq. 5 is a rotational diffusion term with a Wiener process W_i. The second term is a relaxation to the orientation of the cell's shape elongation. The cell elongation is identified by the principal eigenvector of the shape deformation tensor[29,32]

$$\mathbf{S}_i = \begin{bmatrix} S_{i,0} & S_{i,1} \\ S_{i,1} & -S_{i,0} \end{bmatrix} \tag{6}$$

which is symmetric and traceless and has the two components

$$S_{i,0} = \frac{1}{8}\int_\Omega \left[\left(\frac{\partial\phi_i}{\partial y}\right)^2 - \left(\frac{\partial\phi_i}{\partial x}\right)^2\right]d\mathbf{x} \quad \text{and} \quad S_{i,1} = -\frac{1}{4}\int_\Omega \left[\frac{\partial\phi_i}{\partial x}\frac{\partial\phi_i}{\partial y}\right]d\mathbf{x}.$$

Its corresponding eigenvalues are $\lambda_i^\pm = \pm\sqrt{S_{i,0}^2 + S_{i,1}^2}$ and eigenvectors are $\eta_i^\pm = (\frac{S_{i,0}+\lambda_i^\pm}{S_{i,1}}, 1)$. The vector η_i^+ is parallel to the elongation axis of the cell and determines the preferred self-propulsion direction as

$$\beta_i(t) = \begin{cases} \arg(\boldsymbol{\eta}_i^+(t)) & : \ \mathbf{e}_i(t)\cdot\eta_i^+(t) > 0 \\ -\arg(\boldsymbol{\eta}_i^+(t)) & : \ \mathbf{e}_i(t)\cdot\eta_i^+(t) < 0 \end{cases} \tag{7}$$

Therefore, the second term on the right hand side of Eq. (5) aligns $\theta_i(t)$ with $\beta_i(t)$, where $\beta_i(t)$ is the closest direction to $\theta_i(t)$ that is parallel to the elongation axis of the cell. The parameter α controls the time scale of this alignment of the self-propulsion direction with the elongation axis of the cell. There are different possibilities to define the advection velocity $\mathbf{v}_i(\mathbf{x}, t)$ (see Ref.[32] for an overview and comparison). The current form includes approaches of Ref.[29] and, as the elongation is a result of the interaction with neighbouring cells, it accounts for contact inhibition of locomotion[37,38]. The model leads to properties appropriate to describe, e.g., Madin-Darby canine kidney (MDCK) cells[32,39].

To summarise the multi-phase field approach, we model the shape of each cell i in a confluent cell monolayer by a phase field ϕ_i. The evolution in space and time of the phase field is derived on the relaxation of a free energy to incorporate individual cell dynamics and cell-cell mutual interactions such that cells prefer: a lower surface tension while maintaining constant area, to interact with other cells, and to self propel. Cells with higher value of Ca are more deformable. By changing the parameter a in the mutual interaction potential, we can control the tendencies of cell boundaries to overlap. Each cell has a self-propulsion velocity which has a fixed magnitude and a preferred orientation along the elongation of the cell (decay-rate to this controlled by α) with random fluctuations about it (rate controlled by D).

Results

Energy profile of T1 transitions. Within our multi-phase field approach, T1 transitions are neighbour exchange processes with a finite duration. A prototypical time sequence of a T1 transition is illustrated in Fig. 1. Four cells A, B, C and D are involved. Before the T1 transition, the cell junction shared by cells B and D shrink. The T1 transition starts when the cells B and D break contact and move apart. This results in the formation of an extracellular space which we call 'gap'. Cells A and C move towards each other, close the gap, and form a new contact concluding the T1 transition. After the T1 transition, this new junction between cells A and D expands. The junctions that shrink and expand are called T1 junctions. We refer to "Numerical methods" section for the procedure to detect T1 transitions and their durations. A T1 transition not only leads to topological rearrangements of the four neighbouring cells, it also involves deformation of the cells. While details, such as the specific shape of the cells and their deformation, the duration of the T1 transition and the relaxation process differ between T1 transitions, we will demonstrate that robust statistical features of T1 transitions exist.

We define the epicenter of a T1 transition as the point with the minimum total distance from the centers of the involved cells in the neighbour exchange process, midway through the T1 transition. We define the immediate region around the epicenter as the core of a T1 transition, which is of essence because it is the region where T1 junctions shrink and expand, and the gap appears and disappears.

Figure 2a shows the total free energy density midway through a T1 transition. The epicentre is shown by the white dot and the estimated core is highlighted by the green circle. It has a radius $r_{avg} = 0.02L$, where L is the

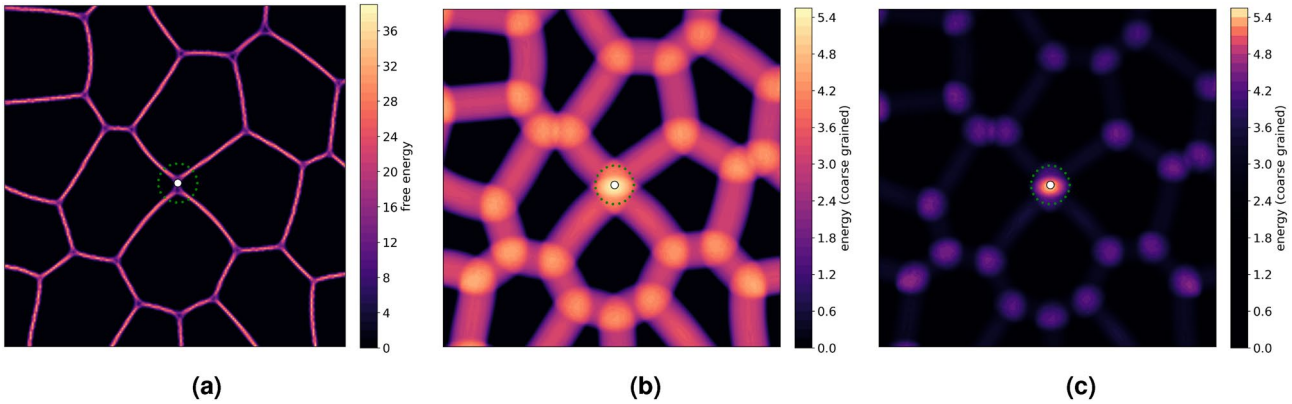


Figure 2. (**a**). Free energy density, in a region surrounding a T1 transition. (**b**) and (**c**) Coarse-grained energy density in a linear and log-scale, respectively. The white dot represents the epicenter of the T1 transition while the green dotted circle represents the coarse graining radius r_{avg}, the estimated core of the T1 transition.

side length of the computational domain. We compute a coarse-grained energy whose value at any point in the domain is the average of the energy density in a circular region centered at that point with radius r_{avg}. Figure 2b shows this coarse grained energy field $f_{r_{avg}}$, which we will call 'energy' field in the following. The signature of triple-junctions and T1 transitions already becomes appealing due to their higher energy. The difference between both is enhanced by using a log scale (see Fig. 2c). Considering this energy field in the epicenter over time provides a spatial-temporal description of T1 transitions. For discussions on the sensitivity of this procedure on r_{avg} we refer to Numerical methods section.

Figure 3a shows the time evolution of this energy averaged over 158 T1 transitions. The time is negative before a T1 transition and is positive after a T1 transition, and is denoted by t_{T1}. The energy during the T1 transitions is excluded, which leads to a discontinuity at $t_{T1} = 0$. The two values at $t_{T1} = 0$ correspond to the averaged energies at the start and the end of the T1 transitions. As the duration of T1 transitions differs, an averaged energy as a function of time during the T1 transition does not provide any meaningful information. Details on the energy during the T1 transition are shown in Fig. 3b using a normalized time. The energy profile in Fig. 3a,b has a peak at the T1 transition. The profile is asymmetric with a strong increase in energy before the T1 transition and a sudden decrease after the T1 transition, followed by a slow relaxation. The asymmetry can be quantified by considering the 75% of the maximum value, which is marked in Fig. 3a. Figure 3c–e illustrate the evolution for one T1 transition, the one depicted in Fig. 1. These figures contain overlays of several snapshots as per the time marked in the figures. The darkest of these snapshots pertains to the latest time. The yellow region marks the estimated core of the T1 transition. The asymmetry before and after the T1 transition, Fig. 3c, e, respectively, is clearly visible. The T1 junctions are longer at $t_{T1} = 5$ compared with $t_{T1} = -5$. During the T1 transition, Fig. 3d, the asymmetry is less pronounced. Most of the deformations are concentrated in the core. These deformations arise as a result of the formation of the gap, and subsequently its disappearance. The shrinking and formation of T1 junctions and the deformations within the core are a signature of the T1 transition. However, they also influence the deformation of the four cells outside of the core, and their neighbours, which can be perceived by the overlayed cell shapes. Interestingly in the depicted T1 transition, the deformations of each of the four cells seems to be persistent before, during and after the T1 transition (see the arrows indicating the direction of deformations). We will elaborate on this and other coarse grained effects in "Chaining of T1 transitions" section. The energy profile indicates an accumulation of energy to reach the energy barrier at the T1 transition. This is due to probing several possibilities in local movement and cell shape deformation, which are coupled by the definition of activity, taking into account cell elongation and contact inhibition of locomotion. After the energy barrier has been overcome, the fast relaxation of the energy can be associated with a steep gradient in the energy landscape in one direction.

The asymmetric shape of the energy profile is robust to changes in most model parameters, as demonstrated in Fig. 4 where α, Ca, a, D and v_0 are varied and the energy profile associated with passive sheared foams is included for comparison. Figure 4b shows the energy rescaled by the maximum energy as changes in Ca directly affect the free energy (see Eq. (2)). Within the range of parameters explored, the changes in the values of alignment parameter α, interaction coefficient a, and diffusivity D have minimal effects on the energy profile. We see that the profile is robust even in absence of noise ($D = 0$) (Fig. 4d). On the other hand, the profile deviates from Fig. 3a for low values of v_0 and Ca. Figure 4e shows that the cell activity v_0 affects the rate at which the cells approach a T1 transition, which is indicated by the slower accumulation of energy for low v_0. However, change in v_0 has a minor effect on the energy relaxation immediately after a T1 transition. The slow relaxation afterwards is largest for large values of v_0. This can be associated with the definition of activity, which is related to cell elongation and at least on average cells elongate in the direction of movement after the T1 transition. The characteristic profile of the accumulation of energy before the T1 transition and the fast relaxation of energy after the T1 transition is also present for low values of Ca (see Fig. 4b). However, as Fig. 4b considers a rescaled energy the actual rates depend on Ca. When Ca is low, cells are less deformable and undergo fewer T1 transitions. The slow relaxation after the sudden decrease only slightly depends on Ca. We would like to point out that the results for low values

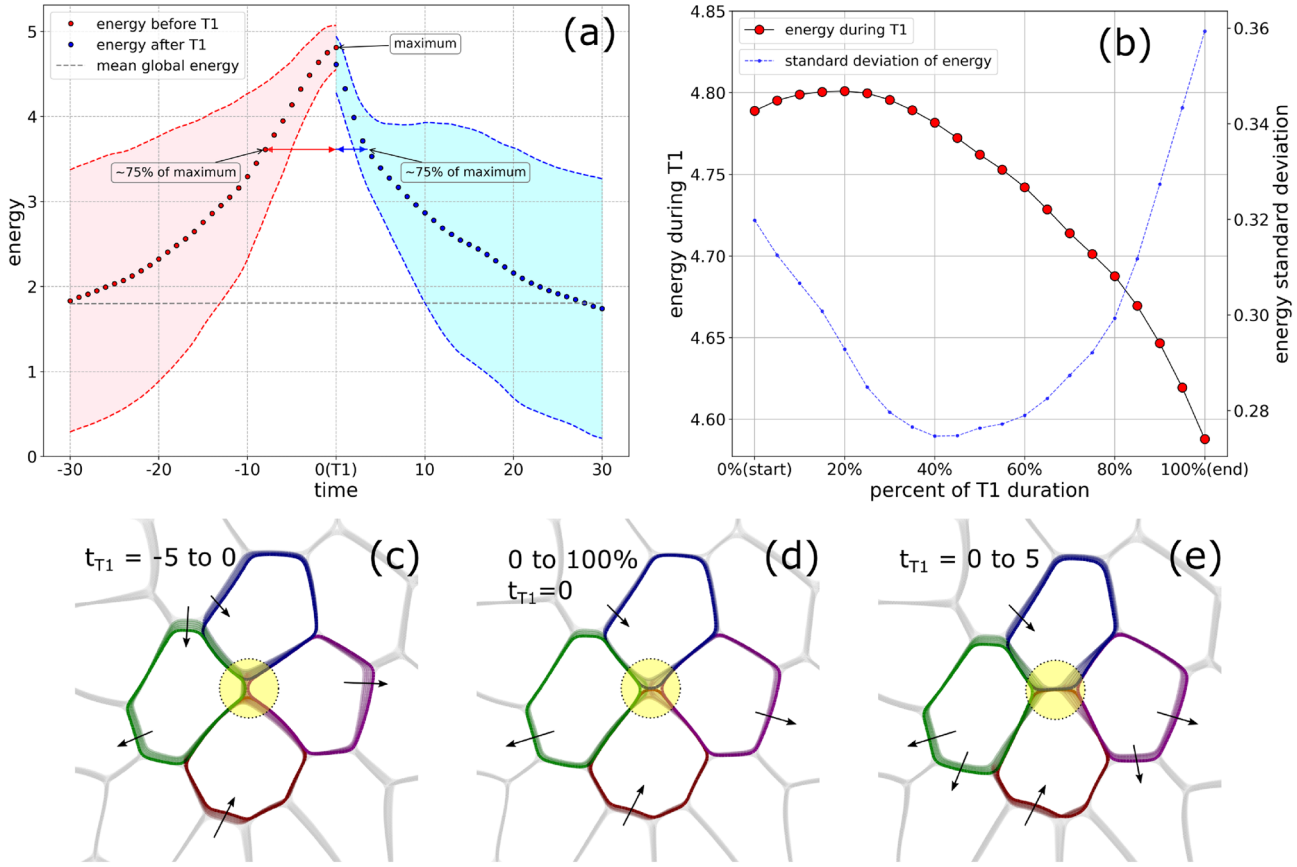


Figure 3. (**a**) Evolution of energy (averaged for 158 T1 transitions) at the epicenter of the T1 transitions. Negative time corresponds to time before a T1 transition and positive time corresponds to time after a T1 transition. The shaded region denotes a width of 1 standard deviation. The gray dashed line is the average energy across the whole domain. (**b**) Average energy profile during a T1 transition as function of percentage of T1 duration. The standard deviation is also indicated. (**c**), **d**) and (**e**) Montages of deformed cells involved in a T1 transition. Each montage is made up of 5 images, that capture the cells at equidistant times, stacked over each other. The darkest colored overlay represents the latest time. (**c**) Cell shapes before the start of the T1 transition, (**d**) during the T1 transition, and (**e**) after the end of the T1 transition. Also see Supplementary Movie 2 for corresponding simulation.

of v_0 and Ca should be considered with care, as the number of T1 transitions considered in these cases is much lower. While the system is still in the fluid phase, the extreme values for $v_0 = 0.1$ and $Ca = 0.05$ already approach the transition to the solid phase.

In passive foams T1 transitions can be induced by applying shear. This is considered by an advection velocity field $v_i(\mathbf{x}, t) = 0.5|x_1 - L/2|$ and the resulting energy profile is compared with the profile from Fig. 3a in Fig. 4f. The profiles differ before the T1 transition and within the slow relaxation, but are similar in the sudden drop of energy right after the T1 transition. The latter reiterates that the energy relaxation right after a T1 transition is independent of activity. The differences in the accumulation of the energy can be associated with the persistent orientation of advection velocity due to shear, which results in collective deformation and a more deterministic approach of the T1 transition. Also the termination of the decay in the passive case results from the restricted possibilities of relaxation due to the applied shear.

Duration and other properties of T1 transitions. As mentioned earlier, the duration of T1 transitions strongly depends on the specific cell arrangements. We now discuss the statistical properties of the duration. Figure 5a shows the probability density of the duration of T1 transitions. The distributions peak at smaller values and have a long tail for larger values. The profiles corresponds to repulsive and adhesive ($a > 1$), and only repulsive interactions ($a = 1$), and are fitted by Gamma distributions. The average duration of T1 transitions for repulsive interactions (3.418 measured for 539 T1 transitions across 3 simulations) is smaller compared to that for repulsive and adhesive interactions (3.826 for 631 T1 transitions across 4 simulations). Keeping other parameters fixed, the average number of T1 transitions in the repulsive and adhesive case was 157.75 while for the repulsive case was 179.66, respectively. Therefore, in the repulsive case, cells undergo neighbour exchanges faster and more often. Figure 5b shows the duration of T1 transitions as a function of the maximum energy reached during a T1 transition. While the data is scattered, it qualitatively shows that high energy T1 transitions are faster. This qualitative result holds for both cases and can be explained by a larger accumulation of energy in

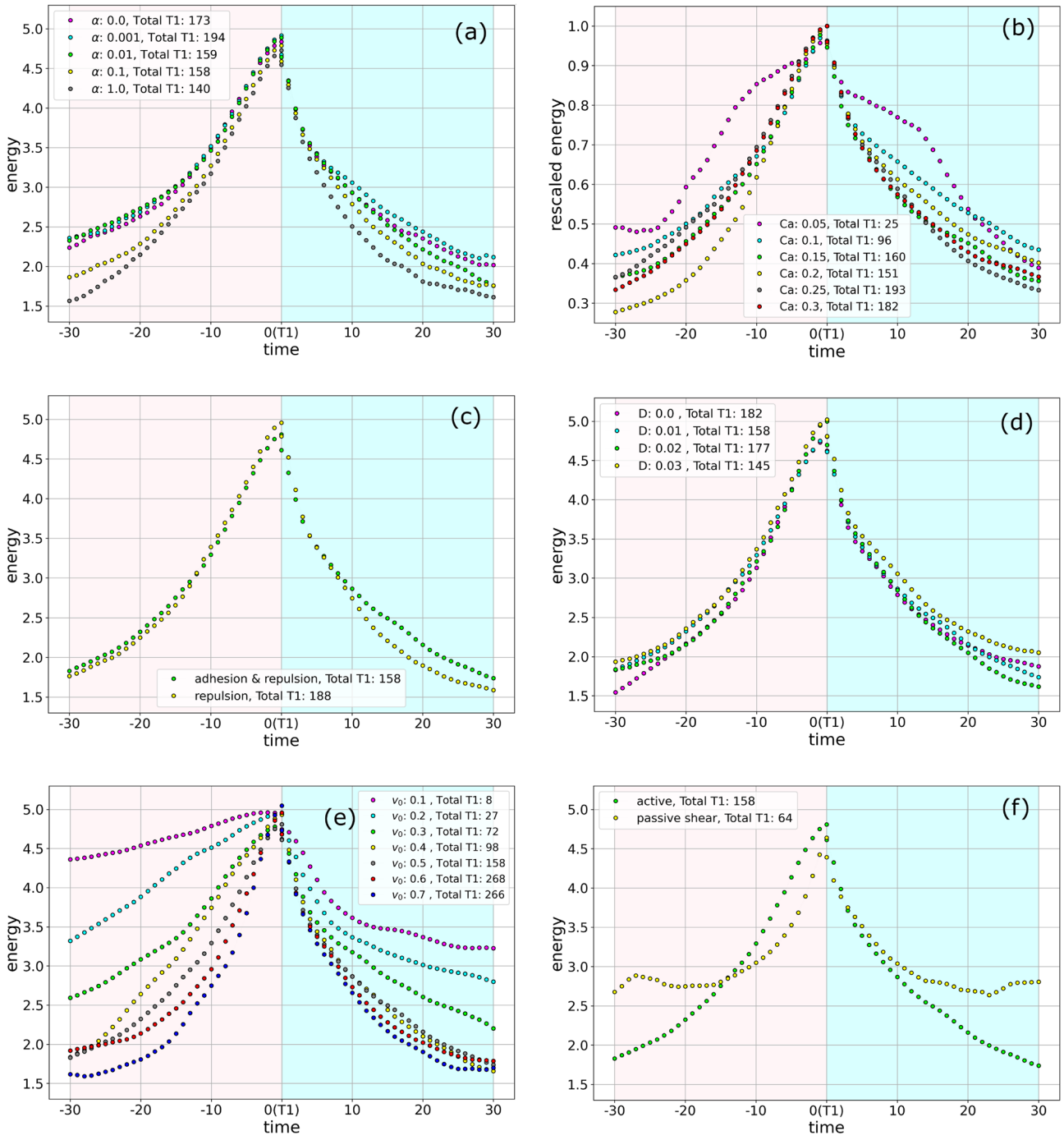


Figure 4. Evolution of energy for different parameter values. The pink and cyan shaded region are used to denote time before and after the T1 transitions, respectively. The number of T1 transition used to obtain these results is indicated. (**a**) The aligning parameter α is varied. (**b**) The parameter to control cell deformability, Ca is varied. As Ca is a parameter that influences the overall total energy, for better comparison the energy is rescaled by division with the maximum energy. (**c**) Adhesion and repulsion corresponds to $a = 1.5$ and repulsion corresponds to $a = 1$. (**d**) The diffusivity D is varied. (**e**) The magnitude of the activity v_0 is varied. (**f**) The passive shear corresponds to advection field $v_i(\mathbf{x}, t) = 0.5|x_1 - \frac{L}{2}|$ while the active case corresponds to parameters in Table 1.

the core, which increases the spatial energy gradients and in turn speeds up the relaxation of the energy, which leads to the shorter duration.

Figure 5c shows the averaged shape index (perimeter/$\sqrt{\text{area}}$) of the four cells involved in a T1 transition as function of time relative to a T1 transition. The asymmetry found for the energy profile and the discontinuity at $t_{T1} = 0$ is also present for this quantity. The cells deform and elongate as they approach a T1 transition and relax afterwards. This increases and decreases their shape index, respectively. The faster relaxation leads to the

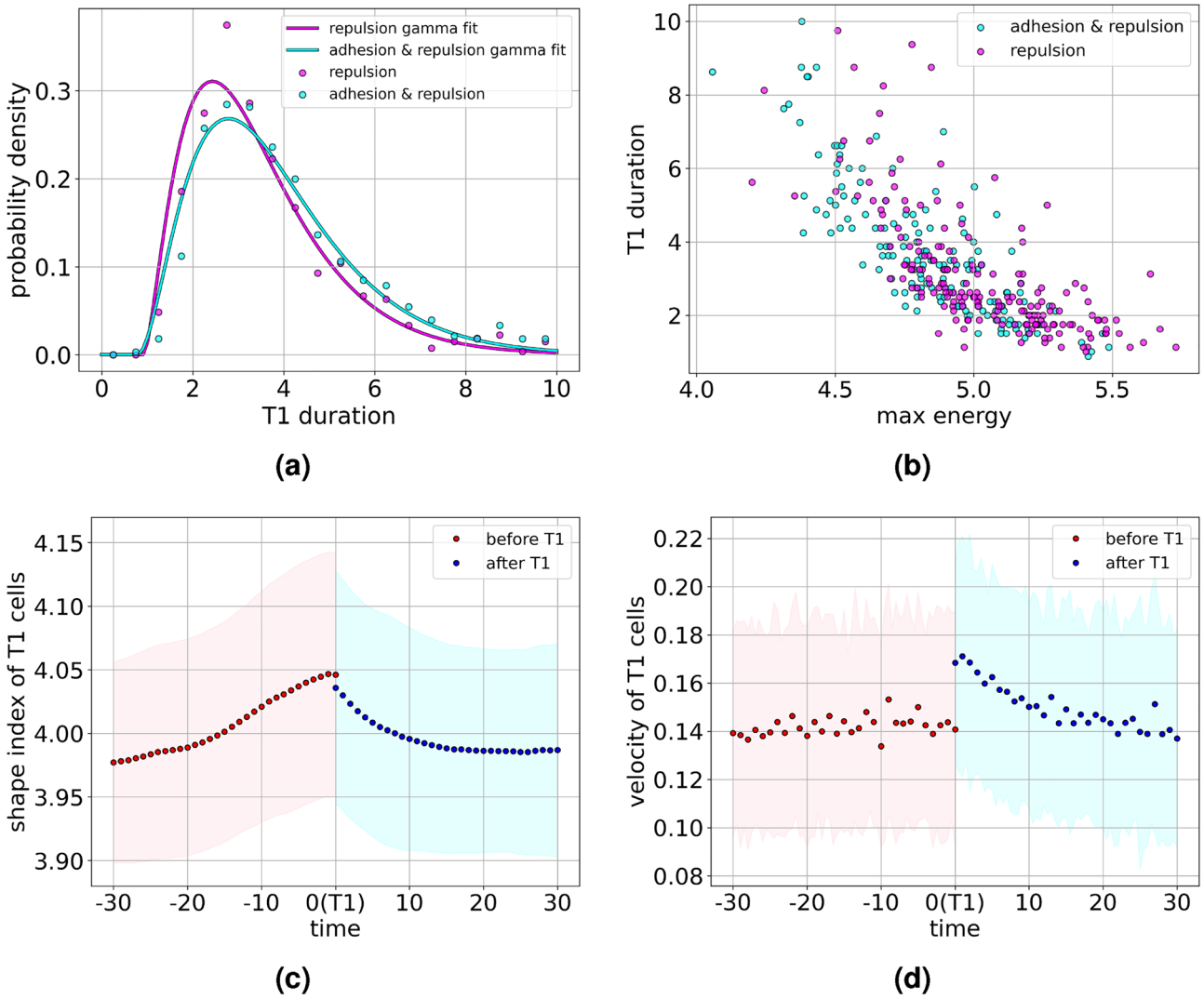


Figure 5. (**a**) Probability density of the duration of T1 transitions for only repulsion interactions (magenta dots) and for both repulsion and adhesion (cyan dots). Both data sets are fitted by Gamma distributions highlighting the exponential tails. (**b**) Scatter plot of duration of T1 transition as function of the maximum energy reached during a T1 transition. (**c**) Evolution of average shape index and (**d**) Evolution of the average velocity of center of mass of the cells involved in the T1 transitions as function of time relative to a T1 transition. The shaded regions mark the standard deviations of both quantities.

asymmetry in the evolution of the shape index. The asymmetry around a T1 transition is also seen in the average velocity of the center of mass of the cells involved in a T1 transition as shown in Fig. 5d. While the velocity is almost constant before the T1 transition, the velocity peaks at the T1 transition and slows down afterwards until it reaches the average value before the T1 transition. The peak in the average velocity of the center of mass is due to the large deformations of the portions of cells within the core and their fast relaxation after the T1 transition. Both quantities, the shape index and the cell velocity of the four cells involved in a T1 transition are also experimentally accessible. These quantities can be related to the energy considered above.

Effect of cell deformability, activity and gaps on T1 transitions. The asymmetric energy profile in Fig. 3a is robust to tuning of most of the model parameters. Significant variations only occur for low values of Ca and v_0 (see Fig. 4b,e). We now analyse the effect of cell deformability and activity on T1 transitions in more detail. This requires a detailed analysis of the influence of gaps. The gap fraction is related to the confluency as confluency $= 100(1 -$ gap fraction). It essentially is a fixed quantity set by the initial data. We fix all parameters as per table 1 and compare two different initial cell sizes, denoted by 'low gap' with gap fraction 0.00048 and 'high gap' with gap fraction 0.00212. Both can be considered as confluent. The number of T1 transitions within the considered time frame is not influenced by this variation. The total numbers of T1 transitions are 162 and 158 for low and high gap cases, respectively. However, the average duration of T1 transitions is reduced by reducing the gap fraction. The values are 2.559 and 3.794 for low and high gap cases, respectively. We measure the gap fraction as the fraction of domain where $\sum_i B(\phi_i)$ is less than a fixed threshold which is set to 0.2. This essentially excludes possible partial overlap of the diffuse interface region of cells and only accounts for gaps at

tri-junctions and rosettes. This makes the measured gap fraction to depend on deformability and activity. For the considered cases, low *Ca* leads to rounder cells with stronger overlap of the diffuse interfaces of the cells, which are in contact. This leads to an increase in the measured gap fraction (see Fig. 6c). A similar dependency, but smaller in magnitude, is found for activity. Larger v_0 lead to stronger interactions between cells and thus more overlap of the diffuse interface region of cells in contact which again leads to an increase in measured gap fraction (see Fig. 6i). The gap fraction in both figures is the average quantity over the considered time frame. Both results and the dependencies discussed below are considered for the 'high gap' setting.

As shown in Fig. 6a, the number of T1 transitions increases with increasing cell deformability parameter *Ca*. Cells that are more deformable can more easily acquire the shape deformations associated with T1 transitions. When *Ca* is low, these deformations are energetically more expensive resulting in fewer T1 transitions. Also the

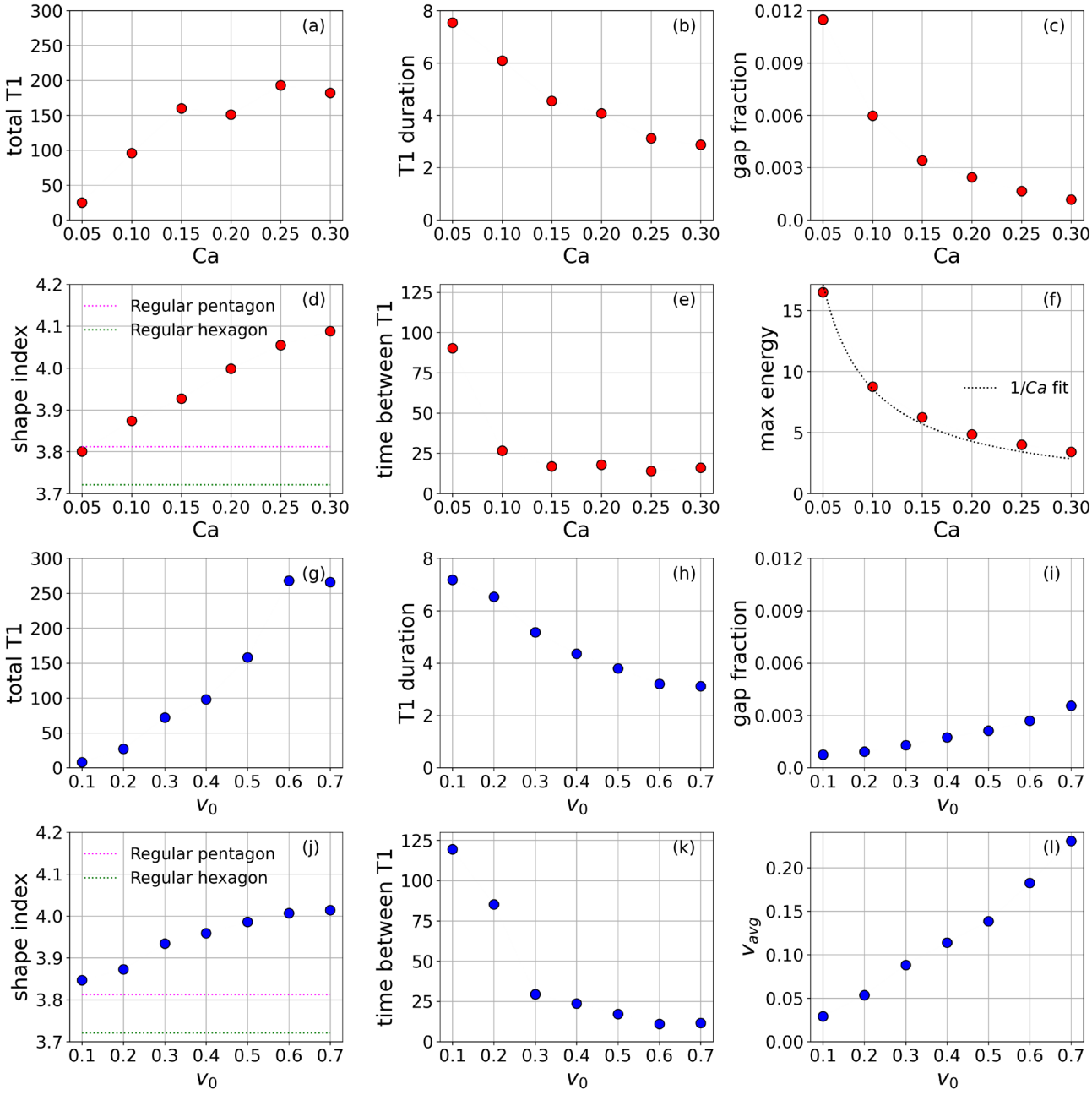


Figure 6. Dependency of various properties on deformability *Ca* (**a**–**f**) and activity v_0 ((**g**)-(**l**)). *Total T1* considers the total number of T1 transitions within the considered time frame, *T1 duration* is the averaged time from start to end of all T1 transitions, *Gap fraction* is the extracellular space, considered as $\sum_i B(\phi_i)$ below a fixed threshold, again averaged over time, *Shape index* considers the averaged shape index of the four cells involved in the T1 transitions. *Time between T1* is the average time a cell spends between successive T1 transitions, *Max energy* is the maximum energy reached at a T1 transition and v_{avg} is the average velocity of center of mass of all cells.

duration of T1 transitions depends on *Ca*, as shown in Fig. 6b. T1 transitions are shorter when cells are more deformable. We suspect that this might be due to the presence of smaller gaps at T1 transitions, as this requires less shape deformation. Figure 6d shows the average cell shape index of the four involved cells in a T1 transition as function of cell deformability *Ca*. The shape index increases as deformability increases. The shape index of $Ca = 0.05$ is less than that of a regular pentagon. The shape index of regular pentagon (3.813) was attributed as the critical shape index for jamming transition in classical vertex models[40] without gaps. It has been argued that gaps influence the mechanical properties and solid-liquid transition[17], which might explain this discrepancy, as our system is still within the fluid phase. Further details, which are related to the previous dependencies are shown in Figs. 6e and f. Figure 6e shows the average time a cell spends between successive T1 transitions as function of *Ca*. This quantity is large for low *Ca* but decreases and plateaus to low values upon increasing *Ca*. Figure 6f shows the maximum energy reached during a T1 transition against *Ca*. We see from the dotted curve that the maximum energy is proportional to $1/Ca$. Recall that $1/Ca$ scales the Cahn-Hilliard energy as per Eq. (2). This means that $\mathscr{F}_{r_{avg}}$ is primarily affected by the Cahn-Hilliard energy, which explains the correspondence of our results with the length of T1 junctions discussed earlier and considered in[17,18].

The dependency on v_0 shows qualitatively similar behaviour for the number of T1 transitions, the duration of T1 transitions, the shape index of the cells involved in T1 transitions and the time a cell spends between successive T1 transitions (see Fig. 6g, h, j, k). The increase in T1 transitions and decrease in the time between T1 transitions with activity is a property of active systems, which are driven out of equilibrium. T1 transitions are topological defects and thus an indication of out of equilibrium. The decrease in duration with increasing activity can again be associated with the decrease in measured gap fraction (see 6i), and also the increasing shape index with activity is a direct consequence of the form of active forcing considered. Figure 6l shows the average velocity of center of mass of all cells as a function of v_0. As expected, activity is primarily converted into motion with an almost linear dependency.

Chaining of T1 transitions. So far, we have analysed robust statistical properties of T1 transitions within their cores. However, we have also seen that these local features influence the position and shape of the four cells involved in a T1 transition, and their neighbours. This can induce new T1 transitions and lead to the formation of chains of T1 transitions as illustrated in Fig. 7. Each of these images consists of 10 tissue states captured at equally-spaced time instants and overlaid on top of each other. The cell shapes outlined in the darkest colors correspond to the latest time. The yellow circles mark the cores of the T1 transitions at those time instants. The chaining of T1 transitions is a result of the assumptions of constant cell area and a confluent monolayer. Any cell

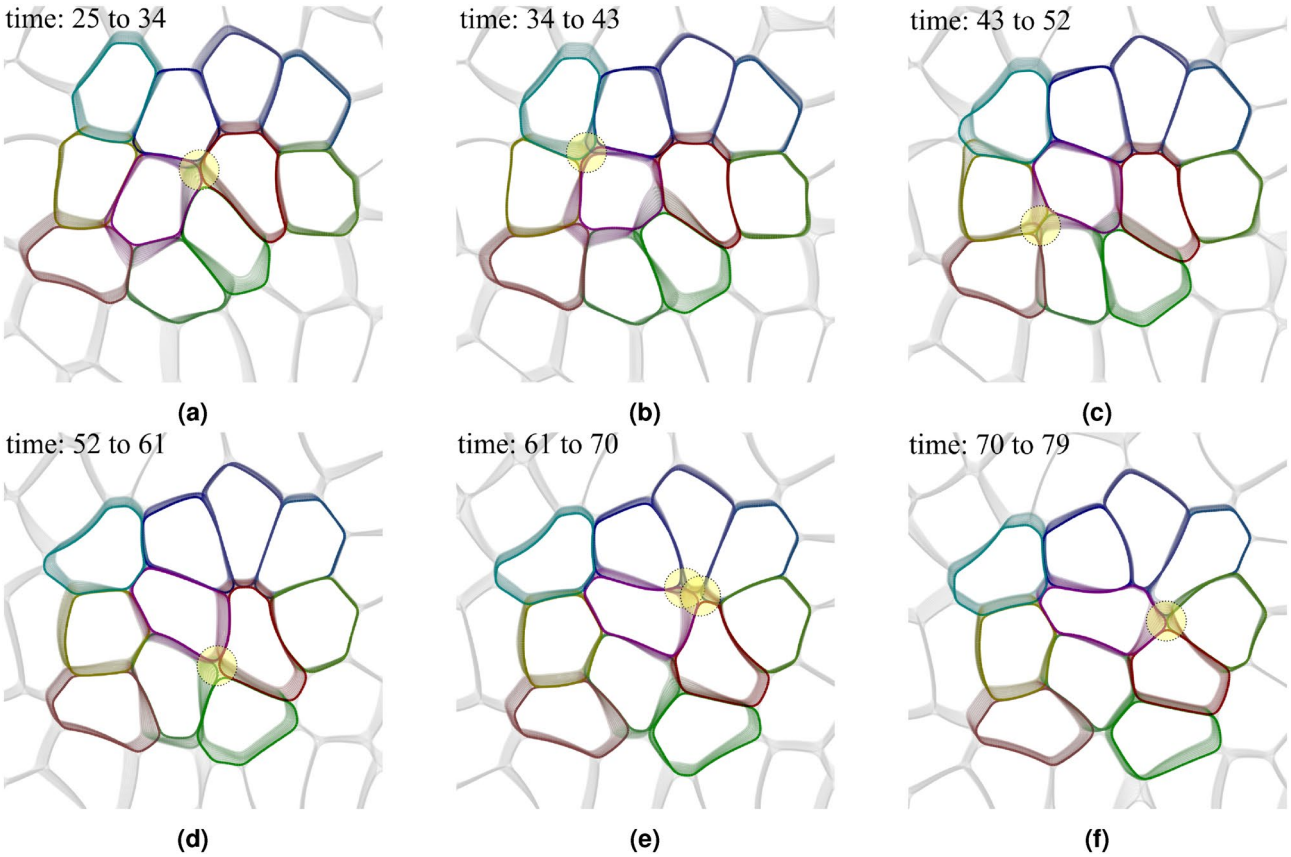


Figure 7. Chaining of T1 transitions. Each panel is a montage of 10 snapshots of tissue configurations taken successively at constant times intervals. Latest time is represented by the cell shapes marked in the darkest color shades. The cores of the T1 transitions are highlighted in yellow. Also see Supplementary Movie 3.

deformation associated with a T1 transition induces deformation of the neighbouring cells and thereby increases the possibility of new T1 transitions. This is further enhanced by activity and the considered propulsion mechanism which favours the direction of elongation. Chaining has been observed and identified as an important feature in gastrulation[41].

This chaining of T1 transitions is also observed experimentally in sheared foams [41] and in our simulations of passive foams which are sheared with a constant shear velocity profile. For $v_0 = 0$, typically one or two T1 transitions occur due to the initial non-equilibrium configuration of the tissue. As cells relax toward an equilibrium state, their motility is reduced which prevents any further T1 transitions. The situation for small v_0 is similar. The tissue becomes jammed by cells being caged amongst their neighbours and no T1 transitions occur[32]. Furthermore, when cell deformability (Ca) is low, the energetic cost for cell deformations that are necessary to undergo T1 transitions is high, which prevents or at least reduces T1 transitions and the tissue also becomes jammed[32]. This corresponds to the low number of T1 transitions in Fig. 4b,e for low Ca and low v_0, respectively.

However, in the considered case in Fig. 7 we are far away from jamming and the chaining of T1 transitions leads to cell deformation propagating to larger scales. This is highlighted in Fig. 8a, which shows the evolution of the cell monolayer in the whole time window considered in Fig. 7 together with the trajectory of the center of mass of the colored cells, which highlights the movement on larger spatial scales. The chaining of T1 transitions is also a source of large-scale flows as evidenced in Fig. 8b. We consider the velocities of the centers of mass of all cells, average this quantity with the neighboring cells and construct a continuous velocity field by interpolating in space. The velocity field is shown together with the cell boundaries at $t = 52$. The mean direction corresponds with the direction of the black path shown in Fig. 8a. However, as the variations in magnitude and direction of the flow field in Fig. 8b indicate, T1 transitions can also induce fluctuations and could play an important role in sustaining chaotic flows (active turbulence) in cell monolayers [42–44].

Discussion

Large-scale tissue deformation requires cellular rearrangements. The simplest rearrangement in confluent cell monolayers is a T1 transition. We have analysed these neighbour exchanges among cells in detail using a multiphase field model and identified a characteristic asymmetric energy profile (see Fig. 3). The energy profile has a peak at the T1 transition. The profile is asymmetric with a strong increase in energy before the T1 transition and a sudden decrease after the T1 transition, which is followed by a slow relaxation. Detailed studies on the dependency of this profile on model parameters show robustness to variations in most parameters. They also allowed to associate the strong energy increase before the T1 transition with the strength in activity. This region is characterized by an accumulation of energy to reach the energy barrier at the T1 transition. This is achieved by probing several possibilities of direction of movement and shape deformation. This process is enhanced by activity, which is quantified by Fig. 4e. In contrast to this, the sudden relaxation after the T1 transition can clearly be associated with energy relaxation. It is almost independent of activity (see Fig. 4e) and cell deformability (see Fig. 4b), and also present in sheared foams(see Fig. 4f). We would like to remark that the behaviour is independent but the actual slope and duration of this regime depends on deformability, as the energy is scaled in Fig. 4b. The sudden decrease is associated with a steep gradient in the energy landscape in one direction set by the deformation of the cells in the core of the T1 transition. The third characteristic region, the slow relaxation, depends on activity and cell deformability. This relaxation profile provides insight in the mechanical properties of the tissue. Similar energy profiles have been obtained by actuation and relaxation of magnetic microdroplets which are injected into the tissue[17,19,35]. In these experiments a slow relaxation is associated with the fluidization

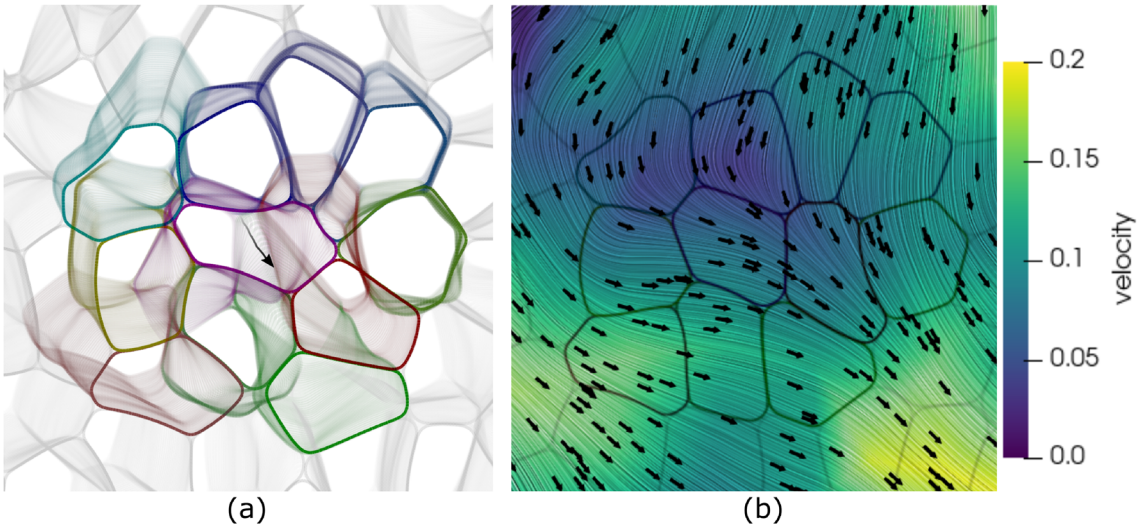


Figure 8. (**a**) Montage of tissue snapshots from time $t = 25$ to $t = 79$ (see figure 7). The black path is the trajectory of the center of mass of the 11 coloured cells. (**b**) LIC visualization of streamlines, magnitude (color) and direction (black arrows) of the flow velocity. The velocity and the cell boundaries correspond to time $t = 52$.

τ	τ_{save}	T	L	ϵ	v_0	a	Ca	In	D_r	α
0.005	0.5	150	100	0.15	0.5	1.5	0.2	0.1	0.1	0.1

Table 1. Default values of the model parameters.

of the tissue[19,35], while stagnation of the relaxation indicates more solid-like behaviour[17] and is associated with irreversible (plastic) tissue rearrangements. We postulate that these mechanical characterizations can also be obtained from the energy decay of the T1 transitions.

In the considered confluent tissue the type of interaction between the cells, if repulsive or repulsive and attractive, seems to play a minor role on the characteristic energy profile of a T1 transition (see Fig. 4c). However, the degree of confluency is known to influence the solid-fluid phase transition[35]. Increasing the extracellular space enhances fluidization. While we only consider the fluid phase, we observe an increased duration of T1 transitions for larger extracellular space. A finite duration of T1 transitions in cell monolayers has been associated with molecular processes and is considered in an adhoc manner in vertex models[22]. Within the multi-phase field model a finite duration is a result of the mechanical properties of the cells and their interactions. An increased duration of T1 transitions is observed for low deformability and low activity (see Figs. 6b and h) respectively. Both indicating more solid-like behaviour, which is consistent with[22], where increased duration of T1 transitions leads to decreasing the overall number of T1 transitions and a possible stiffening of the global tissue mechanics. However, these results don't take extracellular space into account.

Even if characterized locally, due to the confluency in the monolayer, large enough deformations induced by T1 transitions lead to permanent cell deformations in the neighbourhood, which can trigger other T1 transitions, leading to a chaining effect. This behaviour is associated with the foam-like architecture and consistent with previously reported nonlinear tissue mechanics[35]. It is this chaining of T1 transitions which allows for large-scale tissue deformations and flow patterns which can be associated with sustaining chaotic flows (see Fig. 8b).

Our analysis of the energy profile can be applied to experimental setups where the individual cell boundaries can be tracked, and the associated phase fields for each cell shape can be reconstructed to compute the total free energy from Eq. 2 and 3. We believe these results to also hold in more general situations, e.g. for varying cell sizes and varying mechanical cell properties.

Finally, to better understand the emerging dynamics in a specific biological context, larger cell monolayer (>10000 cells) need to be simulated. This would allow for a continuum description of the cell monolayer while resolving microscopic features like cell shape and T1 transitions at high resolutions. However, these are computationally intensive simulations, and sufficient advancement in computing power and improvement in their algorithmic implementations are required.

Numerical methods

Model parameters. Unless otherwise specified, we use the model parameters as per Table 1.

Finite element simulations. The simulations are run for time interval $[0, T]$ discretised into N_t units with a uniform timestep size τ, i.e. $T = N_t\tau$. We employ a semi-implicit discretization in time. Discretization in space follows the finite element method. We adaptively refine the diffuse interface and employ a parallelization approach which scales with the number of cells. For details we refer to[28,32–34,45,46]. The algorithm is implemented in the open-source library AMDiS[47,48].

Detecting T1 transitions. The T1 transitions are detected by tracking the neighbour relations of all cells. If two cells A and B are in contact, their neighbour relation is denoted by (A, B) or (B, A), both of which are equivalent. Suppose, there are four cells as in the Fig. 1. The set of neighbour relations between these four cells before, during and after a T1 transition are $\{(A,B),(B,C),(C,D),(D,A),(B,D)\}$, $\{(A,B),(B,C),(C,D),(D,A)\}$ and $\{(A,B),(B,C),(C,D),(D,A),(A,C)\}$ respectively. Before and after a T1 transition, there are 5 distinct neighbour relations between the four cells. The sets of relations before and after a T1 transition have four elements in common. These common elements make up the set of relations during a T1 transition. The duration of a T1 transition is time difference when the number of neighbour relations between the four cells change from 5 to 4 and back to 5.

Sensitivity of $f_{r_{avg}}$ on r_{avg}. The coarse graining region of a point $\mathbf{p}$ is the region with all points $\mathbf{x}$ such that $|\mathbf{p}-\mathbf{x}| < r_{avg}$. As the free energy is high at the cell edges, the points which include the edges within its coarse graining region around it would have high $f_{r_{avg}}$. Moreover, points with triple junctions (where 3 edges meet) within its coarse graining region would have a higher $f_{r_{avg}}$ due to the presence of longer total length of cell edges. Usually at a given time, $f_{r_{avg}}$ has peaks near the T1 epicenter. This is because, the region around it would have either two triple junctions along with a gap as seen in the snapshots of Fig. 1. Also, it is clear that points that do not have any cell edges within its coarse graining region, would have zero $f_{r_{avg}}$. We have found that increasing the r_{avg} loses information about the T1 transition in the value of $f_{r_{avg}}$ at the epicenter. A larger coarse graining region would entail a larger contribution from the bulk of the interior of the cell and would reduce $f_{r_{avg}}$ at the epicenters such that $f_{r_{avg}}$ at epicenters would not be uniquely discerned as a signature of a T1 transition. On the other hand, reducing r_{avg} would mean that we might not encompass the information of the two triple junctions and the gap formed during the T1 transition. It also increases the deviations in the statistics that we describe. Moreover, if the

energy along the length of the edge is uniform then the energy field $f_{r_{avg}}$ at a point gives an approximate measure of length of edges within the coarse graining region around that point.

Data availability

All data are available from the corresponding author upon reasonable request. The AMDiS implementation and additional codes for pre- and postprocessing are available from the corresponding author upon reasonable request.

Received: 27 January 2023; Accepted: 15 June 2023
Published online: 21 June 2023

References

1. Ladoux, B. & Mège, R. M. Mechanobiology of collective cell behaviours. *Nat. Rev. Mol. Cell Biol.* **18**, 743–757. https://doi.org/10.1038/nrm.2017.98 (2017).
2. Brugués, A. *et al.* Forces driving epithelial wound healing. *Nat. Phys.* **10**, 683–690. https://doi.org/10.1038/nphys3040 (2014).
3. Friedl, P., Locker, J., Sahai, E. & Segall, J. E. Classifying collective cancer cell invasion. *Nat. Cell Biol.* **14**, 777–783. https://doi.org/10.1038/ncb2548 (2012).
4. Guirao, B. *et al.* Unified quantitative characterization of epithelial tissue development. *Elife* **4**, e08519. https://doi.org/10.7554/eLife.08519 (2015).
5. Etournay, R. *et al.* Interplay of cell dynamics and epithelial tension during morphogenesis of the Drosophila pupal wing. *Elife* **4**, e07090. https://doi.org/10.7554/eLife.07090 (2015).
6. Iyer, K. V., Piscitello-Gómez, R., Paijmans, J., Jülicher, F. & Eaton, S. Epithelial viscoelasticity is regulated by mechanosensitive E-cadherin turnover. *Curr. Biol.* **29**, 578–591. https://doi.org/10.1016/j.cub.2019.01.021 (2019).
7. Dye, N. A. *et al.* Self-organized patterning of cell morphology via mechanosensitive feedback. *Elife* **10**, e57964. https://doi.org/10.7554/eLife.57964 (2021).
8. Keller, R. *et al.* Mechanisms of convergence and extension by cell intercalation. *Philosop. Trans. Royal Soc. B Biol. Sci.* **355**, 897–922 (2000).
9. Walck-Shannon, E. & Hardin, J. Cell intercalation from top to bottom. *Nat. Rev. Mol. Cell Biol.* **15**, 34–48. https://doi.org/10.1038/nrm3723 (2014).
10. Rauzi, M. Cell intercalation in a simple epithelium. *Philos. Trans. Royal Soc. B: Biol. Sci.* **375**, 20190552. https://doi.org/10.1098/rstb.2019.0552 (2020).
11. Bi, D., Lopez, J. H., Schwarz, J. M. & Manning, M. L. A density-independent rigidity transition in biological tissues. *Nat. Phys.* **11**, 1074–1079. https://doi.org/10.1038/nphys3471 (2015).
12. Oswald, L., Grosser, S., Smith, D. M. & Käs, J. A. Jamming transitions in cancer. *J. Phys. D Appl. Phys.* **50**, 483001. https://doi.org/10.1088/1361-6463/aa8e83 (2017).
13. Rauzi, M., Verant, P., Lecuit, T. & Lenne, P.-F. Nature and anisotropy of cortical forces orienting Drosophila tissue morphogenesis. *Nat. Cell Biol.* **10**, 1401–1410. https://doi.org/10.1038/ncb1798 (2008).
14. Schall, P., Weitz, D. A. & Spaepen, F. Structural rearrangements that govern flow in colloidal glasses. *Science* **318**, 1895–1899. https://doi.org/10.1126/science.1149308 (2007).
15. Weaire, D. & Hutzler, S. *The Physics of Foams* (Oxford University Press, Oxford, New York, 2001).
16. Stavans, J. The evolution of cellular structures. *Rep. Prog. Phys.* **56**, 733–789. https://doi.org/10.1088/0034-4885/56/6/002 (1993).
17. Durand, M. & Stone, H. A. Relaxation time of the topological T1 process in a two-dimensional foam. *Phys. Rev. Lett.* **97**, 226101. https://doi.org/10.1103/PhysRevLett.97.226101 (2006).
18. Curran, S. *et al.* Myosin II controls junction fluctuations to guide epithelial tissue ordering. *Dev. Cell* **43**, 480-492.e6. https://doi.org/10.1016/j.devcel.2017.09.018 (2017).
19. Kim, S., Pochitaloff, M., Stooke-Vaughan, G. A. & Campàs, O. Embryonic tissues as active foams. *Nat. Phys.* **17**, 859–866. https://doi.org/10.1038/s41567-021-01215-1 (2021).
20. Barton, D. L., Henkes, S., Weijer, C. J. & Sknepnek, R. Active Vertex Model for cell-resolution description of epithelial tissue mechanics. *PLoS Comput. Biol.* **13**, e1005569. https://doi.org/10.1371/journal.pcbi.1005569 (2017).
21. Sknepnek, R., Djafer-Cherif, I., Chuai, M., Weijer, C. J. & Henkes, S. Generating active T1 transitions through mechanochemical feedback (2022). arXiv:2106.12394.
22. Erdemci-Tandogan, G. & Manning, M. L. Effect of cellular rearrangement time delays on the rheology of vertex models for confluent tissues. *PLoS Comput. Biol.* **17**, e1009049. https://doi.org/10.1371/journal.pcbi.1009049 (2021).
23. Drenckhan, W. *et al.* Rheology of ordered foams–on the way to Discrete Microfluidics. *Colloids Surf. A* **263**, 52–64. https://doi.org/10.1016/j.colsurfa.2005.01.005 (2005).
24. Boromand, A., Signoriello, A., Ye, F., O'Hern, C. S. & Shattuck, M. D. Jamming of deformable polygons. *Phys. Rev. Lett.* **121**, 248003. https://doi.org/10.1103/PhysRevLett.121.248003 (2018).
25. Perrone, M. C., Veldhuis, J. H. & Brodland, G. W. Non-straight cell edges are important to invasion and engulfment as demonstrated by cell mechanics model. *Biomech. Model. Mechanobiol.* **15**, 405–418. https://doi.org/10.1007/s10237-015-0697-6 (2016).
26. Nonomura, M. Study on multicellular systems using a phase field model. PLoS ONE **7**, 1–9, (2012). 1109.5246. https://doi.org/10.1371/journal.pone.0033501
27. Palmieri, B., Bresler, Y., Wirtz, D. & Grant, M. Multiple scale model for cell migration in monolayers: Elastic mismatch between cells enhances motility. *Sci. Rep.* **5**, 1–13. https://doi.org/10.1038/srep11745 (2015).
28. Marth, W. & Voigt, A. Collective migration under hydrodynamic interactions: A computational approach. Interface Focus **6**, (2016). 1605.06108. https://doi.org/10.1098/rsfs.2016.0037
29. Mueller, R., Yeomans, J. M. & Doostmohammadi, A. Emergence of active nematic behavior in monolayers of isotropic cells. *Phys. Rev. Lett.* **122**, 048004. https://doi.org/10.1103/PhysRevLett.122.048004 (2019).
30. Loewe, B., Chiang, M., Marenduzzo, D. & Marchetti, M. C. Solid-liquid transition of deformable and overlapping active particles. *Phys. Rev. Lett.* **125**, 038003. https://doi.org/10.1103/PhysRevLett.125.038003 (2020).
31. Camley, B. A. *et al.* Polarity mechanisms such as contact inhibition of locomotion regulate persistent rotational motion of mammalian cells on micropatterns. *Proc. Natl. Acad. Sci. U.S.A.* **111**, 14770–14775. https://doi.org/10.1073/pnas.1414498111 (2014).
32. Wenzel, D. & Voigt, A. Multiphase field models for collective cell migration. *Phys. Rev. E* **104**, 054410. https://doi.org/10.1103/PhysRevE.104.054410 (2021).
33. Wenzel, D., Praetorius, S. & Voigt, A. Topological and geometrical quantities in active cellular structures. J. Chem. Phys. **150**, (2019). 1812.10416. https://doi.org/10.1063/1.5085766
34. Jain, H. P., Wenzel, D. & Voigt, A. Impact of contact inhibition on collective cell migration and proliferation. *Phys. Rev. E* **105**, 034402. https://doi.org/10.1103/PhysRevE.105.034402 (2022).

35. Mongera, A. *et al.* A fluid-to-solid jamming transition underlies vertebrate body axis elongation. *Nature* **561**, 401–405. https://doi.org/10.1038/s41586-018-0479-2 (2018).
36. Mongera, A. *et al.* Mechanics of the cellular microenvironment as probed by cells in vivo during zebrafish presomitic mesoderm differentiation. *Nat. Mater.* **22**, 135–143. https://doi.org/10.1038/s41563-022-01433-9 (2023).
37. Smeets, B. *et al.* Emergent structures and dynamics of cell colonies by contact inhibition of locomotion. *Proc. Natl. Acad. Sci.* **113**, 14621–14626. https://doi.org/10.1073/pnas.1521151113 (2016).
38. Stramer, B. & Mayor, R. Mechanisms and in vivo functions of contact inhibition of locomotion. *Nat. Rev. Mol. Cell Biol.* **18**, 43–55. https://doi.org/10.1038/nrm.2016.118 (2017).
39. Peyret, G. *et al.* Sustained oscillations of epithelial cell sheets. *Biophys. J* . **117**, 464–478. https://doi.org/10.1016/j.bpj.2019.06.013 (2019).
40. Park, J. A. et al. Unjamming and cell shape in the asthmatic airway epithelium. Nat. Mater. 2014 14:10 **14**, 1040–1048, (2015). https://doi.org/10.1038/nmat4357
41. Rosa, M. E. & Fortes, M. A. Nucleation and glide of dislocations in a monodisperse two-dimensional foam under uniaxial deformation. *Philos. Mag. A* **77**, 1423–1446. https://doi.org/10.1080/01418619808214261 (1998).
42. Doostmohammadi, A., Ignés-Mullol, J., Yeomans, J. M. & Sagués, F. Active nematics. Nat. Commun. **9**, (2018). https://doi.org/10.1038/s41467-018-05666-8
43. Wenzel, D., Nestler, M., Reuther, S., Simon, M. & Voigt, A. Defects in active nematics - algorithms for identification and tracking. *Comput. Method Appl. Math.* **21**, 683–692. https://doi.org/10.1515/cmam-2020-0021 (2021).
44. Alert, R., Casademunt, J. & Joanny, J.-F. Active turbulence. *Ann. Rev. Cond. Matter Phys.* **13**, 143–170. https://doi.org/10.1146/annurev-conmatphys-082321-035957 (2022).
45. Marth, W., Aland, S. & Voigt, A. Margination of white blood cells: A computational approach by a hydrodynamic phase field model. J. Fluid Mech. **790**, 389–406, https://doi.org/10.1017/jfm.2016.15 (2016). 1507.01544.
46. Praetorius, S. & Voigt, A. Collective cell behaviour - a cell-based parallelisation approach for a phase field active polar gel model. In NIC Ser., 49, 369–376 (Forschungszentrum Jülich GmbH, Zentralbibliothek, Jülich, 2018).
47. Vey, S. & Voigt, A. AMDiS: Adaptive multidimensional simulations. *Comput. Vis. Sci.* **10**, 57–67. https://doi.org/10.1007/s00791-006-0048-3 (2007).
48. Witkowski, T., Ling, S., Praetorius, S. & Voigt, A. Software concepts and numerical algorithms for a scalable adaptive parallel finite element method. *Adv. Comput. Math.* **41**, 1145–1177. https://doi.org/10.1007/s10444-015-9405-4 (2015).

Acknowledgements

This project has received funding from the European Union's Horizon 2020 research and innovation programme under the Marie Skłodowska-Curie grant agreement No 945371. We acknowledge computing resources provided within project WIR at ZIH at TU Dresden.

Author contributions

H.P.J. implemented the codes, performed all simulations, analysed data and contributed to conceptual development and manuscript writing. A.V. and L.A. contributed to supervision, conceptual development, data analysis and manuscript writing.

Competing interests

The authors declare no competing interests.

Additional information

Supplementary Information The online version contains supplementary material available at https://doi.org/10.1038/s41598-023-37064-6.

Correspondence and requests for materials should be addressed to H.P.J.

Reprints and permissions information is available at www.nature.com/reprints.

Publisher's note Springer Nature remains neutral with regard to jurisdictional claims in published maps and institutional affiliations.

Open Access This article is licensed under a Creative Commons Attribution 4.0 International License, which permits use, sharing, adaptation, distribution and reproduction in any medium or format, as long as you give appropriate credit to the original author(s) and the source, provide a link to the Creative Commons licence, and indicate if changes were made. The images or other third party material in this article are included in the article's Creative Commons licence, unless indicated otherwise in a credit line to the material. If material is not included in the article's Creative Commons licence and your intended use is not permitted by statutory regulation or exceeds the permitted use, you will need to obtain permission directly from the copyright holder. To view a copy of this licence, visit http://creativecommons.org/licenses/by/4.0/.

© The Author(s) 2023

Paper II

From cell intercalation to flow, the importance of T1 transitions

From cell intercalation to flow, the importance of T1 transitions

Harish P. Jain [1,*] Axel Voigt,[2,3,4] and Luiza Angheluta [1]
[1]*Njord Centre, Physics Department, University of Oslo, Oslo, Norway*
[2]*Institute of Scientific Computing, TU Dresden, 01069 Dresden, Germany*
[3]*Center for Systems Biology Dresden, Pfotenhauerstr. 108, 01307 Dresden, Germany*
[4]*Cluster of Excellence, Physics of Life, TU Dresden, Arnoldstr. 18, 01307 Dresden, Germany*

(Received 28 March 2024; accepted 15 July 2024; published 15 August 2024)

T1 transitions, also called cell intercalations, are important sources of fluidization of epithelial cell monolayers. We use a multiphase field model to quantify this tissue fluidization in terms of the relative dispersion of cells and characterize the T1 flow profile. We show that the ensemble-averaged flow profile of a T1 transition has a saddle-point pattern accompanied by a localized burst in cell speed. Although the temporal evolution of the relative dispersion of cells depends on specific model details, the different dispersion curves collapse robustly onto a linear function of the number of T1 transitions, implying an important connection between T1 transitions and mixing in dense systems.

DOI: 10.1103/PhysRevResearch.6.033176

I. INTRODUCTION

Spontaneous flows within epithelial monolayers play a pivotal role in many biological processes including tissue development, wound healing, angiogenesis, and invasion of cancer cells [1–3]. In confluency, cells may migrate collectively while maintaining contact with their neighboring cells, thus preserving cell-cell junctions [1]. However, cells may also migrate relative to each other through structural rearrangements mediated by local events of remodeling of cell-cell junctions. Three main types of cell rearrangements have been distinguished [4–6]. A T1 transition is an event whereby two neighboring cells move apart while two of their neighbors move toward each other and make contact. This corresponds to an event where one junction disappears while another nucleates at the same site and orthogonal to the initial junction. A T2 transition occurs during extrusion/apoptosis events where cells are eliminated from the monolayer corresponding to vanishing junctions. By contrast, a T3 transition is an event associated with cell division inducing the nucleation of new junctions. Notably, T1 events preserve the total cell count within the monolayer, distinguishing them from T2 and T3 transitions.

T1 transitions have been observed in both epithelial [7] and mesenchymal [8] tissues and are important across different stages of gastrulation and organogenesis [9] as well as during cancer metastasis [10]. Empirical evidence shows that myosin II contributes to the buildup of tension at cell-cell junctions, thereby controlling T1 transitions in epithelial tissues [11,12]. However, the interplay between mechanical and biochemical signaling in these events remains a topic of debate [13]. There have been several studies aimed at characterizing the mechanical influence of T1 transitions in tissues [5,6,14–18] and in simulations [15,19–21].

Tissue flow has been explored mostly using coarse-grained approaches for active nematics, active polar matter, and more generally, for active p-atic liquid crystals, whereby spontaneous flows are influenced by their topological defects [22–24]. Several experimental studies have reported on different discrete orientational order (nematic, polar, or in general, p-atic) of cell tissues, corresponding to different lowest-energy topological defects [24–26]. This system dependency may be attributed to different types of cell lines but may also signal that the system is far from a hydrodynamic limit with a well-defined discrete symmetry, thus making the identification of relevant group symmetries and corresponding topological defects a matter of debate. On the other hand, it is becoming more evident that T1 transitions are important sources of tissue flow [19,27]. Qualitative differences between flows occurring at hydrodynamic scales and those induced by structural rearrangements of cells have been identified by comparing hydrodynamic (continuum) simulations with cell-resolved (discrete) simulations [23,28]. How the flows originating at the discrete cell level influence the tissue flow at hydrodynamic scales is far less explored and understood.

In this paper, we aim to bridge this gap to better understand the generic flow patterns due to cell neighbor rearrangements. Within a multiphase field model for a flat and confluent cell monolayer, as discussed in Sec. II, we can compute the average flow profile of a T1 transition, as presented in Sec. III. We demonstrate that T1 transitions are short-lived events of neighbor exchanges, where the involved cells acquire high-speeds and generate fourfold vorticity with alternating circulation. Within our setup, where the total number of cells and their size are fixed, and by using a Lagrangian approach, we demonstrate in Sec. IV that the cell pair dispersion is

*Contact author: harishpj@fys.uio.no

Published by the American Physical Society under the terms of the Creative Commons Attribution 4.0 International license. Further distribution of this work must maintain attribution to the author(s) and the published article's title, journal citation, and DOI.

mediated solely by T1 transitions. We predict a robust scaling of the mean pair separation with the number of T1 transitions, which hints at a generic mechanism of relative dispersion by structural rearrangements. Concluding remarks are presented in Sec. V.

II. MULTIPHASE FIELD MODEL

We model the confluent cell monolayer using the multiphase field modeling approach as in Refs. [29–34] and as discussed in a recent review [35]. Our specific model formulation follows Ref. [19] and is used to simulate the dynamics of a confluent monolayer of $N = 100$ cells. Each cell is described by a phase field variable ϕ_i, with $i = 1, 2, \ldots, N$, which has the bulk values $\phi_i \approx 1$ inside the cell, $\phi_i \approx -1$ outside it, and with a diffuse interface of width $O(\epsilon)$ between them representing the cell boundary. The phase field ϕ_i follows the conservative dynamics:

$$\partial_t \phi_i + \mathbf{v}_i \cdot \nabla \phi_i = \Delta \frac{\delta \mathcal{F}}{\delta \phi_i}, \tag{1}$$

which preserves the area of a cell (incompressible cells). The diffusive relaxation is controlled by minimization of the free energy functional $\mathcal{F} = \mathcal{F}_{\mathrm{CH}} + \mathcal{F}_{\mathrm{REP}} + \mathcal{F}_{\mathrm{ADH}}$. The free energy contains the Cahn-Hilliard energy in degenerate form [36]:

$$\mathcal{F}_{\mathrm{CH}} = \frac{1}{Ca} \sum_{i=1}^{N} \int_{\Omega} g(\phi_i) \left[\frac{\epsilon}{2} ||\nabla \phi_i||^2 + \frac{1}{4\epsilon} \left(\phi_i^2 - 1\right)^2 \right] d\mathbf{x}, \tag{2}$$

where ϵ controls the interface width, Ca is a parameter for tuning the cell deformability, and

$$g(\phi_i) = \frac{2}{3\sqrt{(\phi_i + 1)^2 (\phi_i - 1)^2}}$$

is a term to prevent bulk diffusion ensuring $\phi_i \in [-1, 1]$, without affecting the asymptotic behavior as $\epsilon \to 0$ [36]. In addition, there are two interaction energies, where

$$\mathcal{F}_{\mathrm{REP}} = \frac{a_r}{2In} \sum_{i=1}^{N} \int_{\Omega} \sum_{j \neq i} (\phi_i + 1)^2 (\phi_j + 1)^2 d\mathbf{x} \tag{3}$$

is the repulsion energy to prevent overlap of cell interior, and

$$\mathcal{F}_{\mathrm{ADH}} = \frac{a_a}{2In} \sum_{i=1}^{N} \int_{\Omega} \sum_{j \neq i} \left(\phi_i^2 - 1\right)^2 \left(\phi_j^2 - 1\right)^2 d\mathbf{x} \tag{4}$$

is the adhesion energy that promotes overlap of cell boundaries. In denotes the interaction strength, and a_r and a_a are parameters to tune contribution of repulsion and adhesion energy, respectively. The adhesive part differs from Ref. [19] by rewriting the interaction using the equilibrium condition $\frac{\epsilon}{2} \|\nabla \phi_i\|^2 \approx \frac{1}{4\epsilon} (\phi_i^2 - 1)^2$, see Refs. [33,37–40].

Cell activity is introduced as self-propulsion of each cell through the advection term. The cell advection field is given as

$$\mathbf{v}_i(\mathbf{x}, t) = v_0 \mathbf{e}_i(t) \hat{\phi}_i(\mathbf{x}, t), \tag{5}$$

where v_0 is used to tune the magnitude of activity:

$$\hat{\phi}_i = \frac{\phi_i + 1}{2}, \tag{6}$$

TABLE I. Default values of the model parameters. dt denotes the time step size.

L	T	ϵ	v_0	Ca	In	a_a	a_r	D_r	α	r_{active}	dt
100	150	0.15	0.5	0.2	0.1	1	1	0.01	0.1	1	0.005

and $\mathbf{e}_i = [\cos\theta_i(t), \sin\theta_i(t)]$ is the direction of self-propulsion. The migration orientation $\theta_i(t)$ evolves diffusively with a drift that aligns with the principal axis of cell elongation as

$$d\theta_i = \sqrt{2D_r} dW_i(t) + \alpha[\beta_i(t) - \theta_i(t)]dt, \tag{7}$$

where D_r is the rotational diffusivity, and W_i is the Wiener process.

The cell elongation is identified by the principal eigenvector $\boldsymbol{\eta}_i^+$ of the shape deformation tensor, as described in Ref. [34]. Here, $\beta_i(t)$ is the orientation of the cell elongation and defined as

$$\beta_i(t) = \begin{cases} \arg[\boldsymbol{\eta}_i^+(t)] : \mathbf{e}_i(t) \cdot \eta_i^+(t) > 0 \\ -\arg[\boldsymbol{\eta}_i^+(t)] : \mathbf{e}_i(t) \cdot \eta_i^+(t) < 0. \end{cases} \tag{8}$$

The parameter α controls the time scale of this alignment. Setting $v_0 = 0$ for some cells allows for the modeling of a mixture of active self-propelled cells and passive cells. The activity ratio r_{active} is the fraction of cells for which $v_0 > 0$.

Equation (1) is solved numerically on a square domain $\Omega = [0, L] \times [0, L]$ (where $L = 100$) using periodic boundary conditions for the time $[0, T]$. We are using the finite element method within the toolbox AMDiS [41,42] and the parallelization concept introduced in Ref. [43], which considers each cell on a different core and accounts for short-range interaction between cells to reduce the communication. The system of partial differential equations is discretized in time using a semi-implicit approach. Time step size and mesh resolution are related to ensure stability. For further details and numerical tests, see earlier work from Refs. [19,35,38].

The values of the model parameters are listed in Table I, unless specified otherwise. Movie 1 in the Supplemental Material (SM) [44] shows the cell boundaries in a simulation as per parameters in Table I.

III. FLOW PROFILE OF T1 TRANSITIONS

A T1 transition reconfigures the junctions between neighboring cells as illustrated in Figs. 1(a)–1(c). The two three-way vertices represented by red dots move toward each other, shrinking the corresponding junction [Fig. 1(a)]. Within multiphase field models, T1 transitions occur spontaneously as cells deform and move as a result of activity. Further, in multiphase field models, a T1 transition has a finite duration [19] that starts when the junction vanishes, creating a transient extracellular gap (approximated as a four-way vertex), as shown in Fig. 1(b). The T1 transition concludes when a new pair of three-way vertices nucleate, forming a new junction, as in Fig. 1(c). We define the orientation ζ of a T1 transition as the angle of the newly formed junction with respect to the x axis. We use this angle ζ to reorient different T1

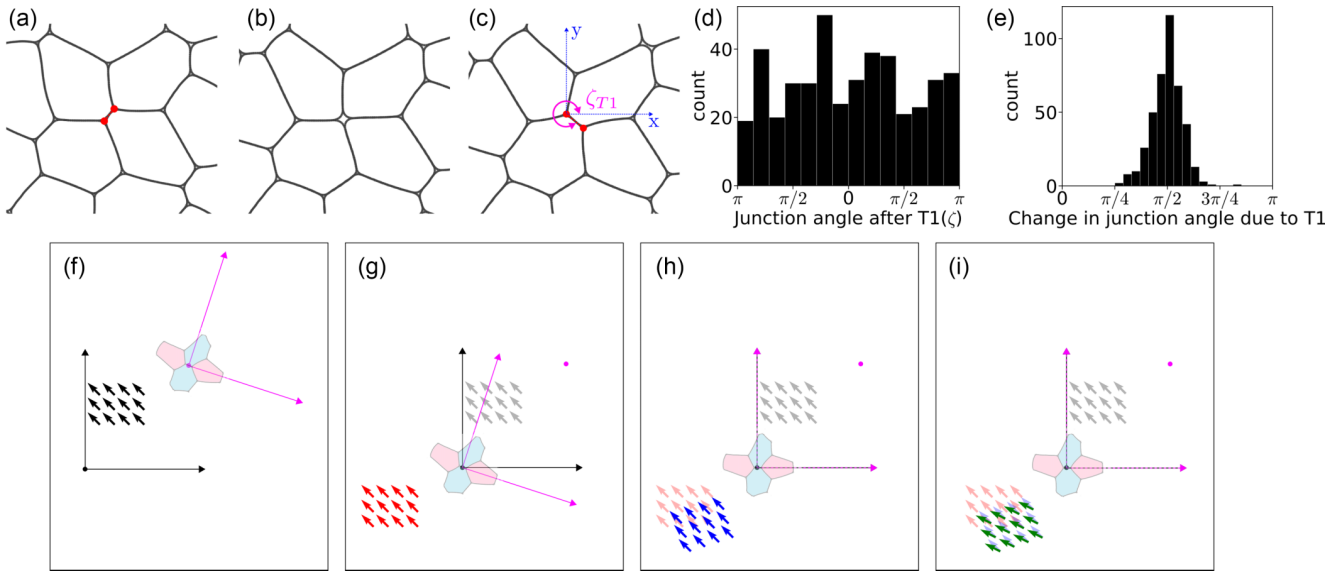


FIG. 1. Configuration of four cells (a) before, (b) during, and (c) after a T1 transition. The three-way vertices involved in the T1 are marked by red dots. Junction angle ζ is the orientation of the newly formed junction after a T1 transition measured counterclockwise from the positive x semiaxis. (d) Histogram of the junction angle after a T1 transition ζ. (e) Histogram of change in junction angle due to the T1 transition. Steps involved in transformation of the velocity field to align it with respect to a T1 transition: (f) A small section of a field is shown in black. A T1 transition is shown with the cells that lose neighbors colored in pink, while the cells that gain neighbors are colored in blue. A magenta reference frame is attached to the epicenter of the T1 and is aligned with the orientation of the T1, ζ. (g) The epicenter is shifted to the origin. (h) The frame is rotated to align with the horizontal axis. (i) The orientation of the vector field is rotated by ζ_{T1}.

transitions and their velocity profiles to compute ensemble-averaged transient flows, as described next.

A. Ensemble average

We start by computing the T1 orientation angle ζ_m of the mth T1 transition in an ensemble of N_{T1} T1 events.

Let us denote the four cells associated with one T1 transition by A, B, C, and D. Before a T1, let the list of cell neighbor pairs be

$$\text{Before T1: } (A,B),\ (A,C),\ (A,D),\ (C,B),\ (D,B).$$

Suppose, at the start of a T1 transition, cells A and B lose contact, and at the end of the T1 transition, cells C and D make contact. This changes the cell neighbor list to

$$\text{After T1: } (C,D),\ (A,C),\ (A,D),\ (C,B),\ (D,B).$$

We denote the start and end times of the mth T1 transition as $t_{m,s}$ and $t_{m,e}$, respectively. Before $t_{m,s}$, the three-way vertices where the cells (A,B,C) and (A,B,D) meet move toward each other, shrinking the common junction between them, and eventually, the junction vanishes at $t_{m,s}$. Between $t_{m,s}$ and $t_{m,e}$, there is an extracellular gap between the four cells. After $t_{m,e}$, two new three-way vertices where the cells (A,C,D) and (B,C,D) meet are created, and they move away from each other. Let $\mathbf{s}_{m,1}$ and $\mathbf{s}_{m,2}$ be the positions of the two three-way vertices a short time after $t_{m,e}$. The orientation of the new junction between $\mathbf{s}_{m,1}$ and $\mathbf{s}_{m,2}$ is $\zeta_m = \arg(\mathbf{s}_{m,1} - \mathbf{s}_{m,2})$. This is also illustrated in Fig. 1(c). Similarly, we can also compute the orientation of the old junction before the mth T1 transition. Figure 1(d) shows the histogram of the orientations of N_{T1} T1 transitions, which implies that the orientations of the T1 transitions are close to being uniformly distributed. Figure 1(e) shows the histogram of the difference in junction angle before and after the T1 transition. The histogram peaks at around $\pi/2$, implying that the junctions before and after a T1 transition are mostly perpendicular to each other.

For each T1 transition, we also find the location of its epicenter as we have done in Ref. [19]. The epicenter is defined as the location of a point whose sum of distances to the four cells involved in the T1 transition is the minimum, at the midpoint time $\frac{t_{m,s}+t_{m,e}}{2}$. We denote the location of the epicenter of the mth T1 transition by $\mathbf{s}_{m,c}$. Essentially, this point lies within the gap formed between the four cells during the T1 transition.

At any given time t, we define the global velocity field as

$$\mathbf{v}_g(\mathbf{x},t) = \sum_{i=1}^{N} \hat{\phi}_i(\mathbf{x},t)\frac{\mathbf{r}_i(t) - \mathbf{r}_i(t-dt)}{dt}, \tag{9}$$

where $\mathbf{r}_i(t)$ is the location of the center of the ith cell at time t, and dt is the time step size. Therefore, $\mathbf{v}_g(\mathbf{x},t)$ in the interior of a cell is equal to the velocity of the center of mass of the cell.

For the mth T1 transition, at any time t, we can transform the global field to obtain its *T1 flow velocity field* as

$$\mathbf{v}_m(\mathbf{x},t) = \mathbf{R}_{\zeta_m}\mathbf{v}_g[\mathbf{R}_{\zeta_m}(\mathbf{x} - \mathbf{s}_{m,c}),t], \tag{10}$$

where $\mathbf{R}_{\zeta_m}$ is the two-dimensional (2D) rotation matrix with rotation angle ζ_m. This $\mathbf{v}_m(\mathbf{x},t)$ is centered such that the epicenter is at the origin, and the junction formed after the T1 transition is aligned along the horizontal axis. Figures 1(f)–1(i) visualize the transformation from $\mathbf{v}_g(\mathbf{x},t)$

to $\mathbf{v}_m(\mathbf{x}, t)$ in three steps for an arbitrary field: (i) the field is translated such that the origin coincides with the epicenter of the T1 transition; (ii) the grid is rotated such that the junction formed after the T1 transition aligns along the horizontal axis; and (iii) the vectors themselves are rotated while being fixed in space to reflect the right orientation with respect to the epicenter. Periodic boundary conditions are considered while transforming the fields by numerically wrapping the computational domain.

Let an arbitrary field f at time τ before and after a T1 transition be denoted by $f(\mathbf{x}, t_{m,s} - \tau)$ and $f(\mathbf{x}, t_{m,e} + \tau)$, respectively. We consider the ensemble average over the N_{T1} transitions measured at time relative to the start or end of a T1 transition as $\langle f(t_{m,e/s} \pm \tau)\rangle = \frac{1}{N_{T1}} \sum_{m=1}^{N_{T1}} f(t_{m,e/s} \pm \tau)$. With this, we define the average of the T1 flow velocity field at time τ after/before T1 as

$$\mathbf{v}_{T1}^{\pm}(\mathbf{x}, \tau) = \langle \mathbf{v}_m(\mathbf{x}, t_{m,e/s} \pm \tau)\rangle. \tag{11}$$

Similarly, the average magnitude of the T1 flow velocity field at τ is given as

$$\overline{v}_{T1}^{\pm}(\mathbf{x}, \tau) = \langle |\mathbf{v}_m(\mathbf{x}, t_{m,e/s} \pm \tau)|\rangle. \tag{12}$$

To further explore the directional motion, we define the average velocity polarization field as

$$\mathbf{p}_{T1}^{\pm}(\mathbf{x}, \tau) = \left\langle \frac{\mathbf{v}_m(\mathbf{x}, t_{m,e/s} \pm \tau)}{|\mathbf{v}_m(\mathbf{x}, t_{m,e/s} \pm \tau)|} \right\rangle, \tag{13}$$

such that $|\mathbf{p}_{T1}^{\pm}| \in [0, 1]$, where $|\mathbf{p}_{T1}^{\pm}| = 0$ corresponds to randomly oriented T1 flow velocities, and $|\mathbf{p}_{T1}^{\pm}| = 1$ for preferred directional orientation of T1 flow velocities.

In Figs. 2(a) and 2(c) and Figs. 2(b) and 2(d), we plot $\mathbf{v}_{T1}^{-}(\mathbf{x}, 0)$ and $\mathbf{v}_{T1}^{+}(\mathbf{x}, 0)$, respectively. The streamlines suggest that the flow comprises quadrupolar vortices with alternating circulation centered at the epicenter. The flow has a saddle-point structure, allowing us to identify the vertical axis of cells making contact and horizontal axis of cells breaking contact. The time evolution of $\mathbf{v}_{T1}^{-}$ and $\mathbf{v}_{T1}^{+}$ is shown in Movies 2 and 3, respectively in the SM [44]. The magnitudes in Figs. 2(a) and 2(b) correspond to $|\mathbf{p}_{T1}^{-}(\mathbf{x}, 0)|$ and $|\mathbf{p}_{T1}^{+}(\mathbf{x}, 0)|$. The approximate profile of the four cells involved in the T1 transition can be discerned by the high values of $|\mathbf{p}_{T1}|$ around the epicenter. The values of $|\mathbf{p}_{T1}|$ inform on the likelihood of the observed orientation of the streamlines, where a higher polarization indicates that the streamlines shown are more likely to occur. The low values of $|\mathbf{p}_{T1}|$ away from the epicenter suggest that cells that are not involved in a T1 do not have a preferred velocity orientation. The magnitudes in Figs. 2(c) and 2(d) correspond to $\overline{v}_{T1}^{-}$ and $\overline{v}_{T1}^{+}$. From Fig. 2(c), we discern that, at the end of a T1 transition, there is a localized surge of speed around the epicenter, suggesting cells involved in a T1 transition move faster than the rest of the cells in the monolayer. From Movie 5 in the SM [44], we see that the speed in the vicinity of the epicenter decays over time to the global average. Before a T1 transition, there is no such surge in $\overline{v}_{T1}$ observed near the epicenter (see Movie 4 in the SM [44]). These results are consistent with those in Ref. [19], where similar results were obtained for the evolution of average speed of the four cells involved in a T1 transition. It would be interesting to compare these flow profiles with the characteristic flow field of defects in coarse-grained active nematics, polar, or more generally, in active p-atic liquid crystals. The corresponding hydrodynamic models have been proposed in Refs. [45,46].

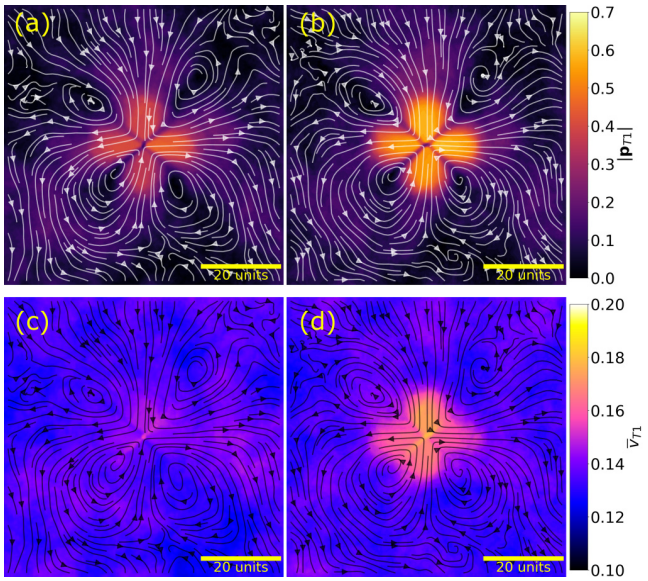


FIG. 2. Ensemble-averaged flow profile of T1 transitions. Streamlines in (a) and (c) correspond to flow at the start of a T1 transition $[\mathbf{v}_{T1}^{-}(\mathbf{x}, 0)]$, and those in (b) and (d) correspond to flow at the end of a T1 transition $[\mathbf{v}_{T1}^{+}(\mathbf{x}, 0)]$. Magnitude of the colormap in (a) and (b) correspond to $|\mathbf{p}_{T1}^{-}(\mathbf{x}, 0)|$ and $|\mathbf{p}_{T1}^{+}(\mathbf{x}, 0)|$. Magnitude of the colormap in (c) and (d) correspond to $\overline{v}_{T1}^{-}(\mathbf{x}, 0)$ and $\overline{v}_{T1}^{+}(\mathbf{x}, 0)$. The cell size (square root of cell area) is ∼10 units. The time evolution of these fields is shown in Movies 2–5 in the SM [44].

The source of this tissue flow is ultimately linked to the dispersion of cell motion. Cells that are caged among their neighbors undergo small shape fluctuations and experience resistance to their motion due to cell-cell interactions. However, these small fluctuations may build up and can bring two three-way vertices closer together. This leads to the accumulation of energy near those vertices. Eventually, this can induce a T1 transition releasing energy, thereby helping the cells to uncage. This is akin to the buildup prior to a slip event in stick-slip dynamics [47]. Provided there is no preferred orientation of the T1 transition [see Fig. 1(d)], the cells move away from their initial neighbors and disperse across the tissue. In the next section, we quantify the statistical properties of cell dispersion.

IV. CELL DISPERSION

The vortical flow induced by T1 transitions is reflected in the dispersion of cells relative to each other and thus in the mixing of cells. We can quantify the flow properties indirectly through the relative dispersion of cells. We use the center of mass denoted by $\mathbf{r}_i$ for the ith cell to track cell migration. The mean-squared displacement of the cells quantifies the single particle dispersion and is given as

$$\sigma^2(t) = \frac{1}{N} \sum_{i=1}^{N} |\mathbf{r}_i(t + t_0) - \mathbf{r}_i(t_0)|^2, \tag{14}$$

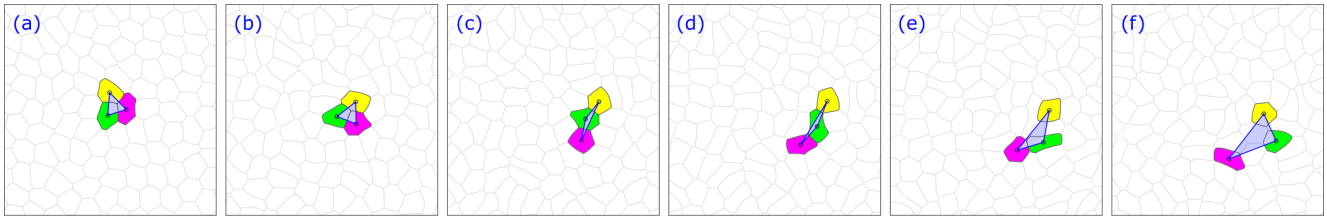


FIG. 3. Temporal snapshots of the evolution of a cell triplet. T1 transitions break the contact between cells in the triplet and increase the area spanned by the triplet.

where N is the total number of cells. This measures how far a cell has migrated from its initial location at t_0 in a time lag t. Similarly, the mean pair separation distance in a time lag t quantifies the relative dispersion and is defined as

$$\Pi(t) = \frac{1}{N_P(t_0)} \sum_{j=1}^{N_P(t_0)} |\mathbf{r}_{j,1}(t) - \mathbf{r}_{j,2}(t)|, \tag{15}$$

where $N_P(t_0)$ is the number of pairs of cells that were neighbors at an initial time t_0. Here, $\mathbf{r}_{j,1}$ and $\mathbf{r}_{j,2}$ are the positions of the two cells corresponding to the jth neighbor pair at t_0. To better quantify the dynamics of the three-way vertices, we also consider the dispersion of triplets. A triplet consists of three cells where each cell is a neighbor to the other two cells. Let $\mathbf{r}_{k,1}$, $\mathbf{r}_{k,2}$, and $\mathbf{r}_{k,3}$ be the positions of the three cells corresponding to the kth triplet. The corresponding lengths of the edges in the triplet triangle are $\bar{a} = |\mathbf{r}_{k,1} - \mathbf{r}_{k,2}|$, $\bar{b} = |\mathbf{r}_{k,2} - \mathbf{r}_{k,3}|$, and $\bar{c} = |\mathbf{r}_{k,3} - \mathbf{r}_{k,1}|$. Given the perimeter of the triangle $\bar{s} = \bar{a} + \bar{b} + \bar{c}$, the triangle area of the kth triplet is $A_k = \bar{s}(\bar{s} - \bar{a})(\bar{s} - \bar{b})(\bar{s} - \bar{c})$. Thus, we can also define the mean triplet separation area as

$$\Lambda(t) = \frac{1}{N_T(t_0)} \sum_{k=1}^{N_T(t_0)} A_k(t + t_0), \tag{16}$$

where $N_T(t_0)$ is the number of triplets of cells at time t_0. Here, $\Lambda(t)$ is the average area of all triangles made by a triplet of cells that were mutually adjacent at time t_0. Snapshots from the evolution of one such triplet triangle are shown in Fig. 3. Geometrically, the dispersion of cells is associated with deformations, translations, and rotations of the triplet triangle. See Appendix A for details on handling the periodic boundary conditions.

The initial area of the triplet triangles is nonzero and is related to the cell size. Notice that the cells remain mutually adjacent for a transient time until the three-way vertex shared between them is destroyed in a T1 transition by merging with another three-way vertex. From hereon, the cells are likely to further separate from each other due to subsequent T1 transitions. The triplet area can also collapse to zero when the three cells become collinear [see Figs. 3(c) and 3(d)].

Figures 4(a)–4(c) show the mean-squared displacement (σ^2) and relative dispersion of pairs (Π) and triplets (Λ) as

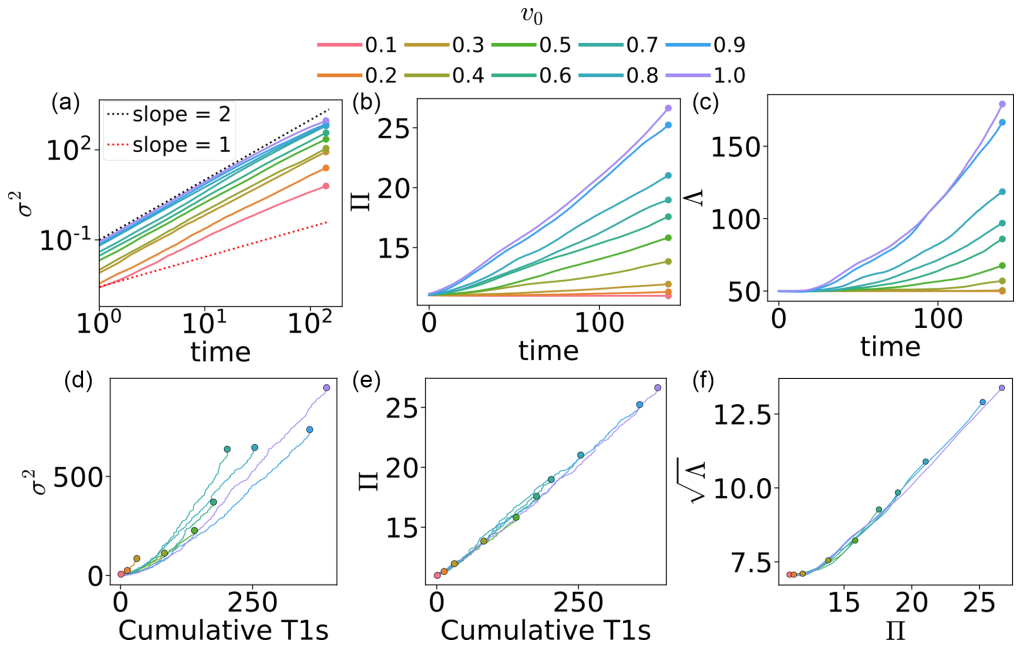


FIG. 4. Evolution of (a) σ^2, (b) Π, and (c) Λ plotted against time. (d) σ^2 and (e) Π plotted against the cumulative number of T1 transitions within the tissue. (f) $\sqrt{\Lambda}$ plotted against Π. Different colors correspond to different cell activities defined by the self-propulsion speed v_0 as per the legend at the top.

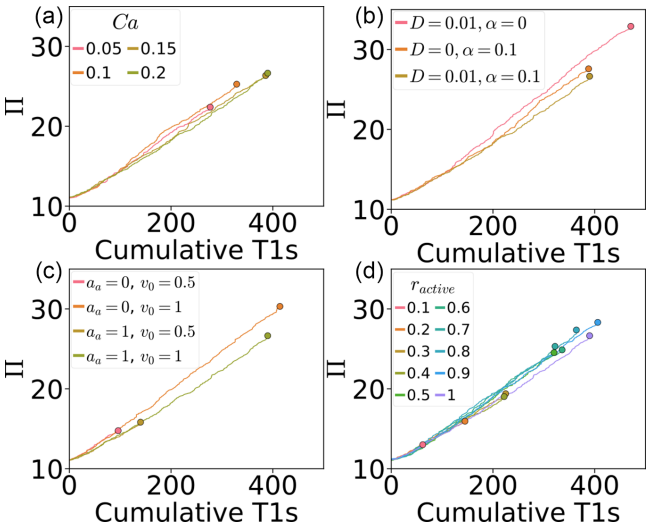


FIG. 5. Data collapse of the relative dispersion curves as a function of the cumulative T1 transitions for various model parameters and setups: (a) Cell deformability (Ca) is varied for $v_0 = 1$. (b) Rotational noise D and shape alignment α are varied for $v_0 = 1$. (c) Repulsion vs repulsion and adhesion cell-cell interaction. (d) Mixtures of active and passive cells with a fraction r_{active} of active cells with $v_0 = 1$.

functions of time lag t for different activities v_0. Within the computational time, we observe that the cells are superdiffusive with a scaling exponent that lies between 1 (normal diffusion limit) and 2 (ballistic limit). For all three quantities, their values at a given time lag increase with cell activity, which is consistent with the observation that the flow fluctuations increase with activity [22] (see also Appendix C). At low activities, we notice that there is almost no dispersion of cell pairs and triplets. While the pair separation Π increases with time lag, the triplet area $\Lambda(t)$ remains constant for a initial transient period. A single T1 transition would destroy the three-way vertex shared by the cells in the triplet, but two pairs out of three initial pairs in the triplet remain. The triplet area starts to diverge when at least one of the cells breaks contact with the other two cells in the triplet, which requires a minimum of two T1 transitions (see Appendix B). Thus, in this initial period, the area of the triplet triangle $A_k(t)$ fluctuates around $A_k(t_0)$. As the cells undergo further T1 transitions and move apart, the area spanned by the triplet Λ increases monotonically with the time lag.

Figures 4(d) and 4(e) show the net dispersion of single cells $[\sigma^2(t)]$ and cell pairs $[\Pi(t)]$ plotted against the cumulative number of T1 transitions within the tissue in time lag t. Interestingly, the curves for Π for different v_0 collapse into a linear master curve. A similar collapse is also present for the triplet area, which shows that these two quantities are directly related to the number of T1 transitions. However, this is not the case for σ^2 because cells can also migrate in local flocks, which affects σ^2 but does not change Π and Λ since the cell-cell connectivity is preserved [1]. In the absence of T1 transitions, cells are topologically caged within their neighbors, and this makes it difficult to generate flow fluctuations (when T2 and T3 transitions are also absent). It takes ∼250 T1 transitions across the tissue of 100 cells, or equivalently 10 T1 transitions per cell, for the mean pair separation to double its value. Two neighboring cells must undergo ∼10 T1 transitions each, such that their cell centers can be two cell widths apart. When $\sqrt{\Lambda}$ is plotted against Π, initially, $\sqrt{\Lambda}$ is constant, and later, it varies linearly with Π [see Fig. 4(f)].

To further explore the robustness of this data collapse, we also vary other model parameters, i.e., cell deformability Ca, rotational noise D, shape alignment α, adhesion parameter a_a, and activity ratio r_{active}. For high values of Ca, the cells are more deformable. The rotational diffusion coefficient D and the rate α at which cells tend to align their preferred direction of motion with the direction of their elongation control the dynamics of the self-propulsion mechanism. For $a_a = 0$, the interactions between cells are purely repulsive, while $a_a > 0$ corresponds to additional attractive interaction between cells. Here, r_{active} is the fraction of cells which have nonzero activity. The mean pair separation distance as a function of cumulative number of T1 transitions for these scenarios is plotted in Fig. 5. In all these scenarios, we see similar scaling behavior, suggesting that T1 transitions affect relative dispersion in similar ways irrespective of model parameters.

V. DISCUSSION AND CONCLUSIONS

In summary, we have put forward a quantitative way to study the connection between T1 transitions, tissue fluidization, and cell dispersion. We have shown that T1 transitions, as topological events of neighbor exchanges, are transient and localized saddle-point flows generating fourfold vortices. The average polarization is high and localized along the principal axes of the saddle point centered at the epicenter of a T1 transition, showing that there is persistent directional flow along these directions which feeds to vortical flow over longer distances. Such flows could possibly contribute to active turbulence within the monolayer [22].

We have demonstrated that tissue flows where cells disperse relative to each other are promoted solely by T1 transitions. While the temporal behavior of the cell dispersion (single, pair, or triplet) depends on the model parameters, we found a robust linear dependence of the relative dispersion of pairs and triplets of cells on the number of T1 transitions. The data collapse of the different dispersion curves onto a linear master curve suggests that the rate of relative dispersion is directly proportional to the occurrence rate of T1 transitions regardless of the underlying nucleation mechanism. This unveils a deeper connection between topological rearrangements and mixing in densely packed systems, in general. As relative dispersion and the number of T1 transitions are measurable observables also in experimental studies of epithelial cell monolayers, our model predictions are accessible for future experimental validation.

ACKNOWLEDGMENTS

L.A. and H.P.J. acknowledge funding by the European Union's Horizon 2020 research and innovation programme under the Marie Skłodowska-Curie Grant Agreement No. 945371. A.V. acknowledges funding by the German Research Foundation within Grant No. FOR3013. We are grateful for

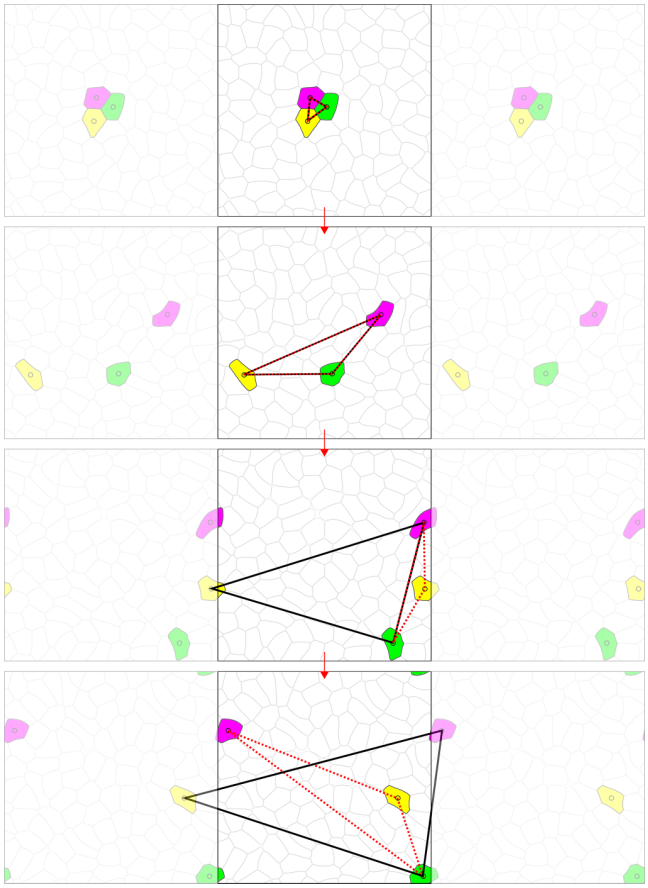


FIG. 6. The triangle with red-dotted sides is connected to the cells in the computational domain, while the triangle with black sides is connected to the location of the cells in an infinite two-dimensional (2D) domain. Time evolves from top to bottom.

discussions with Amin Doostmohammadi, Richard D. J. G. Ho, Per Arne Rikvold, and Dag K. Dysthe.

APPENDIX A: PERIODIC BOUNDARY CONDITIONS

While the general notion of periodic boundary conditions is standard, the definition of the mean dispersion of a single cell (σ^2), cell pairs (Π), and triplets (Λ) requires some additional thought. We essentially assume that, when a cell crosses the periodic boundary, it moves into an identical but distinct copy of the domain that lies adjacent to the domain, as illustrated in Fig. 6. The history of the cell motion is used to determine the modified location of center of mass in the resulting infinite domain.

APPENDIX B: TRIAD DISPERSION

Figure 7 shows an illustration of a section of a hexagonal lattice comprising hexagonal cells. A triangle is marked that joins the cell centers of the three red cells. In the left figure, all three cells are mutually adjacent, while on the right figure, two of the three cells are not in contact. The areas of the triangles are the same in both situations. For a triplet area to diverge significantly, at least one of the three cells must break contact

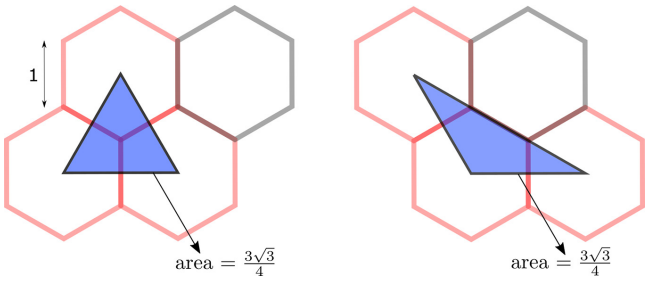


FIG. 7. A triangle joining 3 red cells is shown when (left) all 3 cells are mutually adjacent and (right) one pair are not neighbors.

from the other two cells. This is why, multiple T1 transitions per triplet are required before the mean triplet separation area (λ) starts to increase significantly.

APPENDIX C: GLOBAL STATISTICS

Figures 8(a) and 8(b) show the single-particle dispersion $[\sigma(T)]$ and relative dispersion $[\Pi(T)]$ at a given time lag T as a function of cell activity v_0 and deformability Ca. Both quantities increase monotonically with v_0; only the relative dispersion is sensitive to Ca. This suggests that, on average, cells tend to spread out at the same rate regardless of whether they are stiffer or softer. Nonetheless, stiffer cells tend to disperse less relative to each other than softer cells. To quantify, the collective flocking motion of the cells, we compute the global polar order at a given time as

$$\psi(t) = \frac{1}{N}\left|\sum_{i=1}^{N}\frac{[\mathbf{r}_i(t) - \mathbf{r}_i(t')]}{t - t'}\right|, \tag{C1}$$

such that $\psi(t) \approx 1$ corresponds to cells moving as a flock in the same direction, while $\psi(t) \approx 0$ represents cells moving uncoordinatedly and in random directions. In Fig. 8(c), we see the flocking tendency is higher for stiffer cells. This is

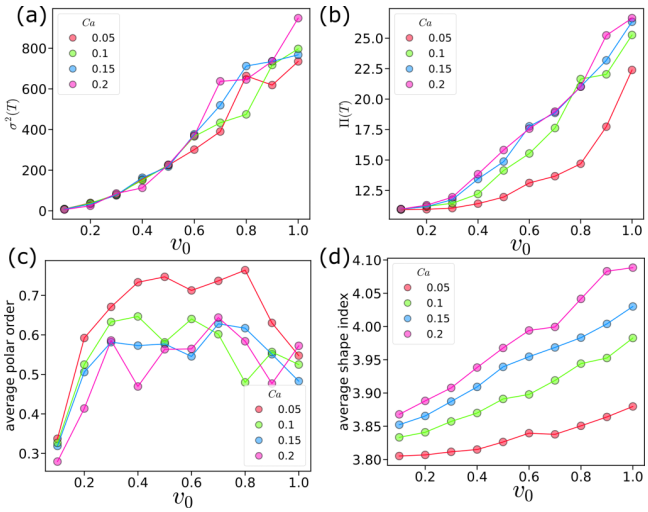


FIG. 8. (a) Mean-squared displacement and (b) mean pair separation for the time lag $T = 150$. (c) Average polar order. (d) Average shape index.

consistent with their tendency to preserve their neighbors (disperse less relative to each other) that helps coordinate their motion better. In Fig. 8(d), we see that the average cell shape index, defined by the ratio of the perimeter of cells to the square root of area of the cells, also increases monotonically with activity and cell deformability.

[1] B. Ladoux and R. M. Mège, Mechanobiology of collective cell behaviours, Nat. Rev. Mol. Cell Biol. **18**, 743 (2017).

[2] A. Brugués, E. Anon, V. Conte, J. H. Veldhuis, M. Gupta, J. Colombelli, J. J. Muñoz, G. W. Brodland, B. Ladoux, and X. Trepat, Forces driving epithelial wound healing, Nat. Phys. **10**, 683 (2014).

[3] P. Friedl, J. Locker, E. Sahai, and J. E. Segall, Classifying collective cancer cell invasion, Nat. Cell Biol. **14**, 777 (2012).

[4] D. Weaire, F. Bolton, T. Herdtle, and H. Aref, The effect of strain upon the topology of a soap froth, Philos. Mag. Lett. **66**, 293 (1992).

[5] R. Etournay, M. Popović, M. Merkel, A. Nandi, C. Blasse, B. Aigouy, H. Brandl, G. Myers, G. Salbreux, F. Jülicher *et al.*, Interplay of cell dynamics and epithelial tension during morphogenesis of the *Drosophila* pupal wing, eLife **4**, e07090 (2015).

[6] B. Guirao, S. U. Rigaud, F. Bosveld, A. Bailles, J. López-Gay, S. Ishihara, K. Sugimura, F. Graner, and Y. Bellaïche, Unified quantitative characterization of epithelial tissue development, eLife **4**, e08519 (2015).

[7] K. D. Irvine and E. Wieschaus, Cell intercalation during *Drosophila* germband extension and its regulation by pair-rule segmentation genes, Development **120**, 827 (1994).

[8] R. Keller, L. Davidson, A. Edlund, T. Elul, M. Ezin, D. Shook, and P. Skoglund, Mechanisms of convergence and extension by cell intercalation, Philos. Trans. R. Soc. Lond. B **355**, 897 (2000).

[9] E. Walck-Shannon and J. Hardin, Cell intercalation from top to bottom, Nat. Rev. Mol. Cell Biol. **15**, 34 (2014).

[10] L. Oswald, S. Grosser, D. M. Smith, and J. A. Käs, Jamming transitions in cancer, J. Phys. D **50**, 483001 (2017).

[11] C. Bertet, L. Sulak, and T. Lecuit, Myosin-dependent junction remodelling controls planar cell intercalation and axis elongation, Nature (London) **429**, 667 (2004).

[12] M. Takeichi, Dynamic contacts: Rearranging adherens junctions to drive epithelial remodelling, Nat. Rev. Mol. Cell Biol. **15**, 397 (2014).

[13] M. Rauzi, Cell intercalation in a simple epithelium, Philos. Trans. R. Soc. B **375**, 20190552 (2020).

[14] M. Rauzi, P. Verant, T. Lecuit, and P.-F. Lenne, Nature and anisotropy of cortical forces orienting *Drosophila* tissue morphogenesis, Nat. Cell Biol. **10**, 1401 (2008).

[15] G. B. Blanchard, A. J. Kabla, N. L. Schultz, L. C. Butler, B. Sanson, N. Gorfinkiel, L. Mahadevan, and R. J. Adams, Tissue tectonics: Morphogenetic strain rates, cell shape change and intercalation, Nat. Methods **6**, 458 (2009).

[16] B. Aigouy, R. Farhadifar, D. B. Staple, A. Sagner, J.-C. Röper, F. Jülicher, and S. Eaton, Cell flow reorients the axis of planar polarity in the wing epithelium of Drosophila, Cell **142**, 773 (2010).

[17] S. Curran, C. Strandkvist, J. Bathmann, M. de Gennes, A. Kabla, G. Salbreux, and B. Baum, Myosin II controls junction fluctuations to guide epithelial tissue ordering, Dev. Cell **43**, 480 (2017).

[18] S. Kim, M. Pochitaloff, G. A. Stooke-Vaughan, and O. Campàs, Embryonic tissues as active foams, Nat. Phys. **17**, 859 (2021).

[19] H. P. Jain, A. Voigt, and L. Angheluta, Robust statistical properties of T1 transitions in a multi-phase field model of cell monolayers, Sci. Rep. **13**, 10096 (2023).

[20] D. Bi, J. H. Lopez, J. M. Schwarz, and M. L. Manning, A density-independent rigidity transition in biological tissues, Nat. Phys. **11**, 1074 (2015).

[21] D. L. Barton, S. Henkes, C. J. Weijer, and R. Sknepnek, Active vertex model for cell-resolution description of epithelial tissue mechanics, PLoS Comput. Biol. **13**, e1005569 (2017).

[22] R. Alert, J. Casademunt, and J.-F. Joanny, Active turbulence, Annu. Rev. Condens. Matter Phys. **13**, 143 (2022).

[23] A. Doostmohammadi, J. Ignés-Mullol, J. M. Yeomans, and F. Sagués, Active nematics, Nat. Commun. **9**, 3246 (2018).

[24] J.-M. Armengol-Collado, L. N. Carenza, J. Eckert, D. Krommydas, and L. Giomi, Epithelia are multiscale active liquid crystals, Nat. Phys. **19**, 1773 (2023).

[25] G. Duclos, C. Erlenkämper, J.-F. Joanny, and P. Silberzan, Topological defects in confined populations of spindle-shaped cells, Nat. Phys. **13**, 58 (2017).

[26] T. B. Saw, A. Doostmohammadi, V. Nier, L. Kocgozlu, S. Thampi, Y. Toyama, P. Marcq, C. T. Lim, J. M. Yeomans, and B. Ladoux, Topological defects in epithelia govern cell death and extrusion, Nature (London) **544**, 212 (2017).

[27] T. Lecuit and A. S. Yap, E-cadherin junctions as active mechanical integrators in tissue dynamics, Nat. Cell Biol. **17**, 533 (2015).

[28] D. Wenzel, M. Nestler, S. Reuther, M. Simon, and A. Voigt, Defects in active nematics—Algorithms for identification and tracking, Comput. Methods Appl. Math. **21**, 683 (2021).

[29] M. Nonomura, Study on multicellular systems using a phase field model, PLoS ONE **7**, e33501 (2012).

[30] B. A. Camley, Y. Zhang, Y. Zhao, B. Li, E. Ben-Jacob, H. Levine, and W. J. Rappel, Polarity mechanisms such as contact inhibition of locomotion regulate persistent rotational motion of mammalian cells on micropatterns, Proc. Natl. Acad. Sci. USA **111**, 14770 (2014).

[31] J. Löber, F. Ziebert, and I. S. Aranson, Collisions of deformable cells lead to collective migration, Sci. Rep. **5**, 1 (2015).

[32] B. Palmieri, Y. Bresler, D. Wirtz, and M. Grant, Multiple scale model for cell migration in monolayers: Elastic mismatch between cells enhances motility, Sci. Rep. **5**, 11745 (2015).

[33] W. Marth and A. Voigt, Collective migration under hydrodynamic interactions: A computational approach, Interface Focus **6**, 20160037 (2016).

[34] R. Mueller, J. M. Yeomans, and A. Doostmohammadi, Emergence of active nematic behavior in monolayers of isotropic cells, Phys. Rev. Lett. **122**, 048004 (2019).

[35] D. Wenzel and A. Voigt, Multiphase field models for collective cell migration, Phys. Rev. E **104**, 054410 (2021).

[36] M. Salvalaglio, A. Voigt, and S. M. Wise, Doubly degenerate diffuse interface models of surface diffusion, Math. Methods Appl. Sci. **44**, 5385 (2021).

[37] R. Gu, X. Wang, and M. Gunzburger, Simulating vesicle-substrate adhesion using two phase field functions, J. Comput. Phys. **275**, 626 (2014).

[38] H. P. Jain, D. Wenzel, and A. Voigt, Impact of contact inhibition on collective cell migration and proliferation, Phys. Rev. E **105**, 034402 (2022).

[39] L. Shen, P. Lin, Z. Xu, and S. Xu, Diffuse interface model for cell interaction and aggregation with Lennard-Jones type potential, Comput. Methods Appl. Mech. Eng. **415**, 116257 (2023).

[40] L. Happel and A. Voigt, Coordinated motion of epithelial layers on curved surfaces, Phys. Rev. Lett. **132**, 078401 (2024).

[41] S. Vey and A. Voigt, AMDiS: Adaptive multidimensional simulations, Comput. Vis. Sci. **10**, 57 (2007).

[42] T. Witkowski, S. Ling, S. Praetorius, and A. Voigt, Software concepts and numerical algorithms for a scalable adaptive parallel finite element method, Adv. Comput. Math. **41**, 1145 (2015).

[43] S. Praetorius and A. Voigt, *Collective Cell Behaviour—A Cell-Based Parallelisation Approach for a Phase Field Active Polar Gel Model*, NIC Series No. 49 (Forschungszentrum Jülich GmbH, Zentralbibliothek, Jülich, 2018).

[44] See Supplemental Material at http://link.aps.org/supplemental/10.1103/PhysRevResearch.6.033176 for Movie of simulation as per parameters in Table 1, and movies of evolution of $|\mathbf{p}^-_{T1}(\mathbf{x})|$, $|\mathbf{p}^+_{T1}(\mathbf{x})|$, $\bar{v}^-_{T1}(\mathbf{x})$ and $\bar{v}^+_{T1}(\mathbf{x})$.

[45] L. Giomi, J. Toner, and N. Sarkar, Hydrodynamic theory of p-atic liquid crystals, Phys. Rev. E **106**, 024701 (2022).

[46] L. Giomi, J. Toner, and N. Sarkar, Long-ranged order and flow alignment in sheared p-atic liquid crystals, Phys. Rev. Lett. **129**, 067801 (2022).

[47] J. P. Sethna, K. A. Dahmen, and C. R. Myers, Crackling noise, Nature (London) **410**, 242 (2001).

Paper III

Emergent cell migration from cell shape deformations and T1 transitions

Emergent cell migration from cell shape deformations and T1 transitions

Harish P. Jain, Richard D.J.G. Ho, and Luiza Angheluta*
Njord Centre
Department of Physics
University of Oslo
(Dated: January 28, 2025)

T1 transitions, which are localised cell rearrangements, play an important role in the fluidization of epithelial monolayers. Using a multi-phase field model and an active elastic solid model, we show that although each cell undergoes T1 transitions in time as uncorrelated, random events, the spatial distribution of these events is highly correlated and is dependent on cell shape. T1 transitions have a dual effect: cells losing neighbours tend to relax their shape, while those gaining neighbours tend to elongate. By analysing the statistics of successive T1 transitions undergone by a deformable cell, we find asymmetric spatial distributions related to how cells lose or gain neighbours. These asymmetric spatial patterns of T1 transitions promote directed cell migration, and form the backbone for coherent flow patterns at tissue scales.

I. INTRODUCTION

Confluent epithelial monolayers, as composed of tightly packed cells with stable cell-cell junctions, exhibit a complex interplay between tissue rigidity, collective migration, and fluidization [1, 2]. These mechanical processes are also important in assisting biological phenomena such as morphogenesis, cancer invasion, and wound healing [3, 4]. Cells within a tissue monolayer exhibit collective migration either by moving together as coherent clusters or through neighbour rearrangements [1]. Even when cells move as coherent clusters, the cells at the outer edges of these clusters undergo neighbour exchanges, such as T1 transitions, with nearby cells. While cells within the monolayer may also undergo T1 transitions when they move at different velocities.

T1 transitions, observed in active cell monolayers [5] and in foams under external forces [6], are fundamental topological transitions. During one T1 transition, a junction between two neighbouring cells shrinks and disappears, while two adjacent cells form a new junction typically oriented perpendicular to the original one. T1 transitions result in changes in neighbourhood connectivity without any change in cell number. Although the geometric features of T1 transitions are well understood, the underlying mechanisms triggering these events vary significantly. In passive systems such as soap films, T1 transitions are driven by external forces [7]. However, for biological tissues, these transitions are influenced by intrinsic cellular properties, such as active cell migration [8, 9], or mechano-chemical feedback involving actomyosin and junctional protein complexes such as a adherens junctions [10, 11].

Despite their importance, many aspects of T1 transitions remain poorly understood. Although these events are thought to dissipate junctional stress and mediate solid-fluid transitions in tissues [12–14], the underlying processes are not yet fully resolved.

T1 transitions sustained by cell activity induce large deformations in cell shape, associated with an energy barrier [8, 15]. Recently, we have shown that T1 transitions triggered by cell activity induce transient quadrupolar flows, leading to the relative dispersion of cells [9]. Interestingly, the rate of relative dispersion is determined by the mean occurrence rate of T1 transitions, regardless of the underlying mechanisms controlling how T1 transitions may occur. However, the spatiotemporal patterns of T1 transitions, hypothesized as chains or cascades of T1 transitions [8, 16] propagating across the tissue to induce tissue fluidization and coherent flow structures on larger scales, remain elusive.

In this paper, we study how T1 transitions driven by cell activity contribute to large deformations in cell shape, which in turn influence where next T1 transitions are likely to occur. To explore the general properties of T1 transitions as neighbour exchange events and as junction remodelling events that dependent on cell shapes, we emply two complementary modeling approaches: the multi-phase field (MPF) model and the active elastic solid (AES) model.

In the MPF model, cells are represented as deformable entities with shape boundaries tracked by a phase field. MPF models have been used to study several emergent properties of epithelial monolayers, such as topological features including T1 transitions [8, 9, 17], p-atic order [18–20], and cell colony growth [21, 22].

Conversely, the AES model represents cells as point-like entities that are self-propelled and connected by elastic springs [23]. This model has been used to reproduce observations of polar ordering in epithelial monolayers [24]. We enhance this model to enable neighbour exchanges based on a geometric condition [25].

In both modeling approaches, we find that each cell undergoes T1 transitions as a Poisson process over time, with the occurrence rate dependent on the cell's self-propulsion activity. This suggests that the Poissonian nature of T1 transitions is likely a property of topological changes in the cell neighbour graph. Additionally, the properties of cell junctions significantly influence the

* luiza.angheluta@fys.uio.no

spatial distribution of T1 transitions, as these depend on the feedback between cell shape deformations and T1 transitions. The MPF model is particularly useful for exploring how this feedback leads to a highly asymmetric distribution of successive T1 transitions across cell junctions.

In Section II we describe T1 transitions in MPF and AES models. Within these models, we demonstrate that T1 transitions, as temporal events triggered by cell activity, follow a Poisson process with a mean rate determined by activity. This is discussed in Section III. By measuring the radial distribution functions, we find that T1 transitions exhibit spatial correlations that decay over time, consistent with the hypothesis of chaining of T1 transitions, as discussed in Section IV. In Section V, we show that T1 transitions induce distinct shape deformations depending on whether a cell gains or loses neighbours. Cells losing neighbours undergo shape relaxation, while those gaining neighbours experience elongation. In Section VI, through the analysis of successive T1 transitions undergone by a cell, we demonstrate that the spatial distribution of T1 transitions is non-uniform and depends on specific topological changes. This spatial non-uniformity leads to the emergence of directional migration. Finally, in Section VII, we summarize the results and provide an outlook on the topic.

II. T1 TRANSITIONS

We consider a 2D confluent monolayer of N cells, with their index labels in the set $\mathcal{M} = \{1, 2, \ldots, N\}$. The neighbour connectivity is expressed in terms of a symmetric neighbour adjacency matrix $\mathcal{N}_{N\times N}$ at time t as

$$\mathcal{N}_{ij}(t) = \begin{cases} 1 & : \ i,j \in \mathcal{M} \text{ are neighbours at t and } i \neq j \\ 0 & : \ \text{otherwise} \end{cases}$$

In a multi-phase field (MPF) model, each cell i is represented by a phase field ϕ_i defined such that $\phi_i \approx 1$ inside the cell and $\phi_i \approx -1$ outside it. The cell boundary is characterized by a thin diffuse region where the phase field transitions smoothly between these two bulk values. Such a representation allows us to model cells of arbitrary shapes. The evolution of the phase field is governed by diffusive relaxation aimed at minimizing a free energy functional, with an advection term due to cell self-propulsion. The mathematical formulation of the model is described in Appendix A and has been previously used in Reference [9]. MPF model parameters are as per Table I unless specified otherwise. The conservative dynamics preserves the total cell area.

A T1 transition, denoted by $\mathcal{T}$, is a neighbour-exchange event of finite duration that involves four cells A, B, C, D. $\mathcal{T}$ starts at time $t = t_{\mathcal{T}}^-$ when cells C and D lose contact and concludes at $t = t_{\mathcal{T}}^+$ when cells A and B establish contact. This rearrangement process is illustrated in Figure 1 (panel a-c). Before $t_{\mathcal{T}}^-$, the junction shared by cells C and D shrinks and vanishes at $t_{\mathcal{T}}^-$, and a new junction between A and B, approximately perpendicular to the previous one, is created at $t_{\mathcal{T}}^+$ and subsequently starts to lengthen [9]. Thus, T1 transitions in MPF models result in the remodelling of cell-cell junctions. This T1 transition can be represented by the set $\mathcal{T} = \{A, B, C, D\} \subset \mathcal{M}$ such that

$$\mathcal{N}_{CD}(t_{\mathcal{T}}^-) = 1 \Rightarrow \mathcal{N}_{CD}(t_{\mathcal{T}}^+) = 0$$
$$\mathcal{N}_{AB}(t_{\mathcal{T}}^-) = 0 \Rightarrow \mathcal{N}_{AB}(t_{\mathcal{T}}^+) = 1,$$

while all other connections shared among the four cells remain unchanged during the T1 duration $\Delta t_{\mathcal{T}} = t_{\mathcal{T}}^+ - t_{\mathcal{T}}^-$. Cells A and B, which gain neighbours during the T1 transition, are referred to as *gainer* cells, while cells C and D, which lose neighbours, are referred to as *loser* cells. During the T1 transition, an extracellular gap is formed between the four cells in the MPF model, as shown in the Figure 1 (panel b). While neighbour exchanges involving more than four cells, forming higher-order rosette structures, are possible in the MPF model, they are extremely rare events in the explored parameter regime and thus their influence is ignored.

A 3-way vertex denoted by the subset $\mathcal{X} = \{i, j, k\} \subset \mathcal{M}$, is a set of three cells which are mutually adjacent, i.e., $\mathcal{N}_{ij}(t) = \mathcal{N}_{jk}(t) = \mathcal{N}_{ki}(t) = 1$, at a given time t. The set of all vertices at time t is denoted by $\Sigma_{\mathcal{X}}(t)$. For a unique $\mathcal{N}(t)$, there exists a unique $\Sigma_{\mathcal{X}}(t)$, which represents a particular neighbourhood topology. T1 transitions are topological changes of $\mathcal{N}$ (or equivalently $\Sigma_{\mathcal{X}}$). From hereon, we will refer to a 3-way vertex as just a vertex.

We determine the position of the vertex $\mathcal{X}$ at time t, denoted by $\mathbf{r}_{\mathcal{X}}(t)$, as the location of the minimum value of the sum of its distances to boundaries of all three cells. The boundary of a cell i is implicitly represented by the contour corresponding to $\phi = 0$, and is represented by the zero-level set $Z_i(t)$ such that

$$Z_i(t) = \{\mathbf{x} \in \Omega \mid \phi_i(\mathbf{x}, t) = 0\}. \tag{1}$$

The position of the vertex $\mathcal{X}$ is then given as

$$\mathbf{r}_{\mathcal{X}}(t) = \arg\min_{\mathbf{x}} \left\{ \sum_{j\in\mathcal{X}} |\mathbf{x} - \mathbf{z}_j| \colon \forall \mathbf{z}_j \in Z_j(t) \right\} \tag{2}$$

In Figure 1g, we show a typical snapshot of a cell configuration in MPF model, while in the Figure 1h, we plot the graph of the corresponding vertices. For each T1 transition $\mathcal{T}$, at time $t_{\mathcal{T}}^-$, two vertices $\mathcal{X}_{\mathcal{T},1}^- = \{A, C, D\}$ and $\mathcal{X}_{\mathcal{T},2}^- = \{B, C, D\} \subset \mathcal{T}$ move toward each other and annihilate (Figure 1a). Similarly, at $t_{\mathcal{T}}^+$, two new vertices $\mathcal{X}_{\mathcal{T},1}^+ = \{A, B, C\}$ and $\mathcal{X}_{\mathcal{T},2}^+ = \{A, B, D\} \subset \mathcal{T}$ are spawned (Figure 1c). Notice that the small gaps formed between cells during T1 transitions correspond to holes in the *graph of vertices* as shown in Figure 1h.

As localised processes of remodelling cell-cell junctions, T1 transitions induce large fluctuations in cell shape and speed, generating transient flows with quadrupolar patterns that result in an increase in the pair-separation distance between cells [8, 9].

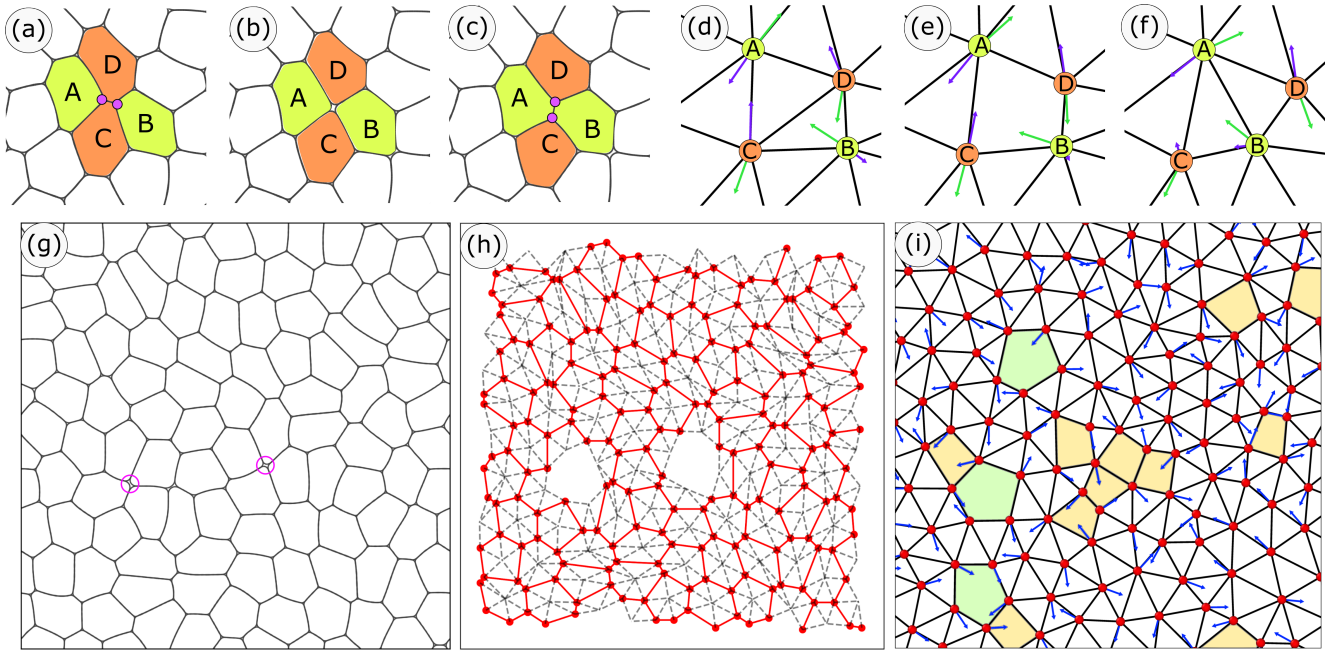


FIG. 1: T1 transition in the MPF model (a-c) and in the AES model (d-f). (a) and (d) before T1; (b) and (e) during T1; (c) and (f) after T1. A T1 transition $\mathcal{T} = \{A, B, C, D\}$ where cells A and B are loser cells, while cells C and D are gainer cells. (a-c) pink markers corresponds to location of vertices that take part in the T1 transition. (d-f) AES: Black line correspond to cell-cell junctions, orange and green circles mark the loser and gainer cells, respectively. The green arrows represents the cell polarity, i.e. direction of self-propulsion, whilst the purple arrow represents the net elastic force. (g) A snapshot of a tissue in the MPF model with the pink circle marking the location of the T1 transitions. (h) The vertices is marked in red, and vertices that are common to two cells are linked by red lines. The black dash lines connect the vertices to the center of mass of the cells. The gaps in the plot corresponds to T1 transitions. (i) Tissue snapshot of AES model. Cells are marked in red, and black bar connects neighbouring cells. Triangles indicate vertices, yellow trapeziums indicates T1 transitions and green polygons denote higher order rosettes. See Movie 1 and Movie 2 in the Supplemental Material for simulations in MPF model and AES model, respectively.

To better understand the interplay between cell shapes and T1 transitions, we also consider an active elastic solid (AES) model where the tissue is idealized as an elastic sheet formed by pointwise cells which are self-propelled and interact with each other through elastic forces. The deterministic evolution of the polarity for the self-propulsion is determined by the torque induced by misalignments between the net elastic force and the cell polarity. Although this model features tissue elasticity, it is not directly related to interfacial forces as is the case for the MPF model. The model is detailed in Appendix B and based on the one introduced in Reference [23]. AES model parameters are as per Table I unless specified otherwise.

In the AES model, the neighbouring cells are initially connected by a predefined cell connectivity graph. In previous works, this graph was quenched in time, resulting in a solid-like response when the tissue is out of its elastic equilibria, or a polar collective migration due to alignment of polarities [23]. We augment this model by introducing a geometric relation of nearest neighbours which is the same as the one proposed in Reference [25, 26] to allow for neighbour exchanges. Explicitly, we connect all cells i and j and remove the connection if there exists any third cell k which satisfies $r_{ij}^2 > r_{ik}^2 + r_{jk}^2$, with r_{ij} being the distance between cells i and j. Most of the neighbour exhanges correspond to T1 configurations as shown in Figure 1 (panels d,e,f) and marked by the yellow quadrilateral shapes in the connectivity graph (see panel i). However, neighbour exchanges involving five cells are also present, as illustrated by pentagonal shapes in panel (i).

For the AES model, note that the T1 transitions are topological changes in the *connectivity graph* and are not directly related to 3-way vertices as in the MPF model. In the MPF model, two cells are considered neighbours if their shape boundaries sufficiently overlap, such that topology changes in the connectivity graphs corresponds in junction remodeling. In the AES model, cells are considered neighbours if they conform to a specific geometric configuration of cell positions. This geometric dependence of neighbourhood topology allows for neighbour

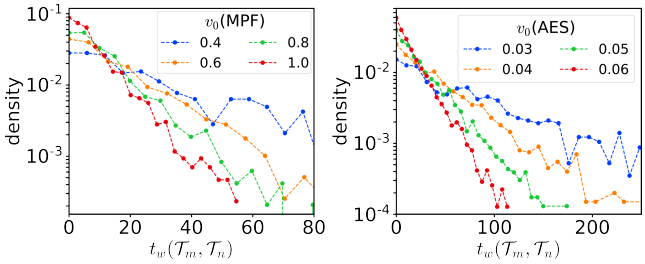


FIG. 2: Waiting time t_w probability density distribution between *successive* T1s $\mathcal{T}_m$ and $\mathcal{T}_n$ undergone by a cell. (a) MPF model: cell activity v_0 is varied. (b) AES model: cell activity v_0 is varied.

exchanges with four or more cells, with neighbour exchanges involving four cells being the most common. By contrast, in MPF models, neighbour exchanges almost always involve four cells within the parameter regime explored. For simplicity, we also use the symbol $\mathcal{T}$ to denote neighbour exchanges in the AES model, even if they involve more than four cells. In the AES model, for our analysis, neighbour exchanges involving more than four cells are counted as one transition, and the algorithm for detecting neighbour exchanges is described in Appendix B.

In the AES model, when the self-propulsion is high, the cells are driven far out of their equilibrium positions imposed by elastic interactions, resulting highly non-uniform distribution of distances between particles, analogous to that of a gas, which is unrealistic limit case for epithelia. Therefore, the AES with neighbour exchanges is valid at sufficiently small activities, where there is still a well-defined reference state for elastic deformations, which is only punctually destroyed by neighbour exchanges. Thus, we restrict ourselves to situations with moderate self-propulsion speeds. Thus, both models have a connectivity graph, encoded within $\mathcal{N}$, where T1 transitions occur as localised neighbour exchange events.

III. WAITING-TIME BETWEEN T1 TRANSITIONS

To quantify the spatiotemporal relations between T1 transitions, we introduce the notion of two *successive* T1 transitions $\mathcal{T}_m$ and $\mathcal{T}_n$ involving cell i i.e. $i \in \mathcal{T}_m$ and $i \in \mathcal{T}_n$. We consider two T1s involving a cell i, *successive* if $t^+_{\mathcal{T}_m} < t^-_{\mathcal{T}_n}$, and if cell i is not part of any other T1 between $t^+_{\mathcal{T}_m}$ and $t^-_{\mathcal{T}_n}$. The waiting time $t_w(\mathcal{T}_m, \mathcal{T}_n)$ between *successive* T1 transitions $\mathcal{T}_m$ and $\mathcal{T}_n$ is defined as the time interval between end of $\mathcal{T}_m$ and start of $\mathcal{T}_n$ i.e., $t_w(\mathcal{T}_m, \mathcal{T}_n) := t^-_{\mathcal{T}_n} - t^+_{\mathcal{T}_m}$.

Figure 2a and Figure 2b show the distributions of waiting times t_w for varying activity (v_0) in the MPF and AES models, respectively. In both cases, the waiting time is exponentially distributed. The average waiting time decreases with increasing activity as cells that move faster are likely to undergo their next T1 sooner. The mean waiting time does not vary significantly with varying deformability Ca (see Figure 1 in Supplemental Material). Cells with lower deformability typically undergo fewer T1 transitions; however, these T1 transitions have a larger duration [8].

Whilst T1 transitions appear Poissonian in time, we show next that T1 transitions are correlated in space. Later, we will use the cell shape of the MPF to describe the spatial correlations in the MPF model.

IV. SPATIAL CORRELATION OF T1 TRANSITIONS

To study the spatial correlations between T1 events, we compute the radial distribution function for pairs of T1 events. We first compute the epicenters of T1 transitions. Within MPF model, the epicenter $\mathbf{r}_\mathcal{T}$ of a T1 transition $\mathcal{T}$ is empirically defined as the location where the sum of distances to the boundaries of all four cells involved in the T1 transition is minimized. This is measured at time midway through the T1 transition, i.e., at $t^m_\mathcal{T} = 0.5(t^+_\mathcal{T} + t^-_\mathcal{T})$ [8, 9]. The location of epicenter is given by

$$\mathbf{r}_\mathcal{T}(t) = \arg\min_{\mathbf{x}} \left\{ \sum_{j \in \mathcal{T}} |\mathbf{x} - \mathbf{z}_j| \colon \forall \mathbf{z}_j \in Z_j(t^m_\mathcal{T}) \right\} \tag{3}$$

The epicenter lies within the extracellular gap created during the T1 transition, as shown in Figure 1b. In the AES model, the epicenter is defined as the average of the positions of the four cells involved in $\mathcal{T}$, i.e.

$$\mathbf{r}_\mathcal{T}(t_m) = \frac{\mathbf{r}_A + \mathbf{r}_B + \mathbf{r}_C + \mathbf{r}_D}{4} \tag{4}$$

with time taken at the end of the T1 transition, $t^m_\mathcal{T} = t^+_\mathcal{T}$.

For a specific time window of size ω, we compute the radial distribution function for epicenters of all T1 transitions that occur within that window. Suppose, in a given time window of size ω starting from time t until time $t + \omega$, there are N_{T1} events and let $\rho = \frac{N_{T1}}{A}$ be the number density of T1 events, where A is the area of the computational domain. Then, the radial distribution function for this particular time window is calculated as

$$g(r, t, t+\omega) = \frac{1}{\rho N_{T1}} \left\langle \sum_{j=1}^{N_{T1}} \sum_{k \neq j} \delta(r - r_{jk}) \right\rangle \tag{5}$$

where δ is the Dirac delta function and r_{jk} is the distance between the epicenters of a pair of T1 transitions indexed by j and k. If τ is the time resolution, then the radial distribution function is calculated as the ensemble average of time windows, $\{(0, \omega), (\tau, \omega + \tau), (2\tau, \omega + 2\tau), \ldots, (T - \omega, T)\}$, such that

$$g_\omega(r) = \frac{\tau}{(T - \omega + \tau)} \sum_{t=0}^{t=T-\omega} g(r, t, t+\omega) \tag{6}$$

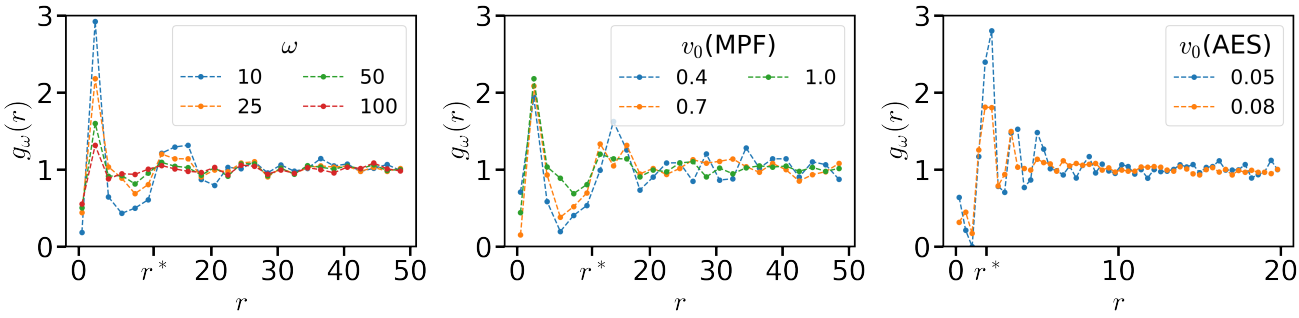


FIG. 3: Radial distribution function $g_\omega(r)$ between T1 transitions for MPF model (a-b) and AES model(c). (a) $g_\omega(r)$ for different time windows for $v_0 = 1$. (b) $g_\omega(r)$ for varying v_0 with $w = 25$. (c) $g_\omega(r)$ for varying v_0 with $w = 10$. r^* is the mean separation distance.

Figure 3a shows the radial distribution function for the MPF model for varying time window sizes ω. The location of the peaks does not vary with window size, but decrease in magnitude. For small ω, $g_\omega(t)$ appears typical of disordered systems with interacting particles. As epicenters of T1 transitions lie in the vicinity of cell-cell junctions, the peaks in the $g_\omega(t)$ must be relate to where the cell-cell junctions are located. Over time, the junctions remodel due to T1 transitions, and so $g_\omega(t)$ flattens as ω increases. Figure 3b shows $g_{25}(t)$ for varying activity v_0 in MPF model. As activity increases, the correlations reduce due to higher rates of junction remodelling [9]. Similar results are observed for the AES model, as shown in Figure 3a, where $g_\omega(t)$ is plotted for varying activity v_0.

The peaks in the AES model lie at units of the mean separation distance r^*, determined by the number density of cells. In the MPF model, the cell separation distance r^* is defined as the diameter of the circle whose area is equal to the cell's area. By contrast to the AES model, the first peak lies at $r \approx 3$, followed by a valley at $r \approx 8$ and then another peak at $r \approx 15$, all within the mean cell separation r^*. Thus, the location of the first two peaks and the first valley in $g_\omega(t)$ for low ω correspond to different cell junctions across a cell. We discussed this further in Section VI by analyzing spatial distributions of *successive* T1 transitions undertaken by a cell.

From here on, we make use of the high shape resolution of cells in the MPF model to discuss the interplay between cell shape and T1 transitions. The shape will also help us better understand the profile of the radial distribution $g_\omega(r)$ of MPF model.

V. SHAPE CHANGES INDUCED BY INDIVIDUAL T1 EVENTS

The cell shape index p defined as

$$p = \frac{\text{Perimeter}}{\sqrt{\text{Area}}}, \tag{7}$$

is a common cell shape descriptor especially for quantifying cross-over regimes in jamming transitions [27]. For instance, in asthmatic airway epithelium, the jamming transition has been associated to a critical shape index of $p \approx 3.81$, below which the cells are jammed [28].

In our MPF model, the cell area remains invariant, meaning that the shape index is determined solely by the cell perimeter. Since the energy is concentrated at the cell-cell junctions, a cell with a higher perimeter (or shape index) possesses a higher associated energy. Therefore, the shape index also serves as an indicator of the energy associated with the shape of a cell.

In Figure 4a, we show the time evolution of the shape index of cells that take part in T1 transitions, averaged over all T1 transitions, as function of the time before and after a T1 transition. The evolution after a T1 transition is shown such that $t_\mathcal{T}^+$ is fixed at zero, with positive time representing the period after $t_\mathcal{T}^+$. Similarly, the time evolution before a T1 transition is shown such that $t_\mathcal{T}^-$ is fixed at zero, with negative time representing the period before $t_\mathcal{T}^-$ [8]. The average shape index of cells in T1 transitions increases before the start of T1, reaches its peak at the start of T1, and falls sharply immediately after the end of T1, followed by a slower relaxation.

However, when plotting the evolution separately for *loser* and *gainer* cells, different patterns become evident. Before a T1 event, the shape index of loser cells increases significantly upon elongation, reaching its peak just before the start of the T1 transition. Meanwhile, the shape index of gainer cells remains constant on average. As the four cells are on the verge of undergoing a T1 event, the gainer cells move towards each other, compressing the loser cells such that the junction shared by the loser cells shrinks [8]. Gainer cells elongate during the T1 transition and reach their maximum shape index after the end of the T1 transition. Whereas, the shape index of loser cells reduce during the T1 transition. At the end of the T1 transition, loser and gainer cells have similar shape indices. After the T1 transition, the shape index of loser cells decays at a faster rate than that of the gainer cells. Thus, the loser and gainer cells experience distinc-

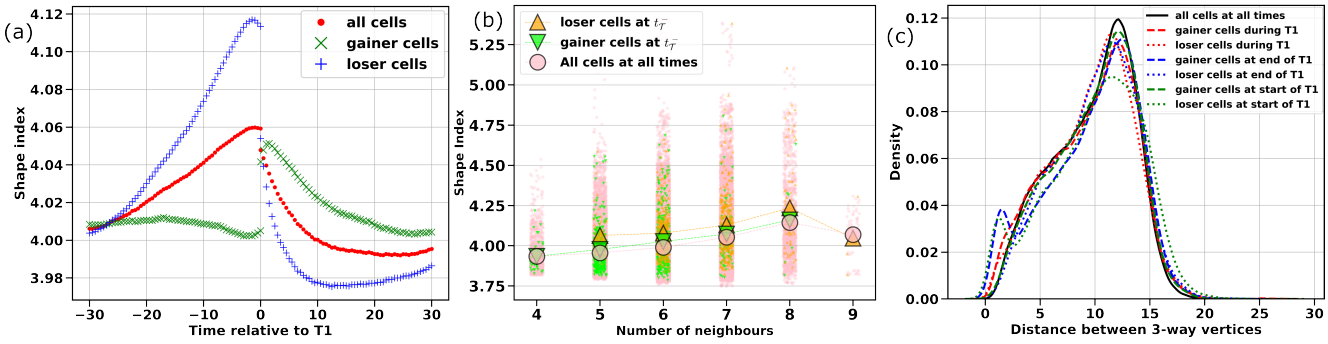


FIG. 4: For the MPF model: (a) Evolution of mean shape index of cells undergoing a T1 transition. Negative time and positive time corresponds to relative time before the start of a T1 transition $t_{\mathcal{T}^-}$, and relative time after the end of a T1 transition $t_{\mathcal{T}^+}$. The mean evolution of gainer and loser cells are also highlighted. (b) Shape index is plotted against the number of neighbours of a cell (blue). The shape index for loser and gainer cells at the start of the T1 transition are also shown. The smaller circles mark individual data, while the larger circles represent the mean value calculated for a particular number of neighbours. (c) Probability density of distance between all pairs of vertices of a cell in various scenarios. The black curve corresponds to distance between all pairs of vertices of a cell, ensembled over all cells at all times. The red curves corresponds to the time when the cell is undergoing a T1 transition($t_{\mathcal{T}}^- < t < t_{\mathcal{T}}^+$), whereas the blue and green curves corresponds to the times $t_{\mathcal{T}}^-$ and $t_{\mathcal{T}}^+$ respectively. Dashed and dotted curves represent to gainer or loser cells, respectively. See Movie 3 in the Supplemental Material for movie of the the evolution of the shape of a cell along with its shape index and number of neighbours.

tive shape deformations due to a T1 transition.

To gain more insights, we plot the distribution of the shape index conditional on the number of neighbours a cell has, for all cells at all times, as shown in Figure 4b. The figure also shows the shape index of *loser* and *gainer* cells at the start of a T1 transition. The mean values, indicated by larger markers, show that the average shape index tends to increase with the number of neighbours. As cells with fewer neighbours have a smaller shape index, T1 transitions lead to shape relaxation of loser cells. Similarly, T1 transitions cause elongation of gainer cells, leading to shape tension. This is despite the fact that loser cells undergo more drastic deformations than gainer cells, as evident from the evolution of shape index in Figure 4a.

Cells with higher activity v_0 undergo more T1 transitions and have a higher mean shape index [8]. As the mean shape index increases with activity and as cells undergo more T1s, they develop transient elongations, or protrusions.

Figure 4c shows the distribution of distances between pairs of cell vertices. The black curve shows the distribution of distances between all pairs of cell vertices for all cells at all times. The other curves are conditional on certain situations a cell is in.

- The red curve shows the distances when the cell is undergoing a T1 transition, during the period $t_{\mathcal{T}}^- < t < t_{\mathcal{T}}^+$.
- The green curve corresponds to the distances at the start of a T1 transition, $t_{\mathcal{T}}^-$.
- The blue curve represents the distances at the end of a T1 transition $t_{\mathcal{T}}^+$.

Overall, the curves are similar, but there is a noticeable small peak at short distances for loser cells at the beginning of a T1 transition and for gainer cells at the conclusion. These peaks indicate that the pair of vertices that are about to annihilate or have recently been created. When two vertices of a cell are close to each other, the shape of the cell is likely very anisotropic (elongated). This explains why the shape index of loser cells peaks before the T1 transition, and the shape index of gainer cells peaks afterward.

VI. EMERGENT DIRECTIONAL MIGRATION

Since cell shape and its tendency to lose or gain neighbours during a T1 transition are interconnected, we now investigate whether the interplay between cell shape and junction remodeling causes coherent flow patterns that span larger length scales than those typical of a T1 transition.

Let $\mathcal{U}_i^-(\mathcal{T})$ and $\mathcal{U}_i^+(\mathcal{T})$ be the set of all vertices that were annihilated and created, respectively, due to the T1 transition $\mathcal{T}$ that involved cell i.

For a pair of *successive* T1s $\mathcal{T}_m$ and $\mathcal{T}_n$ involving cell i, i.e., $i \in \mathcal{T}_m$ and $i \in \mathcal{T}_n$, the following relations hold.

$$\begin{aligned}
\mathcal{U}_i^+(\mathcal{T}_m) &= \{\mathcal{X}^+_{\mathcal{T}_m,c}\} &&: \text{ if } i \text{ is a loser cell in } \mathcal{T}_m \\
\mathcal{U}_i^+(\mathcal{T}_m) &= \{\mathcal{X}^+_{\mathcal{T}_m,1}, \mathcal{X}^+_{\mathcal{T}_m,2}\} &&: \text{ if } i \text{ is a gainer cell in } \mathcal{T}_m \\
\mathcal{U}_i^-(\mathcal{T}_n) &= \{\mathcal{X}^-_{\mathcal{T}_n,1}, \mathcal{X}^-_{\mathcal{T}_n,2}\} &&: \text{ if } i \text{ is a loser cell in } \mathcal{T}_n \\
\mathcal{U}_i^-(\mathcal{T}_n) &= \{\mathcal{X}^-_{\mathcal{T}_n,c}\} &&: \text{ if } i \text{ is a gainer cell in } \mathcal{T}_n
\end{aligned}$$

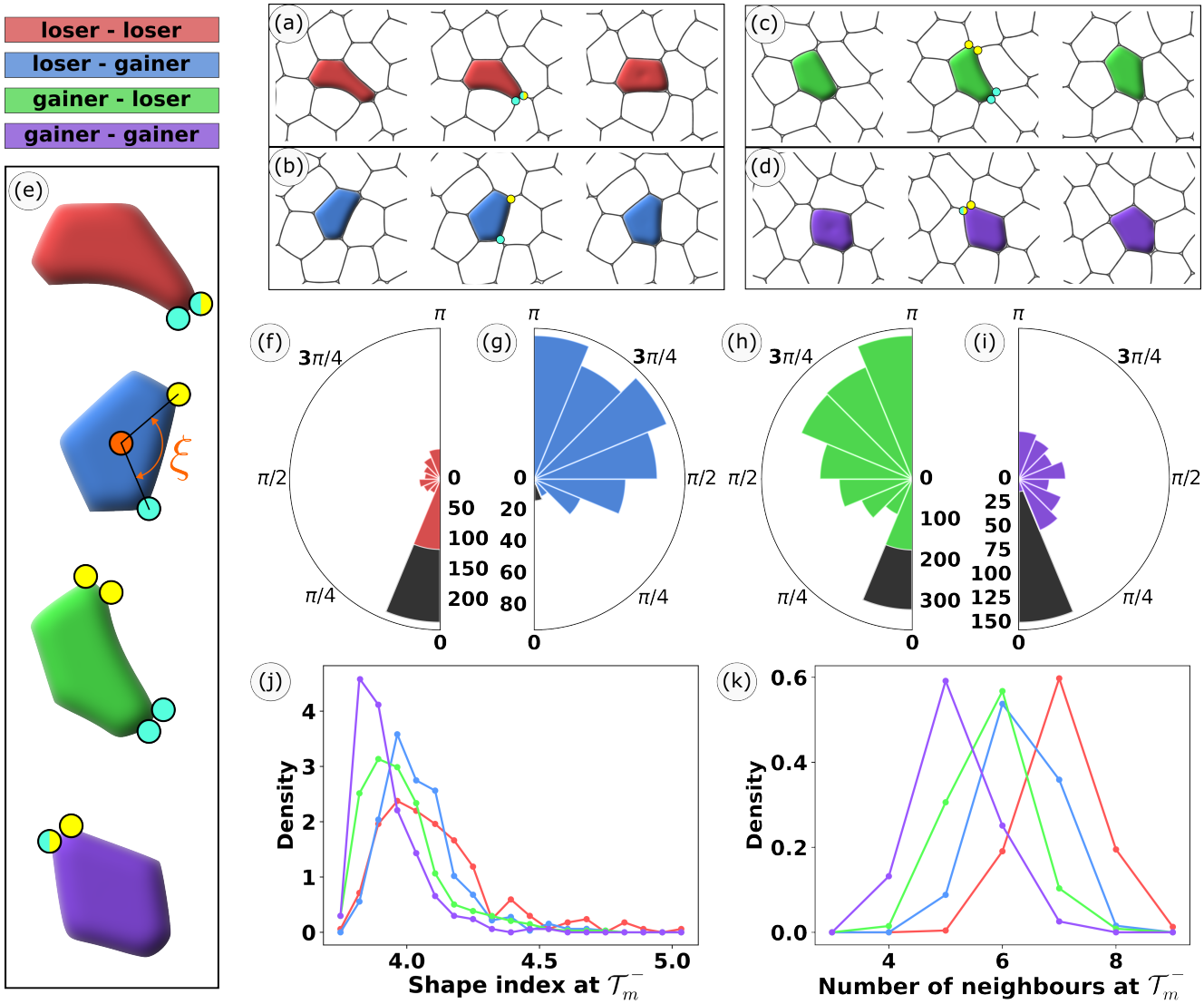


FIG. 5: For the MPF model: (a-d) Four different patterns by which highlighted cell i undergoes two *successive* T1 events, i.e. $\mathcal{T}_m$(1$^{\text{st}}$ T1) and $\mathcal{T}_n$(2$^{\text{nd}}$ T1). The colours correspond to legend at the top-left. $\mathcal{T}_m$ takes places between the left and the middle column, while $\mathcal{T}_n$ takes places between the middle and the right column. The yellow and cyan circles mark the vertices of the highlighted cell that are created in $\mathcal{T}_m$ and annihilated in $\mathcal{T}_n$, respectively. Sometimes, vertices take part in both the T1s, and are marked with both cyan and yellow. (a) *loser-loser*: Red cell loses neighbours in both T1s. (b) *loser-gainer*: Blue cell loses neighbours in $\mathcal{T}_m$ and gains neighbours in $\mathcal{T}_n$. (c) *gainer-loser*: Green cell gains neighbours in $\mathcal{T}_m$ and loses neighbours in $\mathcal{T}_n$. (d) *gainer-gainer*: Purple cell gains neighbours in both T1s. (e) Shows the zoomed highlighted cells from (a-d). (f-i) Fixing the origin to the center of mass of cell i, the difference in orientation of each element in the set of vertices created in $(\mathcal{T}_m)$ (i.e., $(\mathcal{U}_i^+(\mathcal{T}_m))$) with each element in the set of vertices annihilated in $(\mathcal{T}_n)$ (i.e., $(\mathcal{U}_i^-(\mathcal{T}_n))$) is histogrammed over all pairs of *successive* T1 transitions for all cells. An example of the difference in orientation indicated by ξ on the blue cell, as shown in (e). ξ is the difference in orientation of blue and yellow circles measured relative to the orange circle(center of mass). The black colour in (f-i) represents vertices that are created in $\mathcal{T}_m$ and annihilated in $\mathcal{T}_n$. (j) Shape index and (k) number of neighbours of the cell undergoing *successive* T1s measured at the start of $\mathcal{T}_m$, with the color marking the appropriate scenario. The statistics in (f-k) is collected over three simulations.

where $c = 1$ or 2 depending on the vertex which includes cell i.

There are four different scenarios for a cell involved in *successive* T1 transitions, as shown in the Figure 5a-5d, depending on whether a cell is a loser or a gainer cell in the two T1 transitions. These four scenarios are denoted as *loser-loser*, *loser-gainer*, *gainer-loser*, *gainer-gainer*. The vertices of the highlighted cell involved in $\mathcal{T}_m$ and $\mathcal{T}_n$ are marked in yellow and cyan, respectively. In some situations, the same vertex can be involved in both T1 transitions, such that it is created in $\mathcal{T}_m$ and annihilated in $\mathcal{T}_n$, and is appropriately highlighted using both cyan and yellow. This is possible in all four scenarios of *successive* T1 transitions. A cell undergoes a reversible T1 transition in the scenarios *loser-gainer* and *gainer-loser* only if both the vertices involved in the $\mathcal{T}_m$ are involved in $\mathcal{T}_n$. We do not encounter any reversible T1 transitions in the MPF models in the parameter regime we have explored, but we have encountered several T1 transitions where one vertex was involved in *successive* T1 transitions.

For each of the four scenarios of *successive* T1s involving cell i, we first determine the locations of all vertices created after $\mathcal{T}_m$ i.e. $\{\mathbf{r}_{\mathcal{X}}(t^-_{\mathcal{T}_n}) \mid \mathcal{X} \in \mathcal{U}_i^+(\mathcal{T}_m)\}$, and the locations of all vertices that will annihilate in $\mathcal{T}_n$, i.e. $\{\mathbf{r}_{\mathcal{X}}(t^-_{\mathcal{T}_n}) \mid \mathcal{X} \in \mathcal{U}_i^-(\mathcal{T}_n)\}$, both calculated at the start time of $\mathcal{T}_n$ i.e $t^-_{\mathcal{T}_n}$, which is the latest time where the vertices in both $\mathcal{U}_i^+(\mathcal{T}_m)$ and $\mathcal{U}_i^-(\mathcal{T}_n)$ coexist. Then, we determine the location of the center of mass of the cell at $t^-_{\mathcal{T}_n}$ i.e. $\mathbf{r}_i(t^-_{\mathcal{T}_n})$(calculated using Equation A7). We pair every vertex of $\mathcal{U}_i^+(\mathcal{T}_m)$ with every vertex of $\mathcal{U}_i^-(\mathcal{T}_n)$. By pairing vertices in this way, in the scenarios *loser-loser*, *loser-gainer*, *gainer-loser* and *gainer-gainer*, we get 2, 1, 4 and 2 pairs of vertices for each pair of *successive* T1s, respectively.

We fix an origin at the center of mass of the cell, denoted by $\mathbf{r}_i(t^-_{\mathcal{T}_n})$. For each pair of chosen vertices, we find the difference in orientations of both vertices measured relative to the cell center, which we will call *relative orientation*. An example of such a relative orientation is highlighted by the angle ξ on the blue cell in Figure 5e. This process is repeated for all pairs of *successive* T1s and for all cells, and the corresponding histograms are shown in the Figures 5f-5i for all four scenarios. The relative orientation between each vertex pair varies from 0 to π. If the same vertex belongs to both $\mathcal{U}_i^+(\mathcal{T}_m)$ and $\mathcal{U}_i^-(\mathcal{T}_n)$, then the data is highlighted in black, and the relative orientation between such a pair is 0. If both the vertices are on the opposite side of the cells then the relative orientation between such a pair is π. In essence, the distributions in Figures 5f-5i informs on the spatial distribution of *successive* T1s with respect to the cell center. Figure 5j and Figure 5k show the corresponding probability density distributions of the shape index and the number of neighbours of the cell in each of the four scenarios measured at the start of $\mathcal{T}_m$.

For the scenario where a cell loses neighbours in both T1 transitions, i.e., *loser-loser*, we see that the distribution peaks at a low value of relative orientation. This suggests that the pairs of vertices that took part in *successive* T1s are close to each other. A large fraction of these pairs involve one vertex taking part in both T1s. Very few pairs of vertices lie on the opposite sides of the cells suggests that most pairs of *successive* T1s happen close to each other on the same side of the cell. Hence, elongated cells are more likely to undergo *successive* T1s of *loser-loser* kind, as shown in Figure 5j. An elongated cell can relax its shape by retracting its mass towards the cell center along the direction of elongation through T1 transitions (see red cell in Figure 5a). Cells in this scenario also have a higher than average number of neighbours as shown in Figure 5k.

For the scenario *loser-gainer*, both T1s happen mostly on the opposite sides of a cell as the relative orientation between most pairs is greater than $\pi/2$, as shown in Figure 5g. This is akin to a cell retracting mass from one side and moving in the opposite direction. The loser cells which undergo more drastic shape changes during a T1, as shown in Figure 4a, are propelled away from the epicenter [8], and such a cell gains a neighbour on the opposite side.

In the scenario *gainer-loser*, we see two peaks near 0 and π, see Figure 5g. The differences in the distributions for *loser-gainer* and *gainer-loser* suggest that the spatial distribution of *successive* T1s on a cell depends on the order of topological change, even if the net topological change in both scenarios is the same. This might be because gainer and loser cells undergo distinct deformations due to T1 transitions, as shown in Figure 4a. In both *loser-gainer* and *gainer-loser* situations, at the start of the first T1, the average number of neighbours is around 6, suggesting that these two scenarios involve fluctuations about the mean number of neighbours which is approximately 6.

For the scenario *gainer-gainer*, most pairs of vertices of *successive* T1s lie on the same side of the cell, and most of these also involve the same vertex in both T1s, as shown in Figure 5i. If we were to exclude the situations where the same vertex is involved, the remaining pairs are likely to occur at any relative orientation except for very low relative orientation, as indicated by the histogram. Cells that gain two neighbours in *successive* T1s usually have a lower shape index at the start of the first T1 than the other three scenarios, as shown in Figure 5j, as well as a lower number of neighbours, as shown in Figure 5k.

If the distributions of relative orientation of the vertices involved in *successive* T1 transitions were uniform, then T1 transitions would have no preferred orientation for the quadrupolar flow field that arises due to them [9]. However, the non-uniform distributions in Figures 5f-5i suggest an effective directed migration of the cells, depending on the four scenarios, which could lead to emergent flow patterns at larger scales as a result of chaining of T1 transitions.

The non-uniform spatial distribution of paired vertices of *successive* T1 transitions on the cell might be a rea-

son behind the weak polar order within the MPF model, which is typically more than 0.4 [9]. The large number of paired vertices of *successive* T1 transitions occuring at low relative orientation suggest that the *successive* T1 transitions occur close to each other, informing the profile of the radial distribution functions in Figure 3 for the MPF model, where a peak was observed for very low value of radial distance ($r < 5$).

In the MPF model, the orientation of cell activity tends to align with the direction of its elongation, and this rate is controlled by a parameter α (See appendix A for details). However, this alignment is not the reason for the specific spatial distribution of *successive* T1 transitions, as similar distributions are observed even when the activity does not align with cell elongation, i.e., when $\alpha = 0$ (See Figure 2 in the Supplemental Material for corresponding plots). Also, these distributions remain similar even if activity and deformability are varied suggesting a universal emergent behaviour due to the shape response of cells.

Additionaly, we note that every cell that gains neighbours in two *successive* T1s where the vertex created in the first T1 is annihilated in the second T1, also has a neighbouring cell that loses neighbours in both of these T1s. Consider a T1 $\mathcal{T}_m = \{A, B, C, D\}$ where cell A gains a neighbour B. This process creates two vertices: $\{A, B, C\}$ and $\{A, B, D\}$. If one of these vertices is involved in another T1 $\mathcal{T}_n$ by annihilating such that cell A gains another neighbour, then depending on which vertex took part in the T1, either C or D loses contact with B. So, one of C or D loses neighbours in both $\mathcal{T}_m$ and $\mathcal{T}_n$.

VII. CONCLUSIONS:

In summary, we have shown that while cells undergo individual T1 transitions as a Poisson process in time, with a rate determined by cell activity, their spatial distribution is highly correlated. Through detailed statistical analysis of the cell shape index and the number of cell neighbours, we have found that the cell shape deformation in response to T1 transitions is contingent on whether a cell loses or gains neighbours. This finding highlights a dual role of T1 transitions: cells losing neighbours experience shape relaxation with a decrease in the shape index, whereas cells gaining neighbours become elongated, leading to shape tension.

We identify four distinct occurrence patterns of *successive* T1 transitions. These non-uniform distributions across cell junctions lead to cell shape protrusions or retractions, allowing cells to move directionally relative to others, potentially forming flow structures across multiple cells. However, to better understand the emergent fluidisation patterns, longer chains of successive T1 events need to be considered. The spatial correlations of T1 transitions may also be probed using other models, such as the vertex model [29] especially those that allow for complex cell shape deformations as in the Reference [13]. These results are also accessible for experimental verification.

ACKNOWLEDGMENTS

This project is partly funded by the European Union's Horizon 2020 research and innovation programme under the Marie Skłodowska-Curie grant agreement No 945371, and by the University of Oslo, through UiO:Life Science through the convergence environment ITOM. LA acknowledges support in part by grant NSF PHY-2309135 to the Kavli Institute for Theoretical Physics (KITP) and the Gordon and Betty Moore Foundation Grant No. 2919.02.

Appendix A: Multi-phase field model

The multi-phase field model presented here was previously used in Ref. [9], and is based on earlier models in Refs [8, 17]. Consider a set of cells represented by phase-fields $\{\phi_i\}$ defined in $\Omega \subset \mathbb{R}^2$, where $i = 1, 2, \ldots, N$, and N is the total number of cells. The domain Ω is a square of side length L. The interior and exterior of the cell i is identified as the region in Ω with bulk phase values $\phi_i \approx 1$ and $\phi_i \approx -1$, respectively. The interior is phase separated from the exterior through a diffuse interface of width $\mathcal{O}(\epsilon)$. The phase fields ϕ_i evolve according to

$$\partial_t \phi_i + \mathbf{v}_i \cdot \nabla \phi_i = \Delta \frac{\delta \mathcal{F}}{\delta \phi_i}, \tag{A1}$$

while preserving the total cell area. The free energy functional $\mathcal{F}[\{\phi_i\}] = \mathcal{F}_{CH}[\{\phi_i\}] + \mathcal{F}_{INT}[\{\phi_i\}]$ is a sum of energy of the surface and the interaction energy between the cells. The energy of the surface is the Cahn Hilliard energy given as

$$\mathcal{F}_{CH}[\{\phi_i\}] = \frac{1}{Ca} \sum_{i=1}^{N} \int_\Omega g(\phi_i) \left(\frac{\epsilon}{2} ||\nabla \phi_i||^2 + \frac{1}{4\epsilon} (\phi_i^2 - 1)^2 \right) dx, \tag{A2}$$

where Ca is the capillarity number that controls the deformability of the cells, ϵ controls the thickness of cell interface, and $g(\phi) = \frac{2}{3(\phi_i+1)(\phi_i-1)}$ is the diffusion restriction function to prevent bulk diffusion [30]. The first term penalises gradients in the phase field which models cortical tension, while the second term is the demixing part which ensures phase separation between the exterior and interior of the cell. The interaction energy is given as

$$\mathcal{F}_{INT}[\{\phi_i\}] = \frac{1}{In} \sum_{i=1}^{N} \int_\Omega \sum_{j \neq i} \Big(\frac{a_r}{2} (\phi_i + 1)^2 (\phi_j + 1)^2 - \frac{a_a}{2} (\phi_i^2 - 1)^2 (\phi_j^2 - 1)^2 \Big) dx \tag{A3}$$

where, a_r and a_a are used to tune the repulsive and attraction component, respectively. The repulsive part penalises overlap of cell interiors, while the attractive part promotes overlap of cell interfaces.

The cell activity field is given as

$$\mathbf{v}_i(\mathbf{x},t) = v_0 \mathbf{e}_i(t)\hat{\phi}_i(\mathbf{x},t) \tag{A4}$$

where v_0 is the magnitude of activity, $\hat{\phi} = 0.5\phi + 0.5$, and $\mathbf{e}_i = [\cos\theta_i(t), \sin\theta_i(t)]$ is the activity orientation vector. The orientation angle θ evolves according to the stochastic differential equation

$$d\theta_i = \sqrt{2D_r}dW_i(t) + \alpha(\beta_i(t) - \theta_i(t))dt, \tag{A5}$$

where D_r is the coefficient of rotational diffusion and W_i is a Wiener process. The angle $\beta_i(t)$ is the angle of shape polarity defined to be the elongation axis of the cell, and is calculated from the eigenvector corresponding to the largest eigenvalue of the shape deformation tensor, $\mathbf{J}_i^+$ such that

$$\beta_i(t) = \begin{cases} \arg(\boldsymbol{\eta}_i^+(t)) & : \ \mathbf{e}_i(t)\cdot\boldsymbol{\eta}_i^+(t) > 0 \\ \arg(-\boldsymbol{\eta}_i^+(t)) & : \ \mathbf{e}_i(t)\cdot\boldsymbol{\eta}_i^+(t) < 0. \end{cases} \tag{A6}$$

The system of partial differential equations in Equation A1 is considered on a square periodic domain. The system is spatially discretised using finite elements with a semi-implicit discretisation in time, and is solved using adaptive finite element methods using the C++ FEM tool AMDIS [31, 32] with the parallisation approach introduced in Reference [33]. For each simulation, we initialize the system with N square cells arranged in a regular grid with randomly oriented activity, allowing for an initial transient period for cells to mix. We consider the data only after the cell shapes appear sufficiently irregular.

The parameters used are as per Table I unless specified otherwise.

N	L	T	ϵ	v_0	Ca	In	a_a	a_r	D_r	α	dt
100	100	150	0.15	0.5	0.2	0.1	1	1	0.01	0.1	0.005

TABLE I: Default values of the model parameters. dt denotes the timestep size.

The center of mass of a cell i in MPF model is calculated as

$$\mathbf{r}_i(t) = \frac{\int_\Omega \mathbf{x}\hat{\phi}_i dx}{\int_\Omega \hat{\phi}_i dx} \tag{A7}$$

where $\hat{\phi}_i = 0.5\phi_i + 0.5$ is the rescaled phasefield.

Appendix B: Active elastic solid model

The active elastic solid model [23] is a discrete particle model consisting of a collection of N particles at positions $\mathbf{r}_i$ in a flat tissue monolayer. The elasticity of the tissue monolayer is modelled by connecting neighbouring cells with spring-like forces $\mathbf{f}_i = -\nabla_{\mathbf{r}_i} V$ determined by a generic Gaussian potential for the elastic interactions,

$$V = \sum_i \sum_{j=n.of.i} \exp\left\{ -\frac{(|\mathbf{r}_{ij}| - l_{ij})^2}{a_0^2} \right\} \tag{B1}$$

where $\mathbf{r}_{ij} = \mathbf{r}_i - \mathbf{r}_j$ is the separation vector between two cells and l_{ij} is the equilibrium distance between cells. The sum of j is taken over the neighbours on an initially square lattice. The directional self-propulsion follows the cell polarities $\mathbf{p}_i$ which reorients due to a torque induced by elastic interactions. The overdamped dynamics on this system is then described by

$$\dot{\mathbf{r}}_i = v_0\mathbf{p}_i + \frac{1}{\zeta}(\mathbf{f}_i + \xi_i) \tag{B2}$$

$$\dot{\mathbf{p}}_i = \mathbf{T}_i \times \mathbf{p}_i + \eta_i \ . \tag{B3}$$

where the polarity torque is

$$\mathbf{T}_i = \frac{1}{\zeta}(\mathbf{p}_i \times \dot{\mathbf{r}}_i) \ .$$

The translational noise has zero mean and

$$\langle \xi_i(t)\cdot\xi_j(t')\rangle = D_r\delta_{ij}\delta(t-t') \tag{B4}$$

Similarly, the rotational noise also has zero mean and

$$\langle \eta_i(t)\cdot\eta_j(t')\rangle = D_p\delta_{ij}\delta(t-t') \ . \tag{B5}$$

We renormalize the magnitude of polarity to unity at every timestep because the noise is not norm conserving. AES simulations are for 576 cells on a periodic domain of length L with time advancement using the Euler method and with the following parameters unless otherwise given on a figure.

L	T	l_{ij}	$1/a_0^2$	ζ	D_r	D_p	dt
40	5000	2	0.08	1	0.025	0.15	0.1

TABLE II: Default values of the model parameters for AES. dt denotes the timestep size.

Local cell rearrangements are imposed by a geometric rule for nearest neighbours. Namely, cells i and j are considered neighbours if and only if they are closest in distance to their midpoint than any other third cell. Explicitly, we connect all cells i and j and remove the connection if there exists any third cell k which satisfies $r_{ij}^2 > r_{ik}^2 + r_{jk}^2$, with r_{ij} being the distance between cells i and j. This is the same neighbour criterion as in Reference [25]. The neighbour criterion is slightly different than using a Voronoi tesselation. Whilst we do gain information about the duration of T1 transitions, since they no longer occur instantaneously, we do not gain any information about the shape of cells. Because of this, we use the multiphase field model to answer these questions.

In the simulations used in this paper, since we are concerned with the behavior of T1s specifically, we update

the neighbour list at every time-step. We then define a T1 as occuring in the following way: when cells i and j cease to be neighbours this is the start of a potential T1; a T1 occurs when cells m and n become neighbours, where both m and n are neighbours of both i and j; it is cancelled if i and j become neighbours again. According to these rules rosettes are counted as one T1 transition. The neighbour criterion induces changes in the neighbour lists with time.

[1] B. Ladoux and R. M. Mège, Mechanobiology of collective cell behaviours, Nature Reviews Molecular Cell Biology **18**, 743 (2017).

[2] V. Hakim and P. Silberzan, Collective cell migration: A physics perspective, Reports on Progress in Physics **80**, 076601 (2017).

[3] P. Friedl and D. Gilmour, Collective cell migration in morphogenesis, regeneration and cancer, Nature Reviews Molecular Cell Biology **10**, 445 (2009).

[4] A. Brugués, E. Anon, V. Conte, J. H. Veldhuis, M. Gupta, J. Colombelli, J. J. Muñoz, G. W. Brodland, B. Ladoux, and X. Trepat, Forces driving epithelial wound healing, Nature Physics **10**, 683 (2014).

[5] K. D. Irvine and E. Wieschaus, Cell intercalation during Drosophila germband extension and its regulation by pair-rule segmentation genes, Development **120**, 827 (1994).

[6] D. Weaire and N. Rivier, Soap, cells and statistics—random patterns in two dimensions, Contemporary Physics **25**, 59 (1984).

[7] J. Stavans, The evolution of cellular structures, Reports on Progress in Physics **56**, 733 (1993).

[8] H. P. Jain, A. Voigt, and L. Angheluta, Robust statistical properties of T1 transitions in a multi-phase field model of cell monolayers, Scientific Reports **13**, 10096 (2023).

[9] H. P. Jain, A. Voigt, and L. Angheluta, From cell intercalation to flow, the importance of T1 transitions, Physical Review Research **6**, 033176 (2024).

[10] C. Bertet, L. Sulak, and T. Lecuit, Myosin-dependent junction remodelling controls planar cell intercalation and axis elongation, Nature **429**, 667 (2004).

[11] J. T. Blankenship, S. T. Backovic, J. S. Sanny, O. Weitz, and J. A. Zallen, Multicellular Rosette Formation Links Planar Cell Polarity to Tissue Morphogenesis, Developmental Cell **11**, 459 (2006).

[12] A. Mongera, P. Rowghanian, H. J. Gustafson, E. Shelton, D. A. Kealhofer, E. K. Carn, F. Serwane, A. A. Lucio, J. Giammona, and O. Campàs, A fluid-to-solid jamming transition underlies vertebrate body axis elongation, Nature **561**, 401 (2018).

[13] S. Kim, M. Pochitaloff, G. A. Stooke-Vaughan, and O. Campàs, Embryonic tissues as active foams, Nature Physics **17**, 859 (2021).

[14] A. Mongera, M. Pochitaloff, H. J. Gustafson, G. A. Stooke-Vaughan, P. Rowghanian, S. Kim, and O. Campàs, Mechanics of the cellular microenvironment as probed by cells in vivo during zebrafish presomitic mesoderm differentiation, Nature Materials **22**, 135 (2023).

[15] D. Bi, J. H. Lopez, J. M. Schwarz, and M. L. Manning, Energy barriers and cell migration in densely packed tissues, Soft matter **10**, 1885 (2014).

[16] M. E. Rosa and M. A. Fortes, Nucleation and glide of dislocations in a monodisperse two-dimensional foam under uniaxial deformation, Philosophical Magazine A **77**, 1423 (1998).

[17] D. Wenzel, S. Praetorius, and A. Voigt, Topological and geometrical quantities in active cellular structures, Journal of Chemical Physics **150**, 10.1063/1.5085766 (2019).

[18] R. Mueller, J. M. Yeomans, and A. Doostmohammadi, Emergence of active nematic behavior in monolayers of isotropic cells, Physical review letters **122**, 048004 (2019).

[19] T. B. Saw, A. Doostmohammadi, V. Nier, L. Kocgozlu, S. Thampi, Y. Toyama, P. Marcq, C. T. Lim, J. M. Yeomans, and B. Ladoux, Topological defects in epithelia govern cell death and extrusion, Nature **544**, 212 (2017).

[20] J.-M. Armengol-Collado, L. N. Carenza, J. Eckert, D. Krommydas, and L. Giomi, Epithelia are multiscale active liquid crystals, Nature Physics **19**, 1773 (2023).

[21] M. Nonomura, Study on Multicellular Systems Using a Phase Field Model, PLOS ONE **7**, e33501 (2012).

[22] H. P. Jain, D. Wenzel, and A. Voigt, Impact of contact inhibition on collective cell migration and proliferation, Physical Review E **105**, 034402 (2022).

[23] E. Ferrante, A. E. Turgut, M. Dorigo, and C. Huepe, Elasticity-based mechanism for the collective motion of self-propelled particles with springlike interactions: a model system for natural and artificial swarms, Physical review letters **111**, 268302 (2013).

[24] E. Lång, A. Lång, P. Blicher, T. Rognes, P. G. Dommersnes, and S. O. Bøe, Topology-guided polar ordering of collective cell migration, Science Advances **10**, eadk4825 (2024).

[25] R. D. Ho, S. O. Bøe, D. K. Dysthe, and L. Angheluta, Role of tissue fluidization and topological defects in epithelial tubulogenesis, Physical Review Research **6**, 023315 (2024).

[26] S. B. Nissen, S. Rønhild, A. Trusina, and K. Sneppen, Theoretical tool bridging cell polarities with development of robust morphologies, Elife **7**, e38407 (2018).

[27] D. Bi, X. Yang, M. C. Marchetti, and M. L. Manning, Motility-driven glass and jamming transitions in biological tissues, Physical Review X **6**, 021011 (2016).

[28] J. A. Park, J. H. Kim, D. Bi, J. A. Mitchel, N. T. Qazvini, K. Tantisira, C. Y. Park, M. McGill, S. H. Kim, B. Gweon, J. Notbohm, R. Steward, S. Burger, S. H. Randell, A. T. Kho, D. T. Tambe, C. Hardin, S. A. Shore, E. Israel, D. A. Weitz, D. J. Tschumperlin, E. P. Henske, S. T. Weiss, M. L. Manning, J. P. Butler, J. M. Drazen, and J. J. Fredberg, Unjamming and cell shape in the asthmatic airway epithelium, Nature Materials 2014 14:10 **14**, 1040 (2015).

[29] S. Alt, P. Ganguly, and G. Salbreux, Vertex models: From cell mechanics to tissue morphogenesis, Philosophical Transactions of the Royal Society B: Biological Sciences **372** (2017).

[30] M. Salvalaglio, M. Selch, A. Voigt, and S. M. Wise, Doubly degenerate diffuse interface models of anisotropic sur-

face diffusion, Mathematical Methods in the Applied Sciences , 1 (2020).

[31] S. Vey and A. Voigt, AMDiS: Adaptive multidimensional simulations, Computing and Visualization in Science **10**, 57 (2007).

[32] T. Witkowski, S. Ling, S. Praetorius, and A. Voigt, Software concepts and numerical algorithms for a scalable adaptive parallel finite element method, Advances in Computational Mathematics **41**, 1145 (2015).

[33] S. Praetorius and A. Voigt, *Collective Cell Behaviour – a Cell-Based Parallelisation Approach for a Phase Field Active Polar Gel Model*, NIC Series No. 49 (Forschungszentrum Jülich GmbH, Zentralbibliothek, Jülich, 2018).

Supplementary Material

Harish P. Jain, Richard D.J.G. Ho, and Luiza Angheluta*
Njord Centre
Department of Physics
University of Oslo

I. ADDITIONAL FIGURES

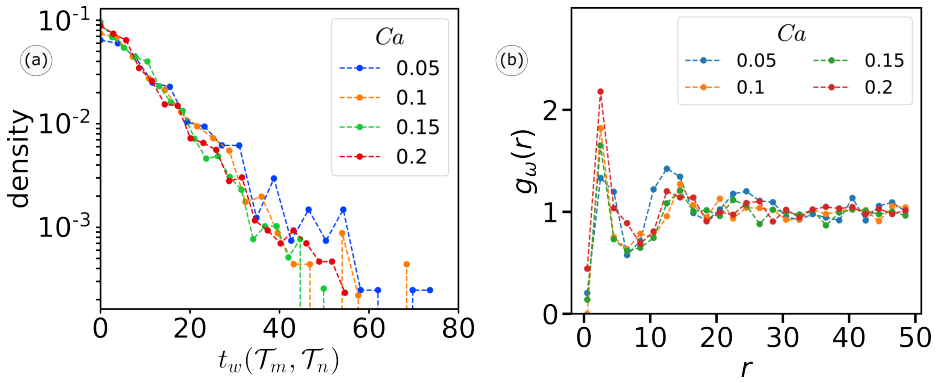


FIG. 1: **Spatiotemporal properties for varying deformability Ca in the MPF model**: (a) Waiting time t_w probability density distribution between *successive* T1s $\mathcal{T}_m$ and $\mathcal{T}_n$ undergone by a cell in the MPF model for varying deformability Ca. (b) Radial distribution function $g_\omega(r)$ between T1 transitions for MPF model for $\omega = 25$ and varying deformability Ca.

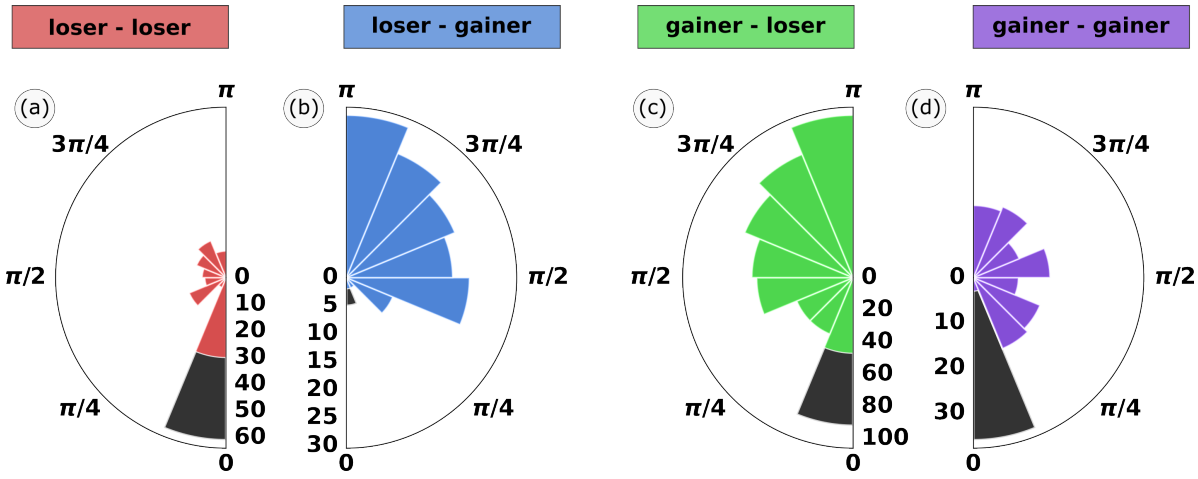


FIG. 2: **Successive T1s in absence of shape alignment** $\alpha = 0$: (a-d) For four different patterns of *successive* T1 events, i.e., $\mathcal{T}_m$(1st T1) and $\mathcal{T}_n$(2nd T1) undertaken by a cell: Fixing the origin to the center of mass of cell i, the difference in orientation of each element in the set of vertices created in $(\mathcal{T}_m)$ (i.e., $(\mathcal{U}_i^+(\mathcal{T}_m))$) with each element in the set of vertices annihilated in $(\mathcal{T}_n)$ (i.e., $(\mathcal{U}_i^-(\mathcal{T}_n))$) is histogrammed over all pairs of *successive* T1 transitions for all cells. The black colour in represents vertices that are created in $\mathcal{T}_m$ and annihilated in $\mathcal{T}_n$. $\alpha = 0$ and other parameters are as per Table I of the main text.

* luiza.angheluta@fys.uio.no

Paper IV

Quantifying the shape of cells - from Minkowski tensors to p-atic order

bioRxiv preprint doi: https://doi.org/10.1101/2025.01.03.631196; this version posted January 3, 2025. The copyright holder for this preprint (which was not certified by peer review) is the author/funder, who has granted bioRxiv a license to display the preprint in perpetuity. It is made available under aCC-BY 4.0 International license.

Quantifying the shape of cells - from Minkowski tensors to p-atic order

Lea Happel[1†], Griseldis Oberschelp[1†], Valeriia Grudtsyna[2], Harish P. Jain[3], Rastko Sknepnek[4,5], Amin Doostmohammadi[2], Axel Voigt[1,6,7*]

***For correspondence:** axel.voigt@tu-dresden.de (AV)

[†]These authors contributed equally to this work

[1]Institute of Scientific Computing, TU Dresden, 01062 Dresden, Germany; [2]Niels Bohr Institute, University of Copenhagen, Kobenhavn, 2100, Denmark; [3]Njord Centre, Physics Department, University of Oslo, Oslo, Norway; [4]School of Life Sciences, University of Dundee, Dundee DD1 5EH, United Kingdom; [5]School of Science and Engineering, University of Dundee, Dundee DD1 4HN, United Kingdom; [6]Center of Systems Biology Dresden, Pfotenhauerstr. 108, 01307 Dresden, Germany; [7]Cluster of Excellence, Physics of Life, TU Dresden, Arnoldstr. 18, 01307 Dresden, Germany

Abstract P-atic liquid crystal theories offer new perspectives on how cells self-organize and respond to mechanical cues. Understanding and quantifying the underlying orientational orders is therefore essential for unraveling the physical mechanisms that govern tissue dynamics. Due to the deformability of cells this requires quantifying their shape. We introduce rigorous mathematical tools and a reliable framework for such shape analysis. Applying this to segmented cells in MDCK monolayers and computational approaches for active vertex models and multiphase field models challenges previous findings and opens new pathways for understanding the role of orientational symmetries and p-atic liquid crystal theories in tissue mechanics and development.

Introduction

The importance of orientational order in biological systems is becoming increasingly clear, as it plays a critical role in processes such as tissue morphogenesis, collective cell motion, and cellular extrusion. Orientational order results from the shapes of cells and their alignments with neighboring cells. Disruptions in this order, known as topological defects, are often linked to key biological events. For instance, defects—points or lines where the order breaks down—can drive cell extrusion (***Saw et al., 2017***; ***Monfared et al., 2023***) or trigger morphological changes in tissues (***Maroudas-Sacks et al., 2021***; ***Ravichandran et al., 2024***). Orientational order is linked to liquid crystal theories and should here be interpreted in a broad sense. Recent evidence extends beyond nematic order, characterized by symmetry under $180° = 2\pi/2$ rotation, to higher-order symmetries such as tetratic order ($90° = 2\pi/4$), hexatic order ($60° = 2\pi/6$), and even general p-atic orders ($2\pi/p$, p being an integer). In biological contexts, nematic order ($p = 2$) has been widely studied in epithelial tissues (***Duclos et al., 2017***; ***Saw et al., 2017***; ***Kawaguchi et al., 2017***), linking defects to cellular behaviors and tissue organization. More complex orders, such as tetratic order ($p = 4$) (***Cislo et al., 2023***) and hexatic oder ($p = 6$) (***Li and Ciamarra, 2018***; ***Durand and Heu, 2019***; ***Pasupalak et al., 2020***; ***Armengol-Collado et al., 2023***; ***Eckert et al., 2023***), have also been observed in experimental systems, offering new perspectives on how cells self-organize and respond to mechanical cues. Understanding and quantifying orientational order and the corresponding liquid crystal theory are therefore essential for unraveling the physical mechanisms that govern biological dynamics.

bioRxiv preprint doi: https://doi.org/10.1101/2025.01.03.631196; this version posted January 3, 2025. The copyright holder for this preprint (which was not certified by peer review) is the author/funder, who has granted bioRxiv a license to display the preprint in perpetuity. It is made available under aCC-BY 4.0 International license.

In physics, p-atic liquid crystals illustrate how particle shape and symmetry influence phase behavior, with seminal works dating back to Onsager's theories (***Onsager, 1949***). Most prominently, hexatic order ($p = 6$) has been postulated and found by experiments and simulations as an intermediate state between crystalline solid and isotropic liquid in (***Halperin and Nelson, 1978***; ***Nelson and Halperin, 1979***; ***Murray and Van Winkle, 1987***; ***Bladon and Frenkel, 1995***; ***Zahn et al., 1999***; ***Gasser et al., 2010***; ***Bernard and Krauth, 2011***). Other examples are colloidal systems for triadic platelets (***Bowick et al., 2017***) or cubes (***Wojciechowski and Frenkel, 2004***), which lead to p-atic order with $p = 3$ and $p = 4$, respectively. Even pentatic ($p = 5$) and heptatic ($p = 7$) liquid crystals have been engineered (***Wang and Mason, 2018***; ***Yu and Mason, 2023***). The corresponding liquid crystal theories for p-atic order have only recently been defined (***Giomi et al., 2022***; ***Krommydas et al., 2023***) and can also be used in biological contexts. However, while in colloidal systems particle shapes remain fixed, in biological tissues, cells are dynamic: their shapes are irregular, variable, and influenced by internal and external forces. These unique properties make quantifying p-atic order in tissues significantly more challenging, as quantification of the cell shapes is required. We will demonstrate that existing methods, such as bond-orientational order (***Nelson and Halperin, 1979***) or polygonal shape analysis (***Armengol-Collado et al., 2023***), often fail to capture the nuances of irregular cell shapes, which has severe consequences on the definition of p-atic order.

To address this, we adapt Minkowski tensors (***Mecke, 2000***; ***Schröder-Turk et al., 2013***)—rigorous mathematical tools for shape analysis—to quantify p-atic order in cell monolayers. Minkowski tensors provide robust and sensitive measures of shape anisotropy and orientation, accommodating both smooth and polygonal shapes while remaining resilient to small perturbations. By applying these tools, we re-examine previous conclusions about p-atic order in epithelial tissues and demonstrate that certain widely accepted results require reconsideration.

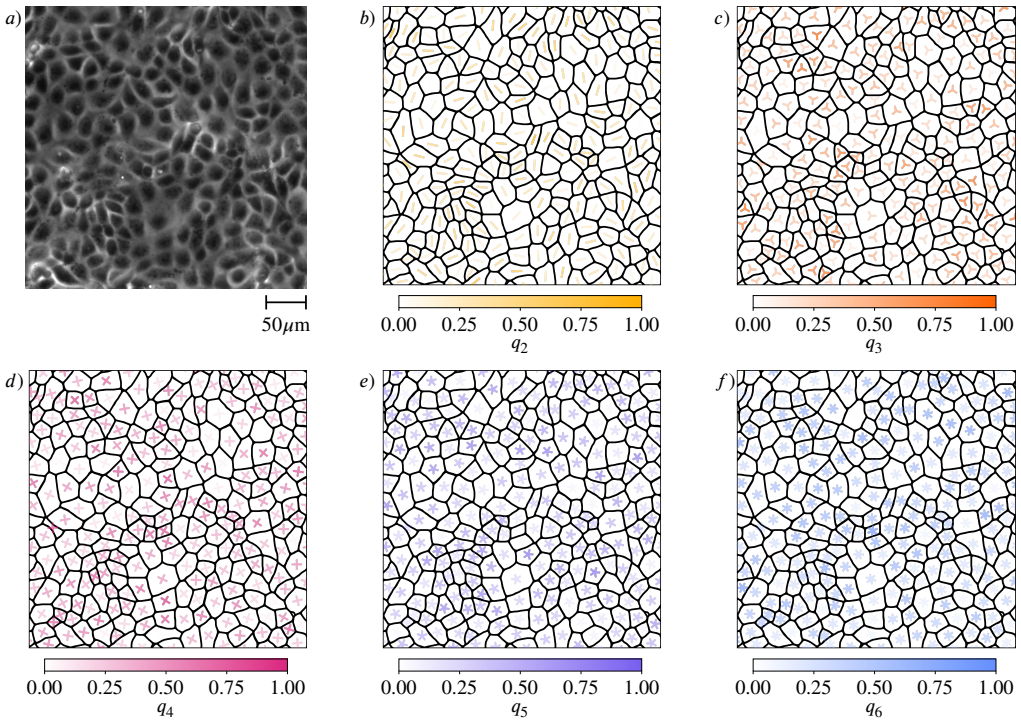
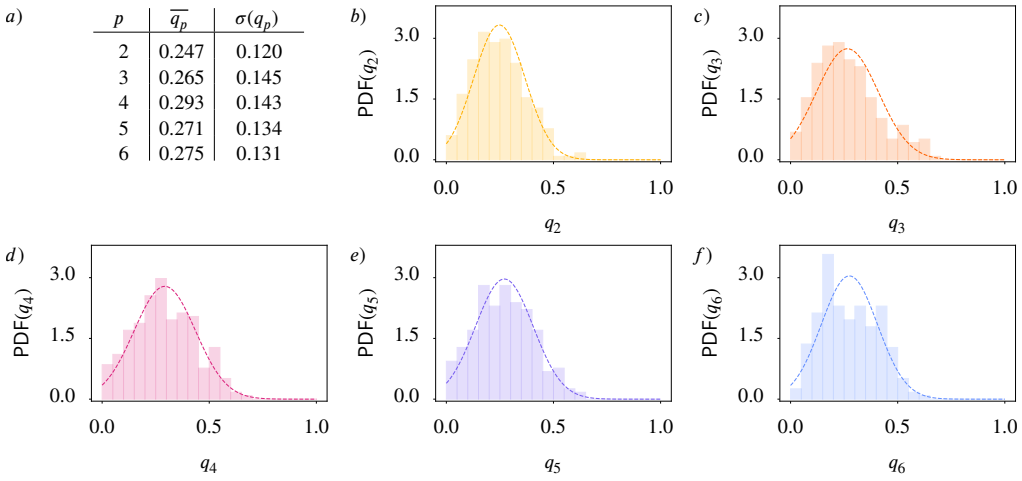


Figure 1. Shape classification of cells in wild-type MDCK cell monolayer. a) Raw experimental data. b) - f) Minkowski tensor, visualized using ϑ_p and q_p, ***Equation 7*** (see Methods and materials) for $p = 2, 3, 4, 5, 6$, respectively. The brightness and the rotation of the p-atic director indicates the magnitude and the orientation, respectively.

bioRxiv preprint doi: https://doi.org/10.1101/2025.01.03.631196; this version posted January 3, 2025. The copyright holder for this preprint (which was not certified by peer review) is the author/funder, who has granted bioRxiv a license to display the preprint in perpetuity. It is made available under aCC-BY 4.0 International license.



p	$\overline{q_p}$	$\sigma(q_p)$
2	0.247	0.120
3	0.265	0.145
4	0.293	0.143
5	0.271	0.134
6	0.275	0.131

Figure 2. Statistical data for cell shapes identified in ***Figure 1*** (see Methods and materials). a) Mean $\overline{q_p}$ and standard deviation $\sigma(q_p)$ of q_p. b) - f) Probability distribution function (PDF) of q_p for $p = 2, 3, 4, 5, 6$, respectively. Normal distributions with the same mean and standard deviations are added to the histograms as a guide to the eye.

Our study leverages a combination of experimental and computational approaches. Experimentally, we analyze confluent monolayers of MDCK (Madin-Darby Canine Kidney) cells, comparing wild-type tissues with E-cadherin knockout variants to explore the role of cell-cell adhesion in orientational order. ***Figure 1*** provide a snapshot of the considered monolayer of wild-type MDCK cells, together with their shape classification by Minkowski tensors. The corresponding statistical data and probability distributions of these quantities are shown in ***Figure 2***. These data already indicate no clear preference of a specific p-atic order and the necessity for robust and sensitive shape classification. Computationally, we employ two complementary models for cell monolayers: the active vertex model and the multiphase field model. These approaches allow us to systematically vary parameters such as cell activity and mechanical properties, providing a comprehensive view of how p-atic order emerges in different contexts.

By combining these robust mathematical tools, experimental insights, and computational models, we establish a reliable framework for quantifying p-atic order in biological tissues. This framework not only challenges previous findings but also opens new pathways for understanding the role of orientational symmetries in tissue mechanics and development.

Methods and materials

Minkowski tensors

Essential properties of the geometry of a two-dimensional object are summarized by scalar-valued size measures, so called Minkowski functionals. They are defined by

$$W_0(C) = \int_C \mathrm{d}C, \quad W_1(C) = \int_{\partial C} \mathrm{d}\partial C, \text{ and } \quad W_2(C) = \int_{\partial C} \mathcal{H}\, \mathrm{d}\partial C, \tag{1}$$

where C is the smooth two-dimensional object, with contour ∂C and $\mathcal{H}$ denotes the curvature of the contour ∂C (see ***Figure 3*** for a schematic description), as reviewed in ***Mecke*** (***2000***). They describe (up to field-specific prefactors) the area, the perimeter and a curvature-weighted integral of the contour, respectively. Minkowski functionals are also known as intrinsic volumes. For convex objects, they have been shown to be continuous and invariant to translations and rotations. Due to these properties and Hadwiger's characterization theorem (***Hadwiger, 1975***), they are natural size descriptors that provide essential and complete information about invariant geometric features. However, these properties also set limits to their use as shape descriptors. Due to rotation

bioRxiv preprint doi: https://doi.org/10.1101/2025.01.03.631196; this version posted January 3, 2025. The copyright holder for this preprint (which was not certified by peer review) is the author/funder, who has granted bioRxiv a license to display the preprint in perpetuity. It is made available under aCC-BY 4.0 International license.

invariance, they are unable to capture the orientation of the shape. To describe more complex shape information the scalar-valued Minkowski functionals are extended to a set of tensor-valued descriptors, known as Minkowski tensors. These objects have been investigated both in mathematical (***Alesker, 1999***; ***Hug et al., 2008***, ***2007***; ***McMullen, 1997***) and in physical literature (***Schröder-Turk et al., 2010a***; ***Kapfer et al., 2012***). Using tensor products of the position vectors $\mathbf{r}$ and the normal vectors $\mathbf{n}$ of the contour $\partial\mathcal{C}$, defined as $\mathbf{r}^a \odot \mathbf{n}^b = \mathbf{r} \odot \ldots \odot \mathbf{r} \odot \mathbf{n} \odot \ldots \odot \mathbf{n}$, the first considered a times and the last b times with $\odot$ denoting the symmetrized tensor product. The Minkowski tensors are defined as

$$\mathbf{W}_0^{a,0}(\mathcal{C}) = \int_{\mathcal{C}} \mathbf{r}^a \,\mathrm{d}\mathcal{C}, \quad \mathbf{W}_1^{a,b}(\mathcal{C}) = \int_{\partial\mathcal{C}} \mathbf{r}^a \odot \mathbf{n}^b \,\mathrm{d}\partial\mathcal{C}, \text{ and } \quad \mathbf{W}_2^{a,b}(\mathcal{C}) = \int_{\partial\mathcal{C}} \mathbf{r}^a \odot \mathbf{n}^b \mathcal{H} \,\mathrm{d}\partial\mathcal{C}. \tag{2}$$

For $\mathbf{W}_j^{0,0}(\mathcal{C}) = W_j(\mathcal{C})$ for $j = 0, 1, 2$, so the Minkowski tensors are extensions of the Minkowski functionals. In analogy to Minkowski functionals also Minkowski tensors have been shown to be continuous for convex objects. Also, analogies to Hadwiger's characterization theorem exist (***Alesker, 1999***). However, for our purpose, the essential property is the continuity. It makes Minkowski functionals and Minkowski tensors a robust measure as small shape changes lead to small changes in the shape descriptor. Due to this property, Minkowski tensors have been successfully used as shape descriptors in different fields, e.g. in materials science as a robust measure of anisotropy in porous (***Schröder-Turk et al., 2010b***) and granular material (***Schröder-Turk et al., 2013***), in astrophysics to describe morphology of galaxies (***Beisbart et al., 2002***), and in biology to distinguish shapes of different types of neuronal cell networks (***Beisbart et al., 2006***) and to determine the direction of elongation in multiphase field models for epithelial tissue (***Mueller et al., 2019***; ***Wenzel and Voigt, 2021***; ***Happel and Voigt, 2024***). However, the mentioned examples exclusively use lower-rank Minkowski tensors $a + b \leq 2$. Higher rank tensors have not been considered in such applications but the theory also guarantees robust description of p-atic orientation for $p = 3, 4, 5, 6, \ldots$. These results hold for smooth contours but also can be extended to polyconvex shapes. Furthermore, known counter-examples for non-convex shapes have very little to no relevance in applications (***Kapfer, 2012***).

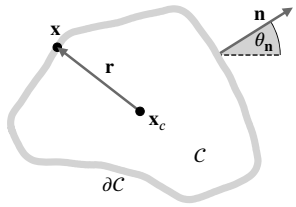


Figure 3. Schematic description of a two-dimensional object $\mathcal{C}$ with contour $\partial\mathcal{C}$. We denote the center of mass with $\mathbf{x}_c$ and vectors from $\mathbf{x}_c$ to points $\mathbf{x}$ on $\partial\mathcal{C}$ with $\mathbf{r}$. The outward-pointing normals are denoted by $\mathbf{n}$, the corresponding angle with the x-axis by $\theta_{\mathbf{n}}$.

Even if all Minkowski tensors carry important geometric information, one type is particularly interesting and will be considered in the following:

$$\boldsymbol{W}_1^{0,p}(C) = \int_{\delta C} \underbrace{\mathbf{n} \odot \mathbf{n} \odot \ldots \odot \mathbf{n}}_{\mathrm{p-}times} \,\mathrm{d}\partial\mathcal{C}. \tag{3}$$

In this case, the symmetrized tensor product agrees with the classical tensor product. If applied to polygonal shapes the Minkowski tensors $\boldsymbol{W}_1^{0,p}(C)$ are related to the Minkowski problem for convex polytops (i.e., generalizations of three-dimensional polyhedra to an arbitrary number of dimensions), which states that convex polytops are uniquely described by the outer normals of the edges and the length of the corresponding edge (***Minkowski, 1897***). Several generalizations of this result exist (***Klain, 2004***; ***Schneider, 2013***), which makes the normal vectors a preferable quantity to describe shapes. However, Minkowski tensors contain redundant information, which asks for an irreducible representation. This can be achieved by decomposing the tensor with respect to the rotation group $SO(2)$ (***Kapfer, 2012***; ***Mickel et al., 2013***; ***Klatt et al., 2022***). Following this approach, one can write

$$\boldsymbol{W}_1^{0,p}(C) = \int_{S^1} \mathbf{u}^p \Psi_C(\mathbf{u}) \,\mathrm{d}\mathbf{u} \quad \text{with} \quad \Psi_C(\mathbf{u}) = \int_{\partial\mathcal{C}} \delta(\mathbf{n}(\mathbf{x}) - \mathbf{u}) \,\mathrm{d}\partial\mathcal{C}, \tag{4}$$

bioRxiv preprint doi: https://doi.org/10.1101/2025.01.03.631196; this version posted January 3, 2025. The copyright holder for this preprint (which was not certified by peer review) is the author/funder, who has granted bioRxiv a license to display the preprint in perpetuity. It is made available under aCC-BY 4.0 International license.

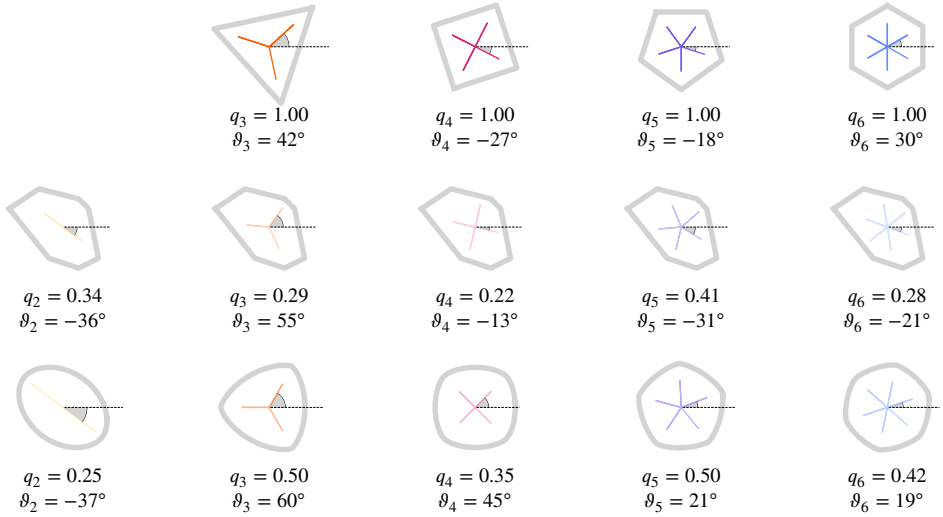


Figure 4. Regular and irregular shapes, adapted from ***Armengol-Collado et al.*** (***2023***) and ***Schaller et al.*** (***2024***), with magnitude and orientation calculated by ***Equation 7***. For regular shapes, the corresponding magnitude of q_p is always 1.0 and the detected angle is the minimal angle of the p-atic orientation with respect to the x-axis. Note that no shape with $q_2 = 1.0$ is shown, as this would be a line. The visualization uses rotationally-symmetric direction fields (known as p-RoSy fields in computer graphics (***Vaxman et al., 2016***)). The brightness scales with the magnitude of the p-atic order, q_p, see colorbars in ***Figure 1***.

with $\Psi_C(\mathbf{u})$ being proportional to the probability density of the normal vectors. Identifying $\mathbf{u} \in S^1$ by the angle θ between $\mathbf{u}$ and the $x-$axis allows to write

$$\Psi_C(\theta) = \sum_{p=-\infty}^{\infty} \psi_p(C) e^{-ip\theta} \quad \text{with} \quad \psi_p(C) = \frac{1}{2\pi} \int_0^{2\pi} \Psi_C(\theta) e^{ip\theta} \, \mathrm{d}\theta. \tag{5}$$

The Fourier coefficients $\psi_p(C)$ are the irreducible representations of $\boldsymbol{W}_1^{0,p}(C)$ and can be written as

$$\psi_p(C) = \frac{1}{2\pi} \int_{\partial C} e^{ip\theta_{\mathbf{n}}} \, \mathrm{d}\partial C, \tag{6}$$

where $\theta_{\mathbf{n}}$ is the orientation of the outward pointing normal $\mathbf{n}$. The phase of the complex number $\psi_p(C)$ contains information about the preferred orientation and the absolute value $|\psi_p(C)|$ is a scalar index. We thus define

$$\vartheta_p(C) = \frac{1}{p} \arctan 2 \left(\Im\psi_p(C), \Re\psi_p(C) \right) + \frac{\pi}{p} \quad \text{and} \quad q_p(C) = \frac{|\psi_p(C)|}{\psi_0(C)}, \tag{7}$$

with $\Im\psi_p$ and $\Re\psi_p$ the imaginary and real part of ψ_p, respectively, and $\psi_0(C) = \frac{W_1(C)}{2\pi}$. We have $q_p(C) \in [0, 1]$ quantifying the strength of p-atic order. ***Figure 4*** illustrates the concept for polygonal and smooth shapes and ***Figure 5*** illustrates the calculation of q_p and ϑ_p at the example of an equilateral triangle. Note that the constant factor of $1/(2\pi)$ in ***Equation 6*** does not influence the result of ***Equation 7*** and is therefore disregarded in ***Figure 5***. Alternative derivations of ***Equation 7*** consider higher order trace-less tensors (***Virga, 2015***; ***Giomi et al., 2022***; ***Armengol-Collado et al., 2023***) generated by the normal $\mathbf{n}$. In this case $\vartheta_p(C)$ (orange triatic director in ***Figure 5*** right) correspond to the eigenvector to the negative eigenvalue and $\vartheta_p(C) - \pi/p$ (gray triatic director in ***Figure 5*** right) to the eigenvector to the positive eigenvalue. For $p = 2$ this tensor based approach corresponds to the structure tensor (***Mueller et al., 2019***).

As pointed out in the introduction, p-atic orders have already been identified in biological tissue and model systems. However, the way to quantify rotational symmetry in these works differs from the Minkowski tensors. In ***Armengol-Collado et al.*** (***2023***) the cell contour is approximated by a

bioRxiv preprint doi: https://doi.org/10.1101/2025.01.03.631196; this version posted January 3, 2025. The copyright holder for this preprint (which was not certified by peer review) is the author/funder, who has granted bioRxiv a license to display the preprint in perpetuity. It is made available under aCC-BY 4.0 International license.

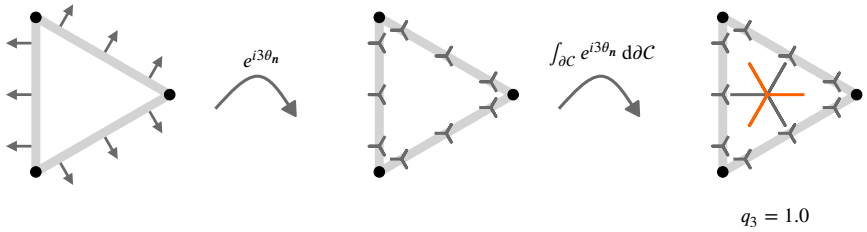


Figure 5. Illustrative description of the definition of q_3 for an equilateral triangle. Considering rotational symmetries under a rotation $120° = 2\pi/3$ means that vectors with an angle of $120°$ or $240°$ are treated as equal. Applied to the normals $\mathbf{n}$ (left), this means that under this rotational symmetry the normals on the three different edges are equal. Mathematically this is expressed through $e^{3i\theta_\mathbf{n}}$ resulting in the triatic director shown instead of the normals $\mathbf{n}$ (middle). One leg of the triatic director always points in the direction as the normal. While only shown for 3 points on each edge, we obtain an orientation with the respective symmetry on every point of the contour $\partial\mathcal{C}$. Considering the line integral along the contour provides the dominating triatic director, shown in the center of mass (right). To get a value between 0.0 and 1.0 for q_3 we normalize this integral with the length of the contour, which corresponds to q_0. As all triatic directors point in the same direction we obtain $q_3 = 1.0$ in this specific example. To be consistent with other approaches we rotate the resulting triatic director by $60° = \pi/3$ leading to the orange triadic director, which is the quantity used for visualization.

polygon with V vertices having coordinates $\mathbf{x}_i$. The considered polygonal shape analysis is based on the shape function

$$\gamma_p(C) = \frac{\sum_{i=1}^{V} |\mathbf{r}_i|^p e^{ip\theta_i}}{\sum_{i=1}^{V} |\mathbf{r}_i|^p}, \tag{8}$$

with $\mathbf{r}_i = \mathbf{x}_i - \mathbf{x}_c$ being the vector from the center of mass $\mathbf{x}_c$ and θ_i being the orientation of the i-th vertex of the polygon with respect to its center of mass. As the center of mass can be computed by $\mathbf{x}_c = \frac{1}{V}\sum_{i=1}^{V} \mathbf{x}_i$ the only input data are the coordinates of the vertices of the V-sides polygon. ***Equation 8*** captures the degree of regularity of the polygon by its amplitude $0 \leq |\gamma_p| \leq 1$ and its orientation ϑ_p which follows as

$$\vartheta_p(C) = \frac{1}{p} \arctan \frac{\Im\gamma_p(C)}{\Re\gamma_p(C)}, \tag{9}$$

with $\Im\gamma_p$ and $\Re\gamma_p$ the imaginary and real part of γ_p, respectively. Instead of the normals $\mathbf{n}$, the descriptor is based on the position vector $\mathbf{r}$. One might be tempted to think that ***Equation 9*** is related to the irreducible representation of $W_1^{p,0}$. This is, however, not the case as the weighting in ***Equation 9*** is done with respect to the magnitude of $\mathbf{r}$, while in $W_1^{p,0}$ the weighting is done with respect to the contour integral. Furthermore, in contrast to the Minkowski tensors, ***Equation 9*** takes into account only the vectors at the vertices and not the vectors along the full cell contour. While this seems to be a technical detail, it has severe consequences. The theoretical basis, which guarantees continuity, no longer holds. This leads to unstable behaviour, as illustrated in ***Figure 6***. While the shape of the polygons is almost identical, there is a jump in γ_3 and γ_4 as we go from four to three vertices. The weighting according to the magnitude cannot cure this, as the magnitude of the shrinking vector is far from zero shortly before this vertex vanishes. In the context of cellular systems, such deformations are a regular occurrence rather than an artificially constructed test case. We will demonstrate the impact while discussing the results and recommend only using robust descriptors such as the Minkowski tensors or their irreducible representations.

We further note that bond order parameters Ψ_p^{bond}, which consider the connection between cells, have also been used as shape descriptors (***Li and Ciamarra, 2018***; ***Durand and Heu, 2019***; ***Pasupalak et al., 2020***). Introduced in ***Nelson and Halperin*** (***1979***), these parameters are

$$\Psi_p^{bond} = \frac{1}{B}\sum_{b=1}^{B} e^{ip\theta_b}, \tag{10}$$

bioRxiv preprint doi: https://doi.org/10.1101/2025.01.03.631196; this version posted January 3, 2025. The copyright holder for this preprint (which was not certified by peer review) is the author/funder, who has granted bioRxiv a license to display the preprint in perpetuity. It is made available under aCC-BY 4.0 International license.

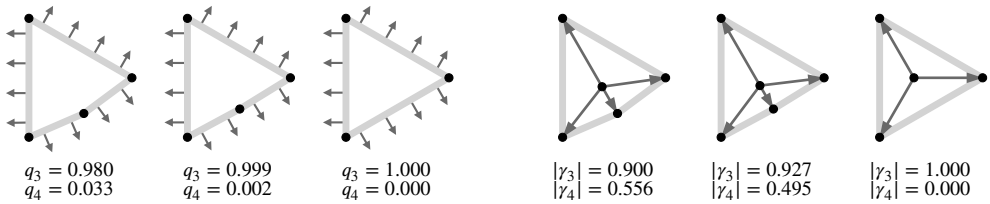


Figure 6. Defining p-atic order for deformable objects requires robust shape descriptors. Shown is the strength of p-atic order for a polygon converging to an equilateral triangle. a) using q_p and b) using γ_p. The considered vectors used in the computations, normals $\mathbf{n}$ of the contour for the Minkowski tensors and $\mathbf{r}_i$ for γ_p, are shown. Note that the choice of the center of mass highly influences the value of γ_p. We here used the described approach following ***Armengol-Collado et al.*** (***2023***).

with B denoting the number of bonds and θ_b the orientation of the bond b. In the context of monolayer tissues, B is understood as the number of neighbors, and θ_b as the orientation of the connection of the center of mass of the current cell with the center of mass of the neighbor b (***Loewe et al., 2020***; ***Monfared et al., 2023***). So cells with the same contour but different neighbor relations lead to different bond order parameters. This characteristic should already disqualify these measures as shape descriptors. However, as discussed in detail in ***Mickel et al.*** (***2013***), they are not robust even for the task they are designed for. We therefore do not discuss them further.

Simulation methods

We consider two modeling approaches, an active vertex model and a multiphase field model. Both have been proven to capture various generic properties of epithelial tissue (***Hakim and Silberzan, 2017***; ***Alert and Trepat, 2020***; ***Moure and Gomez, 2021***). The key aspects of formulations are outlined in ***Box 1*** and ***Box 2***. They refer to (***Koride et al., 2018***; ***Das et al., 2021***; ***Killeen et al., 2022***) and (***Wenzel and Voigt, 2021***; ***Jain et al., 2023***, ***2024b***), respectively. Parameters used within these models are listed in ***Appendix 1 Table 1*** and ***Appendix 1 Table 2***.

The initial configuration for the active vertex model simulations was built by placing N points randomly in a periodic simulation box of length $L \times L$ and ensuring that no two points were within a distance less than r_{cut} from each other. The points were used to create a Voronoi tiling. Typically, such a tiling had cells of very irregular shapes. To make cell shapes more uniform, the centroids of each tile were computed and used as seeds for a new Voronoi tiling. This process was iterated until it converted within the tolerance of 10^{-5}, resulting in a so-called well-centered Voronoi tiling with cells of random shapes but similar sizes. Initial directions of polarity vectors $\hat{\mathbf{n}}_{C_i}$ were chosen at random from a uniform distribution. The initial configuration for the multiphase field model simulations considers a regular arrangement of N cells of equal size in a periodic simulation box of length $L \times L$ with randomly chosen directions of self-propulsion and simulating for several time steps until the cell shapes appear sufficiently irregular. For both models we consider 100 cells and analyse time instances of the evolution.

Experimental setup

Cell culture

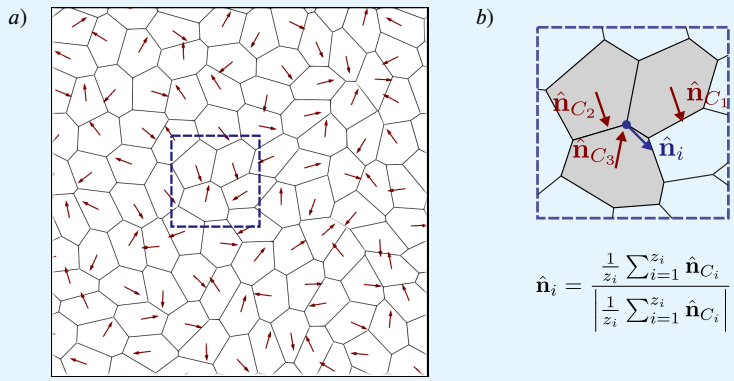
Madin-Darby canine kidney (MDCK) cells were cultured in DMEM (DMEM, low glucose, GlutaMAX™ Supplement, pyruvate) supplemented with $10\,\%$ fetal bovine serum (FBS; Gibco) and $100\,\mathrm{U/mL}$ penicillin/streptomycin (Gibco) at $37\,^{\circ}\mathrm{C}$ with $5\,\%$ CO_2. The cell line was tested mycoplasma.

Monolayer preparation

Cells were seeded on glass-bottom dishes (Mattek) pretreated with $10\,\mu\mathrm{g/mL}$ fibronectin human plasma in phosphate buffered saline (PBS, pH 7.4; Gibco). Fibronectin was incubated for $30\,\mathrm{min}$ at $37\,^{\circ}\mathrm{C}$. The initial cell seeding density was sparse. They were imaged approximately 24 hours after, when a confluent monolayer was formed.

bioRxiv preprint doi: https://doi.org/10.1101/2025.01.03.631196; this version posted January 3, 2025. The copyright holder for this preprint (which was not certified by peer review) is the author/funder, who has granted bioRxiv a license to display the preprint in perpetuity. It is made available under aCC-BY 4.0 International license.

Box 1. Active vertex model



Box 1—figure 1. a) Cell contour of the active vertex model. Red arrows represent the polarity vectors that set each cell's instantaneous direction of self-propulsion. b) Zoom in on a vertex surrounded by three cells showing how the direction of self-propulsion on a vertex is calculated.

The active vertex model is based on models discussed in (***Koride et al., 2018***; ***Das et al., 2021***; ***Killeen et al., 2022***). A confluent epithelial tissue is appreciated as a two-dimensional tiling of a plane with the elastic energy given as (***Honda, 1983***; ***Farhadifar et al., 2007***; ***Honda and Nagai, 2022***)

$$E_{\mathrm{VM}} = \frac{K_A}{2}\sum_C \left(A_C - A_0\right)^2 + \frac{K_P}{2}\sum_C \left(P_C - P_0\right)^2, \tag{11}$$

where A_C and P_C are, respectively, area and perimeter of cell C, A_0 and P_0 are, respectively, preferred area and perimeter, and K_A and K_P are, respectively, area and perimeter moduli. For simplicity, it is assumed that all cells have the same values of A_0, P_0, K_A, and K_P. The model can be made dimensionless by dividing ***Equation 11*** by $e^* = K_A A_0^2$,

$$e_{\mathrm{VM}} = \frac{1}{2}\sum_C \left(a_C - 1\right)^2 + \frac{k_P}{2}\sum_C \left(p_C - p_0\right)^2, \tag{12}$$

where $a_C = A_C/A_0$ (i.e. $l^* = \sqrt{A_0}$ is the unit of length), $p_c = P_C/\sqrt{A_0}$, $k_P = K_P/(K_A A_0)$, and $p_0 = P_0/\sqrt{A_0}$. p_0 is called the shape index, and it has been shown to play a central role in determining if the tissue is in a solid or fluid state (***Bi et al., 2015***).

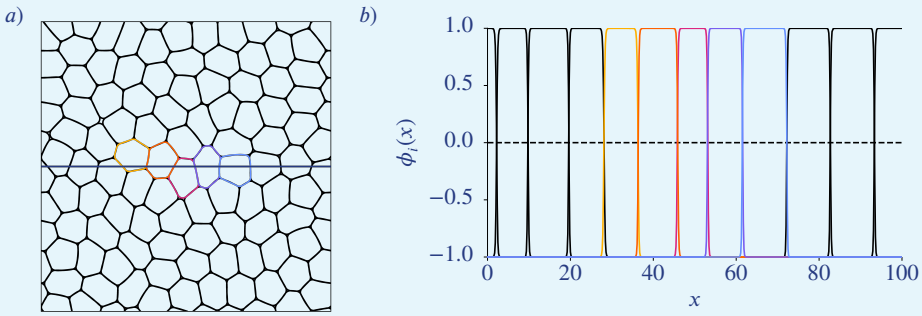
One can use ***Equation 11*** to find the mechanical force on a vertex i as $\mathbf{F}_i = -\nabla_{\mathbf{r}_i} E_{\mathrm{VM}}$, where $\nabla_{\mathbf{r}_i}$ is the gradient with respect to the position $\mathbf{r}_i$ of the vertex. The expression for $\mathbf{F}_i$ is given in terms of the position of the vertex i and its immediate neighbours (***Tong et al., 2023***), which makes it fast to compute. Furthermore, cells move on a substrate by being noisily self-propelled along the direction of their planar polarity described by a unit-length vector $\hat{\mathbf{n}}_{C_i}$ from which the polarity direction at the vertex $\hat{\mathbf{n}}_i$ is defined, see Box 1 - figure 1 b), where z_i is the number of neighbours of vertex i. It is convenient to write $\hat{\mathbf{n}}_i = \cos(\alpha_i)\mathbf{e}_x + \sin(\alpha_i)\mathbf{e}_y$, where α_i is an angle with the $x-$axis of the simulation box. The equations of motion for vertex i is a force balance between active, elastic, and frictional forces and are given as

$$\dot{\mathbf{r}}_i = v_0\hat{\mathbf{n}}_i + \frac{1}{\gamma_{fr}}\mathbf{F}_i, \quad \dot{\alpha}_i = \xi_i(t), \tag{13}$$

where v_0 is the magnitude of the self-propulsion velocity defined as f_0/γ_{fr}. Furthermore the overdot denotes the time derivative, γ_{fr} is the friction coefficient, f_0 is the magnitude of the self-propulsion force (i.e., the activity), $\xi_i(t)$ is Gaussian noise with $\langle\xi_i(t)\rangle = 0$ and $\langle\xi_i(t)\xi_j(t')\rangle = 2D_r\delta_{ij}\delta(t-t')$, where D_r is the rotation diffusion constant and $\langle\cdot\rangle$ is the ensemble average over the noise. Equations of motion can be non-dimensionalised by measuring time in units of $t^* = \gamma_{\mathrm{fr}}/(K_A A_0)$ and force in units of $f^* = K_A A_0^{3/2}$ and integrated numerically using the first-order Euler-Maruyama method with timestep τ.

bioRxiv preprint doi: https://doi.org/10.1101/2025.01.03.631196; this version posted January 3, 2025. The copyright holder for this preprint (which was not certified by peer review) is the author/funder, who has granted bioRxiv a license to display the preprint in perpetuity. It is made available under aCC-BY 4.0 International license.

Box 2. Multiphase field model



Box 2—figure 1. a) Cell contours of the multiphase field model. b) Corresponding phase field functions along the horizontal line in a). Colours correspond to the once in a).

The multiphase field modelling approach follows ***Wenzel and Voigt*** (***2021***); ***Jain et al.*** (***2023***, 2024b). Each cell is described by a scalar phase field variable ϕ_i with $i = 1, 2, \dots, N$, where the bulk values $\phi_i \approx 1$ denotes the cell interior, $\phi_i \approx -1$ denotes the cell exterior, and with a diffuse interface of width $\mathcal{O}(\epsilon)$ between them representing the cell boundary. The phase field ϕ_i follows the conservative dynamics

$$\partial_t \phi_i + \mathbf{v}_i \cdot \nabla \phi_i = \Delta \frac{\delta \mathcal{F}}{\delta \phi_i}, \tag{14}$$

with the free energy functional $\mathcal{F} = \mathcal{F}_{CH} + \mathcal{F}_{INT}$ containing the Cahn-Hilliard energy

$$\mathcal{F}_{CH} = \frac{1}{Ca} \sum_{i=1}^{N} \int_{\Omega} \left(\frac{\epsilon}{2} \|\nabla \phi_i\|^2 + \frac{1}{4\epsilon} (\phi_i^2 - 1)^2 \right) d\mathbf{x}, \tag{15}$$

where the Capillary number Ca is a parameter for tuning the cell deformability, and an interaction energy consisting of repulsive and attractive parts defined as

$$\mathcal{F}_{INT} = \frac{1}{In} \sum_{i=1}^{N} \int_{\Omega} \sum_{j \neq i} a_r (\phi_i + 1)^2 (\phi_j + 1)^2 - a_a (\phi_i^2 - 1)^2 (\phi_j^2 - 1)^2 d\mathbf{x}, \tag{16}$$

where In denotes the interaction strength, and a_r and a_a are parameters to tune contribution of repulsion and attraction. The repulsive term penalises overlap of cell interiors, while the attractive part promotes overlap of cell interfaces. The relation to former formulations is discussed in ***Happel and Voigt*** (***2024***).

Each cell is self-propelled, and the cell activity is introduced through an advection term. The cell velocity field is defined as

$$\mathbf{v}_i(\mathbf{x}, t) = v_0 \mathbf{e}_i(t) \hat{\phi}_i(\mathbf{x}, t), \tag{17}$$

where v_0 is used to tune the magnitude of activity, $\hat{\phi}_i = \frac{\phi_i + 1}{2}$ and $\mathbf{e}_i = [\cos\theta_i(t), \sin\theta_i(t)]$ is its direction. The migration orientation $\theta_i(t)$ evolves diffusively with a drift that aligns to the principal axis of cell's elongation as $d\theta_i = \sqrt{2D_r} dW_i(t) + \alpha(\beta_i(t) - \theta_i(t))dt$, where D_r is the rotational diffusivity, W_i is the Wiener process, $\beta_i(t)$ is the orientation of the cell elongation and α controls the time scale of this alignment.

The resulting system of partial differential equations is considered on a square domain with periodic boundary conditions and is solved by the finite element method within the toolbox AMDiS (***Vey and Voigt, 2007***; ***Witkowski et al., 2015***) and the parallelization concept introduced in ***Praetorius and Voigt*** (***2018***) is considered, which allows scaling with the number of cells. We in addition introduce a de Gennes factor in $\mathcal{F}_{CH}$ to ensure $\phi_i \in [-1, 1]$, see ***Salvalaglio et al.*** (***2021***).

bioRxiv preprint doi: https://doi.org/10.1101/2025.01.03.631196; this version posted January 3, 2025. The copyright holder for this preprint (which was not certified by peer review) is the author/funder, who has granted bioRxiv a license to display the preprint in perpetuity. It is made available under aCC-BY 4.0 International license.

Live cell imaging

Samples were imaged using Nikon ECLIPSE Ti microscope equipped with a H201-K-FRAME Okolab chamber, heating system (Okolab) and a CO_2 pump (Okolab) which maintained them at $37\,^{\circ}\mathrm{C}$ and at $5\,\%$ CO_2. Phase microscopy images were taken each 10th minute using a 10× NA=0.3 Plan Fluor objective and Andor Neo 5.5 sCMOS camera.

Image analysis

The time-series were xy-drift corrected using Fast4DReg plugin ***Laine et al.*** (***2019***), ***Pylvänäinen et al.*** (***2022***) in FIJI. Cells were segmented and tracked using the python module CellSegmentation-Tracker (https://github.com/simonguld/CellSegmentationTracker), which utilizes both Cellpose ***Stringer et al.*** (***2021***) and Trackmate ***Tinevez et al.*** (***2017***). A Cellpose model was trained by manual segmentation of the phase contrast images.

Results

Quantifying orientational order in biological tissues can be realized by Minkowsky tensors. The orientation ϑ_p and the strength of p-atic order q_p in ***Equation 7*** can be computed for any integer p. These quantities describe how cell shapes align with specific rotational symmetries. A recurring challenge in the field is determining whether q_p values for different p can be meaningfully compared. This question is particularly important for interpreting nematic (q_2) and hexatic (q_6) orders, which describe distinct symmetries but often coexist in biological systems. However, a direct comparison is problematic as q_2 and q_6 reveal significant differences in their ranges: $q_2 = 1.0$ represents an idealized line shape that is unattainable for cells, while $q_6 = 1.0$ corresponds to a perfect hexagon observed in experiments and simulations. To further address this, we analyze simulation data from two computational models, examining how deformability and activity—key determinants of tissue mechanics—affect q_p values and their interplay. We employ the active vertex model and the multiphase field model, both of which incorporate activity and deformability. These two parameters are recognized as crucial for capturing the coarse-grained properties of confluent tissues (***Jain et al., 2023***, ***2024b***). By leveraging these complementary frameworks, we ensure that our conclusions are robust across model-specific assumptions and parameter regimes. This dual approach allows us to systematically investigate how these models capture tissue behavior, particularly regarding cell shape variability and resulting p-atic orders.

In the active vertex model, deformability is controlled by the target shape index p_0, reflecting the balance between cell-cell adhesion and cortical tension. The multiphase field model, by contrast, encodes deformability through the capillary number Ca, which directly incorporates cortical tension. Although these models differ conceptually, both have been validated in studies of cell monolayer mechanics, including solid-liquid transitions, neighbor exchange dynamics, and stress profiles (***Fletcher et al., 2014***; ***Alt et al., 2017***; ***Li et al., 2019***; ***Balasubramaniam et al., 2021***; ***Wenzel and Voigt, 2021***; ***Sknepnek et al., 2023***; ***Melo et al., 2023***). Importantly, the active vertex model enforces confluency by design, while the multiphase field model approximates it through dynamic cell-cell interactions, leading to differences in topological rearrangements and cell shape representations.

We vary activity strength (v_0), the shape index (p_0), and the capillary number (Ca), ensuring all parameter combinations remain in the fluid regime. Fluidity was confirmed using metrics such as the mean square displacement (MSD) (***Loewe et al., 2020***), neighbor number variance (***Wenzel and Voigt, 2021***), and the self-intermediate scattering function (***Bi et al., 2016***). Using Minkowski tensors, we computed ϑ_p and q_p values as described in ***Equation 7***, focusing on $p = 2$ and $p = 6$ due to their biological relevance. In solid-like states, such as hexagonal cellular arrangements, hexatic order ($p = 6$) is the appropriate descriptor, as hexagons exhibit $60^{\circ} = 2\pi/6$ rotational symmetry. Hexatic order has been extensively studied in biological systems (***Li and Ciamarra, 2018***; ***Durand and Heu, 2019***; ***Pasupalak et al., 2020***), and its importance in cellular organization is well-documented. In fluid-like states, cells often become elongated, exhibiting nematic order ($p = 2$), characterized by $180^{\circ} = 2\pi/2$ rotational symmetry. Elongated cell shapes are also common in

bioRxiv preprint doi: https://doi.org/10.1101/2025.01.03.631196; this version posted January 3, 2025. The copyright holder for this preprint (which was not certified by peer review) is the author/funder, who has granted bioRxiv a license to display the preprint in perpetuity. It is made available under aCC-BY 4.0 International license.

specific cell types, such as fibroblasts. Quantifying nematic order using q_2 is particularly relevant, as nematic configurations and defects have been linked to critical biological processes, including hydra morphogenesis (***Maroudas-Sacks et al., 2021***) and cell death (***Saw et al., 2017***).

Independence of q_2 and q_6

Recent studies suggest a hexatic-nematic crossover in epithelial tissues, where hexatic order dominates at small scales and nematic order prevails at larger scales (***Eckert et al., 2023***; ***Armengol-Collado et al., 2023***, ***2024***). To explore this relationship, we examine the distribution of (q_2, q_6) values across deformability-activity parameter pairs in both models (***Figure 7***). Despite structural

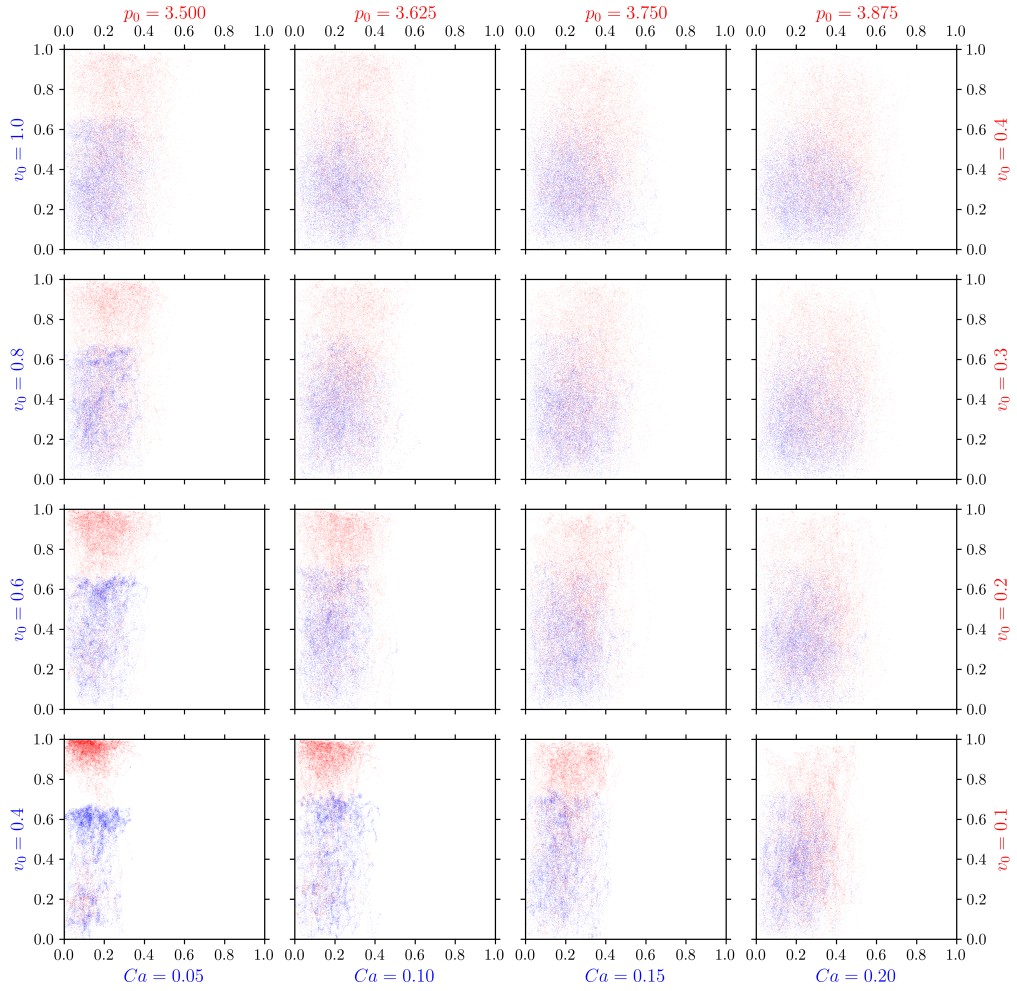


Figure 7. Nematic ($p = 2$) and hexatic ($p = 6$) order are independent of eachother. q_6 (y-axis) versus q_2 (x-axis) for all cells in the multiphase field model (blue) and active vertex model (red). For each cell and each timestep we plot one point (q_2, q_6). Each panel corresponds to specific model parameters; Ca and v_0 for multiphase field model, and p_0 and v_0 for the active vertex model, representing deformability and activity, respectively.

differences between the models, both show consistent trends. Closer examination shows that in near-solid regimes (***Figure 7*** lower left), q_2 and q_6 values cluster tightly due to restricted shape fluctuations. However, even in this regime, small q_2 values can correspond to either small or large q_6 values, and vice versa. In more fluid-like regimes, with higher activity and higher deformability (***Figure 7*** upper right), q_2 and q_6 values become highly scattered. Each q_2 value spans a broad range of q_6 values, and vice versa, demonstrating their independence. These findings underscore that q_p

bioRxiv preprint doi: https://doi.org/10.1101/2025.01.03.631196; this version posted January 3, 2025. The copyright holder for this preprint (which was not certified by peer review) is the author/funder, who has granted bioRxiv a license to display the preprint in perpetuity. It is made available under aCC-BY 4.0 International license.

values for different p measure distinct aspects of cell shape anisotropy and cannot be meaningfully compared directly.

This conclusion also holds on larger length scales. In order to test the hypothesis of a hexatic-nematic crossover at larger length scales (***Armengol-Collado et al., 2023***) we consider a coarse-graining of q_2 and q_6 across spatial domains. Details are described in ***Appendix 2***. ***Appendix 2 - Figure 13*** and ***Appendix 2 -Figure 14*** show the results for the active vertex model and the multiphase field model, respectively. The results show no consistent trends indicative of a crossover, regardless of the considered model and coarse-graining radius. Instead, the apparent convergence of Q_2 and Q_6 values (coarse-grained values of q_2 and q_6) with increasing activity or deformability simply reflects the same trends observed at the individual cell scale.

Dependence of q_p on activity and deformability

The previous analysis demonstrated that comparing q_p across different values of p is not meaningful. However, fixing p and exploring q_p under varying physical conditions offers valuable insights into how tissue properties such as activity and deformability influence cell shape and orientational order. We again focus on nematic ($p = 2$) and hexatic ($p = 6$), as shown in ***Figure 8*** and ***Figure 9***. Additional results for $p = 3, 4, 5$ are provided in ***Figure 8—figure Supplement 1–Figure 8—figure Supplement 3*** (fixed activity) and ***Figure 9—figure Supplement 1–Figure 9—figure Supplement 3*** (fixed deformability). In all plots all cells and all time steps are considered. In ***Figure 8***, we vary deformability (p_0 in the active vertex model and Ca in the multiphase field model) while keeping the activity v_0 constant. Results are presented for the active vertex model (left column) and the multiphase field model (right column). Activity increases from bottom to top rows. Both models show qualitatively similar trends in the probability density functions (PDFs) of q_2 and q_6. For $p = 6$, increasing deformability shifts the PDF of q_6 to the left, indicating lower mean values. In contrast, for $p = 2$, higher deformability leads to higher q_2 values, reflected in a rightward shift of the PDF. This trend is confirmed by the mean values, shown as a function of deformability (p_0 and Ca, respectively) in the inlets. Additionally, the PDFs broaden with increasing deformability, and this effect is more pronounced at lower activity levels. A notable difference between the models is the range of q_p values. In the multiphase field model, q_p rarely exceeds 0.8 due to the smoother, more rounded cell shapes, whereas the active vertex model often produces higher q_p values. In ***Figure 9***, deformability is held constant while activity v_0 is varied. Results are again shown for the active vertex model (left column) and the multiphase field model (right column), with increasing activity indicated by brighter colors. Deformability increases from bottom to top rows. The trends mirror those observed in ***Figure 8***. Increasing activity reduces the mean value of q_6 while increasing q_2, see inlets. The effects of activity are more pronounced at lower deformabilities; at higher deformabilities, differences between parameter regimes diminish. The results agree qualitatively with the ones obtained for the measures $|\gamma_2|$ and $|\gamma_6|$ reported in (***Armengol-Collado et al., 2023***, Extended Data Fig. 3). Note that in the calculation of γ_p every cell is approximated by a polygon. Therefore, also for the multiphase field model the obtained values range up to 1.0. The overall behavior of q_2 and q_6 is summarized in ***Figure 10***, which shows the mean values $\overline{q_2}$ and $\overline{q_6}$ as functions of activity and deformability. For both models:

- $\overline{q_2}$ increases with higher activity or deformability
- $\overline{q_6}$ decreases with higher activity or deformability.

This behaviour is consistent with a trend towards nematic order in more dynamic regimes and toward hexagonal order in more constrained, less dynamic regimes. The first is further confirmed by recent findings in analysing T1 transitions and their effect on cell shapes ***Jain et al.*** (***2024a***). These studies suggest that cells transiently elongate when they are undergoing T1 transitions. As the number of T1 transitions increases with activity or deformability ***Jain et al.*** (***2024b***) this elongation contributes to the observed behavior. The second is consistent with the emergence of hexagonal

bioRxiv preprint doi: https://doi.org/10.1101/2025.01.03.631196; this version posted January 3, 2025. The copyright holder for this preprint (which was not certified by peer review) is the author/funder, who has granted bioRxiv a license to display the preprint in perpetuity. It is made available under aCC-BY 4.0 International license.

arrangements in solid-like states. Corresponding results for $p = 3, 4, 5$ are shown in ***Figure 10—figure Supplement 1***.

Comparison with experiments

Next, we apply shape descriptor framework to experiments on epithelial cells. We consider a monolayer of Madine-Derby-Canine-Kidney (MDCK) cells. We consider two types of cell monolayers: MDCK wild type cells and MDCK E-cad KO cells, which have the E-cadherin protein removed. These E-cad KO cells have weaker cell-cell adhesion strengths and previous studies have shown that compared to wild-type cells, the E-cad KO cells have lower velocities, same spreading area, higher aspect ratio, and higher stiffness ***Balasubramaniam et al.*** (***2021***); **?**. The slower movement of E-cad KO cells compared to the wild-type cells suggest their lower activity, and their higher stiffness can be intepreted as having lower deformability compared to the wild-type cells. However, care must be taken in directly comparing the two cell types and directly comparing to simulation results , as the key parameters varied in simulations—cell activity and deformability—are difficult to manipulate in isolation in experiments. One complicating factor is the strong dependence of cell shape on cell density, as previously reported (***Eckert et al., 2023***). Higher cell densities generally lead to rounder cell shapes, which we confirmed in two distinct experimental setups (see ***Figure 11***). For both wild-type MDCK cells and E-cadherin knockout variants, increased cell density corresponded to lower mean values of q_2, consistent with rounder cell geometries. For higher values of q_p, however, this density-dependent effect was less pronounced. A plausible explanation lies in the geometry of shapes for larger q_p. Rounded shapes close to a circle can yield relatively high q_p values for certain p, such as the example shown in the third row of ***Figure 4***. Distinguishing such shapes from perfect circles requires highly accurate data, which can be difficult to obtain in experimental imaging, potentially masking density-dependent effects for $p = 6$.

Importantly, due to the substantial differences in cell density between wild-type cells and E-cadherin knockout variants, direct comparisons between these two experimental conditions would be unjustifiable. Density influences cell shape too strongly to isolate other effects in these datasets. Despite these limitations, we observed qualitative agreement between experimental and computational results regarding the independence of q_2 and q_6 (see ***Figure 12***). Both measures appear to be unrelated, reinforcing the conclusion that nematic ($p = 2$) and hexatic ($p = 6$) order describe distinct aspects of cell shape and alignment. Consequently, comparing q_2 and q_6 directly is not meaningful, whether in simulations nor in experiments.

Sensitivity of the results on the considered shape descriptor

In order to demonstrate that other methods, such as polygonal shape analysis ***Armengol-Collado et al.*** (***2023***) fail to capture the nuances of irregular cell shapes we also use ***Equation 8*** as a shape descriptor for the considered datasets. For the experimental data and the multiphase field model this first requires an approximation of the cell shape by a polygon. For finding the vertices of the polygon we consider the Voronoi interface method (***Saye and Sethian, 2011***, ***2012***), see ***Appendix 3***. The corresponding figures to ***Figure 1***, ***Figure 2*** and ***Figure 4*** are shown in ***Appendix 3 Figure 16***, ***Appendix 3 Figure 17*** and ***Appendix 3 Figure 15***, respectively. While already these results show quantitative differences, the failure of the approach can best be seen in the qualitative difference between ***Figure 10*** and the corresponding results in ***Appendix 3 Figure 18***, which, instead of the monotonic trend for activity and deformabilty, exhibit nonmonotonic trends, peaking at intermediate values of activity or deformability. These divergences highlight the limitations of γ_p in capturing consistent patterns and emphasize the need for stable, reliable shape descriptors like the Minkowski tensors.

For completeness we also provide the corresponding figures to ***Figure 7*** and ***Figure 13*** in ***Appendix 3 Figure 19*** and ***Appendix 3 Figure 20***, respectively. We hereby only consider the active vertex model. The results are similar to the once obtained using the Minkowski tensors and confirm the independence of p-atic order for different symmetries.

bioRxiv preprint doi: https://doi.org/10.1101/2025.01.03.631196; this version posted January 3, 2025. The copyright holder for this preprint (which was not certified by peer review) is the author/funder, who has granted bioRxiv a license to display the preprint in perpetuity. It is made available under aCC-BY 4.0 International license.

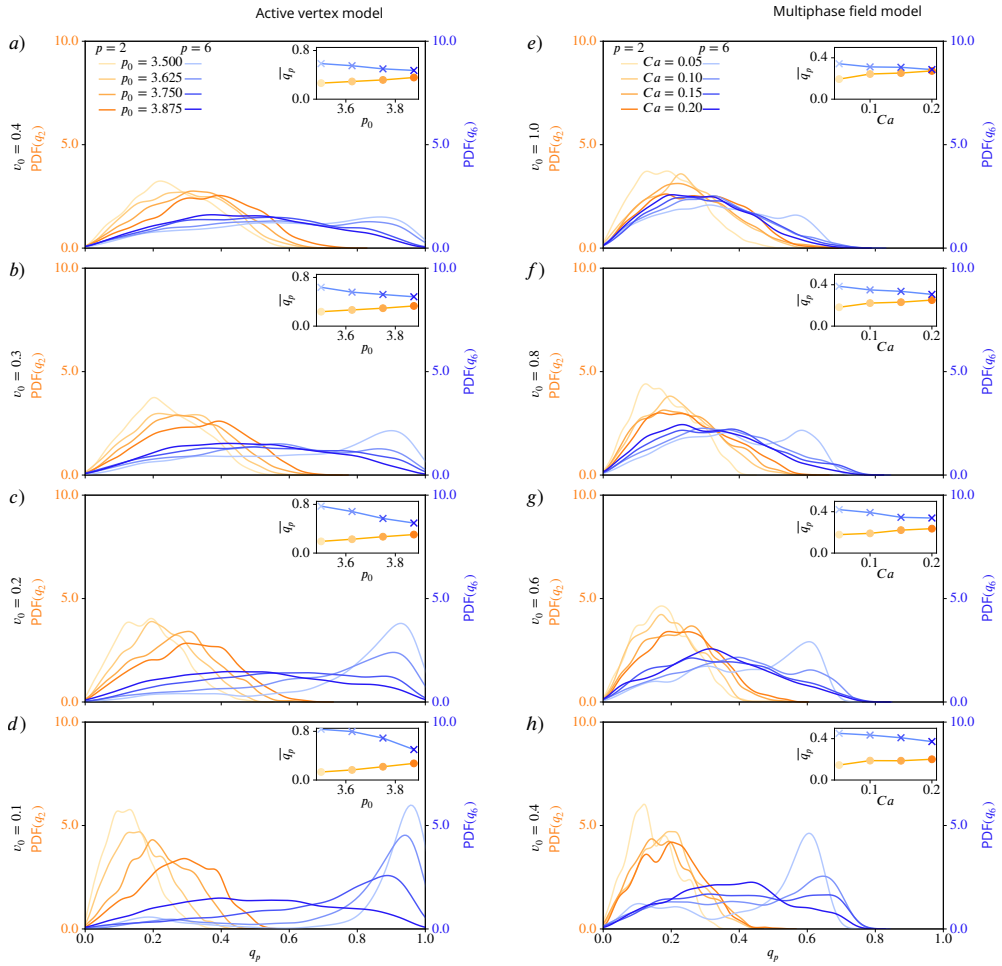


Figure 8. Nematic ($p = 2$) and hexatic ($p = 6$) order depend on deformability of the cells. Probability distribution functions (PDFs) for q_2 (shades of orange) and q_6 (shades of blue), using kde-plots, for varying deformability p_0 or Ca and fixed activity v_0. Inlets show mean values of q_2 and q_6 as function of deformability. a) - d) active vertex model, e) - h) multiphase field model for decreasing activity.

Figure 8—figure supplement 1. PDFs for q_3 using kde-plots, for varying deformability p_0 or Ca and fixed activity v_0. Inlets show mean values of q_3 as function of deformability. a) - d) active vertex model, e) - h) multiphase field model for descreasing activity.

Figure 8—figure supplement 2. PDFs for q_4 using kde-plots, for varying deformability p_0 or Ca and fixed activity v_0. Inlets show mean values of q_4 as function of deformability. a) - d) active vertex model, e) - h) multiphase field model for decreasing activity.

Figure 8—figure supplement 3. PDFs for q_5 using kde-plots, for varying deformability p_0 or Ca and fixed activity v_0. Inlets show mean values of q_5 as function of deformability. a) - d) active vertex model, e) - h) multiphase field model for decreasing activity.

bioRxiv preprint doi: https://doi.org/10.1101/2025.01.03.631196; this version posted January 3, 2025. The copyright holder for this preprint (which was not certified by peer review) is the author/funder, who has granted bioRxiv a license to display the preprint in perpetuity. It is made available under aCC-BY 4.0 International license.

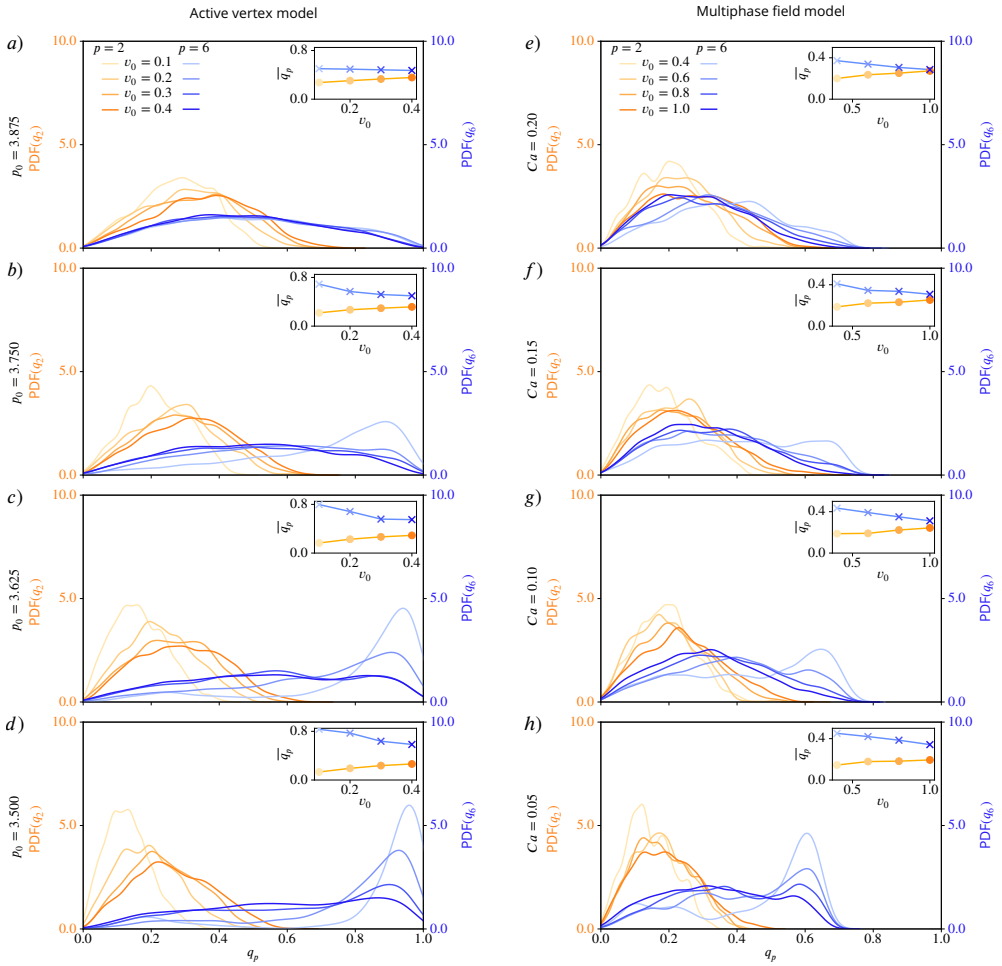


Figure 9. Nematic ($p = 2$) and hexatic ($p = 6$) order depend on activity of the cells. Probability distribution functions (PDFs) for q_2 (shades of orange) and q_6 (shades of blue), using kde-plots, for varying activity v_0 and fixed deformability p_0 or Ca. Inlets show mean values of q_2 and q_6 as function of activity. a) - d) active vertex model and e) - h) multiphase field model for decreasing deformability.

Figure 9—figure supplement 1. PDFs for q_3 using kde-plots, for varying activity v_0 and fixed deformability p_0 or Ca. Inlets show mean values of q_3 as function of activity. a) - d) active vertex model and e) - h) multiphase field model for decreasing deformability.

Figure 9—figure supplement 2. PDFs for q_4 using kde-plots, for varying activity v_0 and fixed deformability p_0 or Ca. Inlets show mean values of q_4 as function of activity. a) - d) active vertex model and e) - h) multiphase field model for decreasing deformability.

Figure 9—figure supplement 3. PDFs for q_5 using kde-plots, for varying activity v_0 and fixed deformability p_0 or Ca. Inlets show mean values of q_5 as function of activity. a) - d) active vertex model and e) - h) multiphase field model for decreasing deformability.

bioRxiv preprint doi: https://doi.org/10.1101/2025.01.03.631196; this version posted January 3, 2025. The copyright holder for this preprint (which was not certified by peer review) is the author/funder, who has granted bioRxiv a license to display the preprint in perpetuity. It is made available under aCC-BY 4.0 International license.

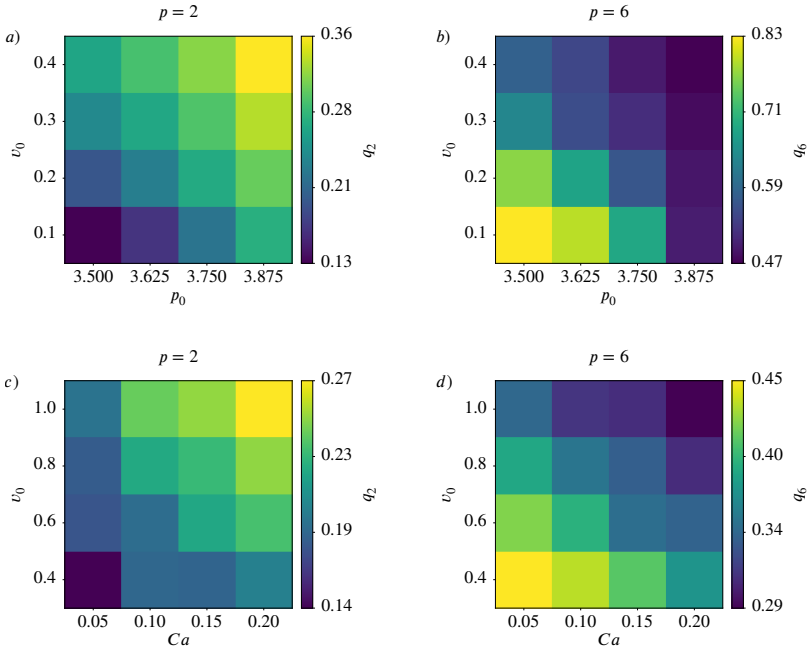


Figure 10. Nematic ($p = 2$) and hexatic ($p = 6$) order depend on activity and deformability of the cells. Mean value $\overline{q_p}$ for $p = 2$ (left) and $p = 6$ (right) as function of deformability p_0 or Ca and activity v_0 for active vertex model (a) and b)) and multiphase field model (c) and d)).

Figure 10—figure supplement 1. Mean value $\overline{q_p}$ for $p = 3$ (left), $p = 4$ (middle) and $p = 5$ (right) as function of deformability p_0 or Ca and activity v_0 for active vertex model (a) - c)) and multiphase field model (d) - f)).

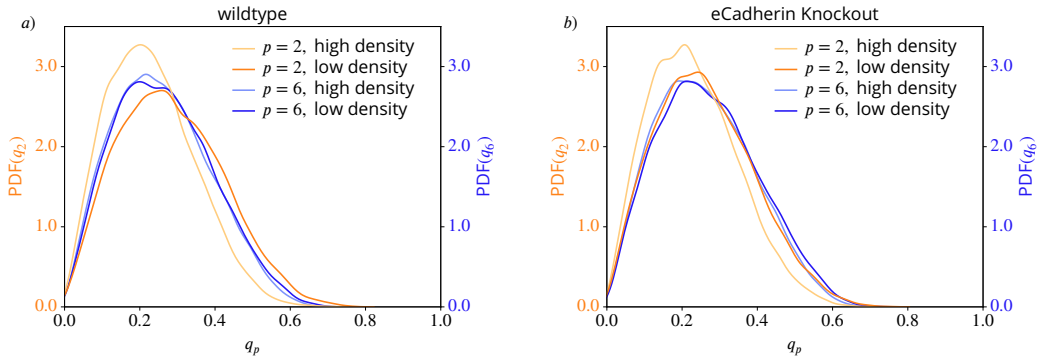


Figure 11. In experimental system of MDCK cells, nematic ($p = 2$) and hexatic ($p = 6$) order respond differently to change in cell density. Probability distribution functions (PDFs) using kde-plots, for q_2 (orange shaded) and q_6 (blue shaded) for different densities in a) wildtype MDCK cell monolayer and b) E-cadherin knockout cell monolayer.

bioRxiv preprint doi: https://doi.org/10.1101/2025.01.03.631196; this version posted January 3, 2025. The copyright holder for this preprint (which was not certified by peer review) is the author/funder, who has granted bioRxiv a license to display the preprint in perpetuity. It is made available under aCC-BY 4.0 International license.

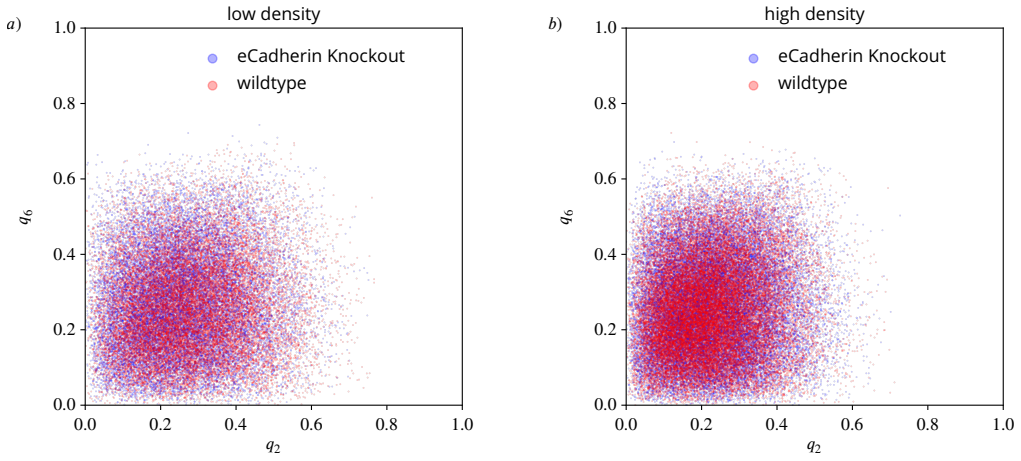


Figure 12. In experimental system of MDCK cells nematic ($p = 2$) and hexatic ($p = 6$) order are independent of eachother for different cell densities and different cell-cell adhesion strengths. q_6 (y-axis) versus q_2 (x-axis) for different densities a) low density and b) high density, for wildtype MDCK cell monolayer and E-cadherin knockout cell monolayer. For each cell and each timestep we plot one point (q_2, q_6).The E-cadherin cells lack an adhesion protein and have therefore weaker cell-cell adhesions.

bioRxiv preprint doi: https://doi.org/10.1101/2025.01.03.631196; this version posted January 3, 2025. The copyright holder for this preprint (which was not certified by peer review) is the author/funder, who has granted bioRxiv a license to display the preprint in perpetuity. It is made available under aCC-BY 4.0 International license.

Discussion

In this study, we introduced Minkowski tensors as a robust and versatile tool for quantifying p-atic order in multicellular systems, particularly in scenarios involving rounded or irregular cell shapes. By applying this framework to extensive datasets from two distinct computational models—the active vertex model and the multiphase field model—we identified universal trends: increasing activity and deformability of the cells enhance nematic order ($p = 2$) while diminishing hexatic order ($p = 6$). The consistency of these findings across two models, despite their inherent differences, underscores the generality and relevance of our results.

While various shape characterization methods, such as the bond order parameter (***Loewe et al., 2020***; ***Monfared et al., 2023***) and the shape function γ_p (***Armengol-Collado et al., 2023***), have been explored in the literature, we demonstrated that the choice of shape descriptor significantly impacts the conclusions drawn. Applying γ_p to data from the active vertex model revealed qualitative discrepancies: for $p = 2$, γ_p and q_p behaved similarly, but for $p = 6$, γ_p exhibited significant changes. Such divergences, together with limited mathematical foundations, highlight the limitations of γ_p in capturing consistent patterns and emphasize the need for stable, reliable shape measures like the Minkowski tensors. In contrast to the bond order parameter or the shape function γ_p the stability of Minkowski tensors can be mathematically justified. We have further demonstrated why bond order parameter or the shape function γ_p fail in certain situations. This finding is not merely a technical nuance; the choice of shape detection method fundamentally influences the interpretation of p-atic order. Consequently, selecting a robust shape descriptor is critical for obtaining meaningful and reproducible insights into orientational order in multicellular systems.

A critical question in the literature has been whether shape measures for different p-atic orders can be directly compared. While some studies have suggested relationships between γ_2 and γ_6 (***Armengol-Collado et al., 2023***), our results refute this notion. We demonstrated that measures like q_2 and q_6 capture fundamentally distinct aspects of cell shape and alignment, and comparing them directly is both mathematically and biologically misleading. We further tested the hypothesis of a hexatic-nematic crossover at larger length scales by coarse-graining q_2 and q_6 across spatial domains. The results showed no consistent trends indicative of a crossover, regardless of the coarse-graining strategy and the considered model. Instead, the apparent convergence of Q_2 and Q_6 values (coarse-grained values of q_2 and q_6) with increasing activity or deformability simply reflected the same trends observed at the individual cell scale. This reinforces the conclusion that comparisons of p-atic orders across different p lack a robust basis and that claims of crossovers require careful reconsideration.

Our findings suggest that p-atic orders should be studied independently across length scales, as they describe complementary aspects of cellular organization. The coexistence of distinct orientational orders emphasized in different studies—such as nematic ($p = 2$) (***Duclos et al., 2017***; ***Saw et al., 2017***; ***Kawaguchi et al., 2017***), tetratic ($p = 4$) (***Cislo et al., 2023***), and hexatic ($p = 6$) (***Li and Ciamarra, 2018***)—is not contradictory but highlights the rich, multifaceted nature of cellular organization. Rather than searching for a single dominant order, future research should focus on the interplay of different p-atic orders and their associated defects. This suggests to not only consider p-atic liquid crystal theories ***Giomi et al. (2022)*** for one p, but combinations of these models for various p's. Understanding how these orders interact may reveal how they collectively regulate morphogenetic processes.

Connecting p-atic orders to biological function remains a critical avenue for exploration. While the mathematical independence of q_2, q_6, and other shape measures precludes the identification of a universal dominant order, biological systems may exhibit context-dependent preferences. For example, a specific p-atic order might correlate with or drive a key morphogenetic event. Investigating these connections could yield insights into how tissues achieve functional organization and adapt to environmental cues. As such, while it is difficult to speak of dominating orders from a mathematical point of view, there could be a dominating order from a biological point of view,

bioRxiv preprint doi: https://doi.org/10.1101/2025.01.03.631196; this version posted January 3, 2025. The copyright holder for this preprint (which was not certified by peer review) is the author/funder, who has granted bioRxiv a license to display the preprint in perpetuity. It is made available under aCC-BY 4.0 International license.

meaning the p-atic order connected to the governing biological process.

Acknowledgments

We acknowledge fruitful discussions with Björn Böttger and Brendan Tobin. HJ acknowledges funding by the European Union's Horizon 2020 research and innovation programme under the Marie Skłodowska-Curie grant agreement No. 945371. RS acknowledges support from the UK Engineering and Physical Sciences Research Council (Award EP/W023946/1). AD acknowledges funding from the Novo Nordisk Foundation (grant No. NNF18SA0035142 and NERD grant No. NNF21OC0068687), Villum Fonden (grant No. 29476), and the European Union (ERC, PhysCoMeT, 101041418). AV acknowledges funding from the German Research Foundation (Award FOR3013 "Vector- and tensor-valued surface PDEs") and computing resources provided by JSC through MORPH and by ZIH through WIR. Views and opinions expressed are however those of the authors only and do not necessarily reflect those of the European Union or the European Research Council. Neither the European Union nor the granting authority can be held responsible for them.

References

Alert R, Trepat X. Physical models of collective cell migration. Annual Review of Condensed Matter Physics. 2020; 11:77–101.

Alesker S. Description of continuous isometry covariant valuations on convex sets. Geometriae Dedicata. 1999; 74:241–248.

Alt S, Ganguly P, Salbreux G. Vertex models: from cell mechanics to tissue morphogenesis. Philosophical Transactions of the Royal Society B: Biological Sciences. 2017; 372(1720):20150520.

Armengol-Collado JM, Carenza LN, Eckert J, Krommydas D, Giomi L. Epithelia are multiscale active liquid crystals. Nature Physics. 2023; 19:1773–1779.

Armengol-Collado JM, Carenza LN, Giomi L. Hydrodynamics and multiscale order in confluent epithelia. eLife. 2024; 13:e86400.

Balasubramaniam L, Doostmohammadi A, Saw TB, Narayana GHNS, Mueller R, Dang T, Thomas M, Gupta S, Sonam S, Yap AS, Toyama Y, Mège RM, Yeomans JM, Ladoux B. Investigating the nature of active forces in tissues reveals how contractile cells can form extensile monolayers. Nature Materials. 2021; 20(8):1156–1166.

Beisbart C, Barbosa MS, Wagner H, Costa LdF. Extended morphometric analysis of neuronal cells with minkowski valuations. The European Physical Journal B. 2006; 52:531–546.

Beisbart C, Dahlke R, Mecke K, Wagner H. Vector- and tensor-valued descriptors for spatial patterns. In: Mecke K, Stoyan D, editors. *Morphology of Condensed Matter: Physics and Geometry of Spatially Complex Systems* Berlin, Heidelberg: Springer Berlin Heidelberg; 2002.p. 238–260.

Bernard EP, Krauth W. Two-step melting in two dimensions: first-order liquid-hexatic transition. Physical Review Letters. 2011; 107:155704.

Bi D, Yang X, Marchetti MC, Manning ML. Motility-driven glass and jamming transitions in biological tissues. Physical Review X. 2016; 6:021011.

Bi D, Lopez J, Schwarz JM, Manning ML. A density-independent rigidity transition in biological tissues. Nature Physics. 2015; 11(12):1074–1079.

Bladon P, Frenkel D. Dislocation unbinding in dense two-dimensional crystals. Physical Review Letters. 1995; 74:2519–2522.

Bowick MJ, Manyuhina OV, Serafin F. Shapes and singularities in triatic liquid-crystal vesicles. Europhysics Letters. 2017; 117(2):26001.

Cislo DJ, Yang F, Qin H, Pavlopoulos A, Bowick MJ, Streichan SJ. Active cell divisions generate fourfold orientationally ordered phase in living tissue. Nature Physics. 2023; 19(8):1201–1210.

bioRxiv preprint doi: https://doi.org/10.1101/2025.01.03.631196; this version posted January 3, 2025. The copyright holder for this preprint (which was not certified by peer review) is the author/funder, who has granted bioRxiv a license to display the preprint in perpetuity. It is made available under aCC-BY 4.0 International license.

556 **Das A**, Sastry S, Bi D. Controlled neighbor exchanges drive glassy behavior, intermittency, and cell streaming
557 in epithelial tissues. Physical Review X. 2021; 11(4):041037.

558 **Duclos G**, Erlenkämper C, Joanny JF, Silberzan P. Topological defects in confined populations of spindle-shaped
559 cells. Nature Physics. 2017; 13(1):58–62.

560 **Durand M**, Heu J. Thermally driven order-disorder transition in two-dimensional soft cellular systems. Physical
561 Review Letters. 2019; 123(18):188001.

562 **Eckert J**, Ladoux B, Mège RM, Giomi L, Schmidt T. Hexanematic crossover in epithelial monolayers depends on
563 cell adhesion and cell density. Nature Communications. 2023; 14(1):5762.

564 **Farhadifar R**, Röper JC, Aigouy B, Eaton S, Jülicher F. The influence of cell mechanics, cell-cell interactions, and
565 proliferation on epithelial packing. Current biology. 2007; 17(24):2095–2104.

566 **Fletcher AG**, Osterfield M, Baker RE, Shvartsman SY. Vertex models of epithelial morphogenesis. Biophysical
567 Journal. 2014; 106(11):2291–2304.

568 **Gasser U**, Eisenmann C, Maret G, Keim P. Melting of crystals in two dimensions. ChemPhysChem. 2010;
569 11(5):963–970.

570 **Giomi L**, Toner J, Sarkar N. Hydrodynamic theory of p-atic liquid crystals. Physical Review E. 2022;
571 106(2):024701.

572 **Hadwiger H**. Vorlesungen über Inhalt, Oberfläche und Isoperimetrie. Springer Berlin Heidelberg; 1975.

573 **Hakim V**, Silberzan P. Collective cell migration: a physics perspective. Reports on Progress in Physics. 2017;
574 80:076601.

575 **Halperin BI**, Nelson DR. Theory of two-dimensional melting. Physical Review Letters. 1978; 41:121–124.

576 **Happel L**, Voigt A. Coordinated motion of epithelial layers on curved surfaces. Physical Review Letters. 2024;
577 132:078401.

578 **Honda H**. Geometrical models for cells in tissues. International review of cytology. 1983; 81:191–248.

579 **Honda H**, Nagai T. Mathematical models of cell-based morphogenesis. Springer; 2022.

580 **Hug D**, Schneider R, Schuster R. The space of isometry covariant tensor valuations. St Petersburg Mathematical
581 Journal. 2007 02; 19:137–158.

582 **Hug D**, Schneider R, Schuster R. Integral geometry of tensor valuations. Advances in Applied Mathematics.
583 2008; 41(4):482–509.

584 **Jain HP**, Hu RDJG, Angheluta L. Emergent directional migration due to interplay between cell shape and T1
585 transitions. Under review. 2024; .

586 **Jain HP**, Voigt A, Angheluta L. Robust statistical properties of T1 transitions in a multi-phase field model of cell
587 monolayers. Scientific Reports. 2023; 13(1):10096.

588 **Jain HP**, Voigt A, Angheluta L. From cell intercalation to flow, the importance of T1 transitions. Physical Review
589 Research. 2024; 6(3):033176.

590 **Kapfer S**. Morphometry and Physics of Particulate and Porous Media. PhD thesis, FAU Erlangen-Nürnberg;
591 2012.

592 **Kapfer SC**, Mickel W, Mecke K, Schröder-Turk GE. Jammed spheres: Minkowski tensors reveal onset of local
593 crystallinity. Physical Review E. 2012; 85:030301.

594 **Kawaguchi K**, Kageyama R, Sano M. Topological defects control collective dynamics in neural progenitor cell
595 cultures. Nature. 2017; 545(7654):327–331.

596 **Killeen A**, Bertrand T, Lee CF. Polar fluctuations lead to extensile nematic behavior in confluent tissues. Physical
597 Review Letters. 2022; 128(7):078001.

598 **Klain DA**. The minkowski problem for polytopes. Advances in Mathematics. 2004; 185(2):270–288.

599 **Klatt MA**, Hörmann M, Mecke K. Characterization of anisotropic gaussian random fields by minkowski tensors.
600 Journal of Statistical Mechanics: Theory and Experiment. 2022; 2022(4):043301.

bioRxiv preprint doi: https://doi.org/10.1101/2025.01.03.631196; this version posted January 3, 2025. The copyright holder for this preprint (which was not certified by peer review) is the author/funder, who has granted bioRxiv a license to display the preprint in perpetuity. It is made available under aCC-BY 4.0 International license.

Koride S, Loza AJ, Sun SX. Epithelial vertex models with active biochemical regulation of contractility can explain organized collective cell motility. APL bioengineering. 2018; 2(3).

Krommydas D, Carenza LN, Giomi L. Hydrodynamic enhancement of p-atic defect dynamics. Physical Review Letters. 2023; 130(9):098101.

Laine RF, Tosheva KL, Gustafsson N, Gray RDM, Almada P, Albrecht D, Risa GT, Hurtig F, Lindås AC, Baum B, Mercer J, Leterrier C, Pereira PM, Culley S, Henriques R. NanoJ: a high-performance open-source super-resolution microscopy toolbox. Journal of Physics D: Applied Physics. 2019; 52(16):163001.

Li X, Das A, Bi D. Mechanical heterogeneity in tissues promotes rigidity and controls cellular invasion. Physical Review Letters. 2019; 123:058101.

Li YW, Ciamarra MP. Role of cell deformability in the two-dimensional melting of biological tissues. Physical Review Materials. 2018; 2(4):045602.

Loewe B, Chiang M, Marenduzzo D, Marchetti MC. Solid-liquid transition of deformable and overlapping active particles. Physical Review Letters. 2020; 125:038003.

Maroudas-Sacks Y, Garion L, Shani-Zerbib L, Livshits A, Braun E, Keren K. Topological defects in the nematic order of actin fibres as organization centres of hydra morphogenesis. Nature Physics. 2021; 17(2):251–259.

McMullen P. Isometry covariant valuations on convex bodies. In: *Second international conference in stochastic geometry, convex bodies and empirical measures, Agrigento, Italy, September 9–14, 1996* Palermo: Circolo Matematico di Palermo; 1997.p. 259–271.

Mecke KR. Additivity, convexity, and beyond: Applications of minkowski functionals in statistical physics. In: Mecke KR, Stoyan D, editors. *Statistical Physics and Spatial Statistics* Berlin, Heidelberg: Springer Berlin Heidelberg; 2000. p. 111–184.

Melo S, Guerrero P, Moreira Soares M, Bordin JR, Carneiro F, Carneiro P, Dias MB, Carvalho J, Figueiredo J, Seruca R, Travasso RDM. The ECM and tissue architecture are major determinants of early invasion mediated by E-cadherin dysfunction. Communications Biology. 2023; 6(1):1132.

Mickel W, Kapfer SC, Schröder-Turk GE, Mecke K. Shortcomings of the bond orientational order parameters for the analysis of disordered particulate matter. The Journal of Chemical Physics. 2013; 138(4):044501.

Minkowski H. Allgemeine Lehrsätze über die convexen Polyeder. Nachrichten von der Gesellschaft der Wissenschaften zu Göttingen, Mathematisch-Physikalische Klasse. 1897; 1897:198–220.

Monfared S, Ravichandran G, Andrade J, Doostmohammadi A. Mechanical basis and topological routes to cell elimination. eLife. 2023; 12:e82435.

Moure A, Gomez H. Phase-field modeling of individual and collective cell migration. Archives of Computational Methods in Engineering. 2021; 28:311–344.

Mueller R, Yeomans JM, Doostmohammadi A. Emergence of active nematic behavior in monolayers of isotropic cells. Physical Review Letters. 2019; 122:048004.

Murray CA, Van Winkle DH. Experimental observation of two-stage melting in a classical two-dimensional screened coulomb system. Physical Review Letters. 1987 Mar; 58:1200–1203.

Nelson DR, Halperin BI. Dislocation-mediated melting in two dimensions. Physical Review B. 1979 Mar; 19:2457–2484.

Onsager L. The effects of shape on the interaction of colloidal particales. Annals of the New York Academy of Sciences. 1949; 51(4):627–659.

Pasupalak A, Yan-Wei L, Ni R, Ciamarra MP. Hexatic phase in a model of active biological tissues. Soft matter. 2020; 16(16):3914–3920.

Praetorius S, Voigt A. Collective cell behaviour – a cell-based parallelisation approach for a phase field active polar gel model. No. 49 in NIC Series, Jülich: Forschungszentrum Jülich GmbH, Zentralbibliothek; 2018.

Pylvänäinen JW, Laine RF, Saraiva BMS, Ghimire S, Follain G, Henriques R, Jacquemet G. Fast4DReg: Fast registration of 4D microscopy datasets. bioRxiv. 2022; https://www.biorxiv.org/content/early/2022/10/14/2022.08.22.504744.

bioRxiv preprint doi: https://doi.org/10.1101/2025.01.03.631196; this version posted January 3, 2025. The copyright holder for this preprint (which was not certified by peer review) is the author/funder, who has granted bioRxiv a license to display the preprint in perpetuity. It is made available under aCC-BY 4.0 International license.

Ravichandran Y, Vogg M, Kruse K, Pearce DJ, Roux A. Topology changes of the regenerating hydra define actin nematic defects as mechanical organizers of morphogenesis. bioRxiv. 2024; p. 2024–04.

Salvalaglio M, Voigt A, Wise SM. Doubly degenerate diffuse interface models of surface diffusion. Mathematical Methods in the Applied Sciences. 2021; 44:5385–5405.

Saw TB, Doostmohammadi A, Nier V, Kocgozlu L, Thampi S, Toyama Y, Marcq P, Lim CT, Yeomans JM, Ladoux B. Topological defects in epithelia govern cell death and extrusion. Nature. 2017; 544(7649):212–216.

Saye RI, Sethian JA. Analysis and applications of the voronoi implicit interface method. Journal of Computational Physics. 2012; 231(18):6051–6085.

Saye RI, Sethian JA. The voronoi implicit interface method for computing multiphase physics. Proceedings of the National Academy of Science. 2011; 108(49):19498–19503.

Schaller F, Kapfer S, Klatt M, Hug D, Last G, Mecke K, Schröder-Turk G, morphometry.org; 2024. https://morphometry.org.

Schneider R. Convex bodies: The Brunn–Minkowski theory. Encyclopedia of Mathematics and its Applications, Cambridge University Press; 2013.

Schröder-Turk GE, Mickel W, Kapfer SC, Schaller FM, Breidenbach B, Hug D, Mecke K. Minkowski tensors of anisotropic spatial structure. New Journal of Physics. 2013; 15(8):083028.

Schröder-Turk GE, Mickel W, Schröter M, Delaney GW, Saadatfar M, Senden TJ, Mecke K, Aste T. Disordered spherical bead packs are anisotropic. Europhysics Letters. 2010; 90(3):34001.

Schröder-Turk GE, Kapfer S, Breidenbach B, Beisbart C, Mecke K. Tensorial minkowski functionals and anisotropy measures for planar patterns. Journal of Microscopy. 2010; 238(1):57–74.

Sknepnek R, Djafer-Cherif I, Chuai M, Weijer C, Henkes S. Generating active T1 transitions through mechanochemical feedback. eLife. 2023; 12:e79862.

Stringer C, Wang T, Michaelos M, Pachitariu M. Cellpose: a generalist algorithm for cellular segmentation. Nature Methods. 2021; 18:100–106.

Tinevez JY, Perry N, Schindelin J, Hoopes GM, Reynolds GD, Laplantine E, Bednarek SY, Shorte SL, Eliceiri KW. TrackMate: An open and extensible platform for single-particle tracking. Methods. 2017; 115:80–90.

Tong S, Sknepnek R, Košmrlj A. Linear viscoelastic response of the vertex model with internal and external dissipation: Normal modes analysis. Physical Review Research. 2023; 5(1):013143.

Vaxman A, Campen M, Diamanti O, Panozzo D, Bommes D, Hildebrandt K, Ben-Chen M. Directional field synthesis, design, and processing. Computer Graphics Forum. 2016; 35(2):545–572.

Vey S, Voigt A. AMDiS: Adaptive multidimensional simulations. Computing and Visualization in Science. 2007; 10(1):57–67.

Virga EG. Octupolar order in two dimensions. The European Physical Journal E. 2015; 38(6).

Wang PY, Mason TG. A Brownian quasi-crystal of pre-assembled colloidal penrose tiles. Nature. 2018; 561(7721):94–99.

Wenzel D, Voigt A. Multiphase field models for collective cell migration. Physical Review E. 2021; 184:054410.

Witkowski T, Ling S, Praetorius S, Voigt A. Software concepts and numerical algorithms for a scalable adaptive parallel finite element method. Advances in Computational Mathematics. 2015; 41(6):1145–1177.

Wojciechowski KW, Frenkel D. Tetratic phase in the planar hard square system? Computational Methods in Science and Technology. 2004; 10:235–255.

Yu T, Mason TG. Heptatic liquid quasi-crystals by colloidal lithographic pre-assembly. Journal of Colloid and Interface Science. 2023; .

Zahn K, Lenke R, Maret G. Two-stage melting of paramagnetic colloidal crystals in two dimensions. Physical Review Letters. 1999; 82:2721–2724.

bioRxiv preprint doi: https://doi.org/10.1101/2025.01.03.631196; this version posted January 3, 2025. The copyright holder for this preprint (which was not certified by peer review) is the author/funder, who has granted bioRxiv a license to display the preprint in perpetuity. It is made available under aCC-BY 4.0 International license.

Appendix 1
Parameters for the computational models

Appendix 1—table 1. Values of the dimensionless parameters used in the active vertex model

Parameter	Description	Numerical Value
N	Number of cells	100
L	Simulation box size	10
T	Total simulation time	300
k_P	Perimeter elastic modulus	1.0
τ	Simulation time step	0.01
v_0	Self-propulsion strength (i.e. activity)	0.1 - 0.4
D_r	Rotation diffusion coefficient	0.05
p_0	Shape index of active cells	3.5 - 3.875

Appendix 1—table 2. Values of the dimensionless parameters used in the multiphase-field model simulations

Parameter	Description	Numerical Value
N	Number of cells	100
L	Simulation box size	100
T	Total simulation time	150
ϵ	Interface width	0.15
τ	Simulation time step	0.005
v_0	Self-propulsion strength (i.e. activity)	0.4 - 1.0
D_r	Rotation diffusion coefficient	0.01
α	Alignment parameter	0.1
Ca	Capillary number	0.05 - 0.2
In	Interaction number	0.1
a_a	Cell-cell attraction strength	1.0
a_r	Cell-cell repulsion strength	1.0
h	Mesh size	$5h \approx \epsilon$

bioRxiv preprint doi: https://doi.org/10.1101/2025.01.03.631196; this version posted January 3, 2025. The copyright holder for this preprint (which was not certified by peer review) is the author/funder, who has granted bioRxiv a license to display the preprint in perpetuity. It is made available under aCC-BY 4.0 International license.

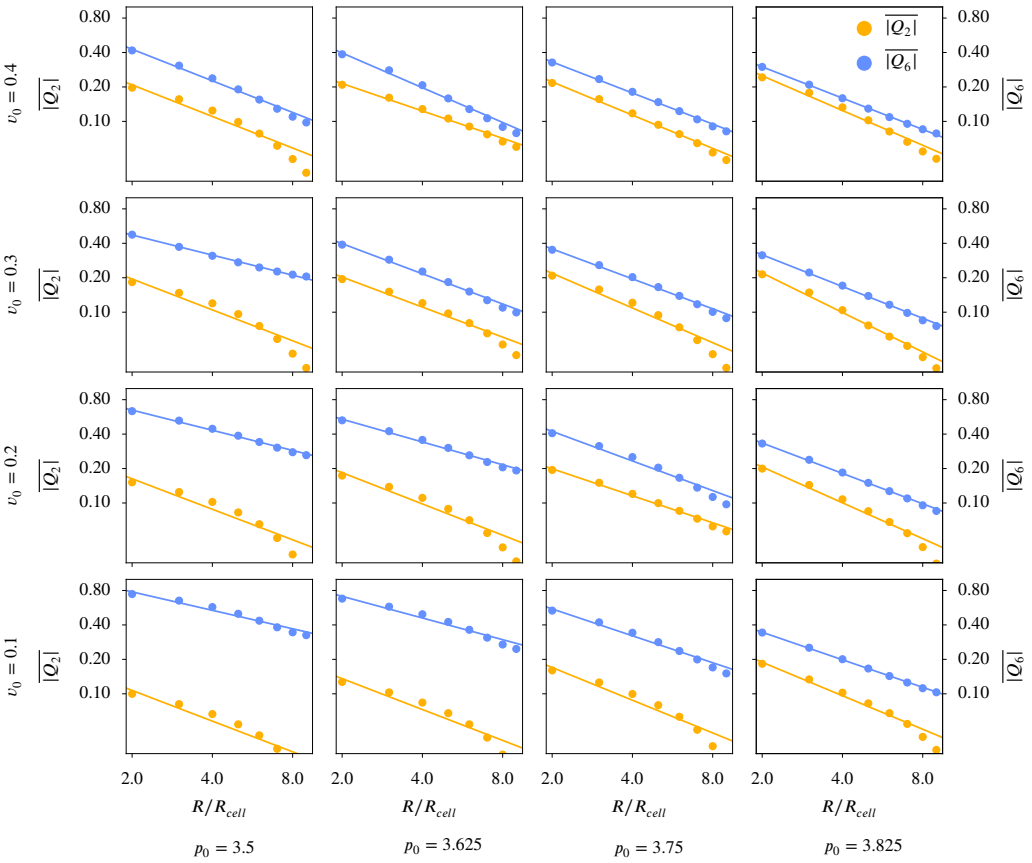
Appendix 2

Coarse graining results obtained with the Minkowski tensor

For comparison with the literature we are considering a coarse-graining, following closely the strategy used in ***Armengol-Collado et al.*** (***2023***). We therefore regard the coarse-grained strength of p-atic order $Q_p = Q_p(\mathbf{x})$, which is the average of all shape functions $\frac{\psi_p}{\psi_0}$ (or equivalently $q_p e^{ip\vartheta_p}$) of cells whose center of mass $\mathbf{x}_c$ lies within a circle with radius R and center $\mathbf{x}$. In a formula this is:

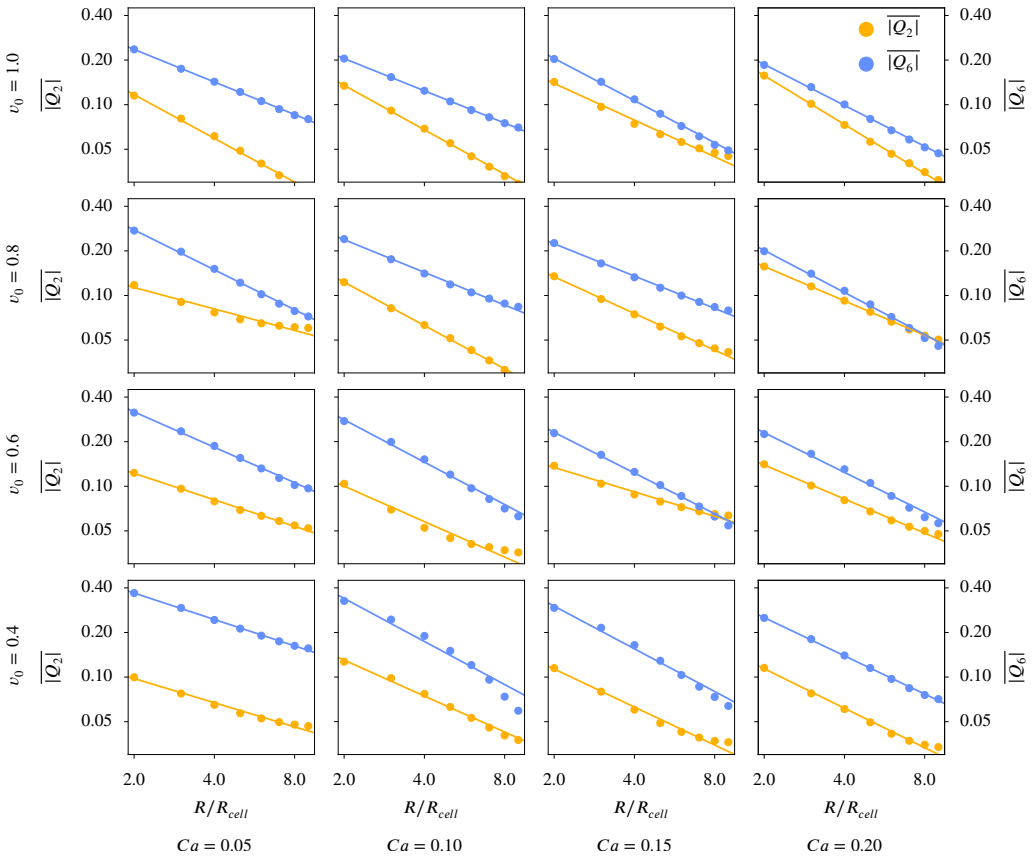
$$Q_p(\mathbf{x}) = \frac{\sum_{j=1}^{100} q_p(C_j) e^{ip\vartheta_p(C_j)} \Theta(R - |\mathbf{x} - \mathbf{x}_c(C_j)|)}{\sum_{j=1}^{100} \Theta(R - |\mathbf{x} - \mathbf{x}_c(C_j)|)} \tag{18}$$

whereby the formula uses that our simulations contain 100 cells. C_i denotes the i–th cell and Θ denotes the Heaviside step function with $\Theta(x) = 0$ for $x > 0$ and $\Theta(x) = 0$ otherwise. As in ***Armengol-Collado et al.*** (***2023***) the position $\mathbf{x}$ is sampled over a square grid with spacing $R_C = \sqrt{\frac{A_C}{\pi}}$ with A_C the cell area. For ***Appendix 2 Figure 13*** and ***Appendix 2Figure 14*** we took the average over all grid points and all time instances. The figures show the resulting data for the active vertex model and the multiphase field model, respectively.



Appendix 2—figure 13. Q_6 versus Q_2 for different coarse graining radii in the active vertex model, calculated according to ***Equation 18***. A logarithmic scaling was used for both axis. q_p and ϑ_p follow from ***Equation 7***, R_C is chosen as $\sqrt{\frac{A_C}{\pi}}$.

bioRxiv preprint doi: https://doi.org/10.1101/2025.01.03.631196; this version posted January 3, 2025. The copyright holder for this preprint (which was not certified by peer review) is the author/funder, who has granted bioRxiv a license to display the preprint in perpetuity. It is made available under aCC-BY 4.0 International license.

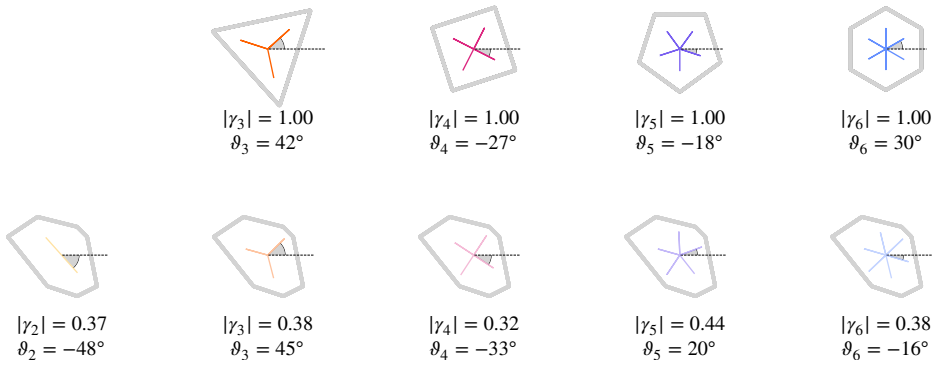


Appendix 2—figure 14. Q_6 versus Q_2 for different coarse graining radii in the multiphase field model, calculated according to ***Equation 18***. A logarithmic scaling was used for both axis. q_p and ϑ_p follow from ***Equation 7***, R_C is chosen as $\sqrt{\frac{A_C}{\pi}}$.

bioRxiv preprint doi: https://doi.org/10.1101/2025.01.03.631196; this version posted January 3, 2025. The copyright holder for this preprint (which was not certified by peer review) is the author/funder, who has granted bioRxiv a license to display the preprint in perpetuity. It is made available under aCC-BY 4.0 International license.

Appendix 3
Results using polygonal shape analysis

To visualize the similarities and differences between q_p and γ_p we show the analogue of ***Figure 4*** using the Minkowski tensors in ***Appendix 3 Figure 15*** using polygonal shape analysis. For regular polygons, both shape characterization methods behave in the same way as seen in the first row. For irregular shapes, like in the 2nd row, they already show a different behaviour. Note that the rounded shapes from ***Figure 4*** are missing in ***Appendix 3 Figure 15*** as γ_p requires a polygon.



Appendix 3—figure 15. Regular and irregular shapes, adapted from ***Armengol-Collado et al.*** (***2023***), with magnitude and orientation calculated by ***Equation 8*** and ***Equation 9***. The brightness scales with the magnitude $|\gamma_p|$.

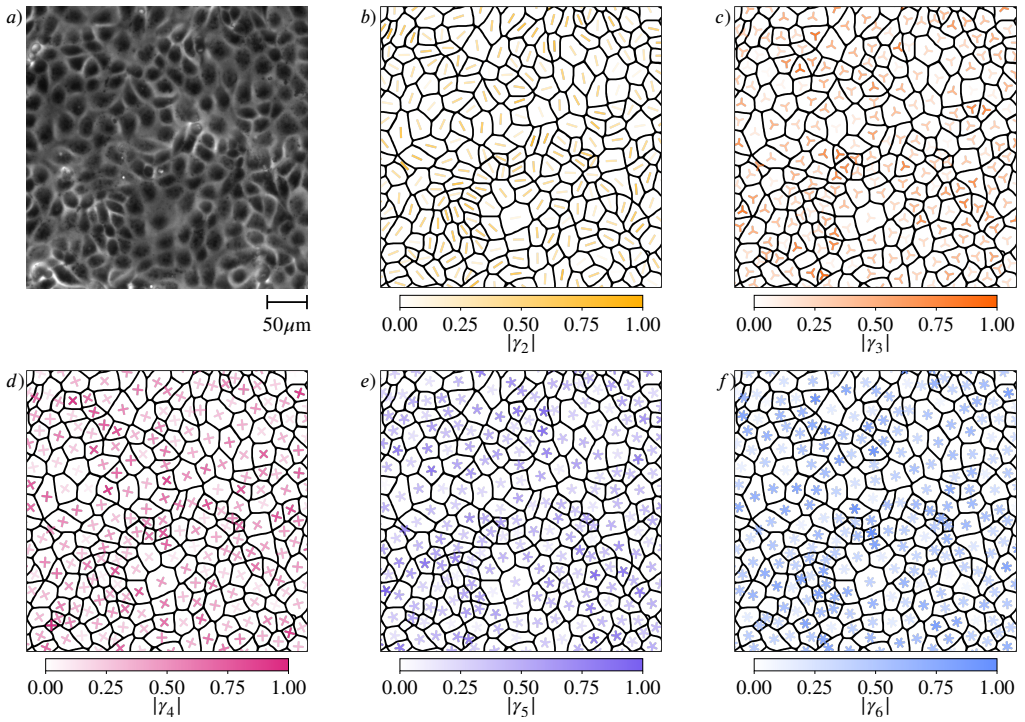
The influence of the choice of the shape characterization method is not only visible in the values for single shapes, it can also be seen in the mean and standard deviation. To illustrate this, we use γ_p to characterize the shapes from the same experimental data as in ***Figure 1*** and ***Figure 2***. The segmented data consists of smooth contours for each cell. As γ_p only works with vertex coordinates the first step is to identify these. Note that this always leads to the approximation of the cell shape with a polygon and therefore to a simplification of the shape. For finding the vertices we consider the Voronoi interface method (***Saye and Sethian, 2011***, ***2012***). Using the so obtained vertices and ***Equation 8*** and ***Equation 9*** leads to the results shown in ***Appendix 3 Figure 16*** and ***Appendix 3 Figure 17***. Compared to ***Figure 1*** and ***Figure 2***, where the Minkowski tensor was used for the same data, we see that the choice of the shape characterization method highly influences the results.

For comparison with the literature we are considering a coarse-graining, following the strategy introduced in ***Armengol-Collado et al.*** (***2023***). We therefore regard the coarse-grained shape function $\Gamma_p = \Gamma_p(\mathbf{x})$, which is the average of all shape functions γ_p of cells whose center of mass $\mathbf{x}_c$ lies within a circle with radius R and center $\mathbf{x}$. In a formula this is:

$$\Gamma_p(\mathbf{x}) = \frac{\sum_{j=1}^{100} \gamma_p(C_j)\Theta(R - |\mathbf{x} - \mathbf{x}_c(C_j)|)}{\sum_{j=1}^{100} \Theta(R - |\mathbf{x} - \mathbf{x}_c(C_j)|)} \tag{19}$$

whereby the formula uses that our simulations contain 100 cells. C_i denotes the i–th cell and Θ denotes the Heaviside step function with $\Theta(x) = 0$ for $x > 0$ and $\Theta(x) = 0$ otherwise. As in ***Armengol-Collado et al.*** (***2023***) the position $\mathbf{x}$ is sampled over a square grid with spacing $R_C = \sqrt{\frac{A_C}{\pi}}$ with A_C the cell area. For ***Appendix 3 Figure 20*** we took the average of Γ_p over all grid points and all time instances. The figure shows the resulting data for the active vertex model.

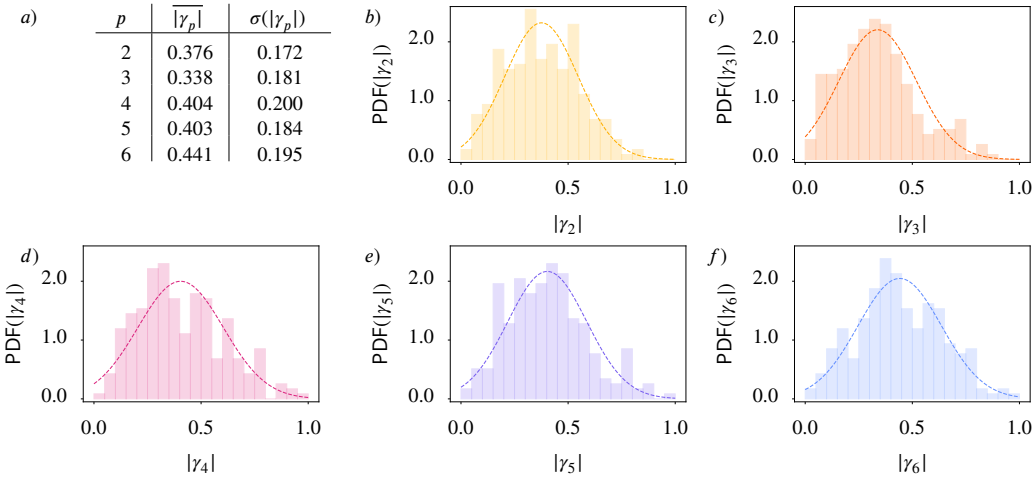
bioRxiv preprint doi: https://doi.org/10.1101/2025.01.03.631196; this version posted January 3, 2025. The copyright holder for this preprint (which was not certified by peer review) is the author/funder, who has granted bioRxiv a license to display the preprint in perpetuity. It is made available under aCC-BY 4.0 International license.



Appendix 3—figure 16. Shape classification of cells in wild-type MDCK cell monolayer. a) Raw experimental data. b) - f) Polygonal shape classification, visualized using γ_p calculated by ***Equation 8*** and ***Equation 9*** for $p = 2, 3, 4, 5, 6$, respectively. The brightness and the rotation of the p-atic director indicates the magnitude and the orientation, respectively.

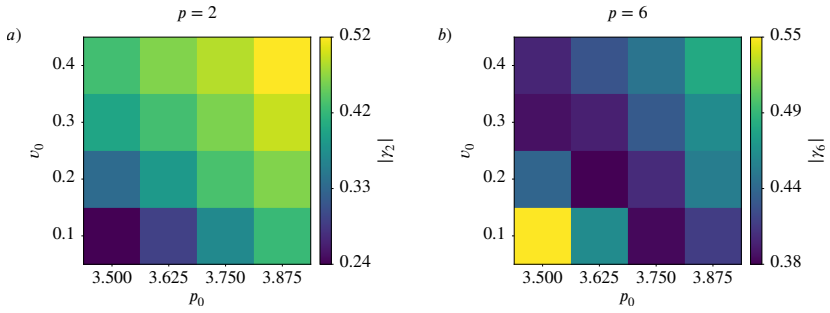
a)

p	$\overline{\lvert\gamma_p\rvert}$	$\sigma(\lvert\gamma_p\rvert)$
2	0.376	0.172
3	0.338	0.181
4	0.404	0.200
5	0.403	0.184
6	0.441	0.195

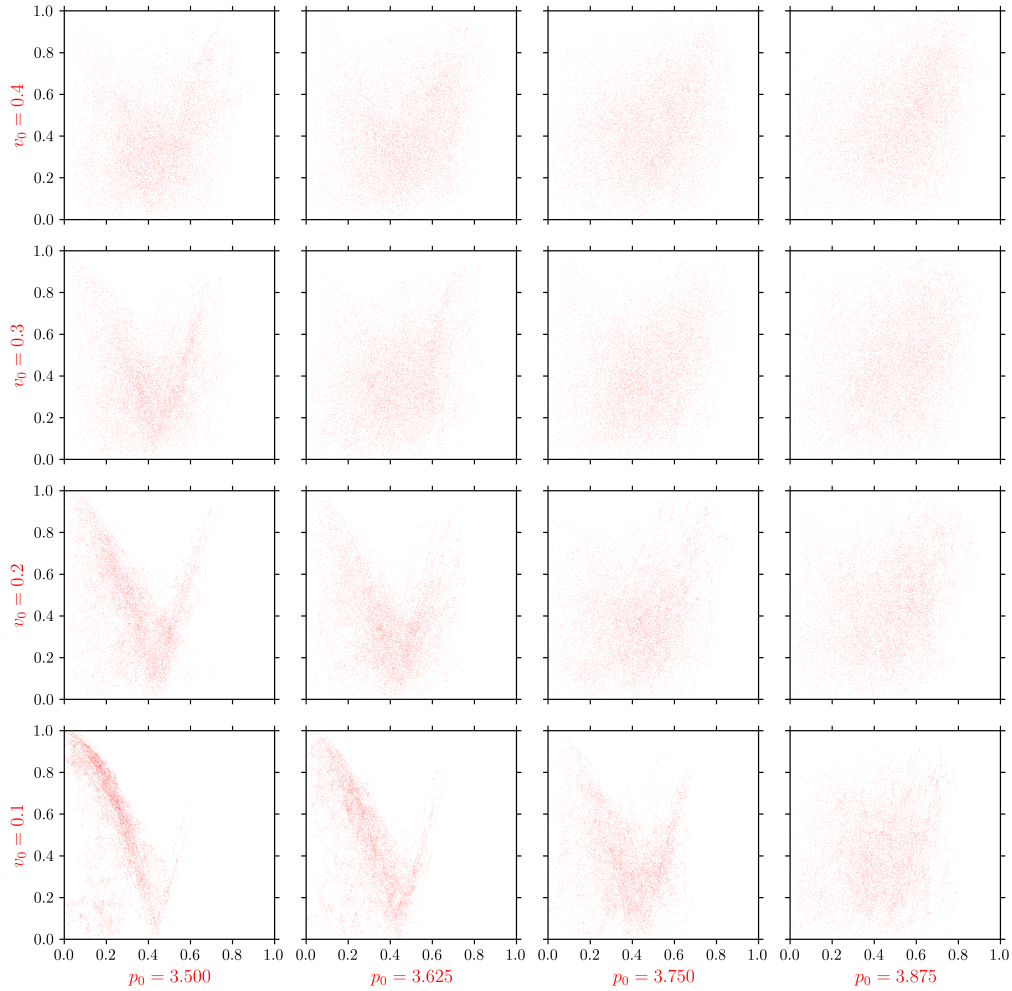


Appendix 3—figure 17. Statistical data for cell shapes identified in ***Appendix 3 Figure 16*** (. a) Mean $\overline{\lvert\gamma_p\rvert}$ and standard deviation $\sigma(\lvert\gamma_p\rvert)$ of $\lvert\gamma_p\rvert$. b) - f) Probability distribution function (PDF) of $\lvert\gamma_p\rvert$ for $p = 2, 3, 4, 5, 6$, respectively. Normal distributions with the same mean and standard deviations are added to the histograms as a guide to the eye.

bioRxiv preprint doi: https://doi.org/10.1101/2025.01.03.631196; this version posted January 3, 2025. The copyright holder for this preprint (which was not certified by peer review) is the author/funder, who has granted bioRxiv a license to display the preprint in perpetuity. It is made available under aCC-BY 4.0 International license.

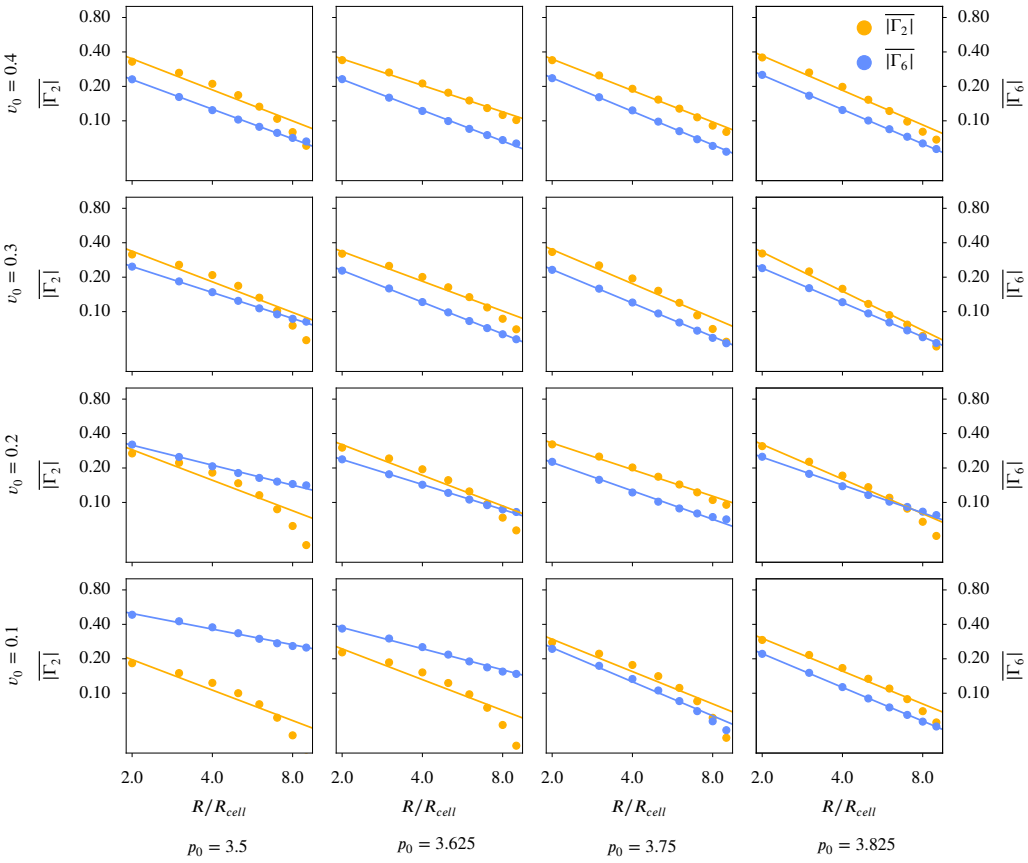


Appendix 3—figure 18. Mean value $\overline{\gamma_p}$ as function of deformability p_0 and activity v_0 for active vertex model. a) nematic order ($p = 2$), b) hexatic order ($p = 6$). While the behaviour of $|\gamma_2|$ qualitatively agrees with the behaviour of q_2, the behaviour of $|\gamma_6|$ is quite different to the one of q_6.



Appendix 3—figure 19. γ_6 (y-axis) versus γ_2 (x-axis) for all cells in the active vertex model. For each cell and each timestep we plot one point (γ_2, γ_6). Each panel corresponds to specific model parameters p_0 and v_0, representing deformability and activity.

bioRxiv preprint doi: https://doi.org/10.1101/2025.01.03.631196; this version posted January 3, 2025. The copyright holder for this preprint (which was not certified by peer review) is the author/funder, who has granted bioRxiv a license to display the preprint in perpetuity. It is made available under aCC-BY 4.0 International license.



Appendix 3—figure 20. Γ_6 versus Γ_2 for different coarse graining radii in the active vertex model, calculated according to ***Equation 19***. A logarithmic scaling was used for both axis. γ_p follows from ***Equation 8***, R_C is chosen as $\sqrt{\frac{A_C}{\pi}}$.

bioRxiv preprint doi: https://doi.org/10.1101/2025.01.03.631196; this version posted January 3, 2025. The copyright holder for this preprint (which was not certified by peer review) is the author/funder, who has granted bioRxiv a license to display the preprint in perpetuity. It is made available under aCC-BY 4.0 International license.

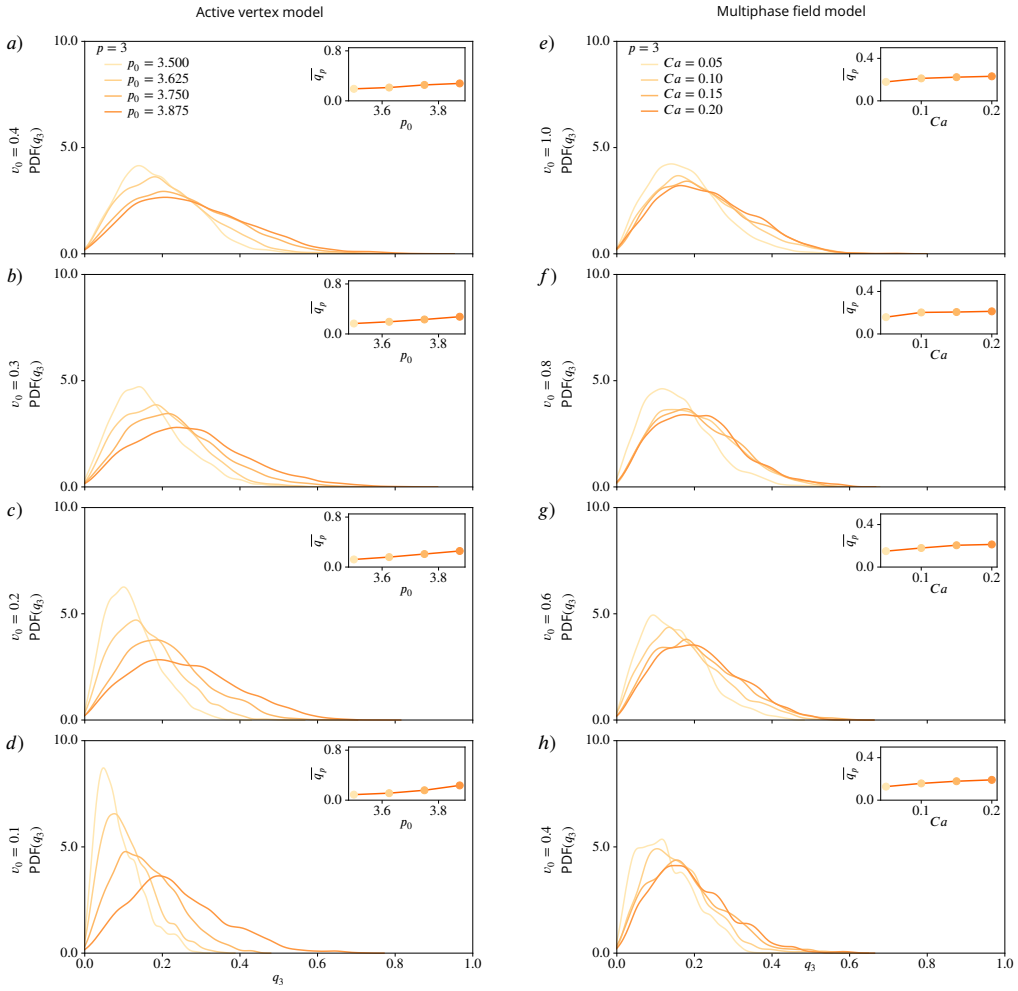
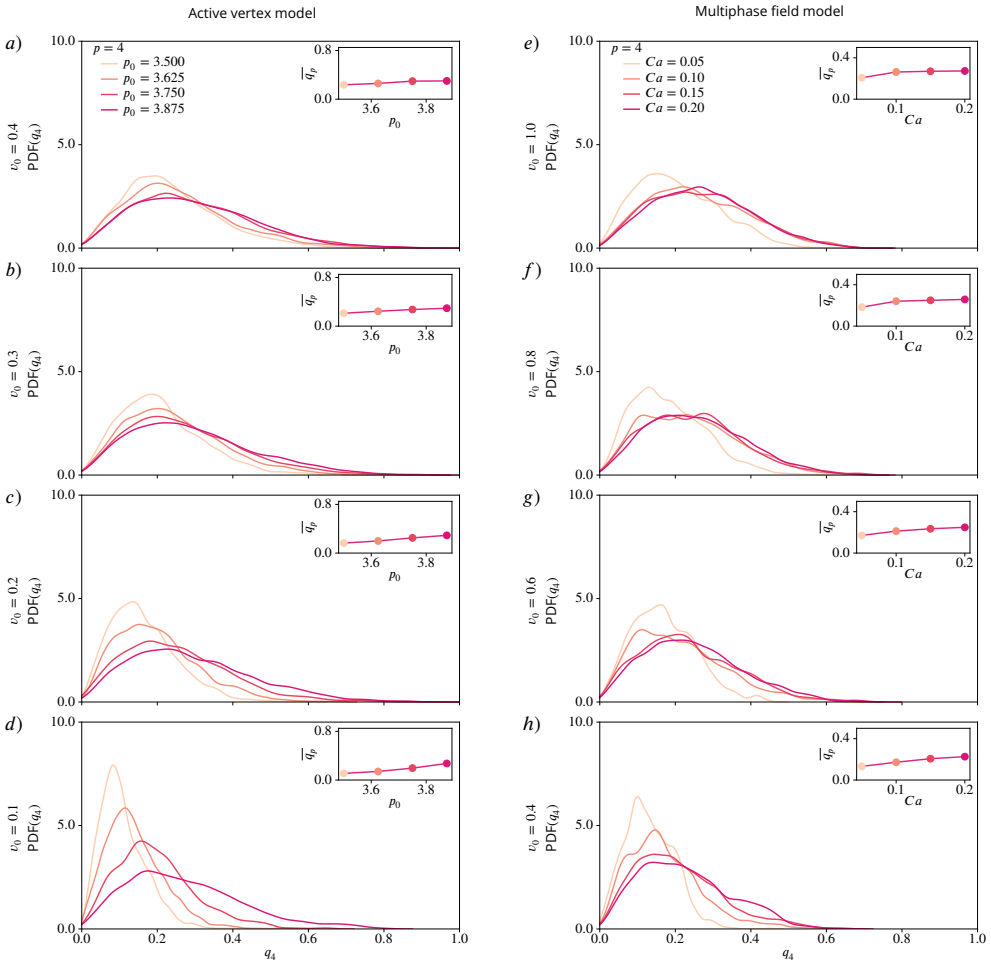


Figure 8—figure supplement 1. PDFs for q_3 using kde-plots, for varying deformability p_0 or Ca and fixed activity v_0. Inlets show mean values of q_3 as function of deformability. a) - d) active vertex model, e) - h) multiphase field model for descreasing activity.

bioRxiv preprint doi: https://doi.org/10.1101/2025.01.03.631196; this version posted January 3, 2025. The copyright holder for this preprint (which was not certified by peer review) is the author/funder, who has granted bioRxiv a license to display the preprint in perpetuity. It is made available under aCC-BY 4.0 International license.



733

Figure 8—figure supplement 2. PDFs for q_4 using kde-plots, for varying deformability p_0 or Ca and fixed activity v_0. Inlets show mean values of q_4 as function of deformability. a) - d) active vertex model, e) - h) multiphase field model for decreasing activity.

bioRxiv preprint doi: https://doi.org/10.1101/2025.01.03.631196; this version posted January 3, 2025. The copyright holder for this preprint (which was not certified by peer review) is the author/funder, who has granted bioRxiv a license to display the preprint in perpetuity. It is made available under aCC-BY 4.0 International license.

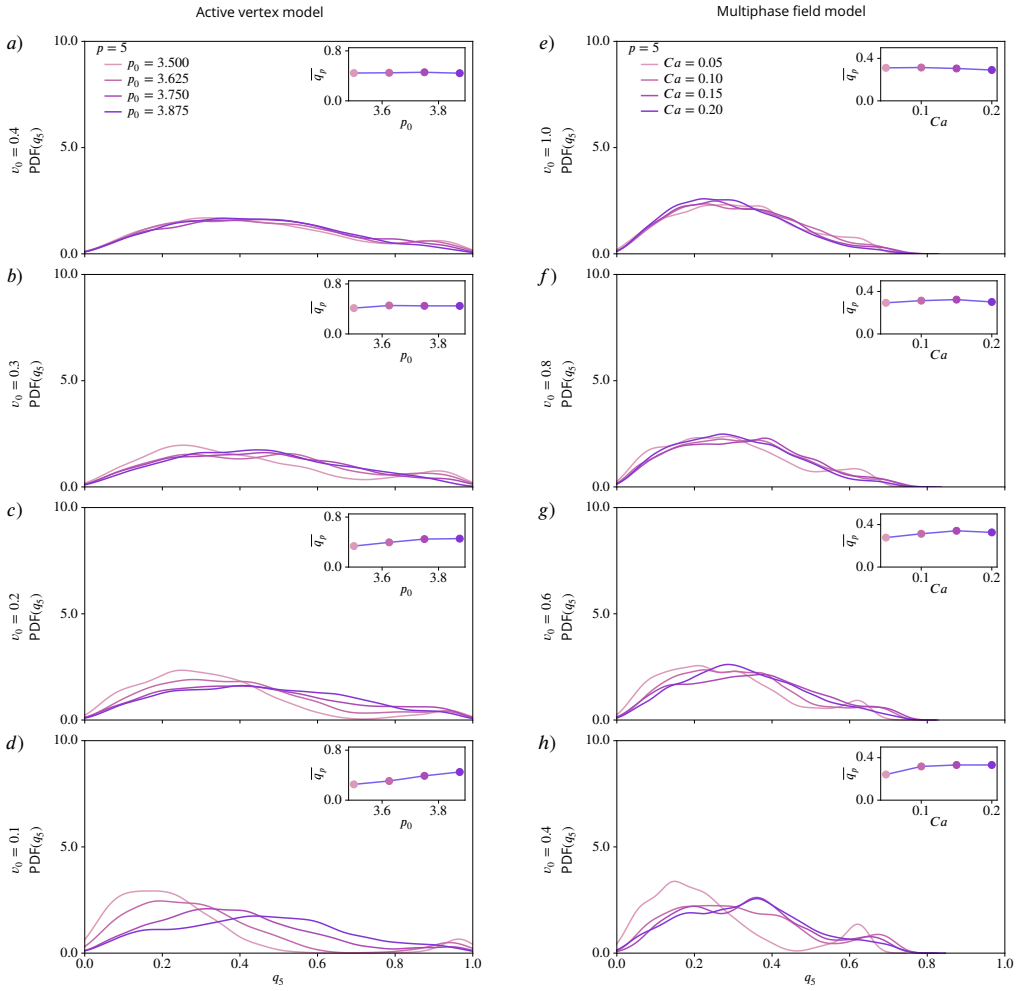


Figure 8—figure supplement 3. PDFs for q_5 using kde-plots, for varying deformability p_0 or Ca and fixed activity v_0. Inlets show mean values of q_5 as function of deformability. a) - d) active vertex model, e) - h) multiphase field model for decreasing activity.

bioRxiv preprint doi: https://doi.org/10.1101/2025.01.03.631196; this version posted January 3, 2025. The copyright holder for this preprint (which was not certified by peer review) is the author/funder, who has granted bioRxiv a license to display the preprint in perpetuity. It is made available under aCC-BY 4.0 International license.

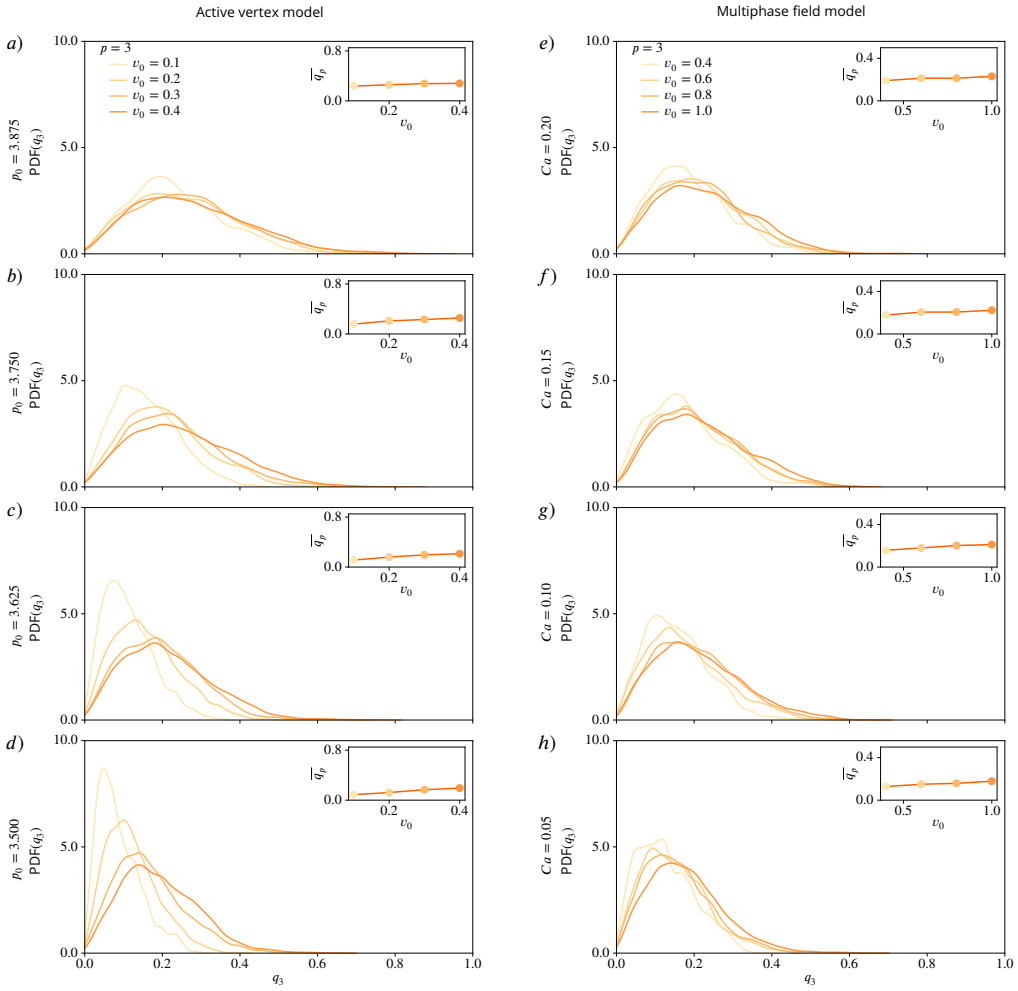


Figure 9—figure supplement 1. PDFs for q_3 using kde-plots, for varying activity v_0 and fixed deformability p_0 or Ca. Inlets show mean values of q_3 as function of activity. a) - d) active vertex model and e) - h) multiphase field model for decreasing deformability.

bioRxiv preprint doi: https://doi.org/10.1101/2025.01.03.631196; this version posted January 3, 2025. The copyright holder for this preprint (which was not certified by peer review) is the author/funder, who has granted bioRxiv a license to display the preprint in perpetuity. It is made available under aCC-BY 4.0 International license.

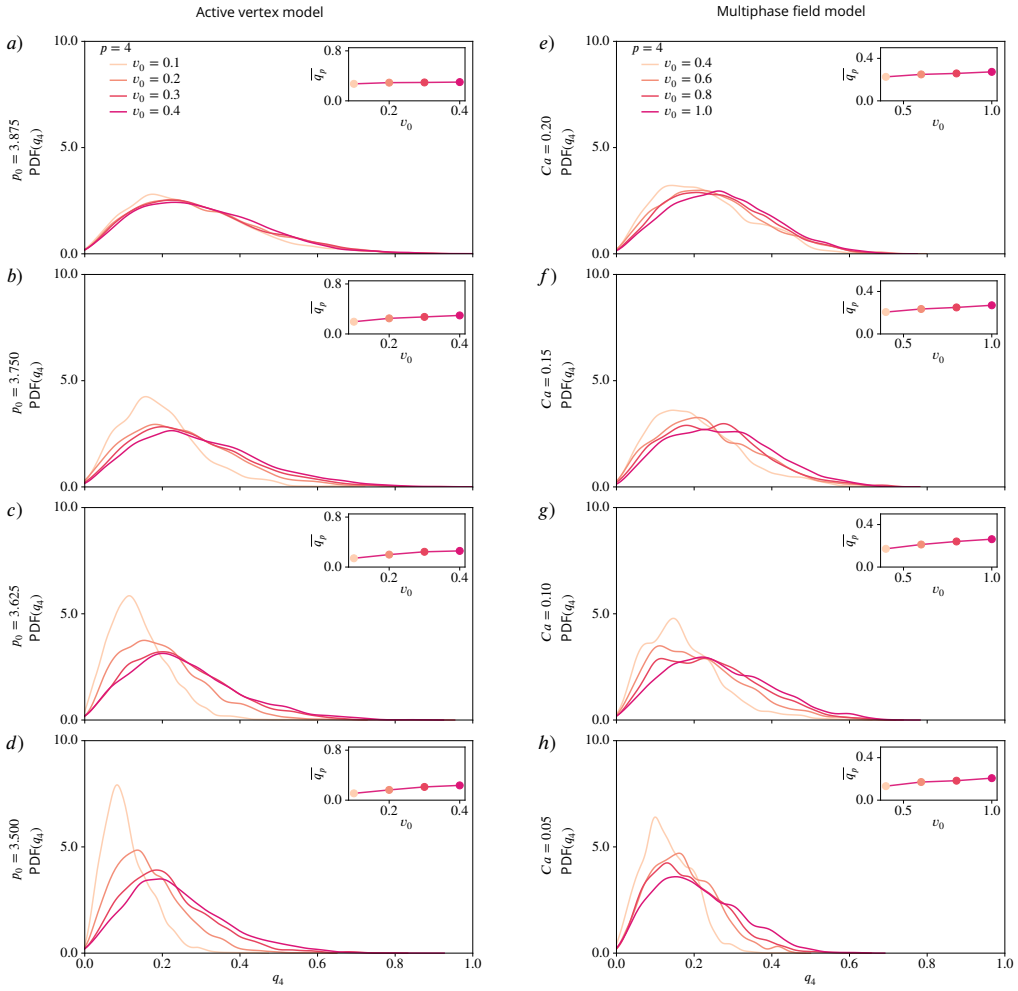


Figure 9—figure supplement 2. PDFs for q_4 using kde-plots, for varying activity v_0 and fixed deformability p_0 or Ca. Inlets show mean values of q_4 as function of activity. a) - d) active vertex model and e) - h) multiphase field model for decreasing deformability.

bioRxiv preprint doi: https://doi.org/10.1101/2025.01.03.631196; this version posted January 3, 2025. The copyright holder for this preprint (which was not certified by peer review) is the author/funder, who has granted bioRxiv a license to display the preprint in perpetuity. It is made available under aCC-BY 4.0 International license.

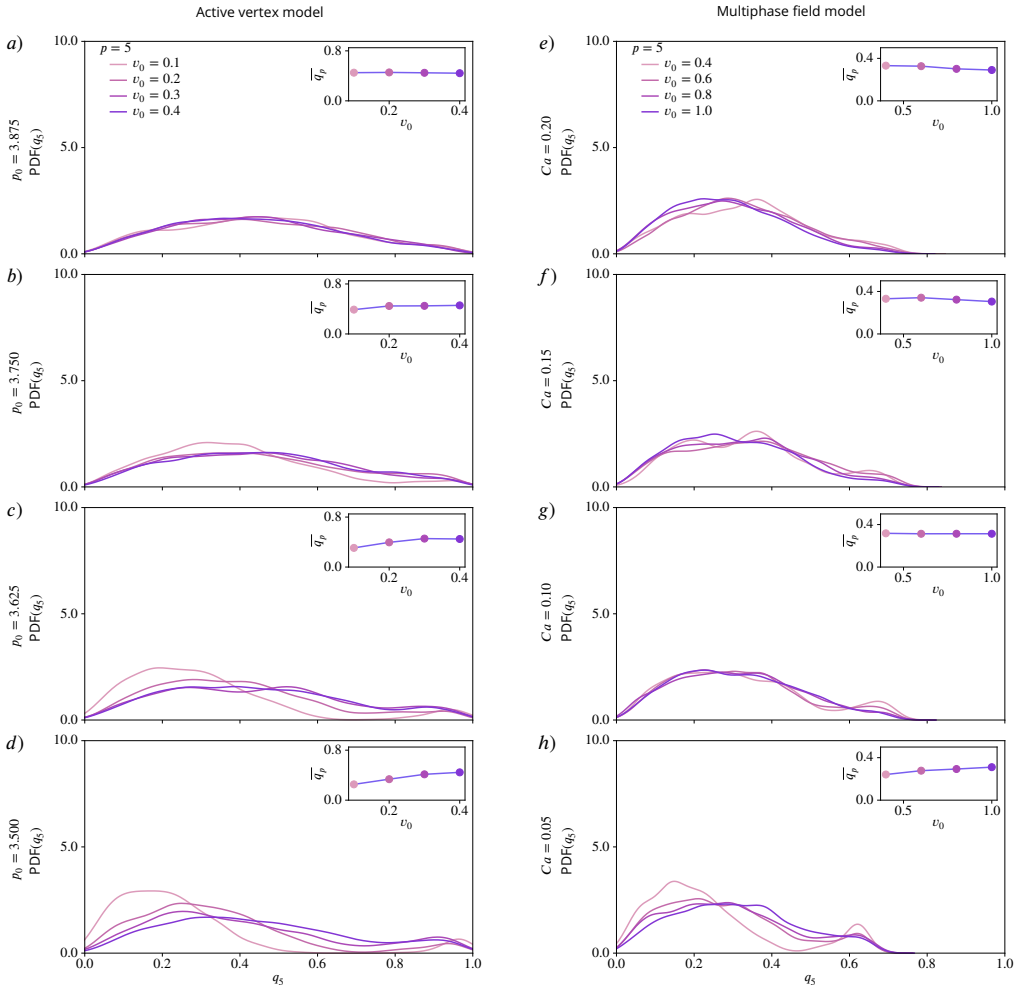


Figure 9—figure supplement 3. PDFs for q_5 using kde-plots, for varying activity v_0 and fixed deformability p_0 or Ca. Inlets show mean values of q_5 as function of activity. a) - d) active vertex model and e) - h) multiphase field model for decreasing deformability.

bioRxiv preprint doi: https://doi.org/10.1101/2025.01.03.631196; this version posted January 3, 2025. The copyright holder for this preprint (which was not certified by peer review) is the author/funder, who has granted bioRxiv a license to display the preprint in perpetuity. It is made available under aCC-BY 4.0 International license.

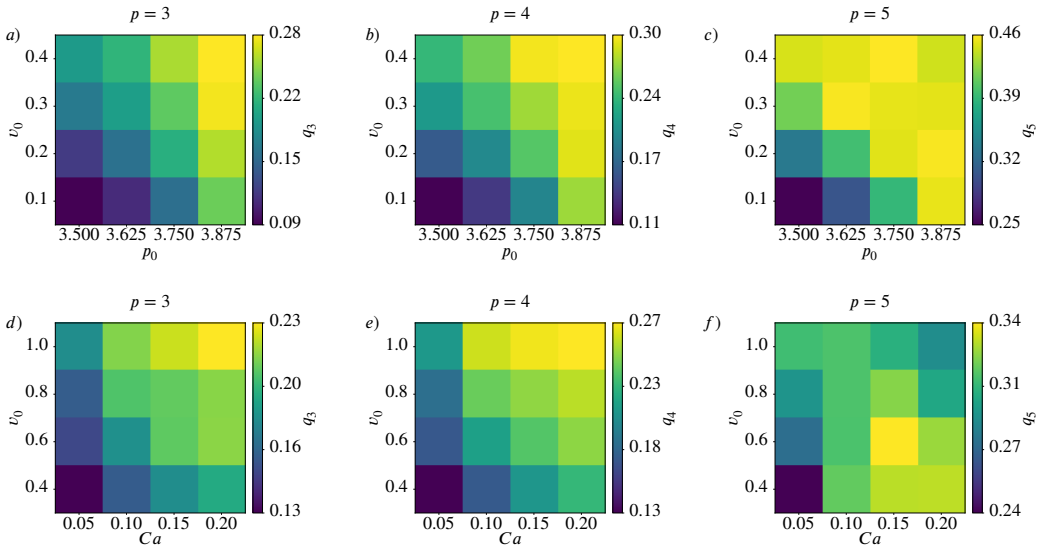


Figure 10—figure supplement 1. Mean value $\overline{q_p}$ for $p = 3$ (left), $p = 4$ (middle) and $p = 5$ (right) as function of deformability p_0 or Ca and activity v_0 for active vertex model (a) - c)) and multiphase field model (d) - f)).